Sounds of geological plumbing systems - How transient fluid circulation processes in faults and volcanoes shape sources and patterns of microseismicity

Gaspard Farge

UNIVERSITÉ PARIS CITÉ
INSTITUT DE PHYSIQUE DU GLOBE DE PARIS
École doctorale STEP'UP, ED 560
Équipe de Dynamique des Fluides Géologiques

SOUNDS OF GEOLOGICAL PLUMBING SYSTEMS

How transient fluid circulation processes in faults and volcanoes shape sources and patterns of microseismicity

GASPARD FARGE

Juillet 2022

Thèse de doctorat de Sciences de la Terre et de l'Environnement, *spécialité* Géophysique

dirigée par CLAUDE JAUPART *et* NIKOLAÏ SHAPIRO

Présentée et soutenue publiquement le 7 Septembre 2022, *devant un jury composé de:*

EMILY BRODSKY	Professeure (UC Santa Cruz)	Rapportrice
CAMILLA CATTANIA	Professeure associée (MIT)	Examinatrice
KRISTEL CHANARD	Chargée de recherche (IGN — UPC, IPGP)	Examinatrice
STÉPHANE RONDENAY	Professeur (Uni. Bergen)	Rapporteur
ALEXANDRE SCHUBNEL	Directeur de recherche (CRNS — ENS)	Examinateur (Pdt.)
CLAUDE JAUPART	Professeur (UPC, IPGP)	Directeur de thèse
NIKOLAI SHAPIRO	Directeur de recherche (CNRS — ISTerre)	Co-directeur de thèse

RÉSUMÉ DE LA THÈSE

L'activité des plus petits séismes détectés dans la Terre est symptomatique des changements infimes qui se produisent sous nos pieds. L'activité microsismique peut notamment être utilisée pour surveiller la façon dont les fluides circulent dans les failles ou les volcans, depuis des sources de fluides en profondeur jusqu'à la surface. Dans les zones de subduction par exemple, des signaux sismiques faibles, intermittents et de basse fréquence appelés tremor, composés de petits événements de basse fréquence (*low-frequency earthquakes*, ou LFEs) sont émis depuis l'interface entre les plaques. Dans ce manuscrit, nous essayons de comprendre comment des processus instables de circulation de fluide dans la zone de faille de subduction peuvent façonner le signal et les motifs spatio-temporels que dessinent le tremor, et comment celui-ci peut donc être utilisé pour diagnostiquer la dynamique du système hydraulique de la faille de subduction.

Dans une première partie, nous caractérisons la source des LFEs à Guerrero, au Mexique, et constatons que leur durée semble indépendante de leur magnitude. Cette observation est incompatible avec la vision classique selon laquelle les séismes devraient être générés par une rupture sur une faille. Elle peut cependant être reproduite par un modèle qui explique la source sismique des LFEs par de rapides changements de pression de fluide dans l'interface de la faille.

La source des LFEs n'est pas le seul indice que de fortes variations de pression de fluide se produisent dans l'interface de subduction. Quand cette zone est exhumée, les affleurements sont marqués par la signature d'ouvertures et de fermetures répétées de la perméabilité de la zone de faille, générant des conditions instables de pression dans le fluide. La dynamique de ce système hydraulique doit contribuer à la complexité des motifs d'activité du tremor, bien qu'elle soit rarement considérée dans les études tentant de les décrire dans leur entièreté.

Dans une deuxième partie, nous élaborons donc un modèle qui permettrait de décrire les processus dynamiques de circulation des fluides dans la faille de subduction, et leur lien avec le tremor. Nous modélisons l'ascension des fluides depuis des sources profondes de déshydratation métamorphique vers la surface, au travers d'un canal perméable dans l'interface de faille. Les segments faiblement perméable du canal entravent le flux, et génère localement de forts gradients de pression. La perméabilité des barrière s'ouvre puis se referme dans un mécanisme de valve, en réponse au gradient local de pression de fluide. Lorsque les valves se rompent, le changement brutal de pression génère un LFE. Les valves voisines communiquent par des transitoires de pression de fluide, qui déclenchent leur ouverture quand une valve à proximité s'ouvre. Cette interaction produit des motifs réalistes de sismicité synthétique, semblables à ceux observés pour le tremor : cascades d'activité, synchronisation et migration de l'activité font apparaissent et se développent sur

plusieurs échelles spatiales et temporelles. Le flux fluide à l'entrée du système contrôle la présence et le style d'activité produite par les valves. Nous montrons que plus les interactions entre valves sont fortes, plus une activité clusterisée dans le temps apparait, et plus les épisodes d'activité se reproduisent périodiquement. La force des interactions transportées par le champ de pression fluide est d'autant plus forte que les valves sont nombreuses et groupées dans le système, et que la valeur du flux d'entrée les rend critiques — proche des conditions d'ouverture ou de fermeture —, et donc susceptible d'interagir. Sur la base de nos résultats, nous émettons l'hypothèse la complexité et des longues périodes de récurrence de l'activité du tremor pourraient provenir du comportement collectif de valves dans la zone de faille, qui façonnent des régimes hétérogènes et transitoires de circulation du fluide, à des échelles spatiales allant de la source à la zone de subduction, et des échelles temporelles allant de la journée à plusieurs années.

Ce étude pose un cadre conceptuel permettant de comprendre comment des conditions de pression de fluide hétérogènes et intermittentes peuvent émerger dans la faille de subduction. Notre modèle permet de concevoir l'émergence à grande échelle de motifs spatio-temporels d'activité grâce à l'interaction entre des sources sismiques individuelles, en décrivant la manière dont un événement sismique déclenche et est déclenché par des changements de pression de fluide. Au-delà des zones de subduction, ce cadre de pensée est applicable à d'autres systèmes géologiques de circulation de fluide, comme les réservoirs magmatiques. Le mécanisme de valve de perméabilité que nous décrivons est une description simplifiée mais efficace, permettant de penser le transport des fluides dans des milieux dynamiques comme étant composé d'événements d'accumulation et débâcle de fluide. De tels processus façonnent l'intermittence du transport de fluide et de l'activité sismique qui en découle, et leur compréhension nous permet d'utiliser les observations sismiques comme un diagnostic des conditions hydrauliques en profondeur.

MOTS CLÉS: Subduction, système magmatique, hydrologie, microsismicité, tremor, seismes basses fréquence

Summary of the Manuscript

The activity of the smallest earthquakes that can be detected in the Earth is a symptom of minute changes that occur beneath our feet. Microseismic activity can in particular be used to monitor how fluid flows in geological plumbing systems like faults or volcanoes, from deep sources of fluid to the surface. In subduction zones for instance, the plate interface emits faint, intermittent, low-frequency seismic signals called tremor, composed of small individual low-frequency earthquakes (LFEs). In this manuscript, we try to understand how unsteady fluid circulation processes in the subduction fault zone can shape the source and spatio-temporal patterns of tremor, how tremor can therefore be used to probe dynamic fluid processes at depth.

In a first part, we characterize the source of LFEs in Guerrero, Mexico, and find that their duration seems independent of their magnitude. This observation is inconsistent with the classical view that earthquakes should be generated by a rupture of the rock. It can however be explained by a model of LFE source that involves fluid pressure transients in the fault interface, fast and strong enough to generate seismic waves.

The source of LFEs is not the sole indicator of strong, localized variations of fluid pressure in the fault zone. Geological observations of fossilized subductions indicate that the fault permeability opens and closes episodically, and that the fluid pressure drops and increases as a result. Such widespread unsteady hydraulic conditions in the fault could be a key factor shaping the complexity of spatio-temporal patterns of tremor activity. They are however seldom considered in attempts to describe the processes at the origin of the full spectrum of tremor patterns observed in subduction zones.

In a second part, we therefore design a framework to describe the unsteady processes of fluid circulation in the subduction fault, and how they trigger elementary tremor events. We model fluid ascent from metamorphic dehydration sources through a permeable channel in the fault interface. Low-permeability segments of the channel impede the flux, locally producing strong pressure gradients. In an elementary valving mechanism, the permeability barriers break open and then heal shut in response to the strength of the local fluid pressure gradient. When valves break they produce a simulated LFE, the rapid fluid pressure transient potentially being the source of seismic waves. Valves can trigger each other through pressure transients. Their interaction lead to realistic, tremor-like patterns: cascades, synchronized bursts and migrations of activity, on both short and long time and space scales. We describe how the fluid input rate in the channel allows for activity, and more specifically which conditions best favor the emergence of realistic patterns of activity. We show that stronger interactions, and therefore more clustered, periodic activity can occur when valves are clustered in space, and when flux conditions make

them more critical, and thus more susceptible to interactions. Based on our results, the emergence of large, complex, long-period activity transients could come from the collective behavior of valve like segments in the interface, shaping large scale valving behavior of the fault interface.

This work provides a conceptual framework to understand how heterogeneous, intermittent fluid pressure conditions can emerge in the subduction fault. Our model of how the seismic source is triggered by the fluid pressure field and affects it in return allows to conceptualize how elementary sources can interact in an hydraulic system, and build up patterns of seismicity. Beyond the subduction zone, this framework has a more general reach to interpret how fluid unsteadily flows in all geologic plumbing systems. The permeability valve mechanism is a powerful yet simple description that allows to think of fluid transport as a series of fluid pressure accumulation and release, that shape intermittent fluid transport, and intermittent seismicity as a symptom.

KEYWORDS: Subduction, magmatic system, hydrology, microseismicity, tremor, low frequency earthquake

REMERCIEMENTS

As I am writing those last words in this manuscript — which might be the first, and even only, words you read —, I realize that the list of all the people I have to thank for is too long for me to go through here. So I will keep it short and professional, hopefully.

First I want to very warmly thank my supervisors, Nikolai and Claude, for making so much time, being so present and helpful throughout those three years, and even five years for Nikolai. I want to thank Claude for his kind encouragements when he saw I was down, and Nikolai for his directivity and friendly realism, which has helped me regain focus many times I was getting lost trying to follow all the leads. I want to thank William for the discussions and external point of view he brought on my work, at a time when I thought I would not regain enthousiasm about my work, and also for making me feel so welcome in the team on the fourth floor of the Green's building. I want to thank Camilla too, for accepting to be in my defense jury of course, but also for the scientific and carreer discussions that made me think about why to continue further in research, and honestly convinced me. Of course, I want to thank all members of my jury, for accepting to read my manuscript, and participating in my defense. I am eager to discuss this work with you.

I think being colleagues is an underrated form of friendship, less engaged than the classical friendship, but as caring and often much lighter, focusing on simply making a nice everyday environment for everyone to thrive in. For that I want to thank everyone in the fantastic Geological Dynamics team, for being the best colleagues I could wish for, at lunch, around coffee, growing tomatoes and strawberries on the balcony, and tasting them for *le goûter*. Sometimes colleagues become the dearest friends. I want to thank Angèle, Cyril, Émilie, Marie, for being *le sang de la veine*, vraiment. Farther from Paris, I want to thank Caroline for skating and dancing, Léonard for walks in the Cambridge night by -10°C, Éric for the Lower Level, and Enrico and Qingyu for helping me practice my Chinese — I hope you will get that if you read it, it's been a long time already. Luc has never really been a colleague, but since we spent so much time on the phone during work hours, he might as well fit in here. I still hope we will one day collaborate, for the most extraordinary project, on the creative edge that separates science and art, on our way to find `the_truth`. Wow, I know.

I want to thank my family, my friends for supporting me and everything, but I suspect most of them will not stumble upon this manuscript. It's ok. If they do however, I want them to know that I feel very proud of getting there, of graduating soon and making a job of thinking about how things in the Earth really work, and that they should know that I love talking to them about it, and that I love them for listening to me.

RÉSUMÉ LONG DE LA THÈSE

L'activité des plus petits séismes détectés dans la Terre est symptomatique des changements infimes qui se produisent sous nos pieds. Dans les dernières années, l'augmentation de la puissance de calcul disponible pour les analyses de données géophysiques a permis une augmentation drastique de la résolution des catalogues de sismicité. Cela a permis de détecter des événements de plus en plus faibles, et ainsi de pouvoir observer les processus lents de libération d'énergie qui se produisent dans les failles et les volcans, qui précèdent, mènent ou suivent les événements de libération d'énergie plus catastrophiques qui rythment le cycle de ces systèmes — éruptions et grands séismes. L'activité microsismique peut notamment être utilisée pour surveiller la façon dont les fluides circulent dans les failles ou les volcans, depuis des sources de fluides en profondeur jusqu'à la surface. Dans les zones de faille, la présence de fluides à haute pression a pour effet de favoriser le glissement en lubrifiant la faille, et donc de ruptures sismiques. Les essaims de séismes générés par des injections de fluides dans les failles — naturelles ou industrielles — migrent dans l'espace selon des motifs caractéristiques, qui semblent dirigés par la diffusion de la pression au sein du système perméable autour de la zone de faille. Dans les volcans, la migration de phases fluides dans le système magmatique est à la source même d'une partie de la sismicité. Des changements rapides et hétérogènes de pression dans le système perméable peuvent mener à de soudaines accélérations du fluide, qui, en interagissant avec la matrice solide du réservoir, génèrent des ondes sismiques basses fréquence. Ces signaux détectés dans les volcans sont appelés tremor volcanique ou séismes longue période (LP), et migrent rapidement au travers du système magmatique soulignant la structure des conduits actifs et les variations de flux dans le temps et l'espace.

Dans les profondeurs des zones de subductions, on détecte des signaux sismiques similaires: le tremor non-volcanique, un signal long, émergent, de basse fréquence, qui semble composé d'événements impulsifs élémentaires, les séismes basse fréquence (*low-frequency earthquakes* ou LFEs). Ces signaux sont émis depuis l'interface des plaques, et leur activité est caractérisée par une intermittence prononcée. Le tremor se produit en épisodes à structure quasiment fractale, étant eux mêmes composés d'épisodes plus courts séparés de courtes périodes de quiescence. Pendant ces épisodes, l'activité migre sur la faille dans des motifs rappelant la sismicité déclenchée par les accélérations du fluide dans les volcans, en migrations à vitesse constante, rapide pour les épisodes d'activité les plus courts, et plus lent pour les épisodes les plus longs. L'intermittence est caractérisée par une récurrence quasi périodique de l'activité, sur des périodes allant du jours pour les sources individuelles de tremor, aux années pour l'entièreté de la zone sismique. Les caractéristiques de source et les motifs spatio-temporels d'activité du tremor semblent nécessiter l'implication de processus instables de circulation de fluide dans l'interface de faille.

Il existe un corpus grandissant d'observations géologiques et géophysiques qui

semble montrer que les fluides provenant de la déshydratation de la plaque circulent chaotiquement dans la région de production du tremor. Les pressions de fluides y seraient extrêmes, contrebalançant la pression lithostatique locale, et varieraient cycliquement, entre épisodes de pressurisation et dépressurisations liés à des ouvertures et fermetures soudaines de la perméabilité de la faille, qui alternativement laisseraient circuler et bloqueraient le flot. Cette dynamique de la faille semble être active à des échelles correspondant à la source sismique (mètres à centaines de mètres), mais aussi à l'échelle de la zone sismique entière (dizaine à centaines de kilomètres), et les grands changements de perméabilité, de pression et de flux semblent être corrélés à des épisodes d'intense activité du tremor. Malgré ces observations, la plupart des efforts de modélisation des processus générant le tremor dans toute sa complexité ne prennent en compte l'hydraulique de la faille que comme un paramètre statique du modèle, affectant la dynamique du glissement, mais n'étant pas affectée par elle. Dans ce manuscrit, nous nous attachons donc à comprendre comment des processus instables de circulation de fluide dans la zone de faille de subduction peuvent par eux seuls façonner le signal et les motifs spatio-temporels que dessinent le tremor, et comment celui-ci peut donc être utilisé pour diagnostiquer la dynamique du système hydraulique de la faille de subduction.

Dans une première partie, nous caractérisons la source des LFEs à Guerrero, au Mexique. Nous sélectionnons 3498 événements des plus impulsifs et de grande amplitude du catalogue, et déterminons leur moment sismique et fréquence coin par une analyse de leur spectre sur plusieurs stations. Les moments sismiques mesurés correspondent à des magnitudes de moment de M2.2 en moyenne, comprises entre M1.7 et M3.9. Les fréquences coins mesurées sont en moyenne autour de 3 Hz et comprises entre 1 et 6 Hz, plus basses d'un facteur dix environ que les séismes classiques de même magnitude. Nous observons que les fréquences coins ne dépendent pas de la magnitude des événements. Cette observation est incompatible avec la vision classique selon laquelle les séismes devraient être générés par une rupture sur une faille. En effet, pour un séisme qui procède d'une rupture dite auto-similaire, la durée de la rupture augmente plus la magnitude du séisme est grand, et donc la fréquence coin du signal — qui est en théorie proportionnelle à l'inverse de la durée — devrait être décroissante en fonction de la magnitude. Un modèle qui expliquerait la source sismique des LFEs par de rapides changements de pression de fluide dans l'interface de faille pourrait expliquer cette observation. Alors qu'une barrière de basse perméabilité cède dans la faille, le fluide sous pression qui s'est accumulé derrière peut soudainement circuler, produisant un transitoire de pression assez rapide et puissant pour générer un signal similaire à celui des LFEs. L'amplitude — proportionnelle au moment sismique mesuré — de ces événements dépend de l'amplitude du transitoire de pression, et peut donc varier, a priori. Cependant, la durée de la source sismique est contrôlée par la vitesse de diffusion du transitoire de pression. Dans ce modèle, et en accord avec notre observation, les durées et fréquences coins devraient donc avoir une valeur caractéristique dépendant des conditions hydrauliques locales dans la faille, et indépendante de l'amplitude du saut de pression.

La source des LFEs n'est pas le seul indice que de fortes variations de pression

de fluide se produisent dans l'interface de subduction. Quand cette zone est exhumée, les affleurements sont marqués par la signature d'ouvertures et de fermetures répétées de la perméabilité de la zone de faille, générant des conditions instables de pression dans le fluide. La dynamique de ce système hydraulique doit contribuer à la complexité des motifs d'activité du tremor, bien qu'elle soit rarement considérée dans les études tentant de les décrire dans leur entièreté. Dans une deuxième partie, nous élaborons donc un modèle qui permettrait de décrire les processus dynamiques de circulation des fluides dans la faille de subduction, et leur lien avec le tremor. Nous modélisons l'ascension des fluides depuis des sources profondes de déshydratation métamorphique vers la surface, au travers d'un canal perméable dans l'interface de faille. Pour refléter l'hétérogénéité des conditions de transport du fluide dans la faille, la perméabilité du canal est décrite comme étant forte, mais localement, des segments de basse perméabilité agissent comme des barrières au flux de fluide, générant une hétérogénéité du gradient de pression quand le système est soumis à un flux constant. Autour des barrières de basse perméabilité, le gradient de pression est fort. Pour modéliser des processus de débouchage de la perméabilité de l'interface de faille, nous décrétons que si le gradient de pression au travers des barrières de basse perméabilité excède une valeur seuil, la barrière cède, et la perméabilité locale augmente brutalement, simulant un processus d'ouverture. Cette ouverture laisse le flux circuler brutalement, générant un fort transitoire de pression qui peut être à la source d'un LFE. Dans notre description, chaque ouverture de barrière est donc synchrone d'un événement sismique élémentaire. Lorsque le flux au travers de la valve est assez bas, le gradient de pression atteint une deuxième valeur seuil, plus basse que celle permettant l'ouverture, et la perméabilité de la barrière se rebouche. Ce mécanisme d'ouverture et fermeture de la perméabilité de la zone de faille nous permet de décrire l'évolution des conditions de transport du fluide dans la faille de manière intermittente. Chaque barrière se comporte comme une valve, et l'action combinée de nombreuse valve fait émerger des pressions de fluides variables et hétérogènes dans l'interface de faille, comme mis en évidence par de nombreuses observations.

Nous mettons en évidence que l'activité des valves dans ce système est soumis à l'intensité du flux d'entrée. Il existe un domaine de flux délimité par deux valeurs critiques, qui produit nécessairement des gradients de pression déclenchant l'ouverture des valves quand elles sont fermées, et leur fermeture quand elle sont ouverte. Quand le flux d'entrée du système est compris entre ces valeurs critiques, les valves s'ouvrent puis se ferment cycliquement, et de manière permanente. Dans ces conditions, le flux, la pression de fluide et les conditions de transport sont intermittentes dans le système, et la sismicité se produit de concert, reflétant cette intermittence. Par ailleurs, lorsqu'une valve s'ouvre, le transitoire de pression qui est généré peut affecter les valves voisines, et déclencher leur ouverture. Cette interaction permet l'apparition de cascades d'ouvertures de valves — et donc de sismicité — qui se propagent vers l'amont et l'aval du canal. Elles sont le composant élémentaire de motifs plus complexes qui émergent dans le système alors que les interactions entre valves leur permet de synchroniser leur activité. Comme pour le tremor observé,

celui que nous simulons est épisodique, les périodes de haute activité sont elles même intermittentes, la sismicité migre le long du canal à petite et grande échelle, et dans certains cas, l'activité est très régulière, et de longues périodes émergent. Dans ces cas là, la synchronisation de l'activité de nombreuses valves dans le système fait apparaitre un comportement de valve de l'ensemble du système, très similaire à ce qui a été décrit et modélisé pendant les épisodes de tremor et glissement lent dans les zones de subduction.

Dans un dernier chapitre, nous explorons comment la force des interactions entre valve contrôle le style d'intermittence produite par le système, dans quels cas l'activité est relativement constante, et au contraire, dans quels cas elle se synchronise en épisodes intermittents, et se reproduisant à des intervalles plus réguliers. Deux paramètres contrôlent la force des interactions, la distance entre valves, et la valeur du flux d'entrée. À partir d'un système à deux valves, nous montrons que plus les valves sont proches, plus les événements qu'elles produisent sont proches dans le temps, le transitoire de pression qui porte l'interaction ayant moins de distance à parcourir. Dans un système avec de nombreuses valves distribuées dans l'espace, la proximité entre valve — qui résulte soit du nombre de valves dans le système, soit de leur regroupement en clusters dans l'espace — contrôle la force de l'interaction. Plus les valves sont proches en moyenne, plus elles interagissent. De son côté, la valeur du flux d'entrée contrôle la proximité des valves au seuil de rupture, et donc leur susceptibilité à être déclenchées par un transitoire de pression généré par l'ouverture d'une valve voisine. Quand ces deux paramètres permettent aux valves d'interagir fortement, l'activité est plus intermittente, et de longues périodes d'activité émergent. En conclusion, nous montrons que l'émergence de l'intermittence caractéristique au tremor doit être due à une interaction forte entre segments de valves dans le système hydraulique, produite soit par leur nombre ou proximité dans le système, soit par leur proximité à la rupture. Sur la base de nos résultats, nous émettons l'hypothèse la complexité et des longues périodes de récurrence de l'activité du tremor pourraient provenir du comportement collectif de valves dans la zone de faille, qui façonnent des régimes hétérogènes et transitoires de circulation du fluide, à des échelles spatiales allant de la source à la zone de subduction, et des échelles temporelles allant de la journée à plusieurs années. Ces caractéristiques du système hydraulique de la zone de subduction doivent être héritées de la structure de l'interface des plaques, qui elle même est modelée par la structure de la plaque plongeante. Notre modèle permet donc une interprétation des conditions hydrauliques dans l'interface de faille sur la base de la caractérisation des motifs de sismicité basse fréquence que l'on peut y détecter.

Ce étude pose un cadre conceptuel permettant de comprendre comment des conditions de pression de fluide hétérogènes et intermittentes peuvent émerger dans la faille de subduction. Notre modèle permet de concevoir l'émergence à grande échelle de motifs spatio-temporels d'activité grâce à l'interaction entre des sources sismiques individuelles, en décrivant la manière dont un événement sismique déclenche et est déclenché par des changements de pression de fluide. Au-delà des zones de subduction, ce cadre de pensée est applicable à d'autres systèmes géologiques de cir-

culation de fluide, comme les réservoirs magmatiques. Le mécanisme de valve de perméabilité que nous décrivons est une description simplifiée mais efficace, permettant de penser le transport des fluides dans des milieux dynamiques comme étant composé d'événements d'accumulation et débâcle de fluide. De tels processus façonnent l'intermittence du transport de fluide et de l'activité sismique qui en découle, et leur compréhension nous permet d'utiliser les observations sismiques comme un diagnostic des conditions hydrauliques en profondeur.

Table of Contents

Part I

Introduction

Chapter 1

Introduction

Contents

1.1 Microseismic activity probes hydraulic processes in geological systems

In the past few years, the rapid enhancement of computing power, allowing the implementation of computation-heavy algorithms, has led to a leap forward in earthquake detection capabilities. It has drastically lowered the magnitude of the smallest detected events, and thus increased their number. Small earthquakes are much more frequent than larger earthquakes: in most places of the world, earthquakes of a given magnitude (M_w1 for instance) are ten times more frequent than earthquakes one magnitude point bigger

(M_w2) (Gutemberg & Richter, 1944). With lower and lower completeness magnitude — the magnitude above which one can consider that virtually all earthquakes are detected in a catalog —, the catalogs now image fainter, slower, smaller-scale processes in the Earth. The study of small earthquakes ($M_w < 3$), or *microseismicity*, now seems key to understand the finer workings of geological systems as they provide a finer and finer observation coverage in both time and space, spanning periods thought quiescent between more intense events (eruptions in volcanoes, large earthquakes on faults) (Brodsky, 2019). The improvement of microseismic catalogs allows to precisely map structures at depth, illuminating fault geometry (Ross et al., 2020), the shape and size of seismic areas deep on the subduction interface (Rubin & Armbruster, 2013), or the geometry of magmatic plumbing systems (Hotovec-Ellis et al., 2018; Journeau et al., 2022). By more finely recording the changes in earthquake activity in time, smaller microseismic data allows to detect more elusive fore-shock activity, and in general map the minute seismic signature of the nucleation processes that precede larger fault ruptures (Ross et al., 2019). As the number of detected small earthquake go up, the time between detected events is also lower and lower, allowing to get finer and finer insight into dynamic processes. The activity of small, low-frequency events on subduction faults has for instance been used as a proxy signal for short, slow, low-amplitude slip events deep on faults, which geodetic signature is otherwise hidden in the noise (Frank, Radiguet, et al., 2015; Rousset et al., 2019).

In general, small seismic events can be used to monitor and characterize minute stress changes on pre-stressed structures, like faults near the rupture criterion (Brodsky & van der Elst, 2014), or high-pressure fluid flow in magmatic systems (Benson et al., 2008; Journeau et al., 2022). Such stress transfer is often mediated by elastic, viscous or plastic changes in the rock, but in both volcanic and tectonic settings, processes of fluid circulation can also trigger and shape microseismic activity. It has been known for several decades now that the injection of fluids in the crust — *e.g.* for wastewater disposal from industrial oil and gas extraction processes, or heat collection from geothermal reservoirs — triggers microseismic swarms of earthquakes (Cornet et al., 1997; Ellsworth, 2013; Majer et al., 2007; Nicholson & Wesson, 1992; Raleigh et al., 1972). The evolution of the seismicity rate in those swarms differ from classical, Omori behavior of seismicity observed in faults (Omori, 1895). As the seismicity is controlled by the temporary injection of fluids — or processes that it triggers — and not by a permanent tectonic forcing, the seismicity rate transiently rises, is maintained high for a time, and decays. Such swarms of seismicity also occur in places where no fluid is injected in the crust by anthropic activity. Because the seismicity in those settings has similar patterns, studies have linked it to natural processes of circulation of fluids in the crust,

from deep sources towards the surface along permeable pathways, around faults (De Barros et al., 2020; Horálek & Fischer, 2008; Ross et al., 2020), in geothermal systems (Shelly et al., 2013) or in magmatic systems (Hotovec-Ellis et al., 2018).

Two factors can explain the triggering of fluid-induced seismicity: simple triggering by fluid pressure increase, or triggering mediated by aseismic slip on the fault. On the one hand, as fluids diffuse in the permeable crust, the local fluid pressure p increases, countering the overburden normal stress σ on fracture planes, and thus lowering the effective normal stress $\sigma_{eff} = \sigma - p$. When the effective normal stress that clamps them shut decreases, faults are brought closer to the failure point, as the tangential stress τ can overcome the friction on the fault. This explanation is coined the *effective normal stress principle*, and is based on the Coulomb failure criterion, that states that a fault ruptures when

$$\tau > C + f(\sigma - p), \tag{1.1}$$

where C is the cohesion of the material in the fault, and f the friction coefficient of the interface. Such a simple interpretation seems to be enough to explain migrations of seismicity that follow a diffusion pattern: as fluid diffuses, it brings small faults to failure and thus triggers earthquakes (*e.g.* S. A. Shapiro et al., 2002). However, in many cases, the spatio-temporal patterns of activity are more complex, and seem to indicate that the fluid pressure increase on the fault could interact with aseismic slip transients, that in turn trigger sources, by increasing the local tangential stress on seismogenic parts of local faults (De Barros et al., 2020; Ross et al., 2017; S. Wei et al., 2015). Field scale experiments of fluid injection in shallow faults seem to confirm this interpretation (Guglielmi et al., 2015): for natural and anthropic fluid injection in the crust, the fluid pressure source could act only as the trigger, initiating an aseismic slip transient that governs the propagation of seismicity (Bhattacharya & Viesca, 2019). Recent studies of the same experiment have however complexified this vision, showing that permeability can change by nearly two orders of magnitude as the slip and high fluid pressure transient travels across the fault, triggering seismicity as it progresses (Cappa et al., 2022). This evolution in the interpretation of the same dataset highlights that dynamic fluid circulation processes can be a fundamental component in explaining how fluid-related seismicity evolves in time and space, but that they are still poorly understood.

Such an implication of fluid in triggering seismicity does not only have an impact on the spatiotemporal patterns of activity, it also influences the source processes of microseismic events, that can be observed through seismic measurements (Lengliné et al., 2014; Lin et al., 2016). One of the clearest

examples of this is volcanic long-period seismicity:*tremor* or *long-period* earthquakes. Since they have been first observed, those phenomena have been linked with magmatic fluid circulation processes (B. A. Chouet, 1996; Koyanagi et al., 1987), because of the specificities of their signal: a sometimes monochromatic, especially low frequency content. When signals similar to volcanic tremor and long-period earthquakes have been detected deep on the interface of subduction zones (Katsumata & Kamaya, 2003; Obara, 2002), it was first suggested that the unusually low frequency of their signal was due either to an unusual rupture process (Ide, Beroza, et al., 2007), or to metamorphic fluid circulation around the fault interface, by analogy to volcanic processes (Katsumata & Kamaya, 2003). Although tectonic (or non-volcanic) tremor and *low-frequency earthquakes* have then been associated with slip on the interface (Ando et al., 2010; Obara et al., 2004; Rogers, 2003; Shelly et al., 2007a), almost excluding the fluid circulation hypothesis, there is mounting evidence that, as long period seismicity in volcanoes, low frequency seismicity in faults is closely associated with fluid circulation processes that shape their source processes and spatio-temporal patterns of activity.

On subduction faults, the circulation of fluid can be responsible for lubricating the plates' interface, producing deep slow slip transients that can load the plate interface enough to trigger the largest megathrust earthquakes (Bedford et al., 2020). Such hydraulic processes on the subduction fault remain enigmatic, but thanks to its high seismicity rate, the quality of monitoring in subduction zones producing it, and recent improvements in the resolution of catalogs of low-frequency events (Frank et al., 2014; Poiata et al., 2021), low-frequency seismicity makes an exceptional probe of the slow and faint processes leading to such catastrophic events. Therefore, our objective in this thesis will be to further the understanding of the link between fluid flow in the subduction zone and the production of low-frequency seismicity there. More generally, we hope to build a conceptual framework that can help understand better the dynamic of fluid flow in geological systems, and how it relates to seismicity. In the next pages, we describe the characteristics of low-frequency seismicity, and what is known of the hydraulic processes underlying it.

1.2 The seismic source of low-frequency seismicity

1.2.1 Source characteristics of low-frequency events in faults

In subduction zones, low-frequency seismicity locates mostly along the plate interface, between 30–60 km depth (Bostock et al., 2012; Frank et al., 2014; Shelly et al., 2006), slightly deeper than the "seismogenic zone" of the plate interface that produces megathrust earthquakes. Two major phenomena can be singled out by observing seismic waveforms: *tremor*, a long, non-impulsive signal with a characteristic frequency of about 1–8 Hz, and *low-frequency earthquakes* (LFEs), impulsive signals that can be found within tremor, with clear S-wave arrivals, and a similar frequency content as tremor. The sources of tremor and LFEs can be located to the plate interface as localized, finite patches that repeatedly activate, producing similar waveforms each time (Chestler & Creager, 2017b; Rubin & Armbruster, 2013). Because both phenomena share similar frequential content, colocate and occur at the same time, tremor is thought to be made of swarms of small, elementary LFEs (Shelly et al., 2006). Thanks to their characteristics as impulsive, locatable, repeated sources, LFEs are well-fitted to investigate the physical processes that generate tremor activity. Figure 1.1 displays the characteristic location, waveforms and spectral content of LFEs and tremor in subduction zones.

Those phenomena occur on the plate interface at pressures (about 1 GPa) and temperatures (350–550°C) that mostly prohibit brittle fracture, favoring a more ductile accomodation of the shear stresses due to the slab subduction (Platt et al., 2018). This part of the fault interface is described as a frictional transition, between shallow regions where fault slip is unstable, and can accelerate to seismogenic speeds, and deeper regions where fault slip is stable, continuously and aseismically creeping without accelerating (Lay et al., 2012; Scholz, 1998). Low-frequency earthquakes have unusual source properties, that differentiates them from classical earthquakes. The main characteristic of tremor and LFEs is of course their particular frequency content. For events of a similar magnitude, LFEs have a characteristic frequency on the order of 10 times lower than regular earthquakes (Farge et al., 2020; Shelly et al., 2007b, *cf* Chapter 2). The spectrum of their body waves is quite similar to an earthquake's, but shows a much lower corner frequency f_c — the frequency delimiting the high-frequency decay of the spectrum and the low-frequency content — that seems to indicate a longer duration $T \sim 1/f_c$ of the source process. In Cascadia (Bostock et al., 2015) and Guerrero (Farge et al., 2020, *cf* Chapter 2), their corner frequency seems to be invariant with

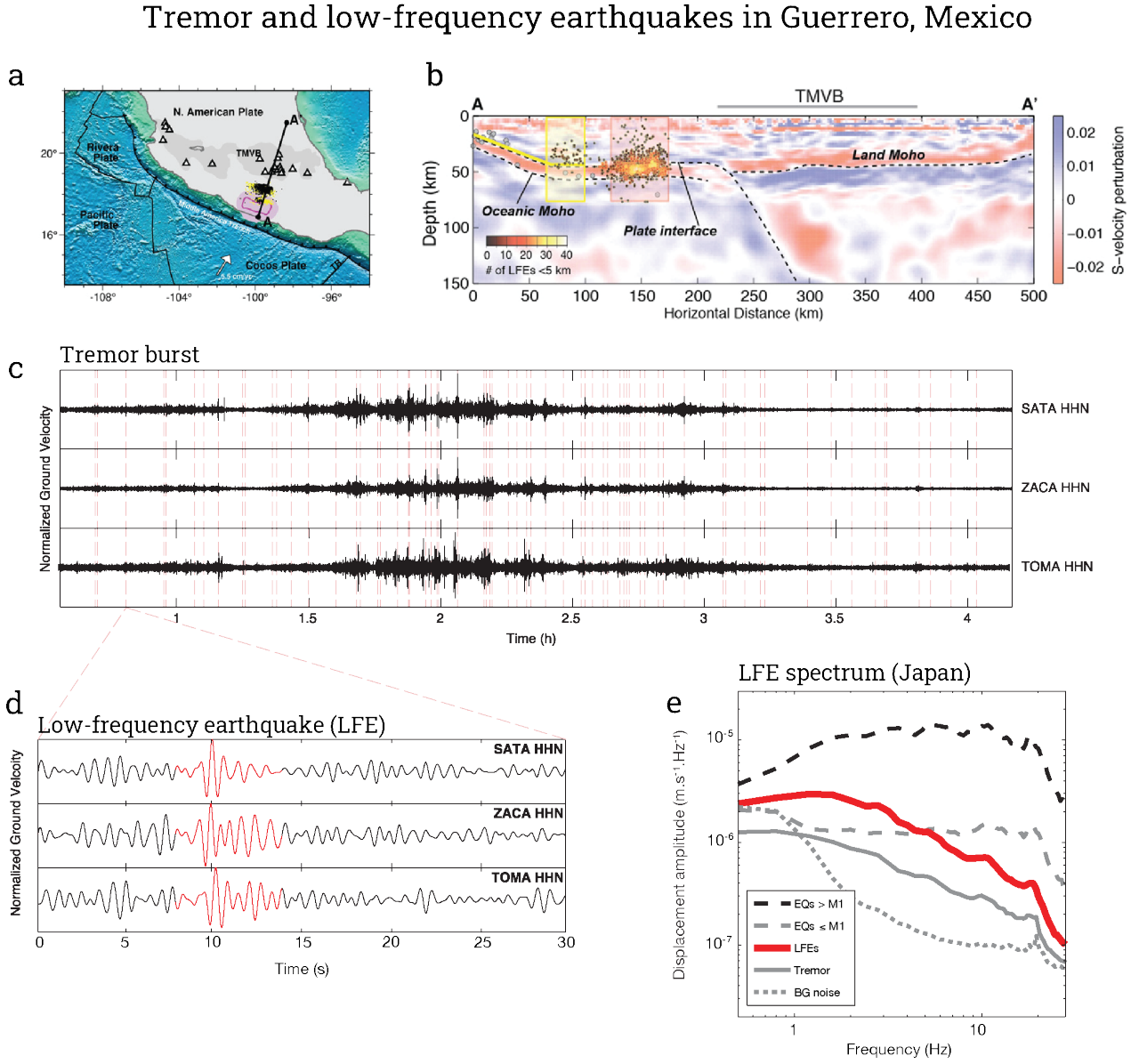

Figure 1.1: Caption on next page.

Figure 1.1 — *(a) Map of the Guerrero (Mexico) tremor zone. The black dots represent tremor events, and purple shaded areas the slow-slipping parts of the fault. Triangles represent volcanoes, in the transmexican volcanic belt. (b) Tomography image of the A-A' transect, overlaid with LFE detections from Frank et al. (2014), as points colored with the density of source. LFEs cluster around the plate interface, in two zones. The oceanic crust appears with a strong low-velocity anomaly, possibly indicating the presence of high-fluid pressure fluid. (d) Tremor burst signal over a few hours, recorded on one horizontal component of three stations in the Guerrero tremor zone, filtered between 1–2 Hz. Each light red dashed line represent an LFE detection. (d) LFE waveforms, on recorded by the same stations and components as the tremor waveforms, filtered between 1–2 Hz. In red, the part of the signal that is inferred to be the S-wave of the LFE. (e) Stacked amplitude spectra of the displacement for different events detected in the Shikoku tremor region: small and large earthquakes, LFEs, tremor and background noise. See Shelly et al. (2007b), Figure 2 for details. The LFE's signal has a similar low-frequency amplitude as small earthquakes, but are strongly depleted in high frequency. (a) and (b) are adapted from Audet and Kim (2016), (c) and (d) are adapted from Frank and Shapiro (2014), (e) is adapted from Shelly et al. (2007b).*

respect to the seismic moment of the events: whatever their seismic moment, LFEs' corner frequency range between 1–5 Hz, with very little dependence on their size. This behavior is at odds with the scaling predicted by a simple model of seismic rupture, which predicts a strong dependence of duration and thus corner frequency on seismic moment: as earthquakes grow bigger, the duration of their source increases, and therefore their corner frequency decreases (Kanamori & Anderson, 1975). This deviation from the self-similarity scaling consistent with classical ruptures is not observed everywhere LFEs are detected. For instance, (Supino et al., 2020) find that in this respect, LFEs do not differ with classical earthquakes. In addition to the observation of a potentially constant duration for LFEs in a given region, some studies find that LFEs could result from a scale limited process, that limits their size and therefore their magnitude around a characteristic value (Chestler & Creager, 2017a), which clearly differs from the scale-independence of earthquake magnitudes observed in most seismic regions (Gutemberg & Richter, 1944).

1.2.2 Models of LFE source processes

Although it could be suggested that the especially low-frequency content and characteristic duration of LFEs could be due to a strong attenuation of the medium, that would effectively act as a low-pass filter on the seismic waves (Bostock et al., 2017; Ide et al., 2003), most studies attribute them to the specific source processes that generate LFEs.

1.2.2.1 Slip models of LFEs

Quickly after they were discovered, major bursts of tremor and LFEs have been found to occur at the same time, and colocate with slow slip transient on the deep parts of the subduction interface (Obara et al., 2004; Rogers, 2003). As detection methods improved, smaller and smaller tremor episodes were discovered, linking further and further tremor activity with slow slip on the interface, to the point that it is now used as a proxy to detect geodetically-invisible slip transients (Frank, Radiguet, et al., 2015; Rousset et al., 2019). Because of seismic clues like a radiation pattern consistent with shear slip on the plate interface (Frank et al., 2014; Ide, Shelly, & Beroza, 2007), LFEs have since been thought to be due to the rupture of small, localized patches on a fault which mostly slips slowly and in a stable fashion, but can on the said patches host accelerating slip, after being loaded by the neighboring fault slip (Ando et al., 2010; Lay et al., 2012; Luo & Liu, 2019). In this interpretation, the measured seismic moments and corner frequencies LFEs can be used to deduce rupture parameters. Most studies find that LFEs could be due to slow ruptures (10% to 20% the shear wave speed), on patches of radius on the scale of 100–800 m, with very low stress drops, on the order of 10 kPa (Bostock et al., 2015; Farge et al., 2020; Supino et al., 2020; Thomas et al., 2016, *cf* Chapter 3). The apparent independence of the duration of LFEs on their magnitude could owe to the fact that such ruptures are almost limited to the slip nucleation size, due to the local frictional properties the tremor source region (Cattania & Segall, 2019; X. Wei et al., 2021).

1.2.2.2 Fluid flow models of low-frequency seismicity

A few studies have taken inspiration in the proposed mechanisms for long period tremor and long period events in volcanic systems to try and understand how observed properties of LFEs and tremor could be the result of the implication of strong fluid flow transients in the LFE seismic source mechanism (N. M. Shapiro et al., 2018). One of the principal — yet still debated — mechanism invoked to explain volcanic long-period events and tremor is a fast flow transient of magmatic fluid — gas or melt — in constricted pathways of the magmatic system. As a pocket of high pressure fluid suddenly breaches into a lower pressure area, or a differential of pressure suddenly occurs across a constriction in the conduits, due to movements of fluid on either side for instance, fluid gushes through the constriction, and elastic waves are generated either by the sudden traction force on the walls of the conduits, or the development of a vibrating instability in the conduit walls as fluid passes through (Honda & Yomogida, 1993; Julian, 1994; Ukawa & Ohtake, 1987). Such seismic behavior can be reproduced in the lab. In experiments

of sudden decompression of a fluid that permeates through a fractured rock samples, low frequency accoustic emissions that closely resemble long period seismicity are generated as fluid escapes the tortuous fractures of the rock (Benson et al., 2020, 2008). These fast fluid flow transient should occur as fractures open in a fluid-saturated, heterogeneously pressurized subduction channel, and could play an important role in shaping the source processes and therefore the seismic signature of tremor and LFEs.

Within the fluid-saturated fractures in the subduction interface, fluid should concentrate in discrete, high-porosity, high-pressure pockets (Gold & Soter, 1985). Within pockets the fluid is static, and the pressure gradient with depth should therefore be hydrostatic. As pockets are isolated by collapsed-porosity, low-permeability barriers, there exists strong steps of pressure in between fluid pockets, across low-permeability barriers. When such barriers break in a kind of hydrofracture — a change in pressure in either side of the barrier could for instance enable an accelerating flow event that opens the permeability barrier — the pressure change in the fluid should be strong and fast enough to be transmitted to the rock, and propagate as an elastic wave. N. M. Shapiro et al. (2018) models this event as a single force seismic source: the strong difference of pressure across the permeability barrier results in a force along the gradient of pressure, and as the pockets connect, the fluid pressure gradient suddenly smoothes, the force drops and seismic waves are reverberated in the medium. Figure 1.2 depicts this source mechanism. Such a seismic source radiates in a different way than a shear rupture. However, because LFEs' waveforms are only well observed from directly above, the S-wave radiation pattern from double couple source mechanism corresponding to a shear rupture on the subduction interface is almost undistinguishable from a single force radiation pattern (N. M. Shapiro et al., 2018). Several studies have attempted to characterize the source mechanism of LFEs using the patterns of first impulse, polarity or full waveforms of recorded S-waves at the surface (Ide, Shelly, & Beroza, 2007; Ohmi & Obara, 2002; Wech & Creager, 2007). Such mechanisms seem to always show a strong polarization along an assumed direction of slip, consistent with the tectonic setting, however, the data is quite ambiguous, being as consistent with the radiation pattern of a single force oriented along the updip direction of the subduction interface. In addition to that, the duration of such a source would be controlled by the characteristic duration of the pressure variation across the permeability barrier. When considering that this flow event occurs in a poro-elastic material, one can derive that the duration of the source would be proportionnal to the diffusivity of the fluid in the medium, and independent of the magnitude of the force that generates the seismic waves (N. M. Shapiro et al., 2018). Such a strong, fast fluid pressure transient source would therefore display a simi-

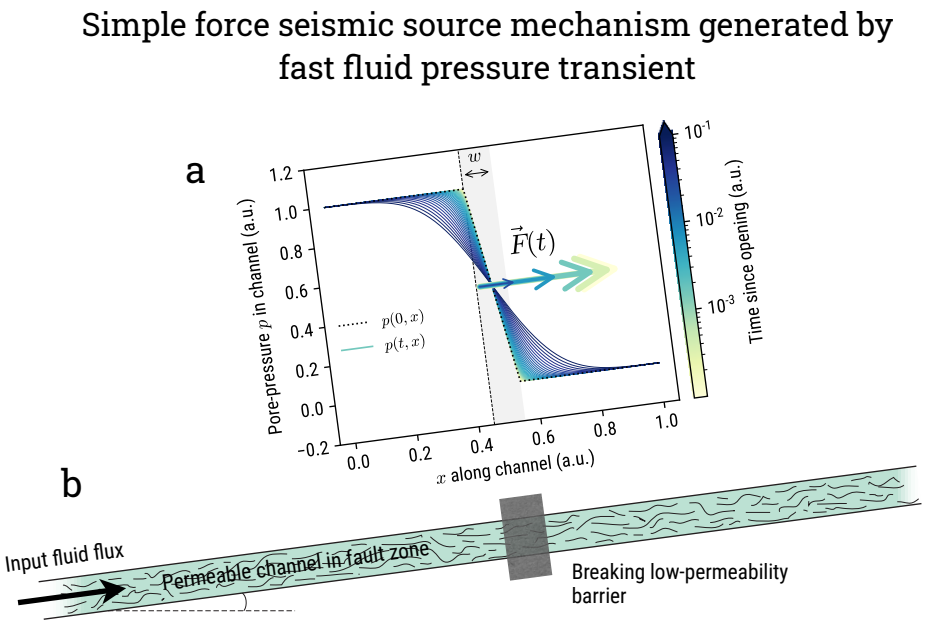

Figure 1.2 — *Model of simple-force seismic source generated by a fast fluid pressure transient in the fault interface. (a) Fluid pressure profile along the channel, and its evolution in time. The force on the porous matrix resulting from the fluid pressure gradient is represented with arrows of size proportional to the force amplitude. Time for each curve and arrow is color coded, going from light at the start of the transient, to dark at the end. The dotted line is the fluid pressure profile before opening. The shaded area represent the extent of the barrier. (b) The fluid pressure transient is generated as a permeability barrier breaks open in the permeable fault zone. Because the barrier impedes fluid flow in the fault zone, a strong fluid pressure gradient accumulates across it, imposing a force on the matrix in the direction of the flow. As the barrier breaks, the force drops, and the generated displacement in the elastic rock radiates seismic waves away from the barrier (N. M. Shapiro et al., 2018).*

lar scaling of seismic moment with duration (Bostock et al., 2015; Farge et al., 2020, *cf* Chapter 3): a range of seismic moments, and a characteristic duration of the event that does not depend on its moment, controlled by the local hydraulic properties of the fault zone.

The amount of observations that link LFEs and tremor to slip on the fault is compelling, and one should not think that LFEs occur wholly without the implication of slip processes on the fault. However, the consistency of such a mechanism with seismic observations and the geologic record of chaotic fluid flow in the fault is a hint that such a mechanism could plausibly be involved in the source processes generating LFEs and tremor, and shape their activity.

1.3 Spatio-temporal patterns of low-frequency seismicity

1.3.1 Migrations of tremor and LFE activity

In contexts of anthropic fluid-induced seismicity, seismic activity is observed to migrate away from the point of fluid injection reaching distances following a clear diffusion pattern: the outtermost extent of the active region extends at a distance R from the injection point for a duration of injection T, and the two parameters follow $R^2 \propto T$ (S. A. Shapiro, 2015; S. A. Shapiro et al., 2002). The diffusion of fluid pressure in the porous medium alone can explain this pattern. As a transient increase in fluid pressure diffuses away from the source — the injection point — the activity increases where pressure allows small ruptures, by lowering the effective normal stress on the fault enough (*cf* equation 1.1). In other words, the seismicity first diffuses quickly away from the pressure source, and its progression slows down as the seismicity front is further and further away from the source.

Although the simple diffusive pattern can sometimes be observed for LFEs and tremor (Kato & Nakagawa, 2020; Poiata et al., 2021), they often proceed in steps: a first diffusive migration accelerating and slowing down along the fault, and a second and sometimes more steps, as if the source of fluid was reactivated further along the fault, generating a second diffusion front. Most frequently, the LFE or tremor activity migrates with a constant speed within each burst of activity. The larger migrations mostly propagate along the strike of the subduction zone on tens to hundreds of kilometers, at velocities in the range of 1 to 10 km/day (less than 1 km/hr) (Kao et al., 2009; Poiata et al., 2021) — in Guerrero, the largest LFE episodes propagate along the almost 100 km-long flat slab section, along dip (Frank et al., 2014). Smaller migrations, spanning a few to tens of kilometers, are faster, in the range of 1–100 km/h (Cruz-Atienza et al., 2018; Frank et al., 2014; Ide, 2012). High-resolution seismological networks can even image short, rapid migrations of tremor, reaching over a hundred of km/hr (Ghosh et al., 2010; Shelly et al., 2007a). The length L of tremor or LFE bursts seems to be inversely related to their propagation velocity V. This behavior in which small scale migrations are much faster than larger scale migrations is reminiscent of a diffusive behavior, for which the propagation rate of a diffusive front follows $V \propto 1/R$, where R is the advancement of the diffusive front. The directivity of the migrations seems to depend on their scale: larger, slower migrations fill the tremorgenic zone across dip, and propagate along the strike of the interface (Ide, 2012; Kao et al., 2009; Poiata et al., 2021), while the shorter,

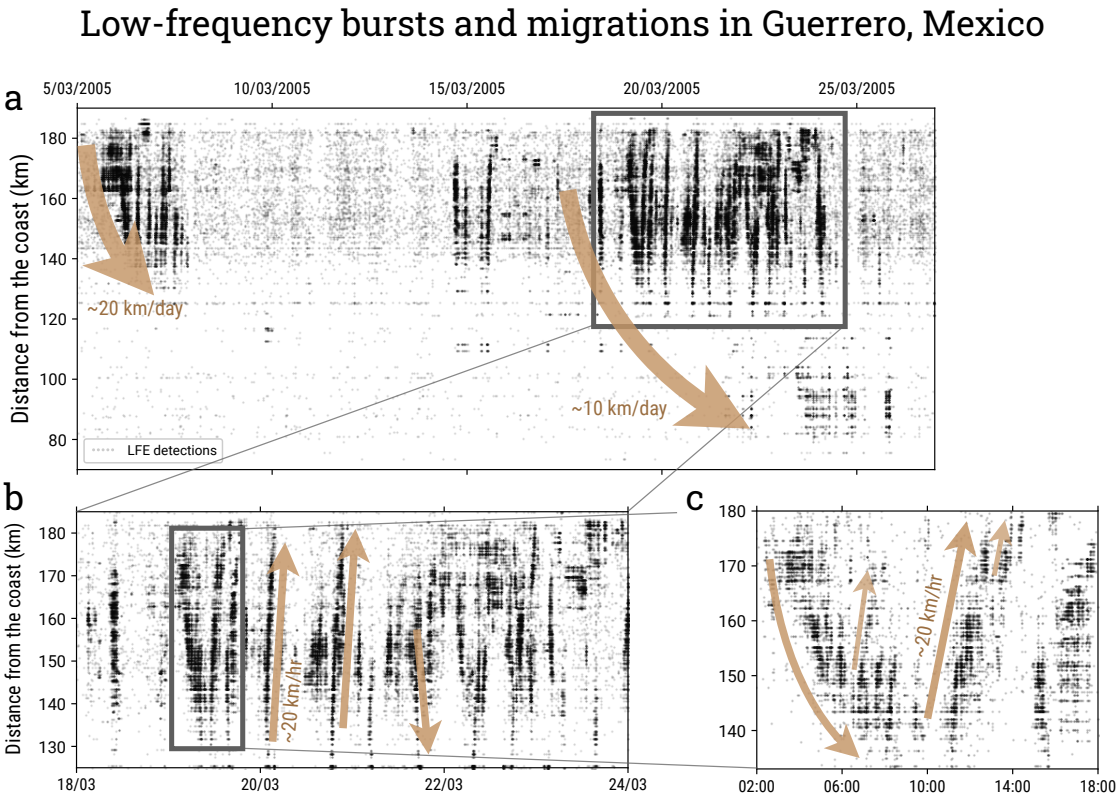

Figure 1.3 *— Bursts and migrations of tremor in Guerrero, Mexico, represented in a time-dip diagram. In (a), (b) and (c), each dot represents a detected LFE, located in the diagram by its occurence time and along-dip distance, from the coast of Mexico. The LFE catalog was compiled by Frank et al. (2014). The three panels show progressive zooms in time and space, highlighting that the activity is intermittent at all time and space scales, and proceeds in slow and fast migrations.*

faster migrations mostly proceed along-dip (Cruz-Atienza et al., 2018; Ghosh et al., 2010; Ide, 2012; Shelly et al., 2007a), with no obvious downdip or updip preference. It should be noted that rapid tremor migrations within a large burst seem to propagate in the reverse direction as the main, slower front, a phenomenon coined "rapid tremor reversals" (Bostock et al., 2015; Houston et al., 2011). In Figure 1.3, we display LFE activity patterns characteristic of the Guerrero tremor zone. Activity is intermittent, at all scales: each zoom demonstrates that an apparent burst is in fact constituted of smaller bursts of activity, separated by periods of relative quiescence. The activity migrates along the dip of the fault, in both up and downdip directions, at velocities ranging from tens of kilometers per day to tens of kilometers per hour.

The most salient feature of LFEs migrations is their constant migration speed, and that different velocities seem to coexist in the same region of activity. In a modeling study of fluid-induced swarm seismicity, Dublanchet

and De Barros (2021) reproduces constant speed, slow and fast migrations. In order to describe the seismic behavior of a prestressed fault in which fluid is locally injected, they describe fault slip in a rate-and-state framework. The fault is mostly stable frictionnaly, with small unstable patches that generate the seismic events. Fluid pressure propagates diffusively, and diffusivity is coupled with fault slip, to reproduce the increase of permeability that slip should trigger on the fault. They observe a slowly propagating front of seismicity away from the injection point, that tracks the propagation of the a slow slip front triggered by the lowered effective normal stress. Fast migrations of seismicity are observed within the slipping region of the fault, and act as cascades: each event triggering neighboring ones. Although their results seem to match closely the migrating behavior of LFEs and tremor, they also conclude that the fluid pressure is only involved in triggering the slip around the injection, and pre-stressing the fault to criticality. Because there is evidence that fluid circulation should be a strong factor shaping tremor activity, a models that only rely on slip to explain patterns should be applied with caution.

Pulse-like propagations of fluid pressure in a fault can occur when considering that a small increase in fluid pressure will also dilate pores, and thus increase the permeability of the medium (Rice, 1992). The fluid pressure then propagates as a pulse within a pocket of high porosity and permeability, in a mechanism akin to porosity waves that can occur in a pressurized, deforming porous medium (Skarbek & Rempel, 2016). In a study of rapid tremor migrations in Guerrero, (Cruz-Atienza et al., 2018) have used this framework to interpret constant-speed propagations of tremor along the dip of the subduction as propagating pulses of activity triggered by high-fluid pressure and slip pulses. Variations of permeability in response to fluid pressure can in general shape complex migrations of fluid along permeable structures, like faults. Ross et al. (2020) for instance interpret the different phases of propagation of seismicity during the Cahuilla swarm as a step by step diffusion of pressure within a fault. As a fluid source fills a confined region along the fault, the seismicity progresses within the region with a diffusive profile, until it meets a barrier of permeability. Then, pressure rises in the confined region, and a seismic event breaks the barrier, setting off a new phase of diffusive propagation of seismicity along the fault. When taken together, all those phases appear as an intermittent but almost linear propagation of seismicity along the fault. Taken to a limit, one could imagine that if the confined pockets of fluid are small enough, this barrier behavior could explain fast, linear migrations on a short scale, as activity cascades from breaking barrier to breaking barrier, triggered by the influx of fluid (N. M. Shapiro et al., 2018).

1.3.2 The intermittence of tremor and LFE activity

The final aspect of tremor activity we want to tackle here is perhaps the most obvious, that tremor occurs in "bursts". Tremor activity is characteristically intermittent, occuring in finite episodes of high activity, separated by periods of low or inexistant activity. When considering that tremor is composed of the cumulated contribution of many elementary sources producing LFEs, the intermittent behavior can be thought of as a phenomenon of synchronization of sources in time: all sources being active or quiescent at the same time. It is a striking component of this system, and characterizing and modeling it could bring strong insight into the deformation and hydraulic processes generating tremor.

A first characteristic of the intermittence of tremor is the quasi-periodicity, or characteristic recurrence times of the largest bursts of tremor. In Cascadia (Brudzinski & Allen, 2007), Guerrero and Oaxaca (Frank & Brodsky, 2019; A. Husker et al., 2019), or the Nankai tremor zones (Poiata et al., 2021), the largest bursts recur relatively regularly, every several months to a few years, almost periodically. When taking a closer look at the activity, it is often hard to define a characteristic size for such bursts, however. Indeed, in some regions, tremor intermittence seem to be scale-free, proceeding in imbricated bursts of all sizes, with different recurrence times depending on their sizes (Frank et al., 2014; Poiata et al., 2021) (*cf* Figure 1.3). This scale free process can however be characterized, by evaluating the frequency of occurence of bursts of all sizes (Frank et al., 2016). This reveals that the clustering of events changes in time, outside of bursts, the activity is smoother, occuring at a more constant rate than during large transients, where events cluster strongly, small bursts building up larger, longer bursts (Frank et al., 2016; Poiata et al., 2021). The level with which sources synchronize to build bursts is also variable in space, and delineates a clear segmentation of the tremorgenic zones, along the strike and dip of the interface (Frank et al., 2016; Poiata et al., 2021).

Many of those characteristics can be explained in a framework where tremor is generated by small shear sources triggered by a slow-slip transient on the subduction fault (Ando et al., 2010; Obara et al., 2004; Rogers, 2003), however, few studies model the full complexity of tremor patterns in a fault slip framework (Luo & Liu, 2019), from the intermittent activity of a source to the emergence of large scale patterns of recurrence and migrations. In such studies, time clustering of activity, migrations and long-period of recurrence of activity burst emerge, consistent with the observed recurrence of episodic tremor and slip events in subduction zones (Luo & Liu, 2019). The heterogeneity of the fault zone, in terms of asperity size and effective normal stress conditions can lead to domains of the fault that trigger early or late, interfer-

ring with larger scale behavior, and provoking the emergence of smaller scale bursts, recurring on a shorter timescale (Luo & Liu, 2021). During large slip transients, strong asperities start slipping, and amplify the triggering effect of the slip around neighboring asperities. In such a framework, the sources synchronize more during slip transient, and can reproduce the observed strong temporal clustering behavior during high tremor activity transients (Frank et al., 2016).

Fluid pressure and permeability are often key to explain the recurrence and intermittence patterns of tremor in such framework, by shaping the heterogeneity of the frictional parameters on the fault for instance (Luo & Liu, 2019). However they are often described in a static manner, without interaction with slip. The dynamic implication of fluid pressure should play a strong role, by shaping slip patterns or directly triggering seismic waves, and its contribution to the emergence of tremor patterns cannot be studied if it remains a simple static parameter in the description of processes that shape tremor. To our knowledge, few studies have tackled this problem in subduction zones. A study by Zhu et al. (2020) however present a model of a fault-valving behavior in a crustal strike-slip fault, in which fluid is channeled towards the surface from a deep source. In their model, slip on the fault generates a permeability increase, and healing processes shut the permeability close and increase the friction on the fault. Their description allows for both changes of pressure and permeability on the fault, and the patterns of slip generated demonstrate that the involvement of a fault-valve mechanism can generate complex, intermittent seismic behavior, as small rupture cascade in the fault in swarm-like patterns, coupled with the ascent of high-pressure fluid and opening permeability. Even though it is not reported in the aforementionned study, the accumulation and release of fluid in a sealed subduction interface could influence the period of activation of fault slip and therefore seismicity, in a larger scale fault-valve mechanism (Frank, Shapiro, et al., 2015; R. Sibson, 1992). On a smaller scale, the propagation of fast diffusive fluid pressure transients could outpace slip, and be responsible for cascading activity, and therefore temporal clustering of sources (N. M. Shapiro et al., 2018).

1.4 Fluid circulation in dynamically permeable systems

An array of geophysical and geological evidence indicates that fluid flow conditions in the permeable subduction channel are near-lithostatic, heterogeneous, and variable. In active subduction zones, seismic imaging of the subduction interface (Gosselin et al., 2020), stress-orientation derived from the

Geological evidence for dynamic fluid circulation in the subduction fault zone

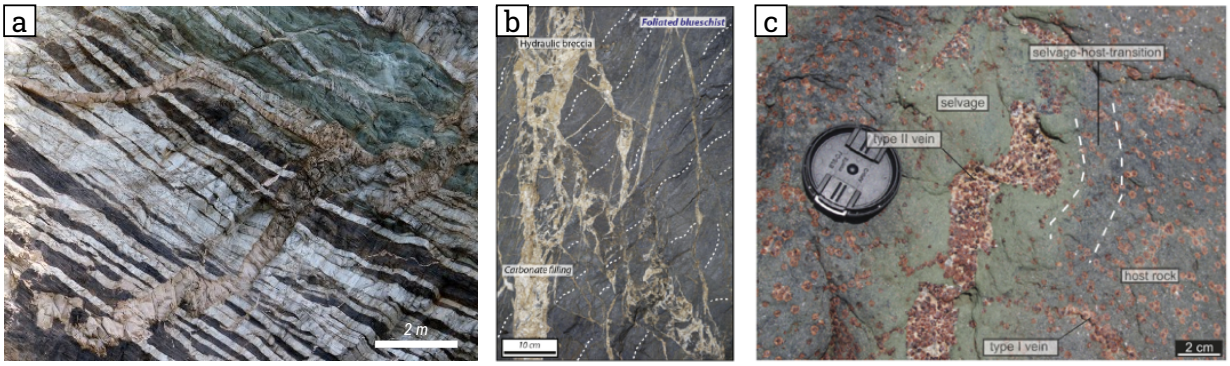

Figure 1.4 — *Geological evidence for transient flow conditions in the subduction fault zone. (a) Evidence for large scale hydrofracturation in the Franciscan Complex, in Catalina Islands, (CA, USA). Picture credit: John Platt, from Aristide (2020). The large, beige magmatic dike cross-cuts parallel quartzic veins, which could be symptoms of repeated episodes of hydrofracturation and catastrophic, overpressured fluid flow in the fault. (b) Hydraulic breccia in a paleo subduction channel, in the Zagros orogen (Iran). The breccia likely comes from hydrofracturation of the blueschist matrix, evidence for overpressurized fluid, and brutal variations of fluid pressure, flow, and permeability of the rock. The picture is from Muñoz-Montecinos et al. (2021), Figure 3E. (c) Veins in the Pouébo eclogite melange, in New Caledonia (France). Type I veins are evidence of progressive concentration of dehydration fluid in the medium. As they interconnect and start forming a network, large type II veins form, and channel fluid from outside the region, as evidenced by the chemical anomalies in the selvage pattern around the veins. The photo is taken from Taetz et al. (2018), where the authors find that the chemical anomaly induced by metastomatic reaction between the external fluid and the host rock can help constrain short residence time of the fuilds in the veins, on the order of months or less. This is further evidence of dynamic flow processes in the fault zone.*

focal mechanisms of plate-interface earthquakes (Warren-Smith et al., 2019), measures of the seismic attenuation above the slab and gravity anomaly measurements (Tanaka et al., 2018) seem to indicate that the high fluid pressure in the tremor source region drop suddenly when episodic tremor and slip occurs in subduction zones, indicating a sudden breach of the seal that confines the fluid in the interface. In outcrops of paleo-subductions, evidence of hydrofracturation (Muñoz-Montecinos et al., 2021) and cyclic vein-opening and healing (Behr & Bürgmann, 2021; Taetz et al., 2018; Tarling et al., 2021) point towards strongly varying and heterogeneous fluid pressure and fluid transport along the subduction channel (Angiboust et al., 2015).

Different processes can generate such changes of permeability. The most explored mechanism is a coupling with slip, in which slip opens up permeability, through damaging that opens micro-cracks for the fluid to circulate

in (Mitchell & Faulkner, 2008), breaking the cement that formed in the gouge of the fault plane an therefore connecting pores through newly formed pathways (Tenthorey & Cox, 2006), or through a dilatant mechanism in which the fault opens during slip, allowing the fluid to circulate (Cappa et al., 2022; Im et al., 2019b; Segall et al., 2010). In either case, slip pumps fluid into the active portion of the fault, and propagates a high-pressure fluid mass as it progresses along the fault. This type of behavior is what is referred to as a "fault-valve" mechanism. However, slip is not necessary to generate strongly heterogeneous and variable conditions of fluid pressure in the fault zone. Mechanisms that only involve the dynamics of the hydraulic system can be sufficient to generate such patterns. We want to highlight two classes of such processes, porosity waves and clogging-unclogging of the porous medium.

Porosity waves occur in mediums where porosity can change in response to a fluid influx and subsequent increase in fluid pressure. As fluid is pumped into the porous fault zone by dehydration reactions, perhaps episodically, a local increase of fluid pressure will propagate as a non-linear, sometimes solitary, wave in the decreasing direction of the fluid pressure gradient, as it dilates the pore space, thus generating new permeability for the fluid to circulate in. The dilation of pore space can be due to a simple poro-elastic effect (Cruz-Atienza et al., 2018; Rice, 1992), or to viscous creep (Skarbek & Rempel, 2016). Such propagations of pulses of high fluid pressure have been linked with the propagation of tremor and slip episodes in subduction zones (Cruz-Atienza et al., 2018; Skarbek & Rempel, 2016). However, as the resulting waves have to follow the gradient of fluid pressure, they cannot be a straightforward interpretation of the many observations of downdip-propagating tremor activity (*e.g.* Ghosh et al., 2010).

In geological porous medium, fine particles can partially clog the permeable pathways, and be mobilized by the flow if the traction force of the flow becomes high enough. Such behavior has been largely studied in the lab, in experiments of filtration of a fluid carrying particles through a model fault in a rock (Candela et al., 2014) or model porous medium (Bianchi, Thielmann, et al., 2018). In such systems, particles aggregate and form clogs in thin pore throats between pores, thus reducing the medium permeability, as represented in Figure 1.5. They are then suddenly removed from the constrictions as the pressure gradient increases across the clogged pathway, and the traction forces generated by fluid flow in the low-permeability clog mobilizes them. In experiments of continuous filtration, jumps of fluid pressure and variations of flow spontaneously occur as the medium clogs and unclogs. The power law size-frequency scaling of such pressure jumps is characteristic of avalanche behavior, implying that several pores could clog and unclog in cascades (Bianchi, Thielmann, et al., 2018). Both experiments and numeri-

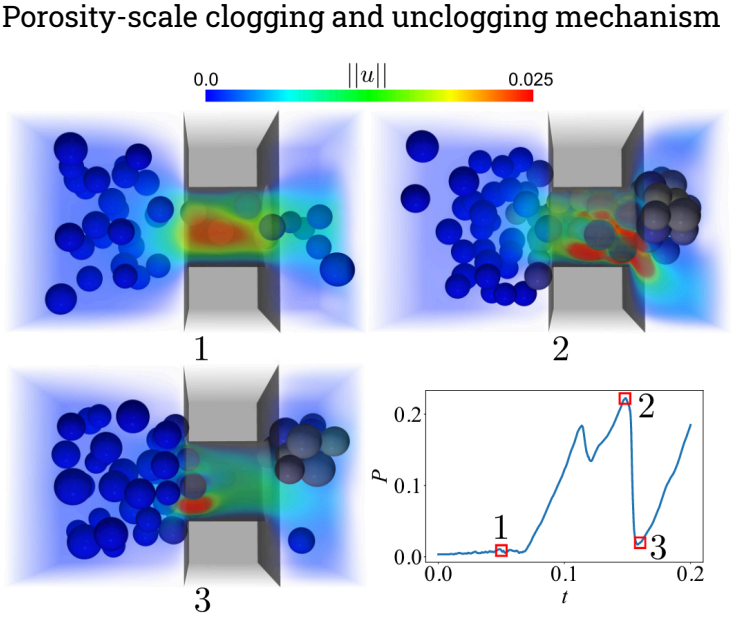

Figure 1.5 — *Snapshots of a modelisation of pore-scale clogging (Jäger et al., 2018). The panel in the lower right represents the evolution in time of the pressure P behind the constriction. In (1) the fluid freely flows through the constriction, in (2) particles clog the constriction and P rises because of the reduced permeability, in (3) the clog is eroded. Flow velocities u are represented with the rainbow colors. Figure taken from Jäger et al. (2018).*

cal simulations of such processes indicate that the imposed pressure gradient across the porous sample, fluid input rate into the sample and the particle size compared to the constrictions control the dynamics of this phenomenon: if the material stays clogged, if it is permanently unclogged as particles cannot deposit, or if intermittently clogs and unclogs (Bianchi, Thielmann, et al., 2018; Jäger et al., 2017b; Souzy et al., 2020). Pressure variations imposed to the fluid can therefore dynamically change the permeability by triggering clogging or unclogging of the pores, as evidenced by experiments of cyclical pressurization of a fluid saturated fracture (Candela et al., 2014). In reality, such behavior has been observed as passing seismic waves mobilize the fluid in shallow crustal faults, producing strong changes of permeability (Manga et al., 2012), and in oil reservoirs, where permeability of the reservoirs oscillates whereas the injection stays constant, due to deposition and erosion of asphalt modifying the permeability of the medium (Sahimi et al., 1999).

Such behavior would be extremely complex to observe in outcrops of paleo-subductions, because high temperatures and pressures would have erased and cristallized evidence of such pore-scale processes. However, it is plausible that either micrometric cataclastic fines (Han & Hirose, 2012) or silica colloids (Amagai et al., 2019) can clog the fracture permeability in the subduction channel, and that such clogging/unclogging processes be active

there (Prasianakis et al., 2017). If the pressure drops resulting from unclogging are strong enough, neighboring clogs could open in cascades, triggered by the flow through the initially breaking clog. Strong, rapid and localized pressure transients would therefore occur along the fault zone, and could propagate in both the up and downdip direction, as unclogging can occur due to an increase of pressure behind a plug, or through a decrease of pressure after a plug. Such rapid changes of pressure can act as a seismic source, or be responsible for triggering one (N. M. Shapiro et al., 2018), and therefore reproduce patterns of intermittent, cyclic and migrating seismicity along the fault, as it clogs and unclogs intermittently. It is not obvious how permeability-scale clogging and unclogging could relate with the evidence of hydrofracturation of the fault zone, but if many plugs can unplug at the same time, it would locally generate strong gradient of pressure that could be responsible for hydrofracturation in the fault. Alternatively, the clogging/unclogging description could be a convenient physical approximation for hydrofracturation, during which the cohesion of the fault zone material is overcome by the stress exerted by locally overpressurized fluid.

These processes are seldom taken into consideration when trying to understand tremor and LFE activity, and therefore their implication is not fully understood. However, because they can be responsible for strong, rapid, localized transients of pressure and permeability, and cyclic and migrating behavior of those transients, they could be a major force in shaping the source and spatio-temporal patterns of tremor activity.

1.5 Motivations for this work

As developed in the previous paragraphs, many aspects of low-frequency seismicity in subduction zones seem to involve complex fluid flow dynamics in the fault zone, from the seismogenic source processes to the processes responsible for the spatio-temporal patterns of activity. Most models that attempt to explain either the source or patterns however mostly focus on the implication of fault slip, often with a narrow range of interaction with fluid pressure or permeability, which does not allow to explore how their dynamics could shape the activity. In the subduction fault zone however, there is pervasive evidence that permeability is strongly dynamic, and that in itself, the dynamics of the hydraulic system are a dominant factor shaping the activity of tremor. In this thesis, our objective is therefore to build a framework that would help us evaluate this impact, in order to answer two complementary questions:

- From observations of the source and spatio-temporal patterns of low-frequency seismicity in subduction zones, can we get more insight into

how fluid dynamically circulates in the fault?

- How does the implication of transient opening and closing of the fault permeability could shape the source, intermittence and migrations of seismicity?

We will focus on the characteristics of low-frequency seismicity in subduction zones highlighted in this introduction: the unusual moment-duration scaling of LFEs, the intermittence of its activity, characterized by highly synchronized, migrating bursts recurring on long timescales, with quasi-periodic regularity. In order to reproduce such patterns and to understand how the hydraulic structure and dynamics in the fault controls the seismicity, we will build a model that links fluid circulation in the fault with source processes of LFEs, to describe how sources can interact through the hydraulic system, thus building emergent patterns of activity. This model will focus on the strong changes of fluid pressure and permeability observed in active and fossilized subduction faults, in order to build a framework that allows to explore their role in shaping the seismicity we observe. It will connect the hydraulics of the system with processes shaping both the source and patterns of tremor and LFE activity, and produce catalogs that can be directly compared with the seismicity observed in subduction zones.

Although we will argue that this framework is more general, we will focus on understanding low-frequency seismicity in subduction zones. Because subduction zones produce megathrust earthquakes that can grow to be larger than $M_w 9$, thus a major threat to the region, they are highly monitored. The long and wide coverage of seismic observations thus provided can help image long-term processes with a high resolution. The quality of this data is precious to understand further the mechanics of tectonic and hydraulic stress accumulation in the fault, and our work will therefore participate in building a more detailed and thorough understanding of the earthquake cycle in these faults. More generally, by directly connecting unsteady fluid circulation processes and seismic activity in a simple model, we provide a framework that helps conceptualize how fluid flows in geological systems, how it shapes seismicity, and in return, what the seismicity can tell us about fluid flow processes. Further understanding microseismicity as a symptom of dynamic flow processes is precious to monitor hazardous systems, such as industrial injection of fluids in the crust that can cause intermediate-size earthquakes, or the build-up towards eruptions in volcanic systems.

This thesis is organized as follows. In a first part, we characterize the source parameters of LFEs in Guerrero, Mexico, in order to further understand their source mechanism, and the possible involvement of transient fluid processes in generating them. In a second part, we elaborate a model of how fluid transport properties should change in response to fluid pressure in the

fault, and how such changes can be responsible for seismicity. We then explore the activity regime of this system, in order to find the hydraulic conditions necessary for a realistic, sustained but intermittent seismicity to occur, under constant fluid flow conditions akin to the constant dehydration in subduction zones. After highlighting intermittence and migration patterns that seem to reproduce the behavior of tremor and LFE activity in subduction zones, we proceed to evaluate how hydraulic interactions in the fault zone shape the temporal clustering and periodicity of the simulated activity. This last part of our work allows us to discuss how the structure of the plate interface should play a role in shaping the hydraulic system of subduction, which then affects how seismicity manifests. Before concluding, we take a final look at the consistency of the modeled processes with the geological observations of fossilized fluid flow processes in subduction zones, and discuss the relevance of this framework to explain volcanic low-frequency seismicity as a symptom of fluid circulation in the plumbing system.

Part II

The source of low-frequency earthquakes

Chapter 2

Characterization of the seismic source of LFEs in Guerrero, Mexico

Contents

2.1 Introduction

LFEs are a member of the "slow earthquake" class of phenomena, regrouping events which seem to be associated with slow slip processes on faults (Beroza & Ide, 2011). Those events exhibit a wide range of durations (from slightly less than 1 s for LFEs, up to nearly a year for slow slip events) and

magnitudes (from around M_w1 up to $M_w7.5$). When accounted as a one family of fault slip processes, their seismic moment M_0 appears to be directly proportional to their duration T (Ide, Beroza, et al., 2007), whereas regular earthquakes align along a $M_0 \propto T^3$ scaling law (Allmann & Shearer, 2009; Houston, 2001; Prieto et al., 2004) due to the self-similarity of the rupture process (Kanamori & Anderson, 1975). However, considering slow-earthquakes as one entity relies on bridging two different scales of observations: geodetic observations of large-scale, long-term (sub-daily at minima) slow slip events and seismic observations of short term events as LFEs, and longer events (30-60 s) called very-low-frequency earthquakes (VLFEs). There seems to be evidence that the shortest slow slip transients measured to this day align along a self-similar moment-duration scaling $M_0 \propto T^3$ (Frank & Brodsky, 2019), and that only at the largest scales it would transition to a $M_0 \propto T$ scaling law (Gomberg et al., 2016). This observation isolates LFEs and VLFEs from the bulk of geodetic observations of slow slip. It brings into question whether they are simply smaller scale manifestations of slow slip, or they have a more complex coupling relationship with it. In particular, LFEs co-occur with slow slip events, and investigating their properties provides key insight to understanding fault state, geometry of activation and overall rupture process during slow slip activity (Beeler et al., 2013; Chestler & Creager, 2017a; Frank, Shapiro, et al., 2015; Houston et al., 2011, *e.g.)*.

In this study, we investigate the moment-duration relationship for LFEs in Guerrero, Mexico. As for regular earthquake, evaluating how moment release scales with source duration is key to understand the dynamics of the process generating LFEs. Similar studies have already been carried out in regions witnessing tremor and slow slip. In Cascadia, LFEs source duration has been found to be very weakly dependent on their seismic moment, scaling along $M_0 \propto T^{10}$ (Bostock et al., 2015). On the other hand, in Nankai, LFEs exhibit a self-similar behavior, scaling along $M_0 \propto T^3$ (Supino et al., 2020). To our knowledge this is the first published work to measure source parameters for LFEs in Guerrero, Mexico. We start with a large LFE catalog compiled by Frank et al. (2014) and select those whose waveforms have a sufficiently high quality to measure their seismic moments and corner frequencies. The latter are estimated with two different methods to check the robustness of the obtained results. Similar to the study of Bostock et al. (2015) for LFEs in Cascadia, we find that for the LFEs in Guerrero the corner frequency is very weakly dependent on the seismic moment.

2.2 Low-frequency earthquakes in Guerrero, Mexico

Slow-slip events (SSE), tectonic tremor, and low-frequency earthquakes have been observed in the state of Guerrero, Mexico, in the subduction zone of the Cocos plate under the North American plate (Frank et al., 2013; Kostoglodov et al., 2010; Payero et al., 2008). They have been detected in the Guerrero seismic gap — a corridor extending from Acapulco to Mexico City — that has not witnessed major earthquakes ($M_w > 7$) for more than 100 years (Kostoglodov & Pacheco, 1999). This longer recurrence time of major earthquakes compared to adjacent regions can be related to the large SSEs that accommodate a significant fraction of the plates convergence in the Guerrero seismic gap (Radiguet et al., 2012a).

We use the data collected during the Meso-American Seismic Experiment (MASE) (A. Husker et al., 2008; Perez-Campos et al., 2008), between 1 January 2005 and 15 April 2007. Following the work of Frank and Shapiro (2014), we selected a subset of 10 stations out of the 100 total based on their high signal-to-noise ratio (SNR), the continuity in time of their records, and their proximity to the LFE activity (see Figure 2.1). Frank et al. (2014) used this dataset and the method described in Frank and Shapiro (2014) to compile a large catalog of 1.8 million LFEs grouped in 1120 families of repeating events. We use this catalog as a starting point in our study. It should be noted that the events in the catalog are detected by a matched-filter search using template events, filtered between 1 and 2 Hz. This band-pass is narrower than the range most studies of LFEs using matched-filter search have used up to now, usually 1–8 Hz (*e.g* Bostock et al., 2015; Chamberlain et al., 2014)

Nonetheless, we show in appendix 2.A that performing the matched-filter search in a narrow band does not bias the event detection and measurements of events' seismic moments and corner frequencies. Within the range of measured seismic moments, events with a corner frequency higher than 1 Hz do not have a lower probability of being detected because of the band-limited nature of detection.

2.3 Selection of LFEs with high-quality waveforms

The catalog of Frank et al. (2014) has been created on the network-based template matching detection method (Gibbons & Ringdal, 2006, for instance). The advantage of this method is that it detects many events with very weak signals hidden in the noise. At the same time, the signal-to-noise ratio for most LFEs in the final catalog is too low to be suited for a determination

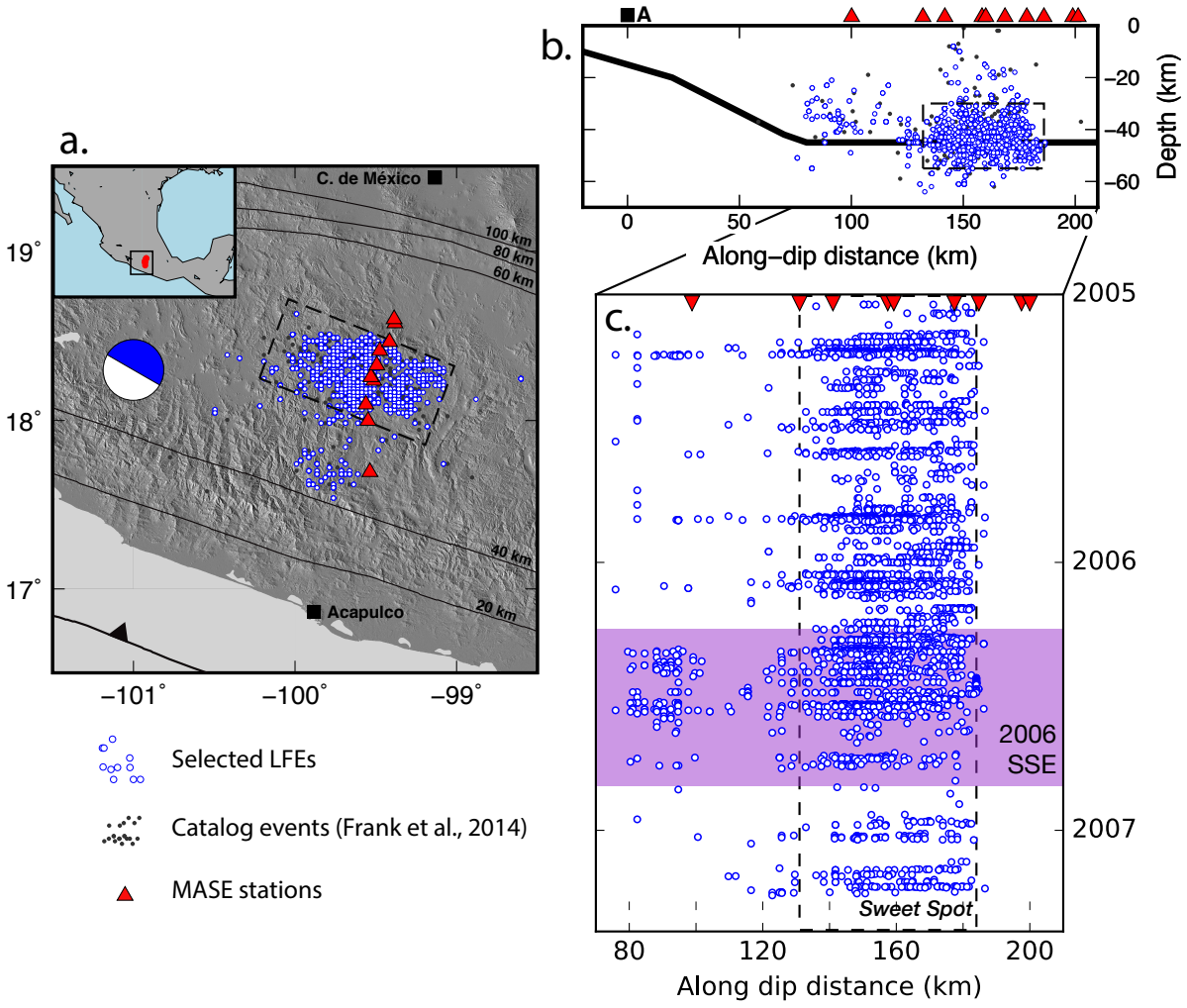

Figure 2.1 *— Spatial and temporal distribution of the selected LFEs. Selected LFEs are plotted as white and blue dots, the bulk catalog of Frank et al. (2014) is in gray. Subduction interface depth contours are displayed in black (Kim et al., 2010). The focal mechanism corresponds to an average mechanism computed from cataloged LFE detections (Frank et al., 2013). (c.) shows the time-dip distribution of the events.*

of their source parameters. Therefore, we selected LFEs with high-quality waveforms that could be used to robustly measure their seismic moments and corner frequencies.

Some single-component waveforms of catalog detections are contaminated with very high amplitude spikes, instrumental noise or waves from strong earthquakes. In these cases, useful signals are masked and corresponding waveforms cannot be used for determination of the LFE source parameters. We remove those seismograms from the analysis. Determination of seismic moment requires knowing the earthquake source location. However, LFE family locations determined by Frank et al. (2014) contain a strong uncertainty on position in the direction perpendicular to the station array. This uncertainty is inherent to the linear observation geometry of the MASE network. Consequently, a few families of LFEs have templates with diffuse seismic phases, indicating that their measured position is loosely constrained. We therefore remove those families of events from our analysis.

We establish a set of criteria to automatically select LFEs and waveforms suitable for measuring the source parameters. We select 5 s long signals starting 2 s before the cataloged detection time of LFE S-waves.

This allows us to capture the most impulsive part of the S-wave signal, and allows for slight location and detection time imprecisions. This is done so as to trade-off between keeping a maximum of information and not allowing for too much diffuse seismic energy in the form of other seismic phases and events. By isolating the most impulsive part of the wave train, we best constrain the characteristic frequencies and seismic moment of the event.

In a next step, we reject signals with low amplitude and impulsivity to exclude false detections and contaminations with surface waves. First we define two frequency ranges in which we determine both an impulsivity I and an amplitude A: they will allow the criterion to be more flexible as for which events are taken into consideration. The impulsivity is calculated as the ratio of the seismic energy in the waveform time window $\mathcal{W}$ to the seismic energy contained in a three times larger background time window $\mathcal{B}$ around the detection, containing it:

$$I = \frac{\int_{\mathcal{W}} s(t)^2 dt}{\int_{\mathcal{B}} s(t)^2 dt} \tag{2.1}$$

where $s(t)$ is the velocity signal. I varies between 0, for least impulsive, and 1, for most impulsive. It is used as a proxy of the detection SNR, but it also addresses the difficulty of defining what is noise within the tremor, where the LFE rate is very high. The amplitude is calculated as the maximum of the envelope of the filtered signal within the 5 s time window. For this purpose,

the waveforms are converted into complex analytical signals $s^A(t)$:

$$\begin{aligned} s^A(t) &= E(t) \,.\, e^{i2\pi f^i(t)} \\ A &= \max_{\mathcal{W}}(E(t)) \end{aligned} \tag{2.2}$$

$E(t)$ is the signal envelope and $f^i(t)$ is its instantaneous frequency. The latter will be used later on to determine the corner frequency of the selected LFEs.

Amplitudes and impulsivities are computed for all events on each channel of each station in the 1–2 Hz frequency band. This frequency range is characteristic of Mexican tremor signal in velocity, and has been shown to yield the best SNR for LFEs in this region (Frank et al., 2014; Payero et al., 2008).

So as to robustly ensure that the detection is a correctly located LFE we also base the selection criterion on the correlation coefficient used in the making of the LFE catalog. It is a measure of the correlation of an event waveforms on all 15 detection channels to the stacked-waveforms template of its family (Frank et al., 2014). We consider the highest absolute values of the correlation coefficient to represent a well-constrained location and an impulsive event. As a sum of 15 normalized correlation coefficients, it is normalized by the number of channels used in the detection of the event and thus varies between 0 and 1.

The selected waveforms have to fulfill the following criterion, where I is the waveform impulsivity and A its amplitude:

- The LFE should be impulsive, but waveforms with very high impulsivity are instrumental noise or earthquake wave arrivals:

$$0.5 < I < 0.92 \tag{2.3}$$

- Higher-amplitude LFEs are generally detected in distant earthquakes waveforms. Therefore, we empirically limit the amplitude of a selected detection to 2×10^{-6} m.s^{-1}. A lower threshold for selection $T_{low}(st, ch)$ is fixed for each station and component (approximately 5×10^{-9} m.s^{-1}). Both bounding values are manually determined using the impulsivity-amplitude distribution on each channel of each station (see Figure 2.2).

$$T_{low}(st, ch) < A < 2 \times 10^{-6}\text{m.s}^{-1} \tag{2.4}$$

For our source analysis, we select LFEs that contain at least 10 different channels satisfying the described criteria and have a network correlation coefficient superior to 0.4. This value has been chosen empirically, as the median of the correlation coefficients in the catalog.

A benefit of the network template matching method is that it allows to detect earthquakes with very close origin times, and thus with overlapping

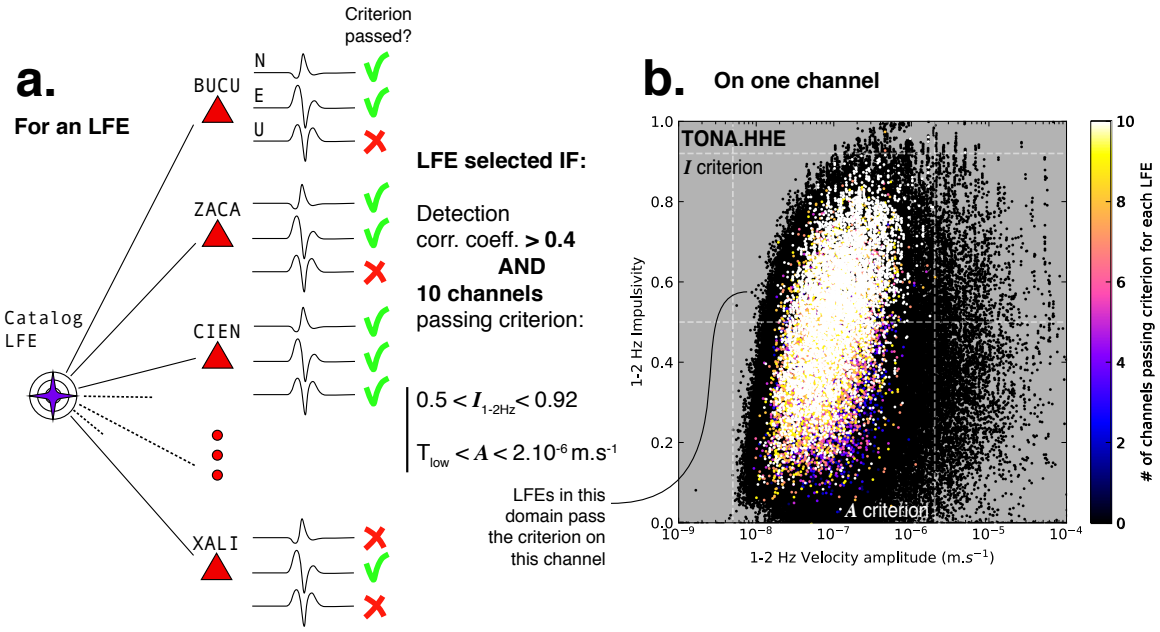

Figure 2.2 — *Selection of LFEs. (a.) Schematic recapitulation of the selection procedure. (b.) Amplitude-impulsivity distribution of all detections recorded on the East component of the station TONA. Each dot is an LFE, its color corresponds to the number of channels on which it is recorded that pass the criteria. Selected LFEs are white dots: they are recorded on 10 or more channels passing the criterion and fulfill the recurrence and correlation requirements. The amplitude and first impulsivity criteria (equations 2.4 and 2.3) are shown with dashed lines. LFEs in the criterion domain pass the criterion on TONA.HHE, but 9 other records passing the criterion on other channels of the network are needed for an LFE to be selected.*

signals at some stations. Overlapping signals are not suitable for the source parameter analysis. Therefore, if several LFEs are detected within a 10 s time window, only the LFE with the highest correlation coefficient, and thus most reliable waveforms, is kept. Figure 2.2 sums up the selection process.

The selection yields 3498 LFEs representing 822 families out of a total of 1120. Each event is recorded on 10 selected channels over the network and shown with blue circles in Figure 2.1. The most impulsive waveforms of two selected LFEs are displayed in Figure 2.3. The selected LFEs exhibit a similar activity behavior in space and time as Frank et al. (2014) observed for the whole catalog. First, they occur mainly in bursts within the sweet spot region. Second, during the 2006 SSE, bursts are no longer limited to the sweet spot, but extend updip in the transient zone. The activity in those two regions resembles the description Frank et al. (2014), the sweet spot has a nearly con-

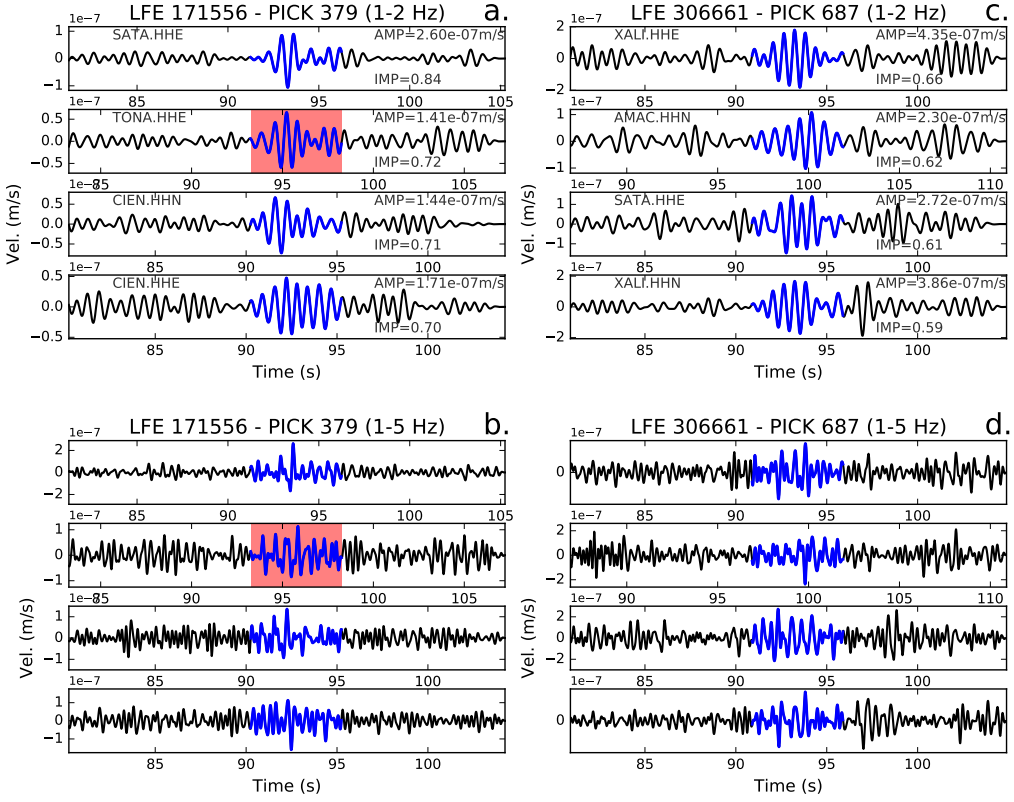

Figure 2.3 — *Selected LFEs' waveforms. The 4 most impulsive waveforms of LFE 379 and 687 are displayed here, 1–2 Hz band-pass filtered ((a.) and (c.)), and between 1 and 5 Hz ((b.) and (d.)). The blue section of the waveform shows the time window used to define the detected signal, the red patch shows which channel's waveforms are used as an example for source parameters characterization in Figure 2.4. Impulsivity and amplitude are indicated for each channel.*

stant activity over the 2-year span, whereas the transient zone is active mainly during the 2006 SSE and more sparse in the inter-SSE period.

2.4 Measuring source parameters

2.4.1 Seismic moment

We estimate seismic moment M_0 from the displacement spectra of S-waves $\widetilde{u}(f)$ that converges to a constant value at low frequencies (Brune, 1970). This constant is proportional to M_0 (Aki & Richards, 2002). For every selected waveform, we can determine the low-frequency spectral asymptotic value ${\Omega_0}^{i,j}$ as:

$$ {\Omega_0}^{i,j} = \lim_{f \to 0} \widetilde{u}^{i,j}(f) = C^{i,j} \, . \, {M_0}^{i,j}, \tag{2.5} $$

where i corresponds to the LFE number and j is an index given to each of the corresponding selected waveforms. The $C^{i,j}$ factor accounts for the source radiation pattern and the seismic wave propagation.

To measure these low-frequency asymptotic values, the 5 s long S-wave velocity waveforms selected in the previous section are first detrended and high-pass filtered above 1 Hz, to remove any influence of spectral leakage of microseismic noise, and then integrated into displacement. The power spectral density (PSD) of the displacement waveforms is computed with the multi-taper method (Thomson, 1982). It gives more robust spectral estimations than a simple discrete Fourier transform, especially for short signals. Taking the square root of this spectral estimation yields the displacement spectral amplitude. The low-frequency value of the displacement spectral amplitude ${\Omega_0}^{i,j}$ is estimated as the geometric mean of the 1–2 Hz portion of the spectral amplitude of displacement, filtered between 1 and 8 Hz (Equation 2.5, and Figure 2.4).

Then, seismic moment estimates from every waveform ${M_0}^{i,j}$ can be retrieved by computing the propagation effects factor $C^{i,j}$. For this purpose, we compute synthetic waveforms for each source-station couple, using LFE family locations from Frank et al. (2014) as hypocenters, an average regional seismic velocity model (Iglesias et al., 2010) and an average LFE focal mechanism, determined by Frank et al. (2013). We used the AXITRA software (Coutant, 2008) based on the discrete wavenumber method (Bouchon, 2003).

After the synthetic seismograms are computed, we select a 5 s long time window around the S-waves, process them in the same way as the LFEs' seismogram and compute their displacement spectrum without attenuation ${}^s_0\widetilde{u}(f)$, where f is the frequency. The seismic wave attenuation effects are modeled in the spectral domain by introducing $a(f)$. A corrected synthetic spectral displacement ${}^s\widetilde{u}(f)$ becomes:

$$\begin{aligned} {}^s\widetilde{u}(f) &= a(f)\,.\,{}^s_0\widetilde{u}(f) \\ a^{i,j}(f) &= exp(\frac{-2\pi f\, X^{i,j}}{2V_S\, Q(f)}), \text{ where } Q(f) = 273\ f^{0.66} \end{aligned} \tag{2.6}$$

where the frequency-dependent quality factor $Q(f)$ for the Guerrero region has determined by Ordaz and Singh (1992), the average shear wave velocity V_S is chosen to be 3.5 km.s^{-1} and $X^{i,j}$ is the source-receiver distance.

We determine the low-frequency asymptote of the synthetic spectrum ${}^s{\Omega_0}^{i,j}$ as the maximum of the synthetic spectrum, filtered between 1 and 8 Hz. Knowing the synthetic source moment ${}^sM_0$ and following equation (2.5), $C^{i,j}$ can be eliminated:

$$\frac{{\Omega_0}^{i,j}}{{}^s{\Omega_0}^{i,j}} = \frac{{M_0}^{i,j}}{{}^sM_0}, \tag{2.7}$$

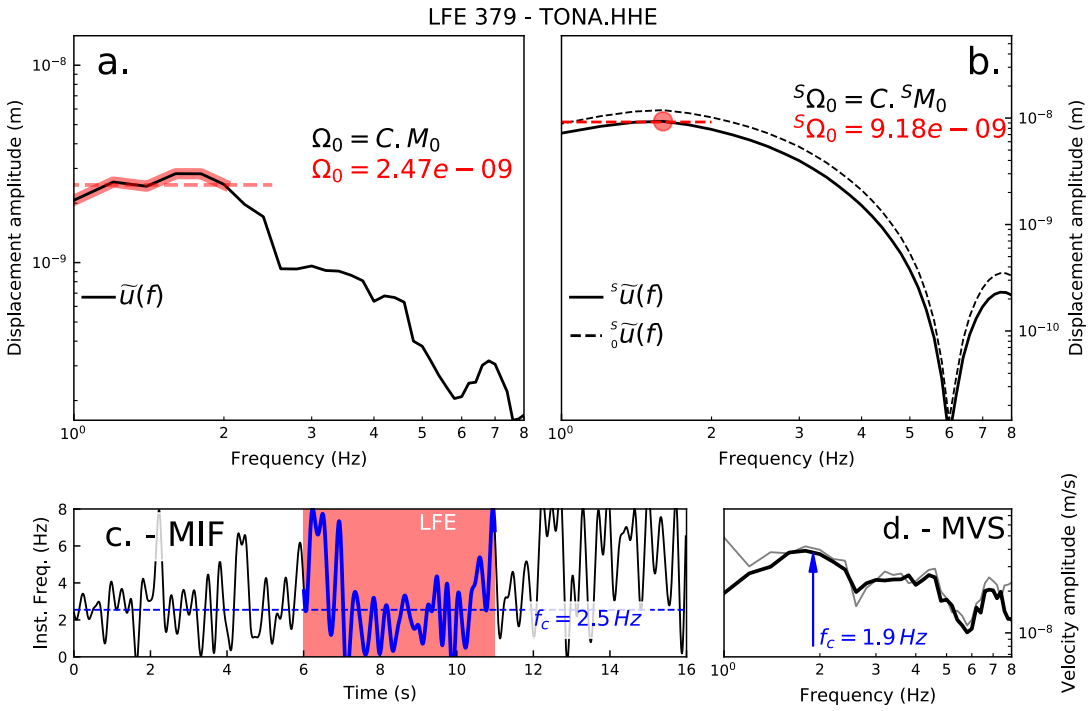

Figure 2.4 *— Determination of the seismic moment M_0 and corner frequency f_c, for an example low-frequency earthquake. Example LFE: nb. 379, channel HHE of station TONA. (a.) Ω_0 is determined as the red plateau of the displacement spectrum. (b.) ${}^s\Omega_0$ is determined as the maximum of the synthetic displacement spectrum, taking into account attenuation. (c.) The corner frequency f_c is measured as the mean instantaneous frequency (MIF) over the waveform time window (see Figure 2.3 for the LFE waveforms), (d.) and as the maximum of the velocity spectrum (MVS) of the waveform. In gray, the un-filtered velocity spectrum, allowing to assess the effects of the 1–8 Hz filter on the spectrum.*

and a seismic moment estimated for each waveform of a selected LFE becomes:

$$M_0{}^{i,j} = {}^sM_0 \frac{\Omega_0{}^{i,j}}{{}^s\Omega_0{}^{i,j}}. \tag{2.8}$$

2.4.2 Corner frequency

We use two different techniques to estimate the corner frequency from all selected waveforms for every LFE, $f_c{}^{i,j}$. For both methods, the waveforms are detrended, corrected for attenuation (see equation 2.6) and band-pass filtered between 1 and 8 Hz to remove any influence of micro-seismic signal and higher frequency noise from the frequency band that correspond to LFEs frequencies. Further discussion on the choice of this frequency band can be found in the appendix, section 2.A.

The first approach consists in automatically picking ${f_c}^{i,j}$ as the frequency corresponding to the maximum in the velocity amplitude spectrum of every waveform. This method is labeled MVS (maximum of velocity spectrum) in the illustrations. The bandpass filter creates a slight amplitude reduction up to 1.5 Hz, which can be seen when comparing the filtered and unfiltered spectra in Figure 2.4. This could shape the spectrum into a peak slightly above 1 Hz, if the actual peak frequency between 1 and 8 Hz is close to 1 Hz. However, we find that the 1–8 Hz filter band is the best compromise between allowing microseismic noise to bias the corner frequency measurement and slightly constraining the shape of the spectrum. The effect on measured corner frequencies of the low-cutoff of the filter is discussed more extensively in section 2.A and can be assessed in figure S2 of the supporting information file.

In the second approach, we estimate the corner frequency as the dominant instantaneous frequency of the S-waves. The waveforms are converted into complex analytical signals (see equation 2.2) and ${f_c}^{i,j}$ is estimated as the mean of the smoothed instantaneous frequency over the 5 s time window containing the S-waves. This method is labeled MIF (mean of instantaneous frequency) in the illustrations. For this method too, the effects of the filter band can be assessed in figure S2 of the supporting information file.

For each LFE, we obtain a final estimate of their moment ${M_0}^i$ and two estimates of their corner frequency ${f_c}^i$, all computed as medians of those measured from individual waveforms selected for this LFE. For each event, the uncertainty on its source parameters is estimated as the standard deviation of the values of the given source parameter measured on each record of the event.

2.5 Results

2.5.1 Seismic moment and corner frequency of LFEs

Seismic moments and corner frequencies estimated for the selected LFEs are shown in Figure 2.5 along with the schematic imprint of the M_0-f_c distribution for classical earthquake, which follows $f_c \propto {M_0}^{-1/3}$, for stress drops ranging from 0.1 to 100 MPa (Allmann & Shearer, 2009), and values of M_0 and f_c determined for LFEs in previous studies. Seismic moments and magnitudes estimated for Mexican LFEs range between $M_0 = 4.9 \times 10^{11}$ N.m ($M_w \sim 1.7$) and $M_0 = 2.3 \times 10^{14}$ N.m ($M_w \sim 3.5$). These values are higher than previous estimations in other regions (Bostock et al., 2015; Ide, Beroza, et al., 2007). The median uncertainty on moment magnitude of $\delta M_w \approx 0.23$. It is mainly due to errors in modeling the velocity structure of the crust, assuming a generic

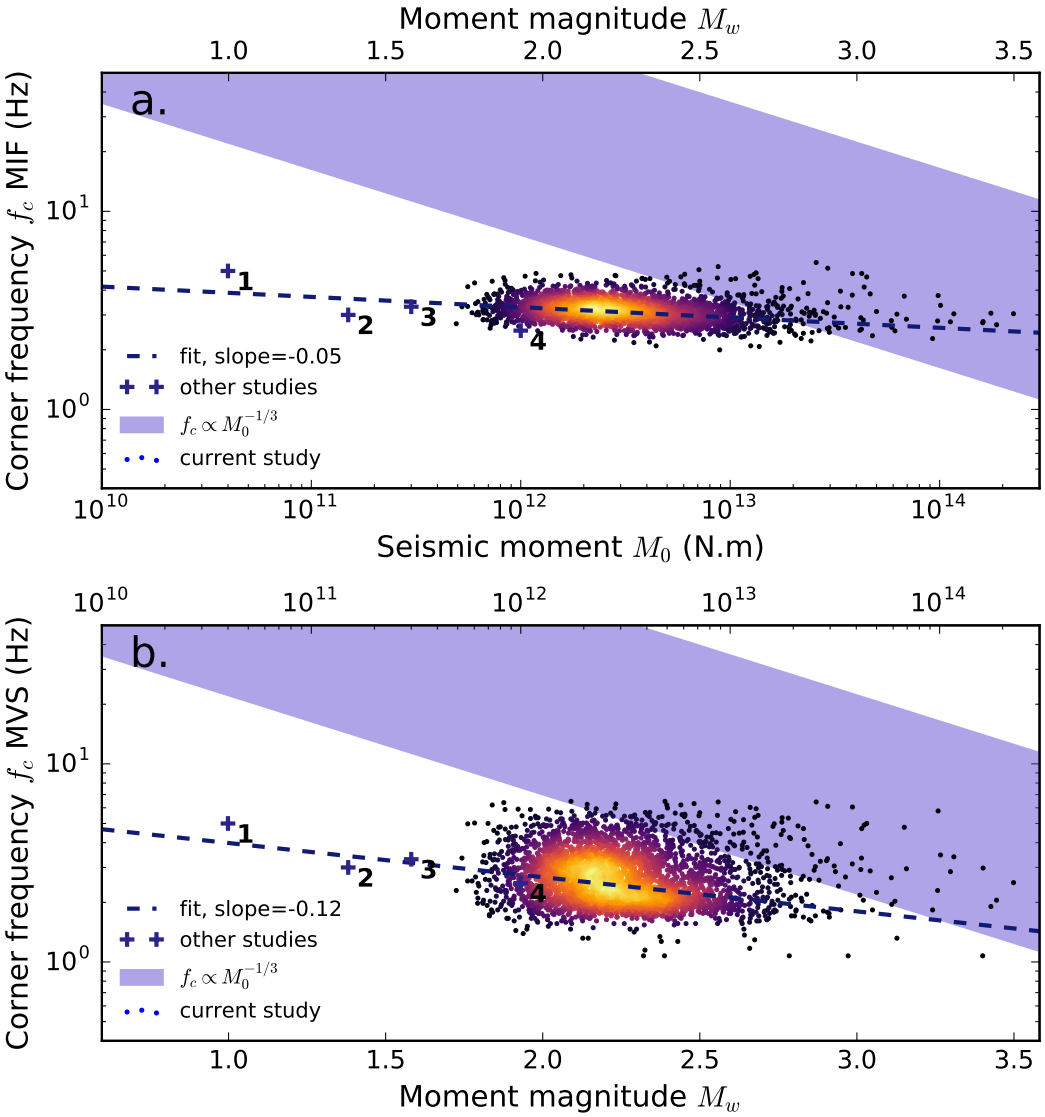

Figure 2.5 — *Distribution of the measured source parameters. The distribution is displayed and colored according to the point density for both methods of determining f_c: (a.) with mean instantaneous frequency (MIF), (b.) as the frequency of the maximum of the velocity spectrum (MVS). Weighted least-square fits to the binned moments (see Figure 2.6) are shown as dotted lines, in each respective plot. Generic values for M_0 and f_c measured in other regions are displayed along the distribution (1. Thomas et al. (2016), 2. Supino et al. (2020), 3. Ide, Beroza, et al. (2007), 4. Bostock et al. (2015)) The self-similarity scaling law for classic earthquakes is represented by the purple patch. The higher bounding line corresponds to a stress drop of 100 MPa and the lower to a stress drop of 0.1 MPa (Allmann & Shearer, 2009; Eshelby, 1957; Madariaga, 1976).*

radiation pattern for all events and large uncertainties on the hypocentral locations (Frank et al., 2014, supplementary figures 3 to 17). The distribution of seismic moments above a threshold magnitude of $M_{wthr} \sim 2.32$ follows a power-law, with an exponent $\beta = 1.62$ (corresponding b-value $b = 2.43$, see Appendix, Figure 2.7).

The measured corner frequencies mean and extrema for each method are displayed in Table 2.1. They are approximately centered around $f_c \sim 3.0$ Hz and fall within the accepted range of characteristic frequencies for LFEs of 1–6 Hz (Bostock et al., 2015; Ide, Beroza, et al., 2007; Shelly et al., 2007b; Thomas et al., 2016). The median uncertainty on corner frequency is $\delta f_c \approx 1.6$ for the maximum of velocity spectrum method, and $\delta f_c \approx 0.8$ for the mean instantaneous frequency method.

Table 2.1 — *Measured LFE source parameters statistics analysis values*

Characterization method	**Corner frequency f_c (Hz)**		
	Min	Median	Max
Maximum of instantaneous frequency (MIF)	2.0	3.2	5.5
Maximum of velocity spectrum (MVS)	1.1	2.6	6.5
Characterization method	**Seismic moment M_0 (N.m)**		
	Min	Median	Max
Low-frequency spectral asymptote	4.9×10^{11}	2.8×10^{12}	2.3×10^{14}
	$M_w 1.7$	$M_w 2.2$	$M_w 3.9$

2.5.2 Moment-duration scaling

The M_0-f_c distribution in Figures 2.5 and 2.6 shows that the corner frequencies seem virtually independent of seismic moment. In order to estimate the scaling law between the source parameters, M_0-f_c points are binned into 35 bins of ascending moment magnitude, containing 100 points each. Moment magnitude of the bin is considered to be the mean M_w of the events in the bin. Corner frequency of the bin ${f_c}^{bin}$ is the weighted mean of the measured corner frequency of the binned events. The weight associated to the corner frequency of event k is chosen to be the inverse of the variance of corner frequencies measured on each record for event k, $w_k = 1/{\sigma_k}^2$. Figure 2.6 shows

the bin distribution and the associated estimation of variability of corner frequency within bin, calculated as a weighted standard deviation:

$$\sigma^{bin} = \sqrt{\frac{\sum_k ({f_c}^{bin} - {f_c}^k)^2 \times w_k}{\sum_k w_k}} \tag{2.9}$$

with ${f_c}^k$ the measured corner frequency for event of index k in the considered bin, $w_k = 1/{\sigma_k}^2$ its associated weight (see above), and ${f_c}^{bin}$ as the bin's corner frequency.

Using the bins M_0 and f_c and their associated weight $w^{bin} = 1/{\sigma^{bin}}^2$, a weighted least-square fit to the following power law is performed, in log-log space:

$$f_c \propto {M_0}^{-\alpha} \iff log(f_c) = A - \alpha log(M_0). \tag{2.10}$$

The resulting values of the slopes confirm that corner frequencies are weakly dependent on seismic moment : for the mean instantaneous frequency method (MIF) used to obtain f_c: $\alpha = 0.052$, for the maximum of velocity spectrum method (MVS): $\alpha = 0.115$, (see Figures 2.5 and 2.6). This result is similar to the moment-duration scaling observed for LFEs in the Cascadia subduction zone by Bostock et al. (2015), where $\alpha \sim 1/10$.

We proceed to estimate the probability density function (PDF) of the exponent of the scaling using a bootstrapping method. For each bin, we keep its moment but pick a new corner frequency from a normal distribution parametrized by the bin's corner frequency $\mu = {f_c}^{bin}$ and by the bin's weighted standard deviation $\sigma = \sigma^{bin}$ (see equation 2.9). An unweighted, least-square fit to a power law (equation 2.10) is then performed on the bin's seismic moment and re-sampled corner frequency. After 200,000 iterations of the previous steps, we obtain an estimate of the probability distribution function for the scaling parameter α. The mean and standard variation of the obtained distribution give a new estimation of the slope and its associated uncertainty. For the MIF method, $\alpha = 0.054 \pm 0.034$, for the MVS method, $\alpha = 0.12 \pm 0.11$. Assuming that α is normally distributed, the probability that it is higher than 0.25 (thus closer to $1/3$) for our $f_c - M_0$ distribution is around 0.12 for the MVS method ($\alpha = 1/3$ is $\sim 1.2\sigma$ away from the mean α), and lower than 10^{-8} for the MIF method ($\alpha = 1/3$ is $\sim 5.7\sigma$ away from the mean α).

The scaling exponent α we measure is thus significantly lower than the earthquake power law exponent $\alpha = 1/3$, for the MIF method at least. The MVS method gives more ambiguous results with regard to the value of the exponent α, due to the wider distribution on f_c.

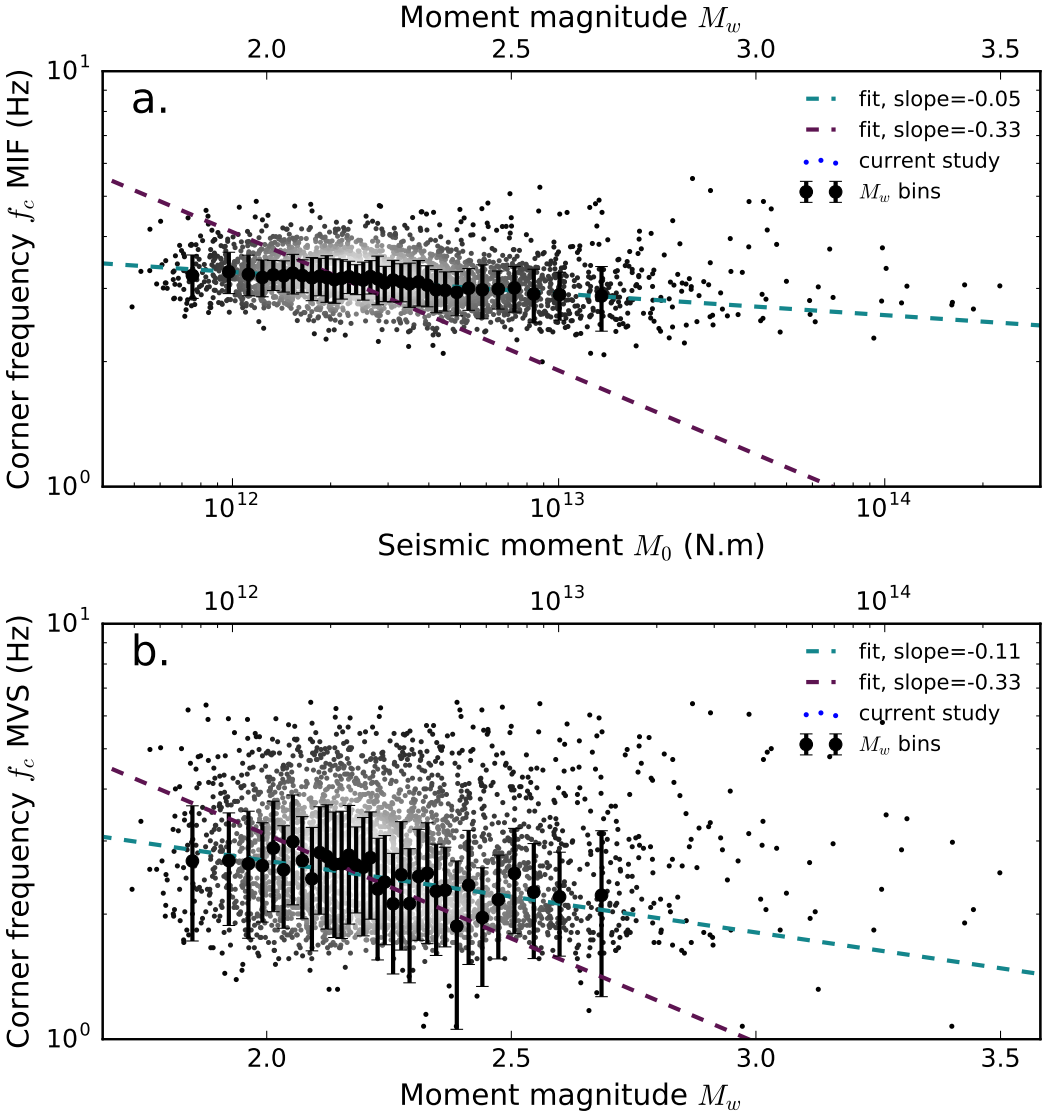

Figure 2.6 — *Binned distribution and uncertainties estimation. The measured M_0-f_c is displayed and colored according to point density, for both the mean instantaneous frequency (MIF) and maximum of velocity spectrum (MVS). Seismic moment and corner frequency are binned, and the weighted standard deviation is shown with the error bars (see text for details). Weighted least-square fits to the binned data are displayed, the fit resulting in the purple scaling has $\alpha = 1/3$ as a constraint.*

2.5.3 Stress-drop variations

The stress-drop for an event of seismic moment M_0 modeled by a circular dislocation of radius r is expressed as follows (Madariaga, 1976):

$$\Delta\sigma = \frac{7}{16}\frac{M_0}{r^3}. \tag{2.11}$$

Assuming a rupture velocity proportional to the shear wave velocity, $v_r \propto V_S$, it follows that the source radius is inversely proportional to the corner frequency (Madariaga, 1976):

$$r \propto \frac{V_S}{f_c}. \tag{2.12}$$

From equations 2.11 and 2.12, and keeping the assumptions that our events originate from regions of constant V_S and share the average corner frequency of our distribution $f_c \sim 3$ Hz, we can express the stress-drop ratio for two events of seismic moment M_{01} and M_{02}:

$$\begin{aligned} &\Delta\sigma \propto M_0 \\ \implies &\frac{\Delta\sigma_1}{\Delta\sigma_2} = \frac{M_{01}}{M_{02}} \end{aligned} \tag{2.13}$$

Using the extrema of the seismic moment distribution, and within the limit of our assumptions, we observe a stress-drop variation of a factor 300 across the range of measured seismic moments. For illustration purposes, we calculate what values would the stress-drop of our events take under the assumption that they have the same rupture speed as classical earthquakes, $v_r = 0.9V_S$. It yields $r = 0.21V_S/f_c$ (Madariaga, 1976), and using equation 2.11, the selected events have stress-drop ranging from 3 kPa to 1 MPa, with most events around 17 kPa ($M_0 \sim 2 \times 10^{12}$ N.m). In the following section, we discuss a possible mechanism for the observed range of stress-drops.

2.5.4 Moment-frequency distribution of LFEs

In Figure 2.7, we represent the complementary cumulative distribution function (abbreviated as CCDF, also called survival function) of seismic moments, $P(M_0 > M_0{}')$. It is computed with $M_0{}'$ regularly spaced in the magnitude range.

The higher-moments tail of the distribution can be described as a power-law distribution, with the following probability density function (PDF) and

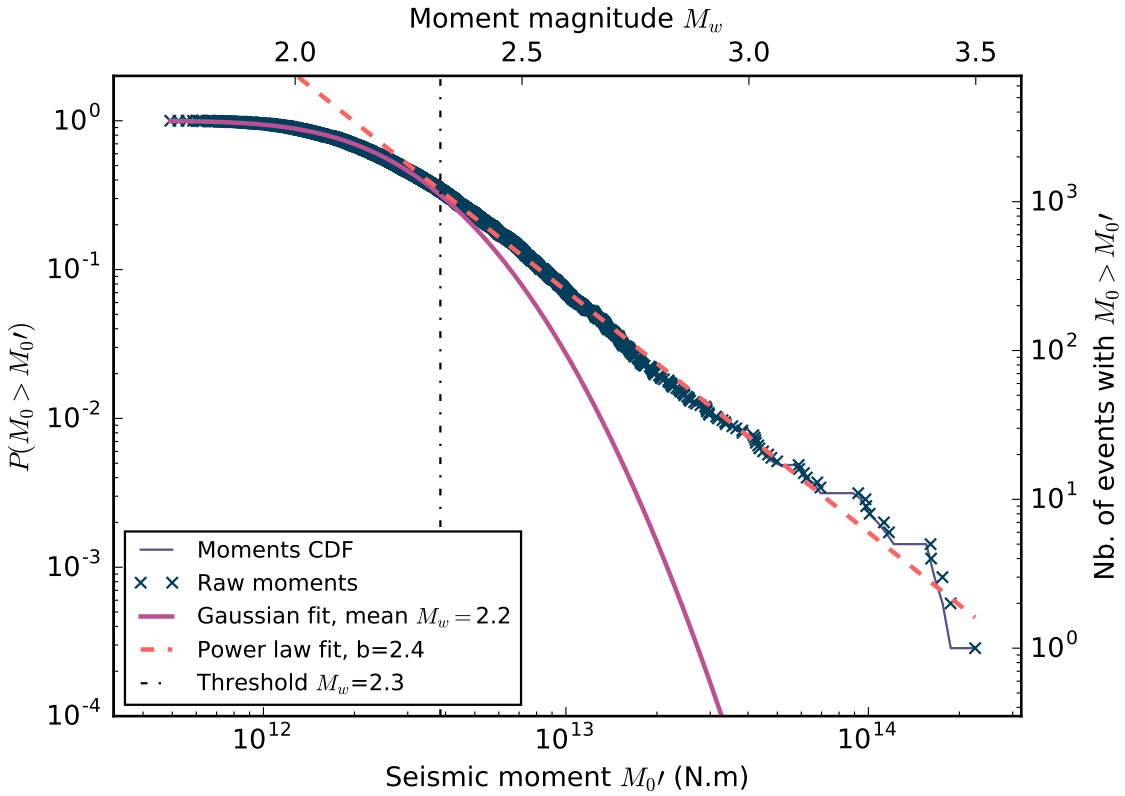

Figure 2.7 — *Moment-frequency distribution of the selected LFEs. The seismic moment complementary cumulative distribution function (CCDF) of our LFEs is modeled by a Gaussian below M_{wthr} 2.32, with mean magnitude M_w 2.4, and by a power law above M_{wthr}, with an exponent corresponding to a b-value of* 2.4.

CCDF:

$$p(M_0) = \frac{\beta}{M_{0thr}} \left(\frac{M_0}{M_{0thr}} \right)^{-\beta-1}$$
$$P(M_0 > M_0') = \left(\frac{M_0'}{M_{0thr}} \right)^{-\beta} \tag{2.14}$$

where M_{0thr} is the lower bound for which the power-law distribution is valid. The power law exponent β relates to the b-value of the Gutenberg-Richter law following: $b = 3/2\beta$. For moments above a threshold M_{0thr}, we perform an un-weighted, least-square fit of the logarithm of the moments CCDF to a power-law. We find that $\beta = 1.62$, and a corresponding b-value of $b = 2.43$. For comparison, b-values of classical seismicity are usually around 1. The threshold magnitude $M_{wthr} = 2.32$ (corresponding to M_{0thr}) is selected so as to minimize the Kolmogorov-Smirnov statistic for the moments' distribution and the fitted power law.

The deviation from a power law at lower moments is often attributed to observational limitations: below a completeness magnitude, events are too weak to all be detected, and it manifests as a deviation from the otherwise assumed power law distribution of moments. Here, the completeness mag-

nitude would thus be $M_{wthr} = 2.32$. The departure from a power-law at lower moments can also be the manifestation of a characteristic scale of magnitude of the events. Several studies report observations of LFEs size distribution being best modeled by exponential laws and thus of a characteristic scale controlling the LFE size distribution (Chamberlain et al., 2014; Chestler & Creager, 2017a). In our case, a normal distribution can be fitted to the distribution of moments below M_{wthr}, parametrized by a mean magnitude $\overline{M_w} = \mu = 2.23$ and a standard deviation $\sigma = 0.19$. The mean magnitude $\overline{M_w} = 2.23$ defines a characteristic scale of the lower-bound of the moment distribution. It is either due to a scale limitation of LFEs in Guerrero, or a manifestation of the limitation of events' detection.

2.6 Discussion and interpretation of the observed scaling law

2.6.1 Scaling laws of earthquakes, slow earthquakes and LFEs

The results of our analysis show that the selected LFEs follow a moment-duration scaling $f_c \propto {M_0}^{-\alpha}$ with an exponent significantly lower than the value for regular earthquakes $\alpha = 1/3$ (Allmann & Shearer, 2009; Houston, 2001; Prieto et al., 2004, among others), around $\alpha \sim 0.1$ and $\alpha \sim 0.05$. The scaling found for selected LFEs in Guerrero concurs with the one found for LFEs in Cascadia by Bostock et al. (2015), who found a power law exponent of $\alpha = 1/10$, quite similar to the scaling described in this paper. It is noteworthy that the detection method used by Bostock et al. (2015) relies on a matched-filter search, similarly to the catalog used in our study. However, we argue that performing a matched-filter search in the 1–2 Hz band sets a lower bound, but no upper bound for the characteristic frequency, for a given seismic moment. Therefore, the values of corner-frequencies should not be the product of the detection method, but reflect the real moment-corner frequency distribution of events, within the measured magnitude range. This argument is developed in appendix 2.A. Interestingly enough, Supino et al. (2020) found the moment-duration scaling for LFEs in Nankai tremor areas to be similar to regular earthquakes, $\alpha = 1/3$. This discrepancy will not be thoroughly discussed here, but brings out intriguing questions, about the possibly different nature of the processes recorded in Guerrero, Cascadia and Nankai, and on the other hand, the potential detection and method biases that can lead to measuring different scalings.

Using a stochastic model describing a slow earthquake rupture (the Brownian slow earthquake model), Ide (2008); Ide and Maury (2018) showed that

large-scale slow earthquakes as slow slip events' duration and seismic moment should follow a $T \propto M_0$ scaling, whereas on the scale of LFEs, slow earthquake events should follow a $T^2 \propto M_0$ scaling, corresponding a value of $\alpha = 1/2$. In Ide (2008), it is noted that, due to the fact that detection is only possible above noise levels, the apparent duration of LFEs should be shorter than expected, bringing them closer to a moment-duration scaling with $\alpha = 1$. The LFEs we analyzed in Guerrero and the LFEs of Cascadia (Bostock et al., 2015) cannot be described by either scaling laws.

There is evidence that the shortest slow slip transients measured to this day are self-similar, exhibiting a $T^3 \propto M_0$ scaling law (Frank & Brodsky, 2019). The exact proportionality measured for larger scales slow earthquakes (Ide, Beroza, et al., 2007) could be due to the fact that the largest ruptures are bounded in their growth by the rheological properties of the fault zone, whereas smaller events growth is un-bounded, and thus self-similar (Gomberg et al., 2016). This geometric argument is valid both for slow and regular earthquakes, and further isolates LFEs moment-duration characteristic values and scaling from the ones of slow and regular slip. For LFEs in Cascadia and Guerrero, a satisfactory physical description that could reproduce the observation of the constant duration and relatively low-frequency content still needs to be devised.

2.6.2 Models for magnitude-independent duration of LFEs

2.6.2.1 A source of constant size, but variable slip

The scaling with $\alpha = 1/3$ for regular earthquake is explained by the self-similarity of the seismic rupture. It develops with a constant ratio between the characteristic length of the rupture and fault slip, and produces a magnitude-independent stress drop (Allmann & Shearer, 2009; Kanamori & Anderson, 1975; Prieto et al., 2004). Events with a wide range of magnitudes but with nearly constant durations could thus be generated by variable amounts of slip on asperities of nearly constant sizes, producing a very limited range of recorded signal duration (f_c) but variable seismic moments (Bostock et al., 2015; Lengliné et al., 2014; Lin et al., 2016). Independently from the current study, Frank and Brodsky (2019) found that, in Guerrero, the seismic moment rate, calculated from LFEs median amplitude during rapid slow slip transients scales with the moment rate calculated using GPS displacements during the same transient events. This reflects that the higher the seismic moment of LFEs, the higher the slip would be around the LFEs source. Combining those two observations leads to thinking of LFE sources in Guerrero as patches of fault of nearly constant area, that are forced to rupture by the surrounding slow, aseismic slip, with variable amplitudes of slip directly related

to the surrounding fault slip. A similar model has been designed to explain the observation of a size-limitation for LFEs in Cascadia, describing the LFE family patch as a collection of subpatches randomly activated, totaling to an apparent source radius of about 300 m (Chestler & Creager, 2017a).

2.6.2.2 Potential effects of fluid circulation and high fluid pressures

Early work on tectonic tremor and LFEs made the hypothesis that they are generated by fluids circulating in the vicinity of the fault zone (Kao et al., 2005; Katsumata & Kamaya, 2003; Obara, 2002). More recent studies have strengthened the link between non-stationnary, metamorphic fluid flow and migrations of LFEs and slow slip activity, based on numerical models of pore-pressure diffusion (Cruz-Atienza et al., 2018) and on analysis of the large-scale, spatio-temporal behavior of LFE activity (Frank, Shapiro, et al., 2015).

A study by Lengliné et al. (2014) reported that microseismic events occurring during water circulation tests display the same independence of corner frequency on seismic moment that we observe for our LFEs. As for the LFEs in this study, they find that stress drop varies on more than two orders of magnitude across the range of moments of their events. Likewise, Lin et al. (2016) reports that microseismic events detected in Taiwan exhibit the same characteristics. Both studies suggest that these observations can be interpreted as a systematic control of the events' stress-drop and duration by dynamic fluid injection. Indeed, fluid injection can reduce the effective normal stress on asperities of the fault where the events occur. As fluid is injected or when aseismic slip is active, rapid, strong, heterogeneous increase of pore pressure in the fault can dramatically decrease the effective normal stress and thus the strength of the fault, triggering seismic slip on localized asperities. Under these conditions, Lengliné et al. (2014) and Lin et al. (2016) argue that the heterogeneity of fluid injection is likely to produce the wide range of stress-drops they observe. As noted by the previous papers, reduced effective normal stress have also been suggested as a cause of the low values of stress drop of VLFEs in Japan (Ito & Obara, 2006). In the light of the similarity of our observations and the ones presented in the discussed studies, dynamic triggering of LFEs by fluid injection could be a relevant mechanism to explain the LFEs' stress drop values.

In order to account for the observation of events' constant duration, Lin et al. (2016) proposes that slip could only be maintained while the pore pressure is high enough to allow for seismic rupture, that is until the injection stops and the high pore pressure transient diffuses. The duration of the recorded seismic event would thus be controlled by the fluid transport properties in the fault zone. Those conditions of rapid, localized fluid injection are plausible within large active fault zones (N. M. Shapiro et al., 2018). In subduction

zones, fluids released by the dehydration of hydrous minerals in the downgoing slab circulate within a permeable channel formed along or within the fault zone (Angiboust et al., 2012; van Keken et al., 2011). If the permeability or width of the channel has strong lateral heterogeneities, N. M. Shapiro et al. (2018) suggests that strong, localized pore pressure transients can be formed. The strong, transient gradients of pore pressure can act as a source of seismic waves. The duration of such a source would thus be the characteristic time taken by a pore pressure transient to diffuse. N. M. Shapiro et al. (2018) shows that as with such a mechanism, this duration is only governed by the transport properties of the fault zone and independent of the source magnitude. Although more precise observations of the source radiation pattern of LFEs and a substantial modeling effort are needed to confirm this hypothesis, it is consistent with our observations.

Another lead to account for the apparent magnitude-independent, low-frequency content of LFEs is to interpret it as the consequence of specific, near-source propagation effects (Bostock et al., 2017). In this study the authors assume the existence of a narrow region with a very strong shear wave attenuation around LFEs source and suggest that the observed depletion in high frequencies can be related to this strong near-source attenuation of seismic waves. Based on accounts of high compressional to shear wave velocity ratio V_P/V_S in seismic cross-section of subduction zones (Bostock et al., 2012; Shelly et al., 2006), tidal triggering of LFE activity (Beeler et al., 2013; Royer et al., 2015; Rubinstein et al., 2008, *e.g.)* and dynamic triggering by teleseismic waves (Rubinstein et al., 2009), the source region of LFEs is thought to be under nearly lithostatic fluid pressures. Laboratory studies indicate that such high fluid content can also be the cause of strong shear wave attenuation (Tompkins & Christensen, 2001).

2.7 Conclusions

We analyzed a subset of carefully selected LFEs from the cataloged events of Guerrero, Mexico (Frank et al., 2014). The subset of LFEs samples a relatively broad range of seismic moments, between $M_w1.7$ and M_w3, with corner-frequencies clustering around 3 Hz, between 1.5 and 6 Hz. Overall, we find corner frequences to be very weakly dependent on seismic moments for LFEs in Guerrero. When trying to describe this relationship with the power law $f_c \propto {M_0}^{-\alpha}$, we retrieve $\alpha = 0.12 \pm 0.11$ and $\alpha = 0.054 \pm 0.034$ for the two sets of corner frequency measurements. In both cases those scalings are significantly different from a self-similar rupture, for which $\alpha = 1/3$.

Recent studies show that the clear departure from self-similarity measured for LFEs in Guerrero and Cascadia is not a necessary feature of LFEs in

all tremor regions across the world. Exploring this regional specificity might bring significant insight on LFEs source physics and lead us to understand more about how deep fault environment affects slow slip processes.

Appendices to Chapter 2

Contents

2.A Effects of bandpass filtering on events corner frequencies

2.1.1 Analysis bandpass filter

In Figure 2.A.1, we see that the tremor seismic energy seems really bounded between 0.8 Hz and 8 Hz. Above this band, high-frequency noise, possibly anthropogenic, is active, below this band, the seismic time-series are dominated by low-frequency noise leaking from microseismic modes. The choice of the 1–8 Hz band-pass filter used to measure corner-frequencies is motivated by this observation.

It is possible that the 1–8 Hz band-pass filter we use biases our measure of the corner frequencies to constrain them in a narrow band above 1 Hz. We tested the influence of the lower cutoff frequency of the band-pass filter on the measured corner frequency. Results of this test are shown in Figure 2.A.2. The distribution of corner frequencies is not drastically modified down to a lower cutoff of 0.2 Hz, where corner frequencies suddenly regroup around 0.2 Hz. This sudden shift is due to the filter band not blocking pollution of micro-seismic noise anymore. In addition to it, corner frequencies are slightly

dragged to lower values, as the lower cutoff decreases from 1 Hz to 0.5 Hz. This should be expected: more and more pollution from micro-seismic noise is allowed in records of events on stations that witness higher amplitudes of micro-seismic noise, due to proximity to the ocean or site effects. On those records, the characteristic frequency will be picked lower, due to the influence of micro-seismic noise. Figure 2.4d is a good illustration of this: the peak of the un-filtered spectrum is located at 1 Hz due to micro-seismic noise influence.

The 1–8 Hz band is thus chosen as a compromise. The lower cutoff is taken far enough from micro-seismic frequencies so that the event signal is not polluted, even at stations where micro-seismic noise has the highest amplitude. Ultimately, it does constrain the corner frequency between 1 and 8 Hz: most events have corner frequencies between 2 and 6.5 Hz, well within the filtering band.

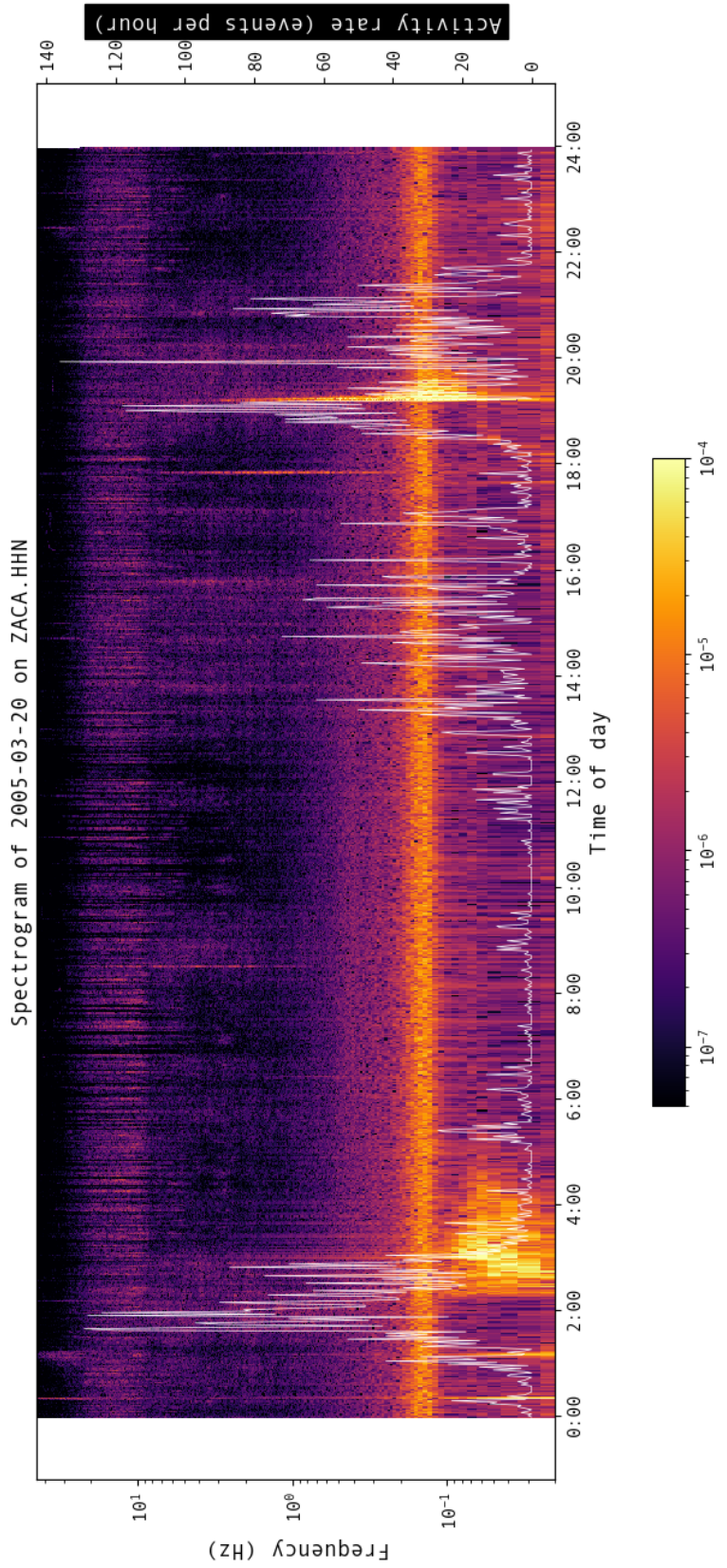

Figure 2.A.1 *— The tremor signal can be observed in the 1–8 Hz frequency, as signal amplitude variations correlated to the hourly rate of event detection. It is clear that there is a nearly constant background noise below 0.8 Hz and above 8 Hz, with an amplitude on the same order as the tremor signal.*

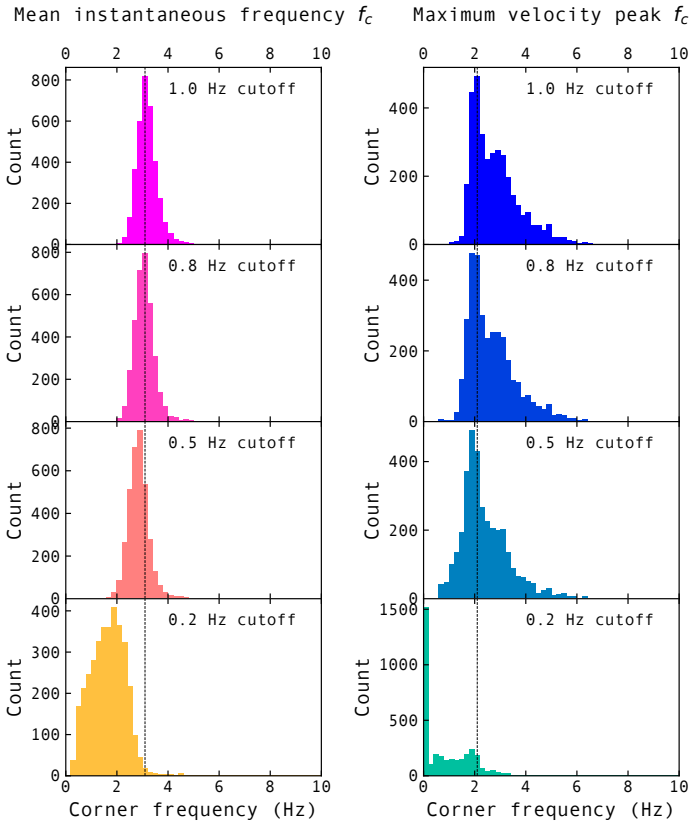

Figure 2.A.2 — *Effects of varying the lower cutoff of the filter are presented for both methods of determination of the corner frequency. In the left column, for the mean instantaneous frequency method, In the right column, for the maximum of velocity spectrum method. The filter band used in the article is 1–8 Hz. For comparison, location of the peak of the current distribution is shown as the black dashed line. Decreasing the lower cutoff of the filter slightly brings the distribution of corner frequencies to lower values, down to 0.5 Hz. Below 0.5, as seen for 0.2 Hz, micro-seismic noise is picked up as characteristic frequency of the signal and pulls the whole distribution to low values.*

2.1.2 Detection bandpass filter

The LFEs of the catalog used in this study were detected using a matched-filter search (or MFS) approach, using template velocity waveforms, band-pass filtered between 1–2 Hz (Frank et al., 2014). A potential concern is that a MFS using a narrow band-pass would only identify events with a characteristic frequency between 1 and 2 Hz. Assuming it is the case, it would bias our analysis towards the observed magnitude-independent corner frequencies.

However, the use of an MFS approach does not constrain the characteristic frequencies of the event between 1–2 Hz, it simply limits detections to signals with energy within this frequency band. Several studies using MFS to detect classic earthquakes are able to detect events with a range of magnitudes, that, through the earthquake moment-duration scaling law, corresponds to a range of characteristic frequency wider than the chosen band-pass (Warren-Smith et al., 2017, Figure 7.(b)), (Frank & Abercrombie, 2018, Figure 5). In our case most events indeed have corner frequencies above 2 Hz and up to 6.5 Hz (see Table 2.1, Figure 2.5).

A compact form of the Brune spectrum for ground motion velocity can be used to compare the detectability of two events: $\widetilde{v}(f)$:

$$\widetilde{v}(f) = C \,.\, M_0 \frac{2\pi f}{1 + (f/f_c)^2}, \tag{2.15}$$

where C is a constant relating to the velocity structure of the medium and the source focal mechanism, M_0 the seismic moment of the event and f_c its corner frequency. For any two events with $f_{c1} < f_{c2}$ but identical moment, for any given frequency f, the corresponding velocity amplitudes will follow $\widetilde{v_1}(f) < \widetilde{v_2}(f)$. In Figure 2.A.3, we represent the velocity spectrum $\widetilde{v}(f)$ of 5 events with various corner frequencies and the same seismic moments. In Figure 2.A.3b, we show the spectral velocity energy in the 1–2 Hz band for events with various corner frequency, but the same seismic moment. This figure shows that in this case, the higher the corner frequency of the event, the higher the amplitude of velocity between 1–2 Hz, and therefore the more detectable the event by the MFS. Events with a higher characteristic frequency than events we detected thus do not have a lower probability to be detected because of the band-pass filter. However, events with a lower corner frequency than events we detect have a lower probability of detection, because the energy of their velocity waveform is lower in the 1–2 Hz band (Fig. 2.A.3). This effect is especially strong for events with $f_c < 1$ Hz. The matched-filter search band-pass thus imposes a lower bound of about 1 Hz on detections' corner frequencies in the range of moments we measure, but no higher bound, except the one imposed by the filter used in the analysis, at 8 Hz.

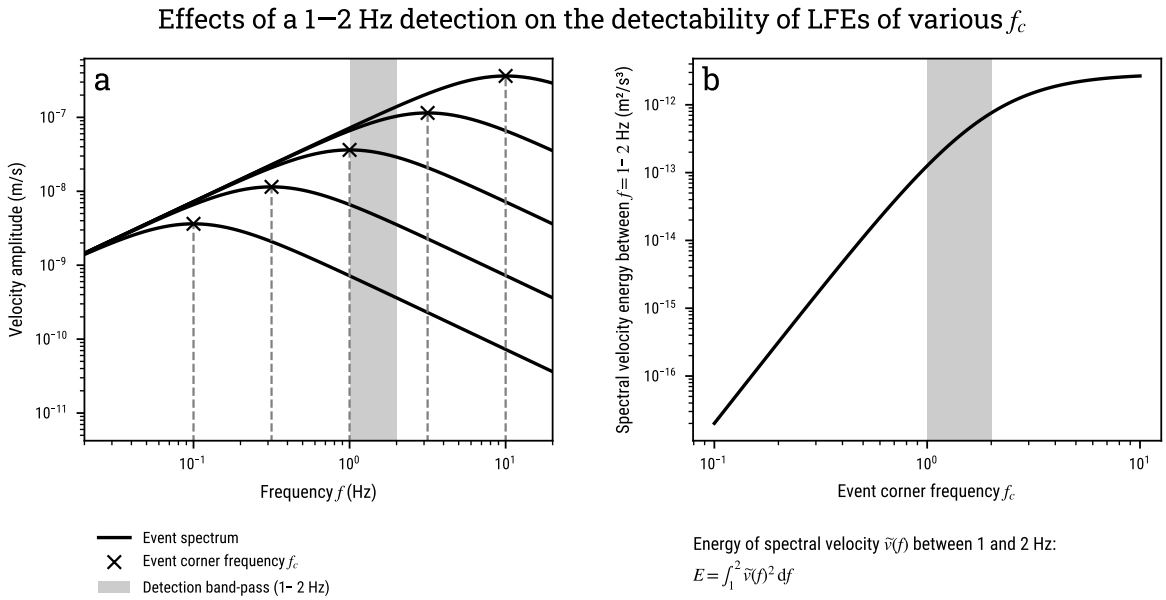

Figure 2.A.3 — *(a) Seismic velocity spectra of 5 events with different corner frequencies but the same seismic moment. Corner frequencies are shown with a cross and dashed line. (b) Spectral velocity energy in the 1–2 Hz band for events with various corner frequencies, and same seismic moment. The "energy" of the velocity waveform is defined as the integral of spectral velocity squared, over the 1–2 Hz band. The higher the energy, the more the event should be detectable. In both panels, the 1–2 Hz frequency band used to detect LFEs is shaded in gray. All events used here are described by a Brune spectrum (Brune, 1970).*

The 1–8 Hz band-limitation that the MFS should impose should allow to detect significant variation of f_c for the range of seismic moments we measure (8×10^{11}–1×10^{13} N.m) — a 1–10 Hz band limitation was enough for Supino et al. (2020) to measure strong variations of f_c, in a similar range of moments. Therefore, we conclude that although the combination of the lower bound on detected f_c inherited from the 1–2 Hz MFS and the upper bound imposed by the analysis low-pass at 8 Hz creates a band-limitation for the detected corner frequency, it is not narrow enough to bias the measurements of the M_0-f_c scaling, so that it is an artifact of band-limited detection.

2.B Effects of attenuation on corner frequency f_c measurements

The spectral characteristics of a seismic signal are shaped both by the properties of the source — its duration, the amount of radiated energy, the variations in the rate of energy release at the source — and the effects of the medium on the signal that propagates from the source — geometric spreading, radiation pattern, attenuation through scattering and anelastic energy dissipation.

In particular, measures of the source's corner frequency trade-off with how the propagating medium attenuates seismic energy at high frequencies. A strongly attenuating medium — for instance in the highly heterogeneous, unconsolidated subsurface — can strongly attenuate the high-frequency part of a seismic signal and produce an apparently-constant corner frequency, independent of the events seismic moment (Abercrombie, 1995). In this section, we discuss our choice of attenuation model for the Guerrero crust, and how an unaccounted, strongly-attenuating source region could be the cause of an apparently-constant corner frequency for LFEs in Guerrero.

2.2.1 Seismic attenuation in the crust of Guerrero

The effects of attenuation on the spectrum of a seismic event can be modeled by an attenuation term $a(f)$ that multiplies the true source spectrum ${}_0\widetilde{u}(f)$ to produce the measured, attenuated spectrum $\widetilde{u}(f)$ (J. G. Anderson & Hough, 1984):

$$\widetilde{u}(f) =_0 \widetilde{u}(f).a(f). \tag{2.16}$$

The attenuation term $a(f)$ depends on frequency, usually with an exponentially stronger attenuation at higher frequencies:

$$a(f) = \exp\left(-\frac{\pi f R}{V_S Q(f)}\right), \tag{2.17}$$

where R is the source-receiver distance, and $Q(f)$ and the seismic quality factor. In order to measure the true corner frequencies f_c of LFEs, we divide the measured spectrum $\widetilde{u}(f)$ of selected events by the modeled effects of attenuation $a(f)$, to obtain the corrected "true" spectrum ${}_0\widetilde{u}(f)$, in which only the effects of source, radiation pattern and geometric spreading should theoretically remain. Corner frequencies f_c are then measured on ${}_0\widetilde{u}(f)$.

Several studies found that attenuation in the crust in Guerrero is weakly frequency dependent, and can be described by a quality factor in the form $Q(f) = Q_0\, f^{\eta}$, with η lower than, but close to 1 (Castro et al., 1990; Mahdyiar, 1984; Ordaz & Singh, 1992; Ottemöller et al., 2002; Singh et al., 1990). When $\eta = 1$, $Q = Q_0\, f$, and $a(f)$ becomes frequency independent (see equation 2.17). Humphrey and Anderson (1992) found that attenuation in the Guerrero crust can be described by such a frequency-independent parametrisation, consistently with the previously mentionned studies. Figure 2.B.1 shows examples of frequency-dependent models for the quality factor Q in Guerrero, measured using S-waves for most of the models. Those attenuation models are quite similar, our choice of attenuation model — where $Q = 273\, f^{0.66}$ (Ordaz & Singh, 1992) — should therefore adequately describe the attenuation in the continental crust of Guerrero.

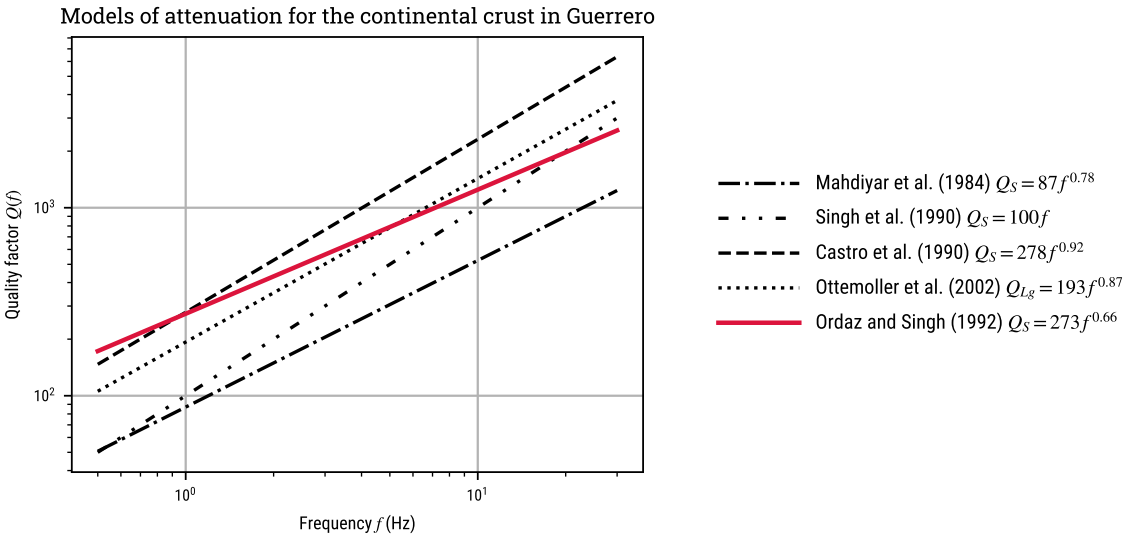

Figure 2.B.1 — *Models of attenuation for the crust of Guerrero. All modeled frequency-dependent quality factors are measured on the S-waves of regional earthquakes, which wave travel through the crust of Guerrero, except for the model by Ottemöller et al. (2002), who measured it on the Lg phase.*

As values of η close to 1 imply that $a(f)$ is nearly frequency-independent, the measured, attenuated spectrum of LFEs in Guerrero and their source spectrum should have the same spectral shape, only varying in amplitude (see equation 2.16). Therefore small imprecisions in the attenuation modeling should have a negligible effect on the measured corner frequency, assuming that the continental crust is the main attenuating layer between LFEs' sources and the instrument at the surface. Figure 2.B.2 shows the effect of various attenuation models on the spectra and measured f_c of events of different seismic moment M_0 and corner frequency f_c. For all expressions of the quality factor for the crust in Guerrero, the way attenuation modifies the true spectrum are very similar. It is also clear that such crustal attenuation does not have a strong impact on the spectral shape between 1–10 Hz, and therefore on the apparent corner frequency. Our choice of model for the attenuation of the crust can therefore be excluded as being responsible for the M_0-f_c scaling we obtain. The details of calculations to obtain Fig. 2.B.2 are described in the next section.

Measures of attenuation in other subduction zones show that the values found in Guerrero — $Q \approx 300$ at 1 Hz, $Q = 1000$ at 8 Hz — are consistent with the high values of attenuation found in the continental crust found of tremor areas. Using earthquake-receiver paths that sample the whole continental crust and parts of the subduction fault under Vancouver Island (Cascadia) Atkinson (1995) and Shikoku (Japan) Takahashi et al. (2014), studies

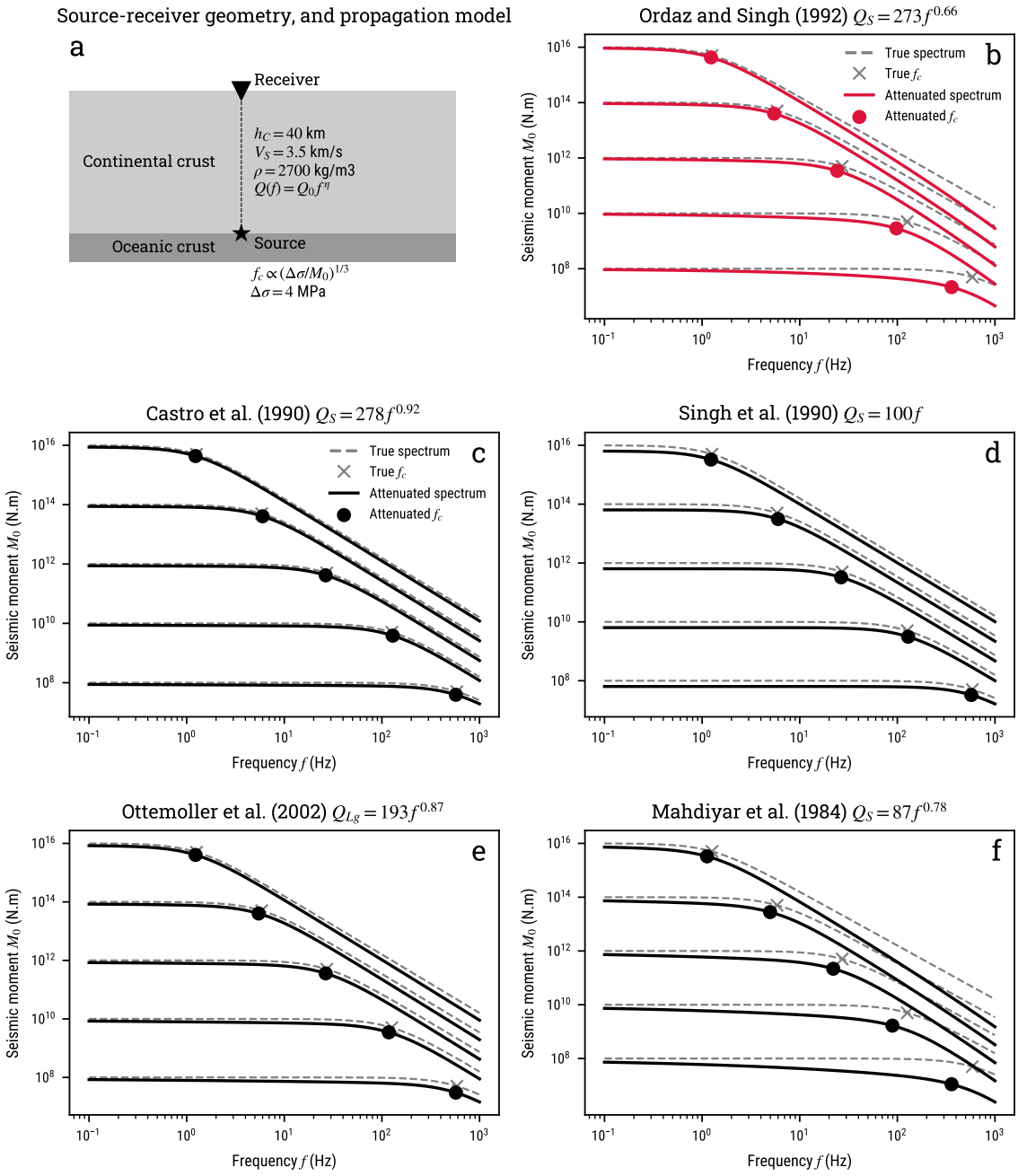

Figure 2.B.2 — *Effects of attenuation on the spectra and apparent corner frequency of earthquakes of different magnitudes and corner frequencies. (a) Source-receiver geometry and physical properties of the source and propagating medium, here only composed of a model continental crust. (b)–(f), True and attenuated spectra for different expressions of the quality factor. The true corner frequency of the model event is symbolized with a cross, and the apparent, attenuated corner frequency is represented as a circle. See section 2.2.2 for more details on the modeling.*

respectively found $Q(f) = 263\, f^{0.49}$ and $Q(f) = 315\, f^{0.5}$. Those laws are sensibly similar to the ones measured in Guerrero. Other studies measure the attenuation using tremor waveforms, and find that at $f = 4.5$ Hz, the full-path attenuation can be described by a quality factor of $Q \approx 500$–800 in Shikoku, Jalisco (Mexico) and Cascadia (Baltay & Beroza, 2013; Yabe et al., 2014). Those results are especially relevant to our case, as they measure the attenuation on the typical path travelled from LFE source to receiver. The fact that these measures are consistent between subduction zones tend to show that the crustal attenuation model should be adequate for Guerrero.

2.2.2 Effects of a highly-attenuating fault zone on LFE spectra

In studies by Z. Wang and Zhao (2019) and Yabe et al. (2014), the presence of intraslab earthquakes in addition to other seismic event at the plates' interface and within the crust allow the authors to measure the attenuation within the fault zone, where LFEs are located. Both studies report that the fault zone should behave as a few-kilometer-thin, highly-attenuating layer, with $Q \approx 100$ for a thickness of 5 km (Yabe et al., 2014). In the next pararagraphs, we investigate the effects of a thin, highly-attenuating layer located just above the LFE sources, and how it could bias corner frequency measurements towards the observed scaling. Such strong attenuation of of the high frequency content of a signal can be responsible of an apparent constant corner frequency for events of different sizes, as pointed out by Abercrombie (1995), who showed that the observation of a constant f_c for small events in California by Archuleta et al. (1982) was likely due to a highly attenuating subsurface ($Q = 5$–30 in the shallowest few hundreds of meters). A similar reasoning could be made for small earthquakes in different parts of the world B. Chouet et al. (1978). We will use this reasoning here to infer what value of the quality factor in the fault zone is necessary to obtain an apparent M_0-f_c scaling similar to the one we measure for LFEs in Guerrero. This approach was developped by J. G. Anderson et al. (1986).

The hypothesis we want to test is that a population of small, self-similar earthquakes which waves propagate in a thin, strongly attenuating fault-zone could exhibit an apparently-constant corner frequency f_c, independent of seismic moment M_0. If values of the quality factor necessary for such a scaling to occur are realistic, the scaling we measure for LFEs could be an artifact due to the un-modeled fault-zone attenuation in our study. The population of small earthquakes are located directly below the receiver, at a depth R. They are self-similar, and their true, un-attenuated displacement spectrum ${}_0\widetilde{u}(f)$ is

described by a simple Brune's spectrum (Brune, 1970):

$$_0\widetilde{u}(f) = \frac{0.84 M_0}{4\pi\rho V_S^3 R} \times \frac{1}{1+(f/f_c)^2}. \tag{2.18}$$

For a self-similar rupture, the corner frequency depends on the stress drop $\Delta\sigma$ and seismic moment M_0 as

$$f_c = 0.49 \left(\frac{\Delta\sigma}{M_0}\right)^{1/3} V_S. \tag{2.19}$$

The population of small earthquakes we use is defined by seismic moments $M_0 = 1e8$–$1e16$ N.m, a stress drop of $\Delta\sigma = 4$ MPa (median stress drop in Allmann & Shearer, 2009), and true corner frequencies $f_c = 1$–500 Hz. Following J. G. Anderson and Hough (1984), we account for attenuation in the crust and fault-zone with a multiplicative term for each, to obtain the measured spectrum $\widetilde{u}(f)$:

$$\widetilde{u}(f) =_0 \widetilde{u}(f)\, a_C(f)\, a_F(f). \tag{2.20}$$

where both the crustal attenuation factor $a_C(f)$ and fault attenuation factor $a_F(f)$ are described by an exponential term (see equation 2.17). The "apparent" corner frequency is defined as the maximum of the measured, attenuated velocity spectrum $\widetilde{u}(f)$.

We first test the effect of crustal attenuation without a highly-attenuating fault zone, and set $a_F(f) = 1$. Figure 2.B.2a describes the source receiver geometry and the velocity and attenuation structure. The source is located at $R = h_C = 40$ km depth, below a homogeneous crust with $V_S = 3.5$ km.s^{-1}, $\rho = 2700$ kg.m^3 and a frequency-dependent quality factor $Q(f) = Q_0\, f^{\eta}$. Panels *(b)–(f)* show the true and attenuated spectra for events with different M_0, f_c. In Guerrero, the crustal attenuation does not strongly affect the spectral shape, and should not have a strong effect on the apparent corner frequency in the 1–10 Hz frequency band we are interested in for the study of LFEs.

In a second experiment, we add a $h_F = 1$ km-thick fault zone above the source and below the $h_C = 40$ km-thick continental crust. Both layers share the same density and shear wave velocity. Crustal attenuation is described by our choice of model $Q(f) = 273\, f^{0.66}$ (Ordaz & Singh, 1992). Fault attenuation is described by a frequency-independent quality factor Q_F. Figure 2.B.3a describes the simulation set up. We test values of the fault-zone quality factor $Q_F = 1$–1000, and for each we obtain the distribution of apparent corner frequency f_c and seismic moment M_0. Figure 2.B.3c shows that for a relatively low quality factor in the fault zone $Q_F = 100$ (similar to what Yabe et al., 2014, found), earthquakes of the same magnitude as the LFEs in Guerrero

($M_0 \approx 5e11$–$1e14$ N.m) have a higher apparent corner frequency than LFEs ($f_c \approx 10$–30 Hz), and their M_0-f_c distribution is very close to their true value, where $f_c \propto M_0^{-1/3}$. Only for an extremely low quality factor $Q_F = 3$ — very high attenuation — the effect of attenuation on the spectrum are significant between 1–10 Hz, and therefore could strongly affect the shape of the spectrum, biasing the measured corner frequency (Figure 2.B.3b and c). In this case, if the attenuation of the fault zone is not corrected for in the measurement of f_c, the apparent M_0-f_c scaling resembles the one we measure for LFEs in Guerrero. Bostock et al. (2017) found with a similar calculation that the M_0-independent corner frequency scaling of LFEs under Vancouver Island could result from the attenuation of a 1 km-thick fault-zone with $Q_S = 3$.

A value of $Q_F = 3$ for S-waves seems unrealistically low, as even the highly-attenuating, sedimentary subsurface rarely goes down to $Q = 5$ (Abercrombie, 1995). More than the absolute value of Q_F, its frequency independence is responsible for the apparent scaling, as it produces a steep high-frequency attenuation: $Q_F = Q_0\, f^0 \implies a_F(f) = \exp(-Cf)$, where C is a constant. A very highly-permeable ($k \geq 1e-12$ m^2), fluid-saturated layer could generate strongly frequency-dependent attenuation, with a low $Q_0 \approx 100$ and $\eta \approx 0$ or even $\eta < 0$ (Müller et al., 2010; Takahashi et al., 2014). If the subduction fault zone can be described as such a highly permeable layer, its attenuation could be responsible for the band-limited nature of tremor and LFEs. However, the extraordinary nature of the attenuation needed to explain this scaling as resulting from propagation effects tends to show that the scaling we measure can be reasonably interpreted as a result of the source properties of LFEs. In the end, more research remains to be done on the attenuation characteristics of the subduction fault-zone, and the consequences of such a high permeability, to assess if propagation effects could realistically be responsible for the apparent M_0-independent corner frequency.

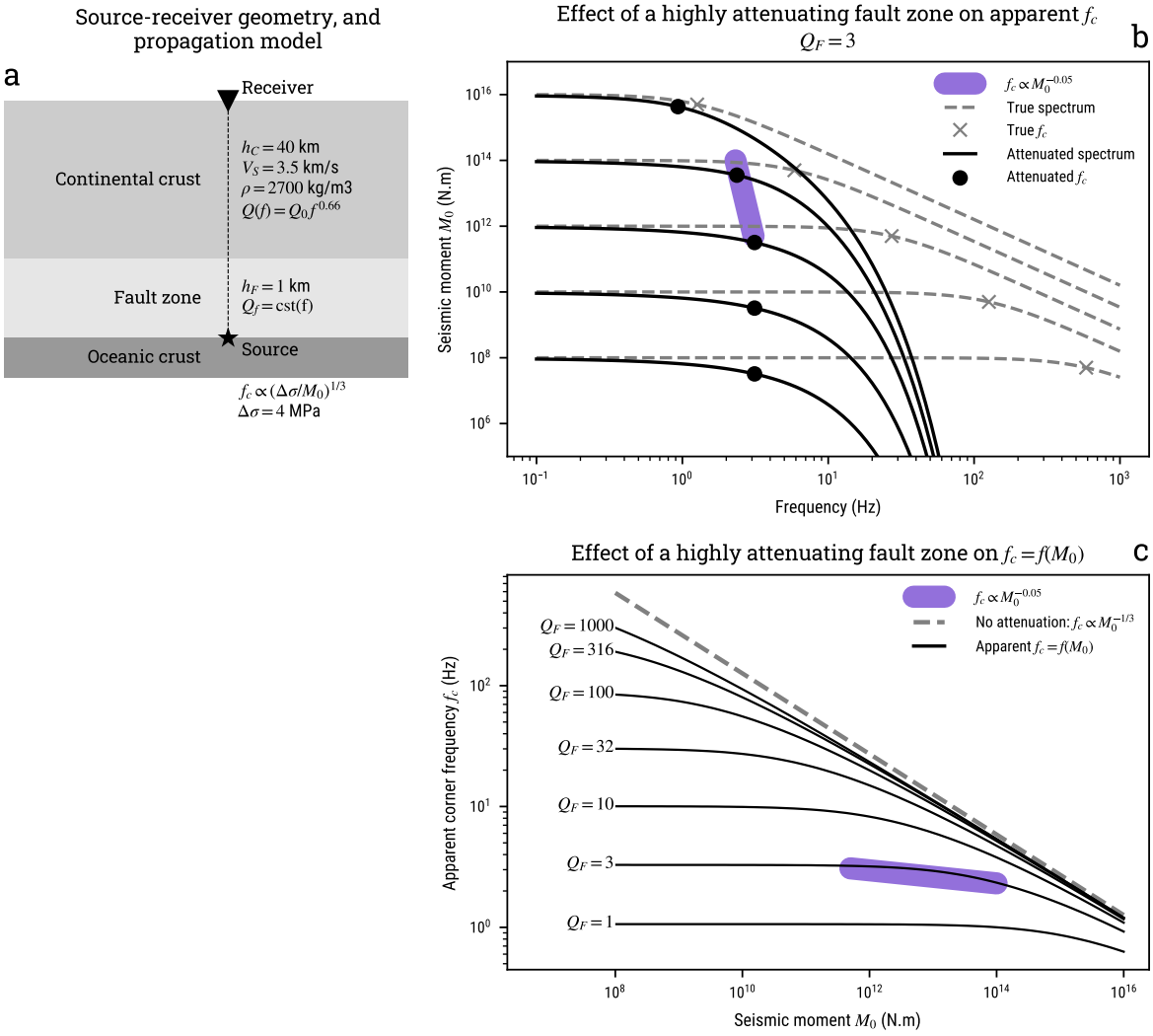

Figure 2.B.3 — *(a) Source-receiver geometry and physical properties of the source and propagating medium, composed of a model continental crust and fault zone. (b) True and attenuated spectra for events of different sizes and magnitudes, for a quality factor in the fault zone of $Q_F = 3$. The true corner frequencies are symbolized with crosses, and the apparent, attenuated corner frequencies are represented as circles. (c) Relationship between seismic moment M_0 and apparent corner frequency f_c for different values of the quality factor in the fault zone Q_F. In (b) and (c), the M_0-f_c distribution for LFEs in Guerrero (present study) is represented approximately in purple.*

Part III

Spatio-temporal patterns of tremor activity

Chapter 3

Tremor generation through fast fluid pressure transients in the permeable subduction interface

Based on: G. Farge, C. Jaupart, N. M. Shapiro, *Episodicity and Migration of Low Frequency Earthquakes Modeled With Fast Fluid Pressure Transients in the Permeable Subduction Interface.* Journal of Geophysical Research: Solid Earth, 126(9), September 2021. ISSN 2169–9313, 2169–9356. https://doi.org/10.1029/2021JB021894

Contents

3.1 Introduction

The extensive records of weak low-frequency seismicity detected in many fault zones over the last two decades provide powerful information on their dynamics. At intermediate depths (30–50 km) in several subduction zones, seismic activity takes the form of tremor (*e.g.*, A. L. Husker et al., 2012; Kao et al., 2005; Obara, 2002; Payero et al., 2008). It now seems clear that tremor is made of swarms of low-frequency earthquakes (LFEs) and many authors use the term "tremor" as a synonym for LFE activity (*e.g.*, Audet & Kim, 2016; Bostock et al., 2012; Frank et al., 2014, 2013; Peacock et al., 2011; Rogers, 2003; Shelly et al., 2006; Song et al., 2009). These LFEs appear to be due to repetitive, impulsive and localized sources (Beroza & Ide, 2011; Frank et al., 2014). High rates of tremor activity are associated with geodetically observed slow deformation episodes called slow-slip events (SSEs) (*e.g.*, Delbridge et al., 2020; Frank, Radiguet, et al., 2015; Kostoglodov et al., 2010; Rousset et al., 2019). The correlation between LFE and SSE activity gave rise to the term Episodic Tremor and Slip (ETS) (Rogers, 2003). In a more general acceptation, transient seismic and geodetic signals that are both generated during inter-seismic phases are often lumped together as *slow earthquake phenomena*. This new class of seismic and geodetic observations holds great promise for improving our understanding of the seismo-tectonic cycle.

According to the framework that prevails today, slow earthquakes are the "slow" analogs of "regular" earthquakes. Geodetic and seismic events are manifestations of the same process of slow slip at transitional depths in fault zones, in between unstable stick-slipping and stable sliding areas.

The transitional part is made of slow sliding patches that are responsible for geodetically detected SSEs and that contain many small embedded frictionally unstable asperities generating LFEs. This framework explains why SSEs and tremor activity are correlated in time and accounts for the S-wave dominated LFE radiation pattern (*e.g.*, Shelly et al., 2007b). Numerical models of these phenomena (*e.g.*, Barbot, 2019; Ben-Zion, 2012; Ide, 2014; Liu & Rice, 2007; Luo & Liu, 2019; Shibazaki & Iio, 2003) are often based on the rate-and-state friction (RSF) formalism developed for "regular" earthquakes (Dieterich, 1992). This efficient modeling approach has two significant shortcomings, however (van den Ende et al., 2018). First, all the dynamic variability of the interface and its surroundings is collapsed onto a planar boundary. Second, it depends on empirical RSF parameters that are not inferred directly from processes occurring within the fault zone. Thus, it is difficult to specify RSF parameters and account for internal fault zone dynamics in a self-consistent manner. These shortcomings may be limiting in the brittle-to-ductile transition zone of subduction faults because the deformation proceeds over an increasingly wide off-fault region as depth increases (Platt et al., 2018). Source dimensions for tremor and LFEs are typically inferred to be a few hundred meters (*e.g.*, Chestler & Creager, 2017a; Sammis & Bostock, 2021; Supino et al., 2020), close to the thickness of the highly deformed permeable fault zone (*e.g.*, Angiboust et al., 2015). This calls for more complete models dealing with processes in the interior of these zones.

There can be little doubt that pore fluid pressures and their variations play a key role in fault zone dynamics (Saffer & Tobin, 2011). From a frictional perspective, high pore pressures reduce the fault's strength, bringing it closer to unstable sliding conditions. Numerous geophysical and geological observations provide evidence for fluid saturation in the subduction interface (Saffer & Tobin, 2011). It is widely believed that fluids are supplied by metamorphic dehydration reactions in the downgoing plate (Frezzotti & Ferrando, 2015; Hyndman et al., 2015; Manning, 1997; van Keken et al., 2011). High values of the V_p/V_s ratio and electrical conductivity indicate that pore fluids are at near-lithostatic pressures (Audet & Kim, 2016; Peacock et al., 2011; Wannamaker et al., 2014, among others), implying that the fault should be very weak. This explains why seismic activity is highly sensitive to very small dynamic stress changes generated by passing teleseismic waves (Rubinstein et al., 2009) or tidal deformation (Beeler et al., 2013; Royer et al., 2015; Rubinstein et al., 2008; Thomas et al., 2009).

There is mounting evidence for large variations of pore pressure on the time scale of the slow-earthquake cycle. During slow slip events, seismic images, gravimetric studies as well as earthquake source mechanisms indicate that pore fluid pressure around the subduction interface drops markedly

(Gosselin et al., 2020; Tanaka et al., 2018; Warren-Smith et al., 2019). The migration of LFE activity is highly suggestive of pore-pressure diffusion (Cruz-Atienza et al., 2018; Frank, Shapiro, et al., 2015). In exhumed subduction interfaces, the brittle-to-ductile transition seems to be intrinsically coupled to transient pore-pressure cycling and fluid transport (Angiboust et al., 2015; Behr & Bürgmann, 2021; Platt et al., 2018). Episodes of fluid accumulation and drainage have been documented in shallow thrust faults and are recorded by metasomatic reactions in host rocks (Angiboust et al., 2014; Saffer, 2015; Taetz et al., 2018). They have been attributed to changes of permeable pathways due to tectonic deformation, precipitation/dissolution or deposition/erosion processes (Giger et al., 2007; Jäger et al., 2017a; Williams et al., 2019). In recent efforts to model ETS phenomena, the emphasis has shifted from a static view of the impact of fluid pressure on RSF parameters to dynamic coupling between time-dependent fluid pressure and slip (*e.g.*, Bernaudin & Gueydan, 2018; Cruz-Atienza et al., 2018; Zhu et al., 2020).

With the recognition that pore fluid pressures are high and variable in the subduction interface, it may not be appropriate to attribute seismic events to seismic slip only, without considering other processes that are active in the fault zone. Indeed, there are indications that the high fluid pressure transients that seem fundamental in shaping tremor patterns may well generate seismic events on their own. Observations do not demonstrate unambiguously that slow slip events and low-frequency seismic radiation are generated by the same process. It is true that these two types of activity are frequently correlated in time, but the sources of seismic and geodetic events are not systematically co-located (*e.g.*, Hirose et al., 2010; Kostoglodov et al., 2010). In addition, in some subduction zones, LFEs do not conform to the moment-duration scaling of classical shear rupture (Bostock et al., 2015, and Chapter 2) and do not follow the Gutenberg-Richter size distribution characteristic of regular earthquake activity (Sammis & Bostock, 2021). Finally, it should be noted that the predominance of S-waves in the seismic signals does not necessarily establish a shear rupture mechanism. S-wave dominated signals can arise from volumetric sources with non-spherical geometries (*e.g.*, Melnik et al., 2020a) or from single-force sources associated with fast local pressure variations (N. M. Shapiro et al., 2018).

Strong arguments in favor of a fluid-related origin for LFEs comes from laboratory studies and volcano seismology. In volcanic systems, shear deformation and slip do not play a predominant role, and yet tremors and LFEs (labelled as long-period earthquakes) are generated in abundance. These events have been attributed to fluid related processes, such as resonance in fluid-filled cracks (B. A. Chouet, 1996), strong flow in tortuous channels (Benson et al., 2008; Julian, 1994) and rapid pressurization of volatiles (Melnik et al.,

2020a; Wech et al., 2020), among others. In some cases, their sources are distributed over large depth intervals of a few tens of kilometers and appear to migrate on time scales of a few months or days (N. M. Shapiro, Droznin, Droznina, Senuykov, et al., 2017). These migrations have been attributed to pore-pressure transients associated with hydraulic connections between different parts of a volcanic plumbing system.

A key piece of information on fault zone dynamics is the distribution of LFEs in space and time. Here, we explore the potential of pressure transients in a permeable subduction interface to generate this type of activity. The structure and hydraulics of such a channel have rarely been studied in relation to seismicity (Aochi et al., 2013; Cruz-Atienza et al., 2018; Segall & Rice, 1995; Zhu et al., 2020). We investigate the behavior of plugs of low permeability in a heterogeneous channel. Pore pressure variations can arise in two different ways. They may be generated by a time-dependent fluid supply, but there are no known mechanisms for strongly fluctuating rates of metamorphic dehydration reactions. Alternatively, one can invoke changes of permeability, as in the classical fault-valve model (R. Sibson, 1992). In this model, an increase of pore fluid pressure can generate an earthquake rupture, which opens up or reactivates fluid pathways leading to an increase of permeability and a decrease of pore pressure. Clogging of pores due to precipitation from circulating fluids or to the trapping of particles then acts to decrease permeability, implying an increase of pore pressure and a new cycle of pressure change. The permeability increase of the first phase of the cycle can be achieved in two different ways. One is shear displacement in association with fault dilation (Im et al., 2019a) — although it appears that, in some cases, this may in fact act to decrease permeability in the slip direction (Auradou et al., 2005). In the other mechanism, high pore pressures can induce fracturing and/or unclogging of small pores and pore throats. In the laboratory, impulsive flushing events similar to hydrofracturation have been observed in densely packed permeable beds due to sudden particle detachment and called *erosive bursts* (Bianchi, Thielmann, et al., 2018; Jäger et al., 2017b). These bursts are associated with sharp pore pressure drops and recur as particles are redeposited. Coupled variations of permeability and pore fluid pressure due to particle clogging and un-clogging have been observed in many laboratory experiments (Bianchi, Thielmann, et al., 2018; Candela et al., 2014) and have been surmised for fault zones (Manga et al., 2012). These phenomena have also been documented in large-scale systems. In some oil fields, for example, long-term records show that the bulk permeability of the reservoir oscillates in relation to cycles of deposition and removal of asphalt aggregates (Sahimi et al., 1999). We therefore argue that these mechanisms are bound to be active in faults, where fluid circulates under high pressure gradi-

ents, carrying precipitates and cataclastic fines that can be deposited and dislodged. In this framework, fast local pore pressure variations (N. M. Shapiro et al., 2018) and/or rupture of brittle heterogeneities due to increased fluid pressure (Fagereng & Sibson, 2010; Kotowski & Behr, 2019) may be responsible for LFEs. We expect that the unclogging or rupture of an individual plug induces pore pressure variations that propagate to neighboring plugs and generates swarms of similar events.

Through the rapid pressure drop that occurs, the unclogging of an individual plug is responsible for a local impulsive force on the solid matrix which generates elastic waves with both compressional and shear polarisation components. N. M. Shapiro et al. (2018) have shown that the radiation pattern of such a single-force source is consistent with seismic observations in subduction zones due to the constrained source-receiver geometry, and that it can account for the weak dependency of LFEs source duration on their magnitude, as observed in Cascadia and Guerrero (Bostock et al., 2015, and Chapter 2). Here, we build on this study to evaluate the seismic patterns that can be generated by a series of interacting plugs in a permeable channel. The clogging/unclogging mechanism does not involve shear rupture explicitly and we will discuss *a posteriori* how it should reflect on slip and its sensitivity at high fluid pressures.

The paper is organized as follows. We first describe the main characteristics of tremor/LFE activity in subduction zones that must be accounted for by any physical model. We then develop a quantitative model, starting with the basic processes that are involved in the clogging and unclogging of a plug and the corresponding equations. Results are described for a range of fluid input rates and a regime diagram is obtained and justified by simple theoretical arguments. The activity patterns that are generated are compared to observed ones, and conditions that must be met for a successful model are specified.

3.2 Tremor patterns observed in subduction zones

We summarize the most salient features of tremor activity in subduction zones. The Guerrero, Mexico, area is particularly appropriate to study LFE activity because it stretches over a distance of more than 100 km along-dip, owing to a low dipping angle. A very large catalog of events is available there (Frank et al., 2014).

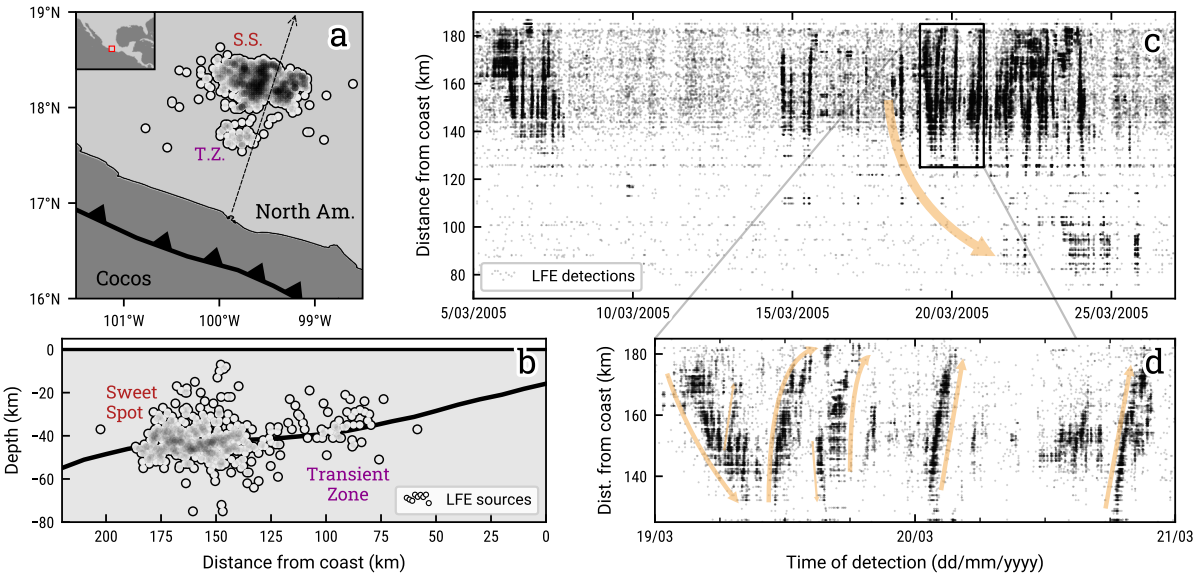

Figure 3.1 — *The Guerrero (Mexico) tremor zone in (a) map view and (b) vertical cross-section. Each dot represents a low-frequency earthquake family from Frank et al. (2014). Thick black lines outline the trench and the subduction interface (data from Hayes (2018)). (c) and (d), LFE activity in a time-location chart from the Frank et al. (2014) catalog. Activity occurs in two patches centered on the subduction interface, a dense downdip one called the sweet spot and a sparser updip one called the transient zone. Tremor activity migrates along the subduction interface in both the updip and downdip directions, as shown by the orange arrows.*

3.2.1 Spatial Segmentation

At a local scale, the fact that LFEs occur in families of recurring events with similar waveforms indicates that they are due to the repeated activation of individual sub-kilometric scale sources (Chestler & Creager, 2017a). In subduction zones, activity is often segmented in the along-strike direction and concentrated in patches (Brudzinski & Allen, 2007; Poiata et al., 2021). In Shikoku, Japan, and elsewhere, events delineate pluri-kilometric striations that are aligned with the subduction direction and that have been linked to the subduction of seamount chains (Ide, 2010). Shorter striations have also been observed in the Olympic Peninsula, Cascadia (Ghosh et al., 2010). In Guerrero, Mexico, activity is split into two well-separated patches along the dip of the interface (Frank et al., 2014; A. L. Husker et al., 2012; Kostoglodov et al., 2010; Payero et al., 2008) (Figure 3.1).

3.2.2 Tremor Migration

Bursts of tremor activity migrate along the subduction interface on time scales of seconds to weeks, and spatial scales from a few to a few hundreds of kilometers. Short-lived, short-distance migrations are often restricted to an individual tremor patch and proceed at rates in the 10–100 km/hr range (on time scales T of minutes to hours over length scales L of tens of kilometers) (Cruz-Atienza et al., 2018; Ghosh et al., 2010). In marked contrast, long-lived, long-distance migrations that connect spatially separated patches are slower, with velocities in the $\sim$ 1–10 km/day range ($T \sim$ weeks to months, $L \sim 100$ km) (Frank, Shapiro, et al., 2015; Kao et al., 2009). Such systematics between time and space scales are reminiscent of a diffusion process, such that $L^2 \propto T$ and therefore $V \sim L/T \propto 1/L$.

In Japan and Cascadia, the largest transients of activity ($T \sim$weeks, $L \sim$100 km) propagate along-strike in a belt lying in a 30 to 60 km depth range. It has been suggested that this depth interval delineates a zone rheologically conducive to slow-slip (Gomberg et al., 2016; Ide, 2012). In Guerrero, Mexico, the active segment of the subducted slab is dipping at a low angle and stretches over as much as 200 km in a 40-50 km depth range (Kim et al., 2010; Pardo & Suárez, 1995). Due to this particularly favorable configuration, it is clear that the largest migrations systematically originate from the deep end of the fault and slowly propagate updip (Frank, Shapiro, et al., 2015).

Short-lived migrations ($T \sim$ minutes to hours) often proceed along striations (Ide, 2012), sometimes in rapid sweeps (Ghosh et al., 2010). Remarkably, these rapid migrations sometimes occur within larger scale migrations, propagating in the reverse direction with respect to the large scale propagation. This has been observed in the along-dip direction in Guerrero, Mexico (Cruz-Atienza et al., 2018; Frank et al., 2014) and in the along-strike direction in Cascadia (Houston et al., 2011).

3.2.3 Temporal Patterns

Tremor activity occurs during episodic *bursts* of events, which are composed of shorter bursts. Temporal clustering of activity covers time scales of years for the largest bursts — often correlated with slow-slip events and long-distance migrations — to days or even minutes for smaller bursts (Idehara et al., 2014; Wech & Creager, 2011) — called *cascades*. The imbrication of small bursts within larger ones makes it difficult to determine a characteristic duration. The shortest bursts proceed over a few minutes, whereas the largest ones can persist for days or even months (*e.g.*, Frank et al., 2014; Ghosh et al., 2010; Shelly, 2015) As a temporal point process, this activity is clustered and does not conform to simple memoryless realizations. It has been analyzed using

non-Poissonian statistics (Beaucé et al., 2019; Frank et al., 2016).

The recurrence interval between tremor bursts decreases with increasing depth along the subduction interface (Wech & Creager, 2011). In addition, the time-clustering of activity can change from one tremor patch to its neighbors (Frank et al., 2016; Idehara et al., 2014), and can evolve as a function of time (Frank et al., 2016). This has been interpreted as evidence for variations of fault zone conditions in both space and time (Frank et al., 2016).

3.2.4 Tremor activity Patterns in Guerrero, Mexico

Figure 3.1 shows the spatio-temporal patterns of LFE activity in the Guerrero tremor subduction segment, which is concentrated in two separate patches. One, called the *sweet spot*, is located at the downdip end of the segment and has a high rate of activity with a high level of time clustering (Frank et al., 2016). The other patch, called *transient zone* (Frank et al., 2014), is further updip and on the whole more quiescent. It hosts episodic bursts of activity with a recurrence interval of about 3 months (Frank et al., 2014), which coincide with short-term SSEs recurrence (Frank, Radiguet, et al., 2015). One of these episodes is displayed in Figure 3.1c. Activity migrates away from the sweet spot over a hundred kilometers updip. These episodes are built from many shorter bursts that may drift in both updip and downdip directions (Figure 3.1d).

The Guerrero subduction zone is also known for its very large SSEs that recur at intervals of about 4 years (*e.g.*, Radiguet et al., 2012b) and are accompanied by intense tremor activity in both the transient zone and sweet spot. These events persist for several months with slow slip occurring mostly updip of the tremor-generating segment. The unstable slipping segment of the fault encroaches upon the transient zone over a small distance, where short-term SSEs are concentrated. During both short and long-term SSEs, tremor activity in the transient zone switches from episodic to highly clustered (Frank et al., 2016).

The most striking feature of the Guerrero subduction zone is perhaps that the patch with maximum tremor activity (the sweet spot) is separated from the patch with largest amount of slow slip (the transient zone) by more than 20 km.

3.3 Model design

In this section, we develop a model for time changes of permeability in a heterogeneous porous channel that runs along the dip of the subduction interface. Based on physical arguments, we associate sudden changes of fluid

pressure with the generation of LFE-like, elementary tremor events.

3.3.1 Diffusion equation for pore pressure variations

Pore connectivity is modeled at a macroscopic level with a permeability that varies along the channel $k(x)$. The fluid mass flux per unit cross-sectional area, $q(x,t)$, depends on pore pressure $P(x,t)$ according to Darcy's law:

$$q(x,t) = -\frac{k(x)\rho}{\eta}\left(\frac{\partial P}{\partial x}(x,t) + \rho g \sin\alpha\right) \tag{3.1}$$

where ρ is the fluid's density, η is the fluid viscosity, α is the dip angle of the subduction interface and g the acceleration of gravity. Mass balance dictates that :

$$-\frac{\partial q}{\partial x}(x,t) = \frac{\partial(\rho\phi)}{\partial t}. \tag{3.2}$$

where ϕ is porosity. We consider that pores are saturated with fluid and neglect temperature changes, which is justified by the small thickness of the channel and the small flow rates that are expected. Changes of the local mass of fluid can be due to the fluid compressibility as well as expanding/contracting pores. This is accounted for by an effective rock-fluid compressibility β, such that:

$$\begin{aligned} \beta &= \frac{1}{\rho\phi}\frac{\partial(\rho\phi)}{\partial P} \\ \implies -\frac{\partial q}{\partial x}(x,t) &= \rho\phi\beta\frac{\partial P}{\partial t}(x,t). \end{aligned} \tag{3.3}$$

For simplicity, we neglect density variations in the body force term in equation (3.1), because they are due to changes of flow-induced dynamic pressure, which account for a fraction of the total pressure, and because they are not expected to play a significant role. We split pressure into a hydrostatic component and a time-dependent dynamic component due to flow noted p. Neglecting changes of fluid viscosity, we obtain the following equation for the dynamic pore pressure component:

$$\frac{\partial p}{\partial t} = \frac{1}{\phi\beta\eta}\frac{\partial}{\partial x}\left(k(x)\frac{\partial p}{\partial x}\right). \tag{3.4}$$

We assume that permeability is piecewise constant. Thus, in each segment, the dynamic pressure obeys a diffusion equation:

$$\frac{\partial p}{\partial t} = \frac{k}{\phi\beta\eta}\frac{\partial^2 p}{\partial x^2}\ , \tag{3.5}$$

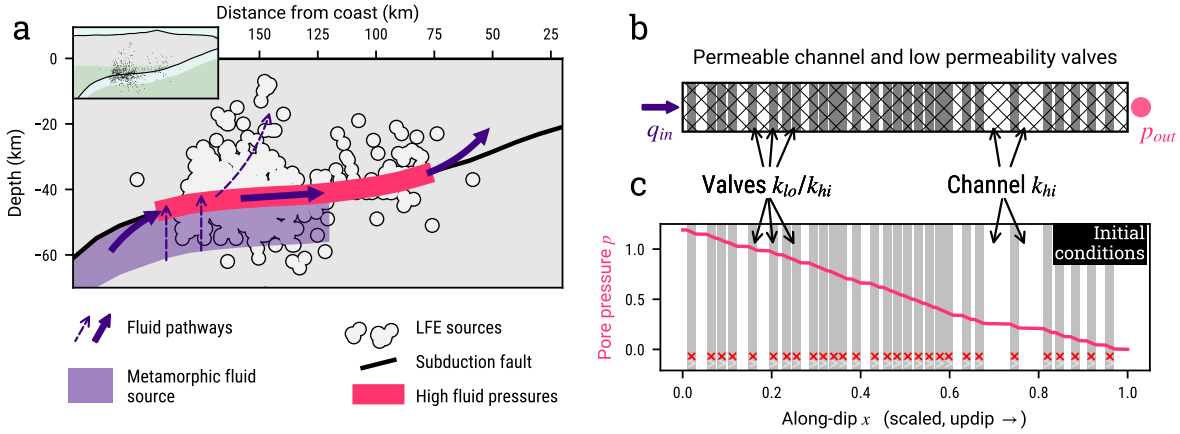

Figure 3.2 — *(a) Schematic representation of a permeable fault zone. Below the tremor source region, metamorphic dehydration reactions release fluid, which is channeled in the permeable subduction interface as it circulates under high fluid pressures. (b) Permeability structure for a 1-D hydraulic model of this system, involving a number of randomly distributed plugs that can open and close under certain conditions. The channel is fed at its base by input fluid flux q_{in}. At the top, the channel is connected to a high permeability region such that the fluid pressure is close to the hydrostatic pressure p_{out}. (c) Initial conditions correspond to steady-state flow regime with a small input flux and all plugs closed.*

with diffusivity $D = k/(\phi\beta\eta)$. Along the modeled channel, D is therefore piecewise constant.

Figure 3.2 shows how we simplify the subduction fluid transport system conceptually and how it is represented as a permeable channel with plugs of low permeability.

3.3.2 A mechanism for large changes of permeability

Our model has two main ingredients, which deal with the nature of the fluid phase and its interaction with the network of pores in the permeable medium. Subduction zone metamorphic fluids are complex silica-saturated mixtures (Frezzotti & Ferrando, 2015; Manning, 1997). As they rise, they undergo decompression and, due to the pressure dependence of solubility, are expected to precipitate either amorphous silica (silica gel) or quartz nanoparticles as well as other mineral phases. Depending on the availability of nucleation sites, precipitation may proceed along the pore walls or in the bulk fluid. High temperature decompression experiments on silica-rich fluids demonstrate that the silica nanoparticles that are generated are readily mobilized by

fluid flow (Amagai et al., 2019; Okamoto, 2019). Small clasts generated by grinding motion along the fault are also likely involved (*e.g.*, Han & Hirose, 2012). As in other deep permeable systems, the interstitial fluid phase is thus expected to carry fines and colloids (Manga et al., 2012).

Natural permeable media are made of pores and fractures connected by thinner throats which have a strong effect on permeability because they determine the effectiveness of fluid pathways through a volume. Capture and/or precipitation of even small amounts of solids within throats can decrease permeability by orders of magnitude (McDowell-Boyer et al., 1986). Calculations by Beckingham (2017) show that, depending on whether pore throats are open or clogged, permeability can change by more than a factor of ten. These changes are associated with negligible porosity variations because pore throats occupy a very small fraction of the total interstitial volume. Thus, the transition between high and low permeability states is very abrupt, as plugging thin throats between larger pores involves very small amounts of sediment. Even if they are much smaller than a pore throat, fines and colloids can get stuck through a jamming process at rates that depend on their concentration (Agbangla et al., 2014; Civan, 2016; Delouche et al., 2020). Clogging can be achieved in a matter of minutes (Candela et al., 2014; Delouche et al., 2020; Manga et al., 2012).

Material that gets stuck in pore throats may be remobilized by the flow (Amagai et al., 2019; Bianchi, Wittel, et al., 2018; Civan, 2016; Jäger et al., 2017b; Kudrolli & Clotet, 2016). Flow exerts a shear stress on the encasing solid, noted σ, that scales with the average pathway diameter d and the pressure gradent $\partial p/\partial x$. If this stress exceeds a certain threshold value noted σ_c, infillings are eroded and transported by the fluid (Civan, 2016). This may occur in catastrophic fashion in events called *erosive bursts* (Bianchi, Thielmann, et al., 2018). Such bursts may be composites of several smaller unclogging events (Bianchi, Thielmann, et al., 2018). The process has been studied in detail by Kudrolli and Clotet (2016). In these experiments, a pure fluid is fed into a polydisperse particle bed. When the flow rate exceeds a threshold value, such that the flow-induced stress exceeds the threshold value σ_c, the flow dislodges and mobilizes the smaller particles. Interestingly, the authors observe small precursor events when the flow rate is just below critical and a large avalanche when the flow rate reaches the critical value. This is due to the collective behavior of particles, as some of them are not able to move if they are in contact with stronger ones that resist detachment. Thus, these particles are only dislodged when their neighbors are, which triggers an erosion avalanche. As long as $\sigma > \sigma_c$, particles cannot remain stuck and incipient coatings of pore walls are eroded, ensuring that fluid pathways stay fully open. Clogging thus requires that $\sigma \leq \sigma_c$. The alternation between ero-

sion and deposition phases leaves little opportunity for particles and colloids to become permanently cemented to one another and to pore walls. Clogging and unclogging events therefore proceed rapidly, and can be considered as instantaneous at the time-scales of LFE activity.

As shown above, these processes have been observed in laboratory experiments on different types of porous media. Owing to their local character, they have not been documented in the field but, on a large scale, simultaneous variations of permeability and fluid pressure in faults (Manga et al., 2012) and oil reservoirs (Sahimi et al., 1999) have been attributed to erosion/deposition processes.

3.3.3 A valve mechanism

We model clogging and unclogging events as follows. Within a long permeable channel, let us consider a clogged plug where fluid pathways are narrow and contorted because they wrap around captured particles (closed state). In this case, the average pathway aperture d and permeability k are both small, with values d_{lo} and k_{lo}, respectively. If and when δp, the pressure difference across the plug, reaches a critical value noted δp_c^{break} such that the shear stress on the plug particles σ is equal to critical value σ_c, unclogging occurs. As a consequence, pore throats are no longer obstructed by particles and permeability increases to $k_{hi} \gg k_{lo}$, in association with an increase of d from d_{lo} to d_{hi} (open state). This drives a lowering of pore pressures upstream of the plug, and an increase downstream. This pressure transient is very rapid initially, and then decelerates, in a diffusion-induced flow transient. A key point is that σ initially increases. Just before unclogging, it is equal to:

$$\sigma_- = \lambda_1 d_{lo} \frac{\delta p_c^{break}}{w} = \sigma_c \tag{3.6}$$

where λ_1 is a coefficient and w is the plug length along the channel. As plug particles are set in motion by the hydraulic stress and can no longer adhere to throat walls, the effective pore aperture d increases from d_{lo} to d_{hi}. In the permeable medium, variables are defined as spatial averages over a representative volume, and this is true for porosity and pressure in particular. As the solid particles get flushed out of the thin throats that connect larger pores, porosity is barely affected and, by the same token, so is the fluid pressure, because it is the average pressure for a group of pores and pore throats, with the larger pores acting to buffer local pressure variations at the pore throat scale. Thus, the pressure differential across the pore is maintained at δp_c^{break}

as the plug opens up (Jäger et al., 2018). Therefore, σ increases to σ_+:

$$\sigma_+ = \lambda_1 d_{hi} \frac{\delta p_c^{break}}{w} \tag{3.7}$$

which is larger than σ_c. σ then decreases gradually as the pressure distribution adapts to the new permeability structure. The plug remains unobstructed as long as σ is larger than σ_c. Clogging occurs when $\sigma = \sigma_c$ such that δp reaches a second threshold value of pressure differential noted δp_c^{clog}:

$$\lambda_1 d_{hi} \frac{\delta p_c^{clog}}{w} = \sigma_c. \tag{3.8}$$

Clogging causes the permeability to drop back to k_{lo}, driving an increase in δp until unclogging occurs again, thus starting a new cycle. This is a valve behavior akin to the toggle-switch of Miller and Nur (2000).

This framework allows an internally consistent mechanism for a succession of unclogging and clogging events. One requirement is that $\delta p_c^{clog} < \delta p_c^{break}$. From equations (3.6) and (3.8), we deduce that:

$$\frac{\delta p_c^{break}}{\delta p_c^{clog}} = \frac{d_{hi}}{d_{lo}}. \tag{3.9}$$

Thus, the fact that $d_{hi} > d_{lo}$ automatically ensures that $\delta p_c^{clog} < \delta p_c^{break}$. One can go one step further using relationships between the average width of fluid pathways d and permeability k. A common parameterization is the Kozeny-Carman equation (Civan, 2016):

$$k = \lambda_2 \frac{\phi d^2}{\tau} \tag{3.10}$$

where λ_2 is a coefficient that depends on the nature of the fluid pathways, *e.g.* tubes or slits, ϕ is porosity and τ is tortuosity. We may neglect variations of porosity, as discussed above, and obtain:

$$\frac{k_{hi}}{k_{lo}} = \frac{\tau_{closed}}{\tau_{open}} \left(\frac{d_{hi}}{d_{lo}} \right)^2 \tag{3.11}$$

where τ_{open} and τ_{closed} are the tortuosities of the open and closed plugs. Fluid pathways are more irregular and contorted in a closed plug than in an open one, implying that $\tau_{closed} > \tau_{open}$. Using equation (3.9, one deduces that:

$$\frac{\delta p_c^{break}}{\delta p_c^{clog}} = \frac{d_{hi}}{d_{lo}} = \left(\frac{\tau_{open}}{\tau_{closed}} \frac{k_{hi}}{k_{lo}} \right)^{1/2}. \tag{3.12}$$

For the small porosity media that are involved here, tortuosity ratio $\tau_{open}/\tau_{closed}$

is likely to be in a $1/2 - 1/4$ range (Ghanbarian et al., 2013). As stated above, permeability changes induced by clogging are typically larger than one order of magnitude (Beckingham, 2017; McDowell-Boyer et al., 1986), which guarantees that $\delta p_c^{break} > \delta p_c^{clog}$. For the sake of further discussion in section 3.4.1, it should be noted that such values of the tortuosity ratio imply that $k_{hi}/k_{lo} > \delta p_c^{break}/\delta p_c^{clog}$.

Figure 3.3 summarizes how these processes are implemented in our model. In valve segments of the channel, permeability responds to the local fluid pressure gradient according to the hysteretical cycle shown in Figure 3.3b.

3.3.4 Valves as elementary seismic sources

At each valve-opening, the fluid pressure gradient that has built up is suddenly dissipated in a rapid, localized diffusion transient. Variations of fluid pressure on each sides of the valve are responsible for temporal changes of the force applied to the solid walls of the permeable medium, which are able to generate seismic waves, as shown by N. M. Shapiro et al. (2018). Other seismic processes may also be triggered. For example, high fluid pressures may induce the seismic rupture of critically-stressed brittle heterogeneities (*e.g.*, Taetz et al., 2018), and an impulsive turbulent flow transient may generate resonance in tortuous pathways (Benson et al., 2008). We thus consider that as they open, valves act as elementary seismic sources and generate LFE-like events.

3.3.5 Permeability values, boundary and initial conditions

We will consider heterogeneous permeable channels with a series of randomly distributed valves. This corresponds to one type of random permeability distribution involving segments where fluid pathways are more contorted than elsewhere. The behavior of any valve depends on what happens in neighboring ones, so that pressures and flow rates must be calculated everywhere in the channel.

Metamorphic reactions occur at different depths depending on the dehydrating material, which includes sediments, serpentinized mantle and hydrated oceanic crust. Focussing on the oceanic crust, dehydration proceeds at depths exceeding the tremor source region (van Keken et al., 2011) and most of this fluid gets trapped in the high permeability subduction interface, sealed from above by the low permeability mantle wedge (Hyndman et al., 2015). Thus, the channel is fed at its base by an input fluid flux q_{in}. For a first instalment of the model, it is instructive to maintain this flux at a constant value. At its updip end, the channel is connected to a high permeability

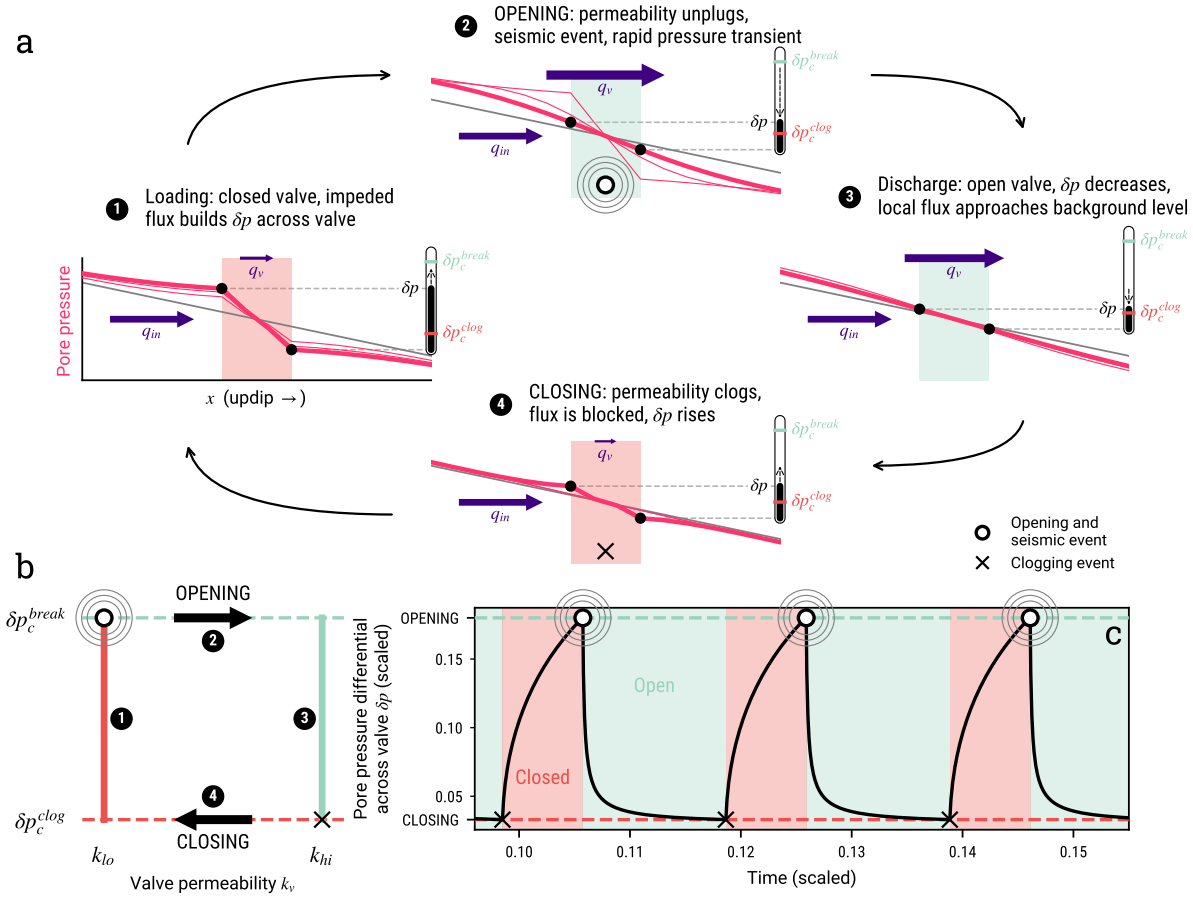

Figure 3.3 — *(a) The 4 stages of the valve mechanism. 1, the valve has been closed and permeability is k_{lo}. δp, the pressure difference across the valve, increases. 2, when δp reaches the threshold value δp_c^{break}, an impulsive unclogging event (an erosive burst) occurs. Particles get flushed out, the valve opens and permeability rises to k_{hi}. 3, valve opening generates a rapid pressure transient that is associated with a low frequency earthquake. 4, when δp decreases to δp_c^{clog}, the deposition of fines and colloids resumes and permeability drops to k_{lo}. The valve closes and a new cycle begins. (b) Hysteretical cycle of pressure difference δp and valve permeability k. (c). Evolution of δp through 3 successive cycles of valve opening and closure for an isolated valve.*

region which may be either continental crust (Hyndman et al., 2015) or an accretionary prism. In this case, pore pressures are close to hydrostatic values, such that the dynamic pressure is zero ($p_{out} = 0$).

For simplicity, we assume that in the channel outside of valves, permeability remains constant at the value k_{hi} and that valves have the same length w in the x direction. Physical variables are made dimensionless using scales described in Table 3.1. Values adopted for the various valve parameters are listed in Table 3.2. Boundary and initial conditions are illustrated in Figure 3.2b,c. We start all simulations with an equilibrium profile corresponding to a low value of flux $q_{in}(t < 0) = 0.09$, such that all valves are closed with permeability k_{lo}. At $t = 0$, q_{in} is changed to its value for the run.

Table 3.1 — *Characteristic dimensions used to scale physical variables*

Variable		Characteristic scale	
x	Distance along channel	$\mathcal{X} = L$	Channel length
z	Depth	$\mathcal{Z} = \mathcal{X}\sin(\alpha)$	Channel vertical depth
t	Time	$\mathcal{T} = \mathcal{X}^2/D$	Diffusive time[a]
p	Pore pressure	$\mathcal{P} = (\rho_r - \rho)g\mathcal{Z}$	Reduced lithostatic pressure differential across channel
q	Massic flow rate[b]	$\mathcal{Q} = k_{hi}\rho/\eta \times \mathcal{P}/\mathcal{X}$	Flux resulting from characteristic pore pressure differential[a]
k	Permeability	$\mathcal{K} = k_{hi}$	Background channel permeability

[a] along a fully open channel, $D = k_{hi}/(\rho\eta\beta)$
[b] per unit channel cross section area

Table 3.2 — *Valve parameters for all simulations presented in this chapter*

	Parameter	Value (scaled)
w	Valve width	0.02
k_{hi}	Open valve permeability	1
k_{lo}	Closed valve permeability	0.05
δp_c^{break}	Threshold p difference for opening	0.04
δp_c^{clog}	Threshold p difference for closing	0.021
q_c^{break}	Flux above which a closed valve can open	0.1
q_c^{clog}	Flux below which an open valve can close	1.05

3.3.6 Numerical implementation

Solutions for the pressure field in time were obtained using a Crank-Nicholson finite difference scheme, with a first order, centered discretization of the second order space derivatives of pressure (Press et al., 2007, section 20.2, pp 1045–1048). The scheme is implicit, centered and second order in time, and is unconditionally stable. Valves are either in an open or a closed state, as described in section 3.3.3 above, and when the pressure differential at their boundary reaches a threshold value, their open/closed state is changed accordingly. Each opening of a valve is counted as a seismic event.

In all simulations presented here, distance along the fault is discretized in dimensionless increments $\delta x = 0.002$ and the dimensionless time step is set to $\delta t = h^2/2D = 2.10^{-6}$. In order to test the accuracy of the numerical implementation, we calculated analytically the pressure variations that follow an unclogging event in and around an isolated valve, and compared them to numerical solutions. Convergence was then tested by lowering both space and time steps, and we verified that accuracy improved with increasingly fine discretization. Section 3.A of the appendix describes the methodology and results of the convergence and accuracy tests.

3.4 Time-dependent valve behaviour

We first use a single valve to show how the activity regime is controlled by the input flux and how an intermittent valving behavior requires certain conditions (Figures 3.4 and 3.5). We then illustrate how neighboring valves interact using 3 valves (Figure 3.6).

3.4.1 A single valve

As mentioned above, the valve mechanism depends on five control parameters, four that describe valve behavior, $k_{lo}, k_{hi}, \delta p_c^{clog}, \delta p_c^{break}$, and the input flux q_{in}. We identify the conditions under which a steady state solution exists, with a valve that is either open or closed. In steady state, the flux through each valve is equal to the input flux:

$$q_{in} = \frac{\rho}{\eta} k_v \frac{\delta p}{w} \tag{3.13}$$

where k_v, the valve permeability, may be equal to k_{lo} or k_{hi}, and where δp is again the pressure difference across the valve. If $\delta p \leq \delta p_c^{break}$ in a closed valve, stuck particles cannot be removed and the valve remains closed. Conversely, if $\delta p \geq \delta p_c^{clog}$ in an open valve, particles cannot be captured and the valve

remains open. These conditions can be expressed as follows, using q_{in}, the flux a valve is subjected to:

$$q_{in} \leq \frac{\rho}{\eta} k_{lo} \frac{\delta p_c^{break}}{w} \left(= q_c^{break}\right) \text{ for a closed valve,} \tag{3.14}$$

$$q_{in} \geq \frac{\rho}{\eta} k_{hi} \frac{\delta p_c^{clog}}{w} \left(= q_c^{clog}\right) \text{ for an open valve.} \tag{3.15}$$

It introduces two threshold values for the fluid flux, noted q_c^{break} and q_c^{clog}, respectively. The two conditions in (3.14) and (3.15) define domains in $(\delta p, k_v)$ space corresponding to a closed valve or an open one in steady-state (Figure 3.4). Table 3.2 lists values for the pressure thresholds and permeabilities, as well as for the flux thresholds used for the valve set up of this study.

Depending on the four valve parameters, there are two different types of solutions. Let us first consider *enhanced permeability variations*, such that $k_{hi}/k_{lo} > \delta p_c^{break}/\delta p_c^{clog}$. In this case, $q_c^{break} < q_c^{clog}$ and there are no steady-state solutions in the $q_c^{break} - q_c^{clog}$ interval (Figure 3.4a). In this interval, the input flux being higher than q_c^{break}, a closed valve will open, and in turn, the input flux being lower than q_c^{clog}, the now open valve will eventually close. Therefore, the valve must constantly switch between open and closed states in order to handle the imposed input flux. This oscillatory regime is illustrated schematically in Figure 3.3.

In the other case, called *enhanced pressure variations*, $k_{hi}/k_{lo} < \delta p_c^{break}/\delta p_c^{clog}$. This implies that $q_c^{break} > q_c^{clog}$ and the domains for a closed valve and an open one overlap in the $q_c^{clog} - q_c^{break}$ interval. In this interval, steady-state solutions are possible for the two valve states (Figure 3.4b). Which one is selected depends on the initial state of the valve. In this case, therefore, there is no valve activity.

This analysis leads to the following instability criterion for the valve:

$$q_c^{break} < q_c^{clog} \iff \frac{\delta p_c^{break}}{\delta p_c^{clog}} < \frac{k_{hi}}{k_{lo}}. \tag{3.16}$$

In a geological context, the tortuosity ratio is small and lies in a restricted range (see section 3.3.3, last paragraph) and in contrast, permeability is expected to change by one order of magnitude (Beckingham, 2017; McDowell-Boyer et al., 1986; Miller & Nur, 2000). Using the argument developed for equation (3.12), where we derive the threshold δp ratio as a function of the permeability ratio, we conclude that the instability criterion should be met in geological porous media where erosion/deposition processes are active. Such permeable systems have been reported to self-organize around these critical erosion/deposition conditions (Kudrolli & Clotet, 2016).

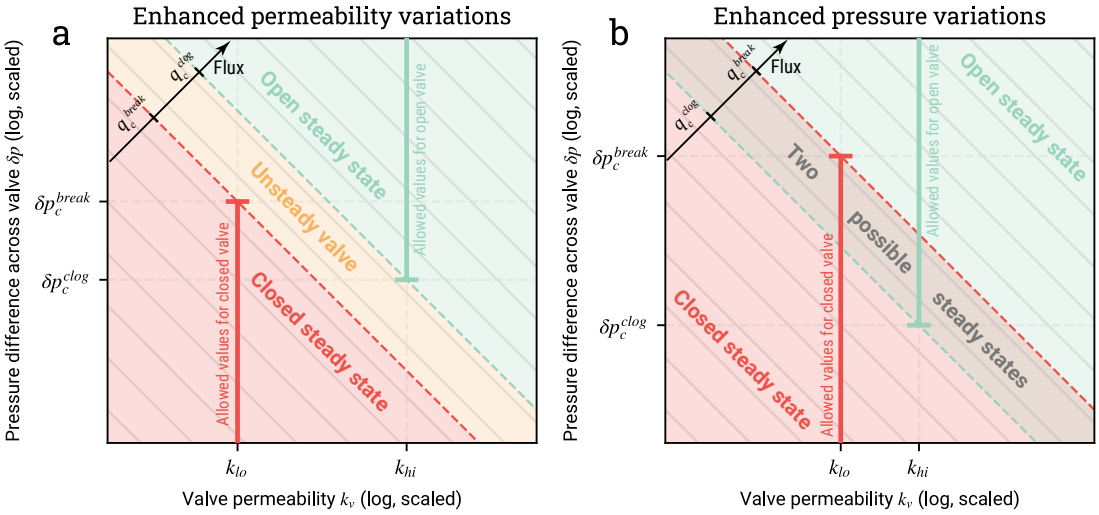

Figure 3.4 — *Requirements for steady-state valve regimes (equations (3.14) and (3.15)) in k-δp space (in log-log scale). The two values for permeability k and threshold values for the valve pressure difference δp are shown with vertical and horizontal dashed lines. In this space, iso-flux contours appear in gray lines of slope -1 in log-log scale (-45°). Blue and red segments indicate values of δp that are allowed for a closed valve and an open one in steady-state, respectively. Steady-state conditions are achieved in the green and red shaded areas. See explanations in the text. (a) Valve with enhanced permeability variations ($k_{hi}/k_{lo} > \delta p_c^{break}/\delta p_c^{clog}$). (b) Valve with enhanced pressure variations ($k_{hi}/k_{lo} < \delta p_c^{break}/\delta p_c^{clog}$).*

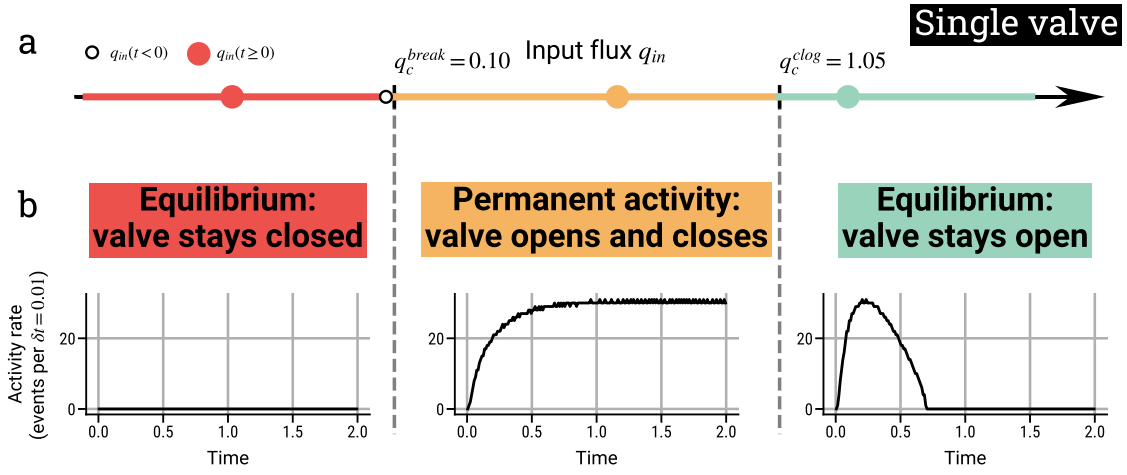

Figure 3.5 — *Influence of the input flux q_{in} on the activity of a single valve. (a) Three intervals of input flux q_{in} are delimited by two threshold values q_c^{clog} and q_c^{break}. (b) Examples of activity rate evolution in time (in black) for each regime. Activity rate is taken as the number of events per $\delta t = 0.01$, scaled unit. An event corresponds to the opening of a valve. Valve parameters are listed in Table 3.2.*

Figure 3.5 shows results for three values of input flux, corresponding to steady-state with a closed valve ($q_{red} < q_c^{break}$), a permanent intermittent regime with an unstable valve that switches between closed and open states ($q_c^{break} < q_{yellow} < q_c^{clog}$), and finally steady-state with an open valve ($q_{green} > q_c^{clog}$). In the first case, q_{red} is too low to allow the valve to open at all, no activity is recorded. In the last case, q_{green} is so high that after an initial transient during which the valve opens and closes to accomodate the incoming flux, the valve ends up open, submitted to a flux that does not allow it to close. In the intermediate case, q_{yellow} is both high and low enough to allow the valve to open when closed, and to close when open. After an initial transient, the valve activates in a very regular fashion.

3.4.2 Valve-valve interaction via pore pressure diffusion

A simulation with three valves shows how the opening of a valve may trigger the opening of adjacent valves (Figure 3.6). In this simulation, the middle valve $v2$ opens up, driving a sudden permeability increase. As a consequence, the δp that has built up across the valve re-equilibrates through diffusion, decreasing pressure updip of the valve and increasing it downdip of it. This induces an increase of pore pressure gradient through the two adjacent valves, eventually bringing them closer to unclogging conditions. We note that such constructive interaction causes migrations of activity in cascades, in both up- and downdip directions (see section 3.5.2).

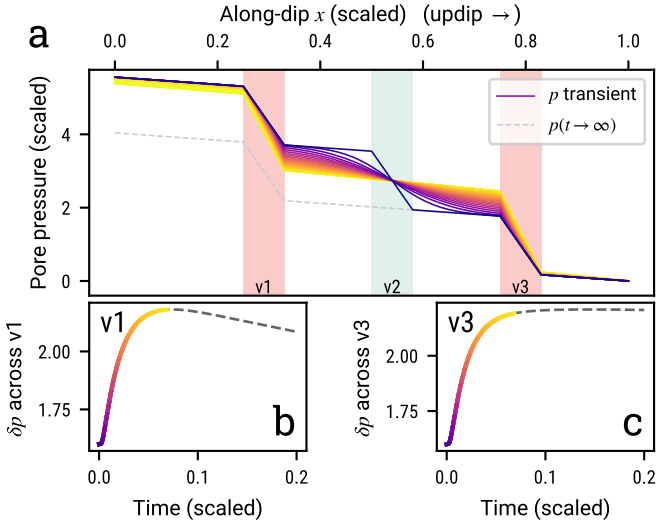

Figure 3.6 — *Interactions between three neighboring valves. (a) Transient evolution of pore pressure from an initial equilibrium profile with all valves closed towards a profile with valves v1 and v3 closed and valve v2 open. Panels (b) and (c): pore pressure difference evolution across valves v1 and v3.*

3.5 The collective behavior of interacting valves

We now explore systematically a model involving 29 randomly distributed valves (Figure 3.2b). With such a valve density, there are patches with valves that are closer together than on average, thus strengthening interactions that may generate spatial patterns of activity. All the valves are identical. We take the same permeability and threshold δp as specified in Table 3.2, implying that the threshold flux q_c^{clog} and q_c^{break} are the same as in previous sections (equations (3.14) and (3.15)). In fault-zones, we expect that conditions for enhanced permeability variations are met (see section 3.4.1, equation (3.16) in particular) and hence focus on the case in which $q_c^{break} < q_c^{clog}$.

3.5.1 Characteristics of valve activity in the permanent regime

Model outputs for runs with low ($q_{in} = 0.16$) and high ($q_{in} = 0.81$) input fluxes are shown in Figure 3.7 and Figure 3.8. At any given time, a simple diagnosis of the state of the system is given by the bulk equivalent permeability k_{eq}. Considering that channel segments and valves constitute hydraulic resistors in series, k_{eq} can be written:

$$k_{eq} = \frac{L}{(L - N_{cl}w)/k_{hi} + N_{cl}w/k_{lo}} \tag{3.17}$$

where N_{cl} is the number of closed valves, and L is the channel length. For any of the three regimes, activity rate, k_{eq} and the pressure difference across the channel Δp reach a dynamic equilibrium around a stable value after an initial transient, thus defining a permanent regime (Figures 3.7 and 3.8).

The analysis of section 3.4.1 for a single valve does not depend on the presence of neighboring valves, and holds for a channel with multiple valves. The three permanent regimes for the 29-valve system are illustrated in Figure 3.9: one with intermittent valve activity and two quiescent ones. Valve activity occurs when the flux is within the q_c^{break}–q_c^{clog} range. Within that range, we find that the activity style changes as a function of the input flux (Figure 3.10). Near the two ends of that range, activity is episodic or time-clustered (see also Figures 3.7 and 3.8), and almost periodic for the highest values of q_{in} (as shown later on, Figures 3.11 and 3.12). For intermediate flux values in the middle of the flux range, activity is random and Poisson-like, with a seemingly constant overall rate. This result holds for the valve distribution displayed in Figure 3.2b, and for 30 other random distributions of 29-valves with the same characteristics (parameters in Table 3.2). This will be discussed in more detail below.

Here, the catalog of synthetic events in space and time is analyzed in the

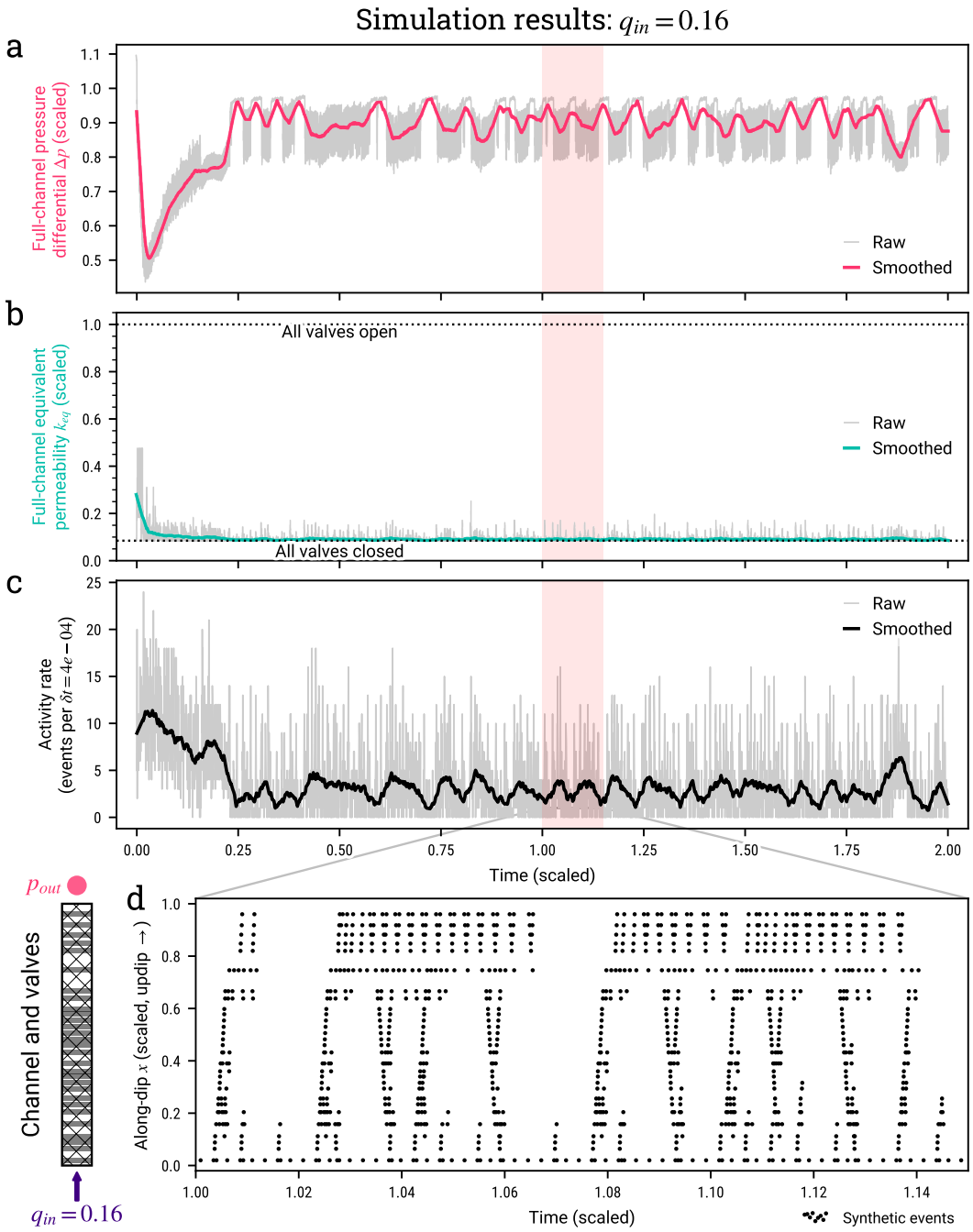

Figure 3.7 — *Time evolution of activity for a channel with 29 randomly distributed valves and a low input flux $q_{in} = 0.16$, just above q_c^{break}. (a) Fluid pressure differential across the channel Δp, (b) equivalent permeability k_{eq} and (c) activity rate (events per $\delta t = 4 \times 10^{-4}$ scaled unit). Raw data in grey and smoothed time series in colors (rolling mean with a window of length $\tau = 0.03$). (d) Time-space diagram of events occurrence within the channel. All valves are initially closed. A permanent regime with intermittent activity is reached after a short initial transient. Valve distribution represented in Figure 3.2, valve parameters are listed in Table 3.2.*

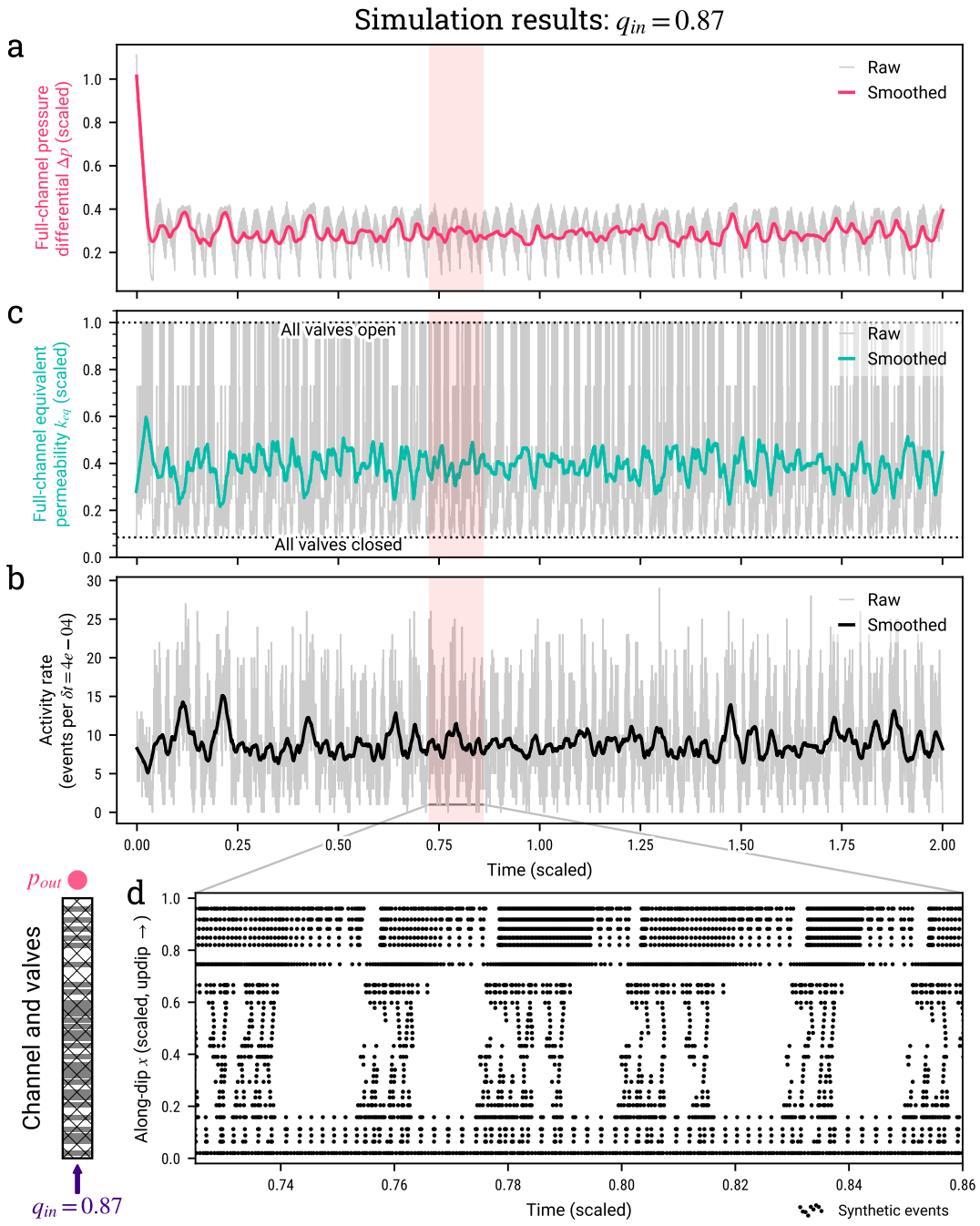

Figure 3.8 — *Time evolution of activity for a channel with 29 randomly distributed valves and a high input flux $q_{in} = 0.81$, just below q_c^{clog}. (a) Fluid pressure differential across the channel Δp, (b) equivalent permeability k_{eq} and (c) activity rate (events per $\delta t = 4 \times 10^{-4}$ scaled unit). Raw data in grey and smoothed time series in colors (rolling mean with a window of length $\tau = 0.03$). (d) Time-space diagram of events occurrence within the channel. All valves are initially closed. A permanent regime with intermittent activity is reached after a short initial transient. Valve distribution represented in Figure 3.2, valve parameters are listed in Table 3.2.*

form of a two-dimensional point process (t_i, x_i) illustrated in time-location graphs (Figures 3.7d, 3.8d, 3.11 and 3.12c). To characterize the level of time clustering (episodicity) of synthetic events, we follow Frank et al. (2016) and use statistical tools for the analysis of temporal point processes (Lowen & Teich, 2005). The main idea is to compute the spectrum of the event count signal autocorrelations, and to estimate the power-law exponent γ of its high frequency decay. A flat spectrum with $\gamma \approx 0$ corresponds to a nearly Poissonian process, whereas γ values that are significantly larger than 0 are indicative of time clustering.

As shown in Figure 3.10a, activity is Poisson-like for intermediate values of the input flux, such that $\gamma \approx 0$. For values of the input flux at both ends of the q_c^{break}–q_c^{clog} range, activity is characterized by high values of γ, indicating time clustering. Time-series of the activity rate reveal episodic bursts (Figure 3.10b). When the input flux is low (close to q_c^{break}), activity appears to be close to scale-invariant clustering with a burst recurrence rate that depends on the time scale of the measurement. For higher values of the input flux close to the upper bound q_c^{clog}, activity proceeds in quasi periodic bursts, with periods that seem to increase with increasing q_{in}.

As the input flux is increased from the lower threshold value q_c^{break} to the upper one q_c^{clog}, the channel is increasingly open on average. This may be assessed from the average proportion of open valves which increases as a function of q_{in} (Figure 3.10c). The proportion of open valves dictates the evolution of k_{eq}, the bulk permeability of the channel as a whole. For a low input flux ($q_{in} \approx q_c^{break}$), valves are closed most of the time and activity bursts are linked to phases of opening. In the other extreme, for $q_{in} \approx q_c^{clog}$, permeability is open most of the time. Swarms of events then occur mainly when the channel shuts down temporarily and valve pressures increase until unclogging conditions are met.

3.5.2 Cascades and migrations of synthetic activity

In the random distribution of valves that was adopted here, there are three patches where valves are closer to one another than elsewhere, around $x = 0.1$, $x = 0.5$ and $x = 0.85$ (Figure 3.11). In patches of closely packed valves, the constructive interaction we describe in Figure 3.6 is responsible for the occurrence of rapid cascades of events.These migrations may proceed in both downdip and updip directions, apparently with similar propagation rates. Obviously, the interaction is weaker and slower for valves that are separated by larger distances. Thus, the rates of cascading and event migration depend on the valve distribution.

Figure 3.11 depicts typical synthetic activity patterns. The input flux is

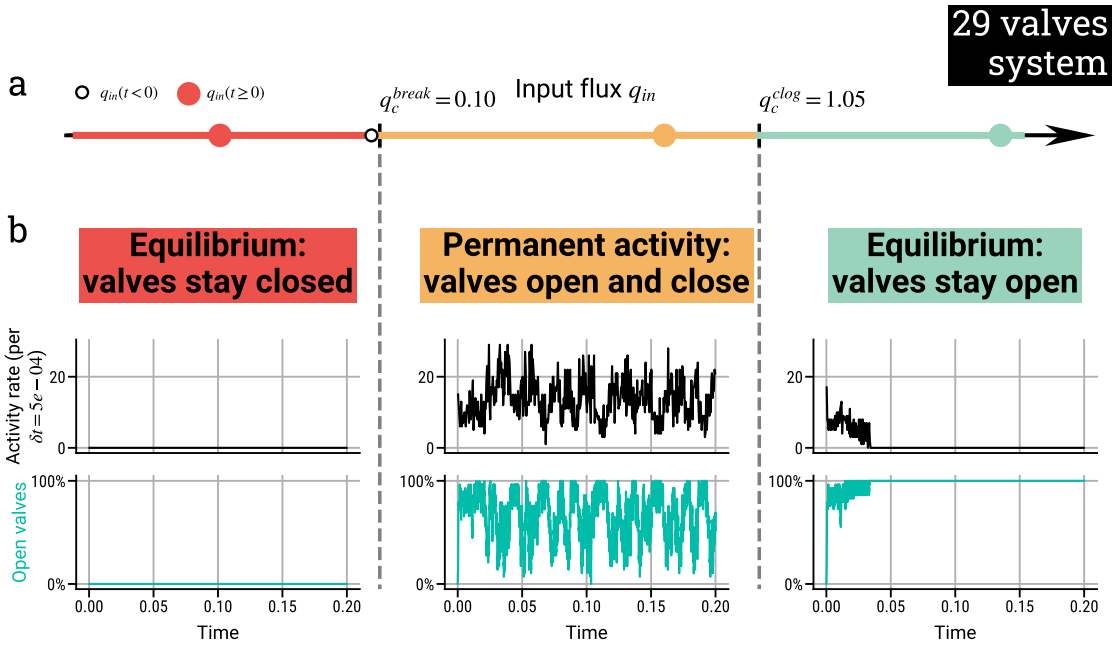

Figure 3.9 — *Influence of the input flux q_{in} in a representative system with 29, randomly distributed valves. (a) Three intervals of input flux q_{in} are delimited by two threshold values q_c^{clog} and q_c^{break}. (b) Examples of activity rate (number of events per $\delta t = 5 \times 10^{-4}$, scaled unit, in black) and proportion of open valves (in cyan) as a function of time, starting at $t = 0$ with all valves closed. Valve distribution represented in Figure 3.2, valve parameters are listed in Table 3.2.*

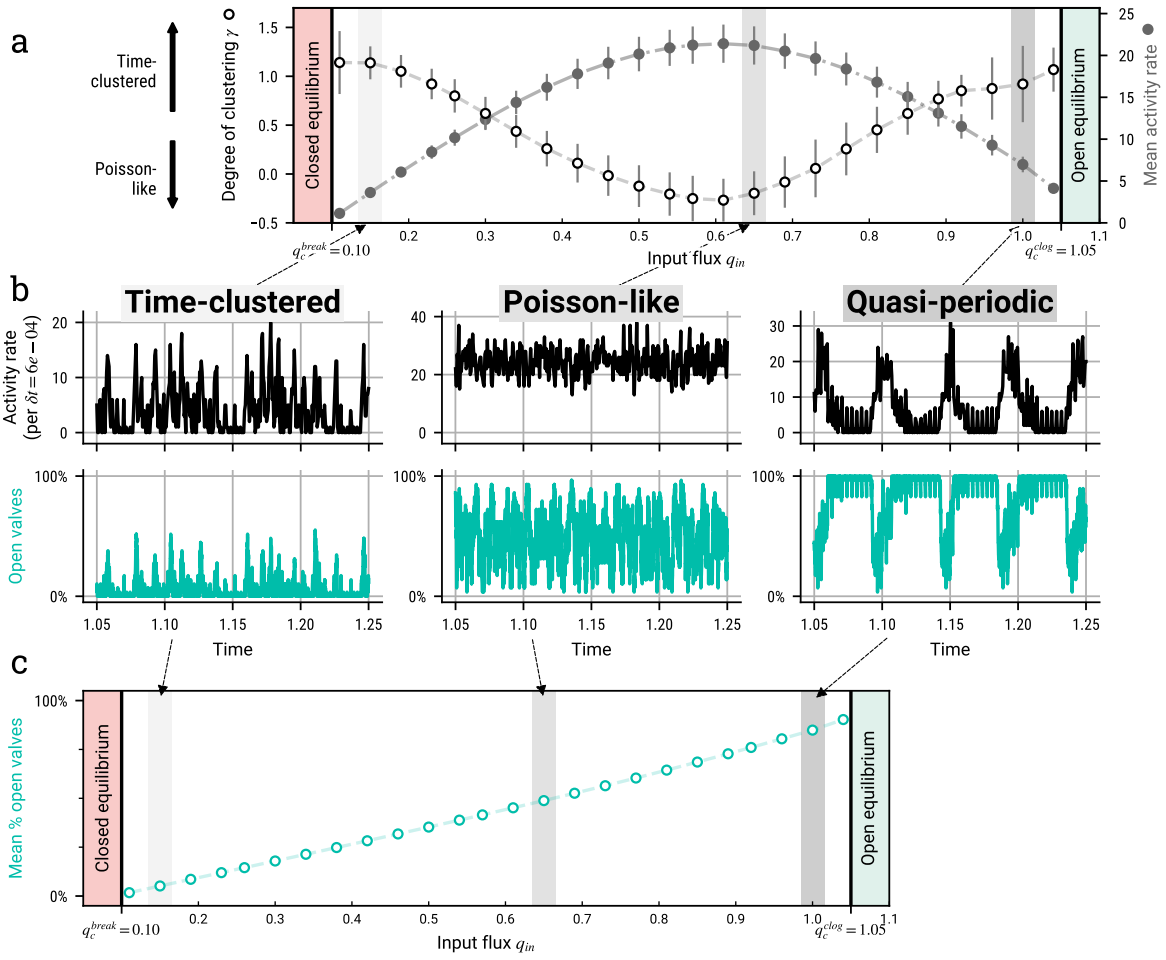

Figure 3.10 — *Different permanent activity styles as a function of the input fluid flux, averaged for 30 different 29-valve systems. (a) In white, the level of time clustering γ: the spectral slope of autocorrelation of event counts (see text) ; in gray, mean activity rate: number of events per unit time, both as a function of input flux q_{in}. For γ close to 0, activity is Poisson-like with no time clustering. The higher γ is, the more clustered and episodic activity is. (b) Activity rate (in black) and proportion of open valves (in cyan) as a function of time for particular simulations within the different regimes. (c) Time-averaged proportion of open valves in simulations, as a function of input flux. In (a) and (c), each dot represent the average value of the variable over 30 different 29-valve systems, at the given flux. Error bars are present in both panels, representing the standard deviation of this measurement over the 30 systems.*

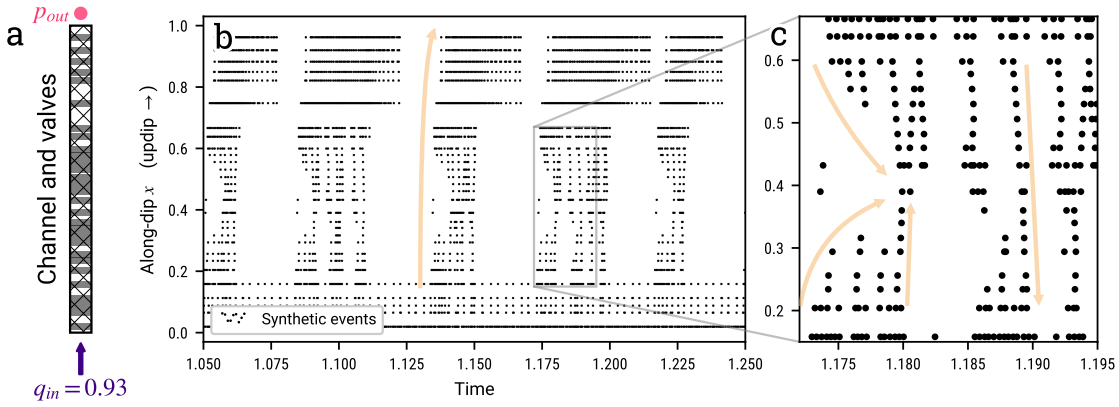

Figure 3.11 — *Synthetic tremor activity patterns. (a) Distribution of valves in the permeable channel. This distribution was generated randomly and contains three large clusters. (b) Activity patterns in space and time. Black dots stand for valve opening events. The lower valve cluster ($x = 0 - 0.18$) is active almost continuously. The middle and upper clusters ($x = 0.2 - 0.65$ and $x = 0.7 - 1$) is activated sequentially in bursts. Within a burst, activity is intermittent too. (c) focus on the activity in the middle valve cluster showing fast, short-scale migrations in both the updip and downdip directions. Valve distribution represented in Figure 3.2, valve parameters are listed in Table 3.2.*

close to the upper threshold q_c^{clog}, $q_{in} = 0.93$. Figure 3.11c shows nearly deterministic patterns of collective behavior at both short time and spatial scales. Cascades of triggering/opening events are associated with migrations of activity that show up as oblique dot alignments in the time-location chart. For this run as well as others, the migration rate of cascades takes similar dimensionless values $v \approx 4 - 6 \times 10^2$, with faster velocities (up to $v \approx 2 \times 10^3$ in dimensionless units) in the densest valve patches.

The fastest migrations appear to start and stop at the edges of densely populated patches. In such a patch, valves are close to one another and act in tandem. This shows up as an activity cluster which hosts its own internal migration patterns. Larger scale valve patches are activated sequentially in the updip direction. These large scale migrations proceed at slower rates than those within a single valve patch (Figure 3.11b). These large-scale migrations propagate at $V \approx 22 \times 10^2$ in dimensionless values from one end of the channel to the other.

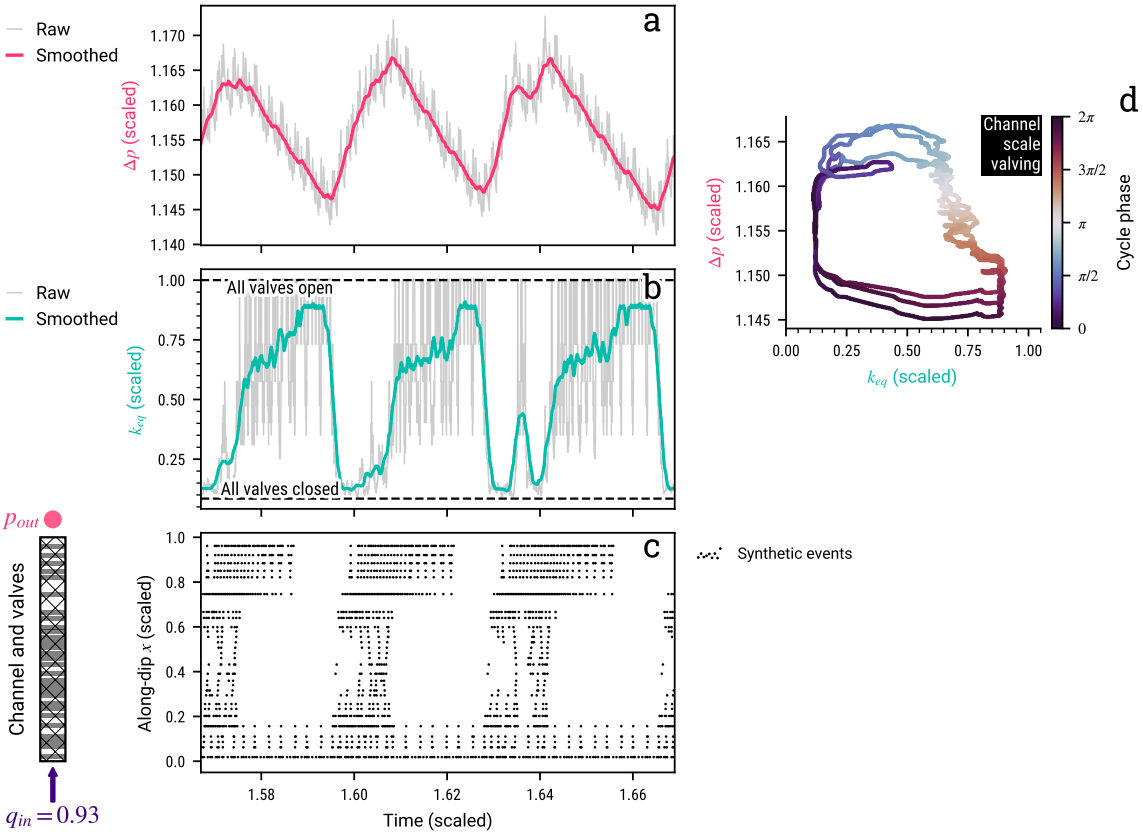

Figure 3.12 — *Cyclic variations of activity for $q_{in} = 0.93$. (a) Pore pressure difference across the whole channel Δp, (b) channel bulk permeability k_{eq}, and (c) time-location chart of events. (d) Activity in (Δp, k_{eq}) space, showing hysteretical cycles like those of a single valve. Valve distribution represented in Figure 3.2, valve parameters are listed in Table 3.2.*

3.5.3 Large-scale valving behavior

Segments of the channel containing a number of closely-spaced valves act like macroscopic valves, such that their equivalent permeability varies in hysteretical cycles with the total pressure difference across them. This behavior is achieved over a large range of scales, from small sets of a few valves to large valve patches and eventually for the full channel. Figure 3.12 depicts the cycles of equivalent permeability k_{eq} and total pressure difference across the whole channel, noted Δp, for three cycles of channel activity. Pore-pressure buildup and release varies in tandem with open/closed permeability phases, thus defining large-scale valving cycles coupled with the occurrence of seismic activity.

3.5.4 Random valve distributions

In order to evaluate the impact of the valve distribution on the previous results, we have generated 30 other random distributions of the same 29 valves

and kept all other parameters at the same values. In all these distributions, the inter-valve distance varies randomly but there are always a number of patches where valves are closer to one another than on average. By construction, the two threshold values of the fluid flux are the same. For all these distributions, the style of activity depends on the fluid flux in exactly the same manner as for the example valve distribution represented in Figure 3.2b, which activity is presented in Figures 3.7, 3.8, 3.9, 3.10b, 3.11 and 3.12. For the 30 valve distributions tested, Figure 3.10a and c show the averaged values of the clustering exponent γ, the mean activity rate and the time-averaged proportion of open valves at each value of the input flux. We observe similar spatio-temporal patterns within individual patches and at the scale of the inter-patch distance as shown in section 3.5.1 for the example valve distribution (Figures 3.11 and 3.12). We conclude that characteristic patterns of synthetic activity do not depend on the specific valve distribution, but should rather depend on valve clustering in space and the average inter-valve distance in the simulated channel.

3.6 Discussion

The key feature of the model is that pore-pressure diffusion induced by the opening of a valve triggers neighboring valve openings. In spite of the model simplicity, the generated activity exhibits complex patterns of migration and time clustering, comparable to seismic observations. An important result is that, for a given valve distribution, $i.e.$ a given permeability structure of the channel, the style of activity depends on the input fluid flux.

In this section, we evaluate the relevance of our model in several ways. The most basic information that can be extracted from the seismic observations consists of activity patterns and the associated time scales. Therefore, we first compare simulated and observed activity patterns from Guerrero, Mexico. Model results have been derived in dimensionless form and we then show that various observations are consistent with the same values for the variables in physical units. Using all these results, we draw general conclusions about the relations between the fluid flux and LFE activity in relation to the characteristics of the permeable subduction interface. We then discuss the impact of assumptions on valve and channel characteristics and directions for future work. In a last part, we evaluate possible extensions of the model.

3.6.1 Comparison with LFE activity patterns in Guerrero

We first observe that activity migrates in both the updip and downdip directions within the sweet spot patch at rates that are faster than that from

the sweet spot to the transient zone (Figure 3.1), as in our simulations. On the longest timescale, LFE activity in Guerrero appears time-clustered (Frank et al., 2016, 2014). Activity bursts recur in episodic fashion and are mostly concentrated in the downdip sweet spot patch. At times, during the most vigorous episodes, activity crosses over into the less active updip transient zone. Our model generates a similar pattern when the input flux q_{in} is near threshold values. At the lower end of the dimensionless operating flux range ($i.e.$ q_c^{break}–q_c^{clog}), the channel is mostly closed and activity emerges when it opens up in episodic fashion. In contrast, at the upper end of the flux range, the channel is mostly open and activity bursts are concentrated at the times of partial channel closure. Therefore, two different sets of values for valve opening/closing δp thresholds, valve permeability and q_{in} could correspond to the Guerrero activity. The first situation is reminiscent of a fault-valve mechanism, as high fault zone permeability correlates in time with seismicity. Several studies interpret tremor activity in Guerrero using this correlation (Cruz-Atienza et al., 2018; Frank, Shapiro, et al., 2015). In the framework of our model, however, the second situation seems as likely as the first one. We thus argue that seismicity bursts may not be systematically linked to an increase of fault permeability and subsequent fluid pressure surge, but may also be due to episodic phases of clogging in the fault, leading to transient fluid pressure build-up and release.

In our calculations, the lowermost patch is always active and is at the origin of larger scale migrations towards the less active upper patch, which trigger activity there. This is reminiscent of what happens in Guerrero (Figure 3.1). This behavior is a consequence of the boundary conditions that are imposed in the model. At the base of the channel, the fixed input flux constantly stimulates activity whereas the fixed pressure that is imposed at the top acts to buffer pressure variations. Thus, activation of the upper valve cluster only occurs once sufficient fluid pressures and volumes have built up in the lower part of the channel.

3.6.2 Scaling numerical results to LFE activity at Guerrero

The main parameter to constrain is the fault-zone diffusivity $D = k/\phi\beta\eta$. Using values from the literature, we end up with a wide range which is not useful. The channel porosity is $\phi = 0.01$–0.05 (Peacock et al., 2011), the fluid-rock effective compressibility is $\beta = 10^{-10}$–10^{-9} Pa^{-1} (Shvab & Sadus, 2015; Wibberley, 2002), and the dynamic viscosity of supercritical water is $\eta = 10^{-4}$–10^{-3} Pa.s^{-1} (Shvab & Sadus, 2015). Values for the background permeability k are very sensitive to the measurement method and, above all, to the spatial scale of the measurement. Here we do not consider laboratory-

scale determinations on drill-core samples and focus on measurements that capture the large-scale channel permeability. This leads to permeability values that can be as small as 10^{-18} m^2 and as large as 10^{-11} m^2 (Doan et al., 2006; Frank, Shapiro, et al., 2015; Hendriyana, 2021; Saffer, 2015). With all these values, we find that diffusivity D lies in a very large 10^{-4}–10^{5} m^2.s^{-1} range.

In order to scale model results to the Guerrero, Mexico, conditions, we need values for the characteristic spatial scale $\mathcal{X}$, fault-zone diffusivity D, and the characteristic time scale $\mathcal{T}$. For this diffusion process, $\mathcal{T} = \mathcal{X}^2/D$. For the Guerrero tremor zone, $\mathcal{X} = 100$ km. Using $D = 10^2$ m^2.s^{-1}, consistent with other estimates based on tremor migrations (Hendriyana, 2021), we obtain a characteristic time scale $\mathcal{T} = 10^8$ s ≈ 3 years. Using values of the hydraulic parameters that are quoted above, a diffusivity of $D = 10^2$ m^2.s^{-1} implies a permeability of $k = 10^{-14}$–10^{-12} m^2.

We next use the simulated activity in Figure 3.11 as a generic case. Such a quasi-periodic behavior allows an unambiguous determination of the characteristic recurrence time between large activity bursts, $T_r \approx 0.05$, and their characteristic duration, $\tau \approx 0.015$, in dimensionless units. Both values are representative of highly time-clustered activity, which occur for both low and high fluid fluxes, and in a large number of 29-valve distributions. Scaling variables back to physical units, we find that $T_r \approx 3$ months and $\tau \approx 2$ weeks, which are close to the estimates of Frank and Brodsky (2019) for Guerrero: $T_r^G = 2$–3 months, $\tau^G = 5$–20 days. In physical units, the migration velocities described in section 3.5.2 scale up to $v = 15$–20 km.hr^{-1} for short, rapid migrations, and to $V = 7$ km.hr^{-1} for the largest migrations that proceed from bottom to top of the channel. In Guerrero, short migrations propagate indeed at velocities of a few tens of kilometers per hour (Cruz-Atienza et al., 2018; Frank et al., 2014), but the larger scale migrations are slower than our model estimate, with a velocity of about 1 km.day^{-1}. This may be attributed to the distance that separates valve patches which has a large impact on the propagation time in a diffusion process.

Using the above physical scales, synthetic activity rates range from 1 event per day for low activity periods to about 40 events per day during bursts in near-critical fluxes, and are uniformly extremely high for intermediate fluxes (Figure 3.10a and b). In Guerrero, average values of the activity rate are typically 600 events per day in a background regime and up to a few thousands of events per day during bursts. The activity rate obviously depends on the number of valves that are accounted for and a channel with only 29 valves does not accurately represent the larger-scale, more complex Guerrero system.

Last, but not least, we evaluate pore pressure and fluid flux values. For

the fluid flux scale, $\mathcal{Q}$, we use the estimate of van Keken et al. (2011) for the Cocos subduction. The fluid flux per unit subduction zone width is $Q_T = 10$ Tg.Myr^{-1}.m^{-1}. Using the thickness of the subduction fault zone inferred from geological observations (Angiboust et al., 2015; Tarling et al., 2019), $h = 200$ m, we obtain a mass flux per unit area equal to $q_T = Q_T/h = 3\ 10^{-7}$ kg.s^{-1}.m^{-2}. This estimate is an average value for the whole subduction zone and the actual fluid flow should be focused into channels at several points along the strike of the fault (Ague, 2014; Piccoli et al., 2021). Such a channeling effect may increase the fluid flux by up to one order of magnitude. With this caveat in mind, we assume that the lower fluid flux threshold q_c^{break}, which is equal to 0.1 in dimensionless units in our simulations, is of the same order of magnitude as the dehydration metamorphic flux. We deduce that $q_c^{break} \approx 3\ 10^{-7} - -3\ 10^{-6}$ kg.s^{-1}.m^{-2}. We then find that the characteristic pressure scale $\mathcal{P} = \eta/\rho k\, \mathcal{Q} \times \mathcal{X} = 30$ MPa – 30 kPa, using the parameter ranges previously estimated.

The pressure difference between the two ends of the channel Δp is close to 1 dimensionless flux unit most of the time. Therefore, in physical units, $\Delta p \approx 30$ MPa–30 kPa. Each closed valve gets unclogged for $\delta p = 0.04\mathcal{P} = 1$ MPa–1kPa. The magnitude of the force that is applied to the plug walls depends on area. For a valve in a channel with a 10^3 m^2 cross-section, N. M. Shapiro et al. (2018) were able to match the amplitude of seismic waves with a pressure drop of 5 MPa. Our channel might have a larger cross-section, and hence allow for large forces with comparatively lower pressure drops. The fact that these values are of the same order of magnitude demonstrates a certain self-consistency of our analysis, backed by independent observations of seismic patterns, geological flux measurements, and seismic characteristics of LFEs.

3.6.3 Perspectives for diagnosing hydraulic conditions in fault zones

According to our model, the rate and style of seismic activity depends on the hydraulic regime of the permeable channel. Provided that tremor and LFEs are seismic expressions of valve-controlled pore pressure variations, tremor patterns can be used to investigate the hydraulics of fault zones, and eventually other natural systems such as hydrothermal fields and volcanoes where similar seismogenic mechanisms have been invoked (Honda & Yomogida, 1993)).

For given valve parameters that meet the condition for instability ($\delta p_c^{break}/\delta p_c^{clog} < k_{hi}/k_{lo}$, equation 3.16), the activity regime depends on a dimensionless input rate of fluid into the channel. This dimensionless input rate is calculated with respect to a Darcy flux for some reference permeability value (chosen to be

k_{hi} here). For application to natural conditions, the same dimensionless input rate can be obtained for different pairs of fluid flux and permeability values. Conversely, the same fluid flux may be responsible for different activity styles in different parts of the subduction interface depending on the local permeability value. In addition, time changes of the fluid flux, due for example to the subduction of more or less hydrated parts of an oceanic plate, may induce changes of activity.

The rate of fluid release by metamorphic reactions depends on the subduction rate and on the type of material that dehydrates. It cannot be the same everywhere as, for example, subduction rates vary by almost one order of magnitude. Therefore, comparing seismicity patterns in different subduction zones is likely to prove very useful. In particular, specific attention should be paid to subduction zone segments that do not seem to generate LFE activity (*e.g.* Bocchini et al., 2021). As shown in this paper, this may be due to a fluid flux that is either very high or very small.

3.6.4 Perspectives for exploring model configurations

The present hydraulic model was designed to evaluate the potential of the clogging/unclogging valve mechanism and to illustrate the various types of activity that can be generated. It can be made more complex in many ways. As discussed above, the migration and spatial patterns of activity depend on the distribution of valves in the domain. The density of valves can be related to the roughness of the subduction interface, which may be inherited from seafloor sedimentary cover or topography prior to subduction. Valve density impacts how strongly and quickly valves can communicate through pressure transients, and might be constrained by comparing magnitude-duration or magnitude-frequency scalings of synthetic and observed LFE activity. Those scalings at the LFE source level could also help constrain valve width and breaking/clogging criteria. We do not expect, however, to discover new activity regimes as solutions are determined by the four valve control parameters introduced above.

In all the cases reported here, all valves are identical, with the same width w, the same low permeability value k_{lo} in a state of clogging and the same values of opening/closing pressure thresholds δp_c^{break} and δp_c^{clog}. In natural conditions, the hydraulic and mechanical properties of the permeable fault zone should depend on the ambient pressure and hence on depth. The depth dependence of valve properties may explain — within the framework of our model — why tremor bursts recur more frequently at the deeper end of LFE areas (Frank et al., 2014; Wech & Creager, 2011). As pressure and temperature increase with increasing depth, both the background and valve perme-

abilities should decrease under pressure. Depending on how permeability changes with depth, a flux that is near-critical for updip valves may well be in the intermediate range for the downdip ones. This may account for the behavior of the Guerrero tremor area, where activity is much more frequent and continuous downdip than updip. With lower permeability, migrations should also be slower. With that in mind, the fast migration rates observed in the sweet spot in Guerrero would imply that valve density might increase in this depth range.

Model parameters that must be explored include the valve characteristics (length, permeability in a state of clogging), the distribution of valves and the total number of valves. However, the valve instability criterion (equation 3.16) constrains how permeability and pressure threshold values can vary. As discussed above, we expect that this condition is met in the pore-pore throat configuration that is relevant to many natural permeable systems (Beckingham, 2017; McDowell-Boyer et al., 1986). Ultimately, a more realistic description of the process should include time-dependent opening and closure processes, but very few constraints on the associated time-scales are available.

We have shown in section 3.5.3 that neighboring valves may act as a single macro-valve in some conditions (Figure 3.12), and this is worthy of a dedicated investigation. Determining which valve spacing and hydraulic conditions enable this behavior is likely to provide key insight into the interaction mechanisms that generate large bursts of activity. One could also allow for some random distribution of valve properties. However, we may draw from our current understanding and predict that the end result would be that only a subset of valves get activated for a given flux. Other boundary conditions than those used here are also worth investigating. For example, the subduction channel may not be connected to a very large permeability medium and allowing for an output flux that depends on pressure may lead to large-scale cyclic activity. In addition, dehydration surges may occur due for example to kinetic constraints on metamorphic reactions or to highly hydrated portions of the downgoing plate crossing the phase-change boundary. Ongoing and future work with similar models will investigate these mechanisms and further explore parametric controls on valve behavior.

3.6.5 Coupling between hydraulic transients and fault slip

An important direction to explore in the future is the coupling between hydraulic transients and fault slip. The latter can be described using a RSF friction parameterization with coefficients that depend on pore pressure (*e.g.*, Luo & Liu, 2019). In such a framework, the main challenge is to constrain the causal relationship between fluid pressure transients, in-channel damage

(valve opening), and slip. A key factor is a high pore pressure because it lowers the fault strength. As discussed in the introduction, most models of RSF fault slip consider that slip comes first and induces a permeability increase through fracturing and dilation. Another perspective to consider is the effect of changes of permeability on frictional stability, which would allow to explore how slip could be influenced by valving in the fault. Unclogging acts to lower pore pressures and hence to increase the fault strength. At the same time, it lowers the effective friction coefficient because it reduces the solid to solid contact area, $i.e.$ the roughness of the fault interface. In this manner, unclogging may induce slip. The fluid pressure component of fault strength may therefore be modulated by the openness of valves because closed valves act as contact points between fracture walls and hence may act as high effective normal stress barriers to slip. The interactions between fault slip, damage and permeability evolution should be explored in depth in coupled physical models.

3.7 Conclusion

In this work, we have developed a model to explain the tremor patterns in subduction zones as symptoms of rapid, strong, localized pressure transients emerging from intermittent fluid transport in a permeable fault interface. We model fluid transport in a 1D permeable channel, fed by a constant input flux. Based on field observations in faults, and laboratory experiments in porous media, we have argued that clogging and un-clogging events occur in the permeable channel, causing large changes of permeability. Based on simple physical and geological arguments, we have shown that such events can alternate in a simple valve mechanism. The strong pressure transient that occurs when a valve opens is able to generate a seismic event, and we have therefore considered valve activity as synthetic seismic activity.

We have found that the behavior of a permeable channel containing valves depends on two valve parameters (pressure ratio $\delta p_c^{break}/\delta p_c^{clog}$ and permeability ratio k_{hi}/k_{lo}). In one case ($\delta p_c^{break}/\delta p_c^{clog} > k_{hi}/k_{lo}$), the channel is in a stable steady-state regime with no valve activity for all values of the input flux. In the other case ($\delta p_c^{break}/\delta p_c^{clog} < k_{hi}/k_{lo}$), the channel is unstable with valves that open and close repeatedly if the input flux is within a well-defined operating range. We have shown that only the latter is relevant to geological systems. Therefore, in this framework, the value of the fluid flux going through a fault zone is a major control on the observed seismicity. For values of the flux outside the operating range, the fault zone is permanently closed or open. For values within the operating range, permeability valves opening and closing in cycles generate permanent activity and intermittent fluid

transport. In this permanently unstable regime, spatiotemporal patterns of modeled tremor emerge from valve-to-valve interactions, and are very similar to those observed in many subduction zones.

Within the operating range for permanent activity, the input flux controls the dynamics of the permeable system. The system is mostly closed for low flux values and mostly open for high values, with time-clustered bursts of activity. For intermediate flux values within the range, the system is mostly open, and closes in quasi-periodic bursts of activity. Furthermore, the activity rate is highest and almost constant through time. Using this model and more elaborate versions of it, one may hope to use microseismicity patterns to probe the hydraulics of permeable fault zones and how they change with time.

APPENDICES TO CHAPTER 3

Contents

3.A Numerical accuracy and convergence tests

Analytical derivation of the diffusion of a pressure ramp

In order to test the accuracy and convergence of our numerical solver for the diffusion equation, we compare the numerical and analytical solutions of the diffusion of a fluid pressure profile that could have been accumulated across a closed valve: a pressure linear ramp from 1 updip to 0 downdip, between x_1 and x_2:

$$p_0(x) = \mathcal{H}(x_1 - x) + \frac{x_2 - x}{x_2 - x_1} \times (\mathcal{H}(x - x1) - \mathcal{H}(x - x2)) \tag{3.18}$$

where $\mathcal{H}$ is the Heaviside function. We choose to test our numerical solver in the case the diffusion of this particular pressure profile as it is analog to the rapid diffusion event at the opening of a valve, and because of the discontinuities in pressure gradient, should be the major source of numerical errors in our solution.

As the diffusion equation is a linear partial differential equation, we express the analytical solution of this problem as the sum of the solution in time of the diffusion of a Heaviside step located in x_1: $\mathcal{S}_0(x) = \mathcal{H}(x_1 - x)$, and of a limited ramp $\mathcal{R}_0$ between x_1 and x_2: $\mathcal{R}_0(x) = \frac{x_2 - x}{x_2 - x_1} (\mathcal{H}(x - x_1) - \mathcal{H}(x - x_1))$.

For a given pressure field $p(x, t)$ defined for x and t in $[-\infty, +\infty]$, following a 1D diffusion equation with diffusivity D:

$$\partial_t p = D\, \partial_x^2 p \quad . \tag{3.19}$$

Using the Fourier transform over the space domain, $\mathcal{F}(p(x,t)) = \tilde{p}(\xi,t)$, the diffusion equation transforms to a first order differential equation.

$$\partial_t \tilde{p}(\xi,t) = -D\xi^2 \tilde{p}(\xi,t) \tag{3.20}$$

with solution $\tilde{p}(\xi,t) = \tilde{p}_0(\xi)\, e^{-D\xi^2 t}$. Transforming back:

$$p(x,t) = p_0(x) * \mathcal{K}(x,t) \tag{3.21}$$

where $p_0(x) = p(x, t = 0)$. Using the inverse Fourier transform, we get $\mathcal{K}(x,t) = \frac{1}{\sqrt{4\pi D t}} e^{\frac{-x^2}{4Dt}}$, the diffusion kernel.

Any transient solution can therefore be computed through the convolution of the initial profile with the diffusion kernel $\mathcal{K}(x,t)$. We apply this method to obtain the analytical solution of the diffusion in space and time of the ramp $p_0(x) = \mathcal{R}_0(x) + \mathcal{S}_0(x)$.

Results of accuracy and convergence tests

Figure 3.A.1 summarizes the results of our convergence and accuracy tests. Both the accuracy and convergence of the numerical diffusion solver are tested by comparing the numerical and analytical solutions for the diffusion of the pressure ramp described above. The error is given by the difference between solutions. The discontinuities of pressure gradient in x_1 and x_2 are responsible for the main error signal, but the physical diffusion smoothes rapidly smoothes it in space. At any given time, the error stays below $4.10^{-}3$ pressure units, for a step of height 1. The RMS error around the valve is at least one order of magnitude lower, demonstrating an overall accurate and stable numerical method.

Convergence is defined as the increase in accuracy of a numerical solution when the discretization it is computed on is refined. Figure 3.A.1 demonstrates the convergence of our numerical scheme in our test case: at three given times after the start of the diffusion, it shows that accuracy increases with finer discretization, or higher number of space steps N_x. As the spatial discretization is refined, the temporal discretization follows using $\delta t = h^2/2D$ to define the time step δt as a function of the space step h.

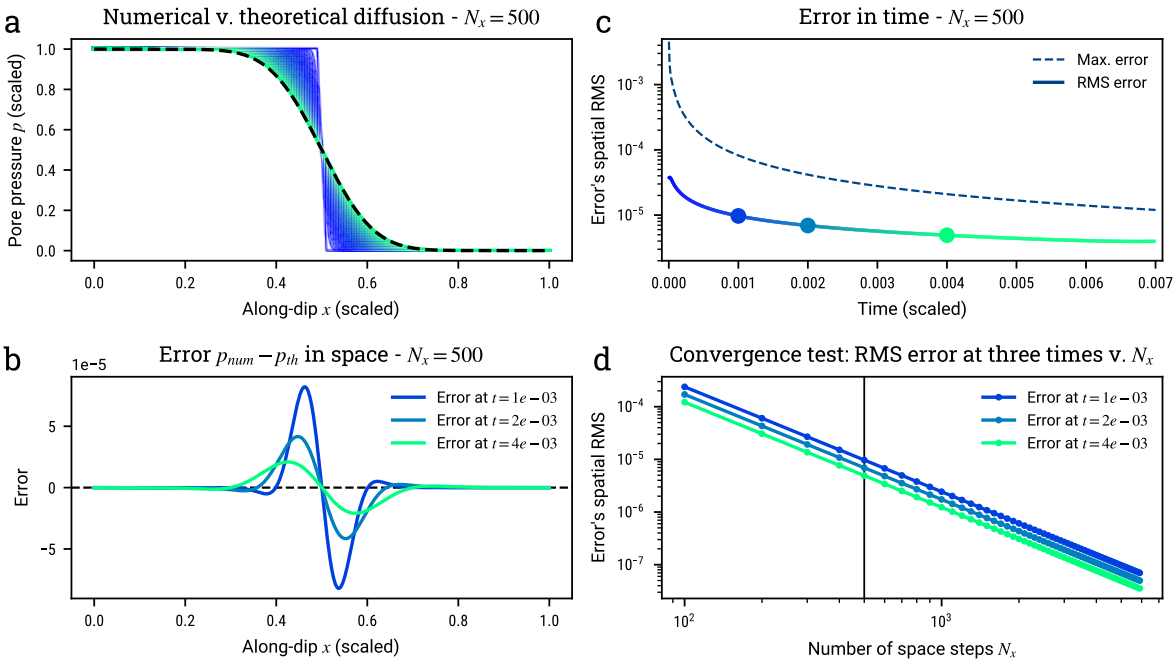

Figure 3.A.1 — *Accuracy and convergence tests, based on the diffusion of a pressure ramp in time and space. (a) Comparison between analytical solution in black dashed line and numerical solution, colored through time. Last time $t = 4.10^{-4}$. (b) Error between numerical and theoretical solutions along the domain, at three given times. (c) Evolution in time of the maximum of the error and root-mean-squared (RMS) error over the domain. (d) RMS error over the domain, at three times during the diffusion of the pressure ramp, as a function of the number of space steps. Convergence of our numerical scheme is shown demonstrated by the increase in accuracy as the space-time discretization is refined.*

3.B Derivation of fracture aperture from permeability values

Using the value of the open permeability of the channel $k = 10^{-14}$–10^{-12}m^2 obtained in Section 3.6.2, and assuming that the permeability is due to fractures oriented in roughly along the plate interface, we can deduce the aperture of the fractures a. Norton and Knapp (1977) formulated the laminar fluid flux into parallel fractures, and found that it can reduce to a Darcy-like form, with a *fracture permeability*

$$k_{fr} = \frac{(2a)^3 n_{fr}}{12} \tag{3.22}$$

where n_{fr} is the frequency of fractures per unit of length across the parallel fracture planes. In a well-preserved outcrop of a subduction channel in the Zagros suture zone (Iran), Muñoz-Montecinos et al. (2021) estimates that around 8% of the surface of the outcrop — both serpentinite matrix and blueschist block — is composed of veins. Assuming we can use this surfacic proportion to directly compute the frequency of fractures in the intact, *in situ* medium, the proportion of fractures can be written $p_{fr} = 0.08 = n_{fr} \times a$, therefore:

$$k_{fr} = \frac{2a^2 p_{fr}}{3}. \tag{3.23}$$

We can then use the values of permeablities mentionned above to find a range of fracture aperture in the medium:

$$a = \sqrt{\frac{3k_{fr}}{2p_{fr}}} \approx 4 \times 10^{-7}\text{–}4 \times 10^{-6}\text{m}^2. \tag{3.24}$$

The fractures in such a medium therefore around the micrometer scale, in the same range as estimated for crack-seal fractures seen in metamorphic rocks (Etheridge et al., 1984; Ramsay, 1980).

Chapter 4

Emergence and control of tremor intermittence and periodicity

---

Contents

4.1 The intermittence of tremor in subduction zones

In subduction zones where it is detected, tremor and low-frequency earthquake (LFE) activity clearly appears to be organized in time. It is intermittent, proceeding in periods of quiescence and episodes of intense activity often called *bursts*, or *episodes* (Brudzinski et al., 2010; Frank et al., 2014; Idehara et al., 2014; Obara, 2002; Rogers, 2003; Shelly et al., 2007b). The strongest episodes of tremor or LFE activity are associated with slow slip events (SSE) on the fault interface (Frank, Radiguet, et al., 2015; Obara et al., 2004; Rogers, 2003; Shelly et al., 2006) and episodes of strong fluid pressure change in the vicinity of the source region of the activity (Frank, Shapiro, et al., 2015; Gosselin et al., 2020; Nakajima & Uchida, 2018; Tanaka et al., 2018; Warren-Smith et al., 2019). The cycle of mechanical and hydraulic stress accumulation and release seems to be the main control on the intermittence of the episodic tremor and slip phenomenon. As fluid is released at depth by dehydration reactions in the subducted oceanic crust (R. N. Anderson et al., 1976), regions of low permeability above the slab can seal fluid around the interface, leading to a high fluid pressure anomaly, observed by geophysical measurements (Calvert et al., 2011; Shelly et al., 2006; Wannamaker et al., 2014) and in exhumed paleo-subduction channels (Angiboust et al., 2015; Behr & Bürgmann, 2021). The locally high fluid pressure leads to decreased effective normal stress on the fault, and therefore lower frictional strength of the plate interface, and slip can nucleate with minor changes of the stress field. As the slip front propagates, fueled and stabilized by the high fluid pressures (Segall et al., 2010), the associated fracturation should open pathways for the fluid to diffuse, along the fault interface or to the overriding plate, towards the surface (Frank, Shapiro, et al., 2015). Fluid pressure in the source region therefore drops as fluid diffuses away in the newly created permeability. As the permeability around the fault heals, a new cycle of pressurization happens again (R. H. Sibson, 2013). This cycle of slip, fluid pressure and strength of the fault interface has been coined *fault-valving* by R. Sibson (1992). The recurrence behavior of large bursts of tremor should therefore be controlled by the dynamics of both the tectonic loading and strength on the interface, and the fluid pressure accumulation and release in the subduction shear zone. Mon-

itoring the characteristics of intermittence of tremor activity on the fault thus provides insight on the hydrological and mechanical state of the fault.

The intermittence of seismic activity can be analyzed using statistical tools describing the temporal clustering of events (Beaucé et al., 2019, 2022; Frank et al., 2016; Idehara et al., 2014; Poiata et al., 2021). In order to characterize it, one can look at the extent with which events occur within clusters compared to the background activity, the distribution size and duration of those clusters, the recurrence delays between them. There is a fundamental difference in the way tremor and LFEs are detected and cataloged. Tremor is a long, non-impulsive signal, and although its source can be located, it cannot be reduced to one or several events, its activity is therefore often cataloged by identifying periods of activity instead of individual events (*e.g.* A. Husker et al., 2019; Wech & Creager, 2008). Low-frequency earthquakes however can perfectly be described as a point process: they are individual, repeating, localized events. They are often considered to be elementary tremor events (Shelly et al., 2006), a direct proxy for tremor activity. In order to characterize the activity of tremor using point process statistical tools, we will work with LFEs catalogs, considering they are just another observational representation of the same phenomenon. While in some locations large bursts of tremor activity recur with a visible and well-defined recurrence timescale, quasi-periodically (Brudzinski & Allen, 2007), in other locations, individual clusters and their recurrence timescales are harder to define because the temporal patterns of activity appear to be scale-free (Frank et al., 2016; Poiata et al., 2021). These different behaviors can be understood statistically as a deviation from a random and independent occurence of events, as event occurence depends on the occurence of events closeby. Clustering should therefore emerge from a process that allows seismic sources to interact and synchronize. The stronger the synchronization, the more clustered in time tremor activity is, thus producing more isolated bursts of activity. With this framework in mind, we think of perfectly periodic burst recurrence as an extreme case of time-clustering: as tremor sources become perfectly synchronized, all sources of a region will activate together, producing well-defined bursts of a characteristic size, that should recur with a periodicity linked to the specific process of energy accumulation and release that drives tremor activity.

The degree of activity synchronization clearly varies between subduction zones, but it is also strikingly segmented along the strike of subduction zones. In the Shikoku tremor zone in Japan, Poiata et al. (2021) shows that seven along-strike segments can be identified in the active tremor region, each characterized by a characteristic temporal clustering of LFE activity. In Figure 4.1, using their LFE catalog, we reproduce their observation by measuring the ex-

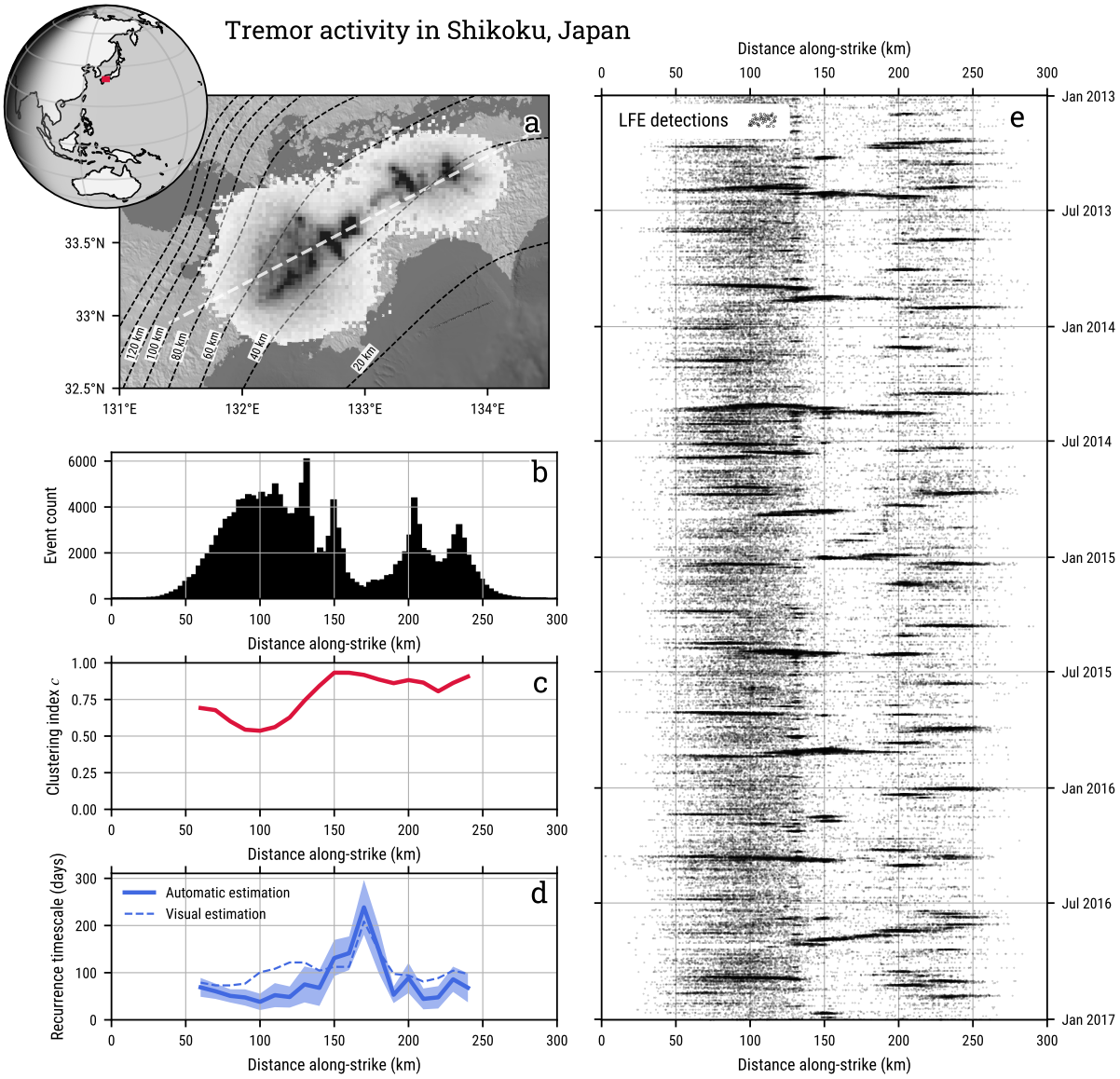

Figure 4.1: Caption on next page.

Figure 4.1 — On previous page. *Patterns of temporal clustering and recurrence of LFE activity, in Shikoku, Japan (2013–2017). (a) 2D histogram of LFE activity in 2.7 km by 2.7 km horizontal bins, colored according to the number of sources projected onto the surface, catalog from Poiata et al. (2021). Depth contours of the slab from Slab2 (Hayes, 2018). The dotted white line indicates a linear fit to the event distribution in space, used as the along-strike direction. (b) Event count binned in 3-km wide bins along-strike, for the full period. (c) Intensity of temporal clustering along-strike, measured by the clustering index c ($c = 0$, no clustering, $c = 1$, all events occur in clusters, see Section 4.2 for details). Bins of 20 km, with a 10 km overlap. (d) Recurrence timescale of clusters along strike, with the same spatial bins as in (c). Clusters of events are detected and their recurrence measured with the algorithm described in Section 4.2. The blue, shaded area around the measurement represents 1-σ interval around the estimated recurrence timescale. The blue dotted line shows a visually estimated recurrence, based on counting the number of high-activity episodes in the observation period. (e) LFE activity along-strike in time, each black dot represents an event. Activity is clearly segmented along strike, in three major segments (see text for details).*

tent to which events cluster in bursts (clustering index c) and the timescale of recurrence of those bursts, in bins of 20 km along the strike of the subduction, with 10 km overlap. More details on the method can be found in Section 4.2. In Figure 4.1a and b, the density of events in space reveals a clear segmentation along-strike. The activity in time and space (Fig 4.1e) and the measured clustering intensity and recurrence timescale (Fig 4.1b and c) allow us to outline three major behavior along-strike. In the western zone (distance along-strike $<$ 125–130 km), activity is characterized by a relatively low level of clustering, a high background rate of events. Bursts are frequent, and recur on timesccales of 2–3 months, although with a strongly variable delay. In the easternmost zone (distance along strike $>$ 180–190 km), activity is much more clustered, and bursts are slightly less frequent, recurring every 3 months in the eastern and western halves of the zone. Finally, in the boundary region between the two zones, the activity is least intense, with a very low background rate, but large transients of activity occasionnaly cross it, every 6 months to slightly less than a year. It is the most temporally clustered activity of the three regions. In the few zones where tremor or LFEs have been cataloged on a wide enough extent along strike, their activity is similarly segmented (Brudzinski & Allen, 2007; A. Husker et al., 2019). In Figures 4.A.2 and 4.A.1, we display the tremor activity in the Cascadia (tremor catalog from Wech & Creager, 2008) and Central American subduction zones (tremor log from A. Husker et al., 2019). In both cases, segments of the subduction zone can be clearly delineated based on the characteristics of the tremor activity they produce: the level with which it is concentrated in bursts and how frequently those recur.

The observed segmentation of LFE and tremor activity patterns along the subduction interface is thought to take its roots in structural heterogeneity and spatially organized dynamic processes in the fault zone (*e.g.* Poiata et al., 2021). On the one hand, the structural properties of the subduction interface, and heterogeneities thereof, crucially determine the distribution of stress and strength on frictional interfaces in the shear zone, and shape how fluid accumulates or circulates in and through the subduction interface. The local geology of the overriding plate (Brudzinski & Allen, 2007), the local dip of the slab, which controls the temperature on the interface (Maury et al., 2018), and the topography of the seafloor on the subducting slab (Ide, 2010) are key parameters controlling the state of stress and therefore the frictional and hydraulic behavior of the interface. These structural characteristics of the slab shape heterogeneous distributions of tremor activity as they affect the distribution of frictional weakness (Cattania & Segall, 2021; Kano et al., 2018; Nakajima & Hasegawa, 2016) and the conditions of fluid circulation in and around the interface: the dehydration rate, how much fluid escapes to the overriding plate or is trapped and channeled along it (Audet & Bürgmann, 2014; Gosselin et al., 2020; Halpaap et al., 2019). On the other hand, dynamic processes like damaging and healing of permeability or friction, or fluid channeling processes can produce heterogeneous patterns of activity on the fault by self-organizing spatially (Halpaap et al., 2019). The memory of previous processes would in this case be the origin of the apparent segmentation of the fault zone, as opposed to intrinsic properties of the components of the subduction system.

Several studies have begun to explore the role of the spatial heterogeneity of frictional properties to explain the different intermittence behavior observed along the strike and dip of the subduction fault (Luo & Liu, 2019; Wech & Creager, 2011). Few studies include permeability and fluid pressure variations to study the role of the hydrological system on shaping patterns of tremor activity (*e.g.* Cruz-Atienza et al., 2018). However, as evidenced in the geological record of subduction channel processes, fluid pressure and permeability are spatially heterogeneous and temporally variable in the tremor source region, through processes of vein opening and healing (Platt et al., 2018; Taetz et al., 2018; Tarling et al., 2021), hydrofracturation (Muñoz-Montecinos et al., 2021) and pressure cycling (Angiboust et al., 2015; Kotowski & Behr, 2019). These strong and sudden variations of permeability and pressure are thought to be closely associated with the generation of seismic waves that are then recorded as tremor or LFEs (Kotowski & Behr, 2019; Muñoz-Montecinos et al., 2022; N. M. Shapiro et al., 2018). In Chapter 3, we have elaborated a model of how fluid pressure transients and variable fluid transport properties of the fault zone can generate complex patterns of

seismicity — temporal clustering, periodic behavior, migrations. We have shown that in this system, the emergence of patterns of activity is based on interactions through fluid pressure transients between elementary permeability valves, which simulate the local changes of permeability and fluid pressure that can be associated with the source processes of LFEs. In this chapter, we will demonstrate how temporal clustering emerges from spatial clustering of our model seismic sources, how hydraulic interactions between tremor sources should be controlled by the local structure of the permeable network in the fault. In turn, we will discuss how the permeability structure and therefore spatial source distribution can be shaped by larger scale structural features of the subduction system, as the topography of the subducted oceanic plate.

4.2 Characterizing clustering intensity and recurrence timescales

In this study, we aim at analyzing seismicity through the prism of how events cluster in time, on which timescales those clusters recur, and how regularly they do so. We design simple measures of the level of clustering of activity, and of timescales of recurrence of clusters of activity, and how variable they are. Those measures are based on an explicit detection of clusters, to avoid the ambiguity of spectral measurements — based on autocorrelation or Fourier analysis of activity time series, for instance (*e.g.* Beaucé et al., 2019) — regarding which specific patterns the measured timescales are related to. In proceeding this way, we assume that the clustering of activity exhibits characteristic scales of cluster size, duration or recurrence delay, which is not always the case for LFE activity (Frank et al., 2016; Idehara et al., 2014; Poiata et al., 2021), or intermittent microseismic activity in general (Beaucé et al., 2019, 2022), where scale-free behavior is often observed. In our case however, it will allow us to assess the degree of synchronization that can be found in activity, assuming that periodicity emerges from an extreme case of synchronization of sources.

The measures and algorithm we will describe in this section are designed to be used automatically and with minimal tuning on both real and simulated catalogs of events, with a focus on being able to characterize both relatively constant and very clustered activity. This will allow us to gain a simple understanding of the characteristics of synthetic seismicity for large batches of simulations (several tens of thousands). Figures 4.2 and 4.3 describe the two steps of this analysis.

4.2.1 Point process description

Based on Lowen and Teich (2005), we introduce elements of the point process formalism that will be used in the rest of the study. In the point process formalism, an event catalog — earthquakes, LFEs, valve openings — can be represented by the function $N_{ev}(t)$, a monotonically increasing function of time t, that increases in steps of 1, when the time is equal to an event time $t = t_i$. The point process can thus be formally written as $\mathrm{d}N_{ev}(t)$. However, a more practical and as complete description of the process is to use the series of event times

$$\{t_i\} \text{ for } 1 \leq i \leq N_{ev}^{tot}, \tag{4.1}$$

where N_{ev}^{tot} is the total number of events considered in the analysed subset. One can also work with the *inter-event times* Δt_i, defined as the time after the previous event

$$\{\Delta t_i\} = t_i - t_{i-1} \text{ for } i > 1. \tag{4.2}$$

The *event count time series* $C_k(\delta t)$, or *sequence of counts*, is another representation of the point process. It counts the number of events in successive and contiguous bins of duration δt, between time $t = k\delta t$ and $t = (k+1)\delta t$:

$$C_k(\delta t) = N_{ev}[(k+1)\delta t] - N_{ev}[k\delta t] \tag{4.3}$$

4.2.2 Characterizing clustering intensity

The objective of this analysis is to quantify the extent to which events occur within clusters, rather than as a more homogeneous process in time. We detect clusters as peaks in the event count time series (see equation 4.3): a count of the number of events in bins of length δt. In our parametrization, peaks of activity are defined as all consecutive bins in which the event count is higher than a given threshold. In order to select more intense periods of activity, peaks are defined as periods during which activity is more intense than 66% of the time, and should therefore cover 34% of the analysed period (Fig 4.2, 4.B.1a and b, 4.B.2a and b): the 34% most active δt-bins. We can define the peak cover f_{peaks} as the fraction of the time covered by peaks, compared to the total time of the analyzed period. Because of the discrete nature of the event counting process, the fraction of the time that is covered by peaks f_{peaks} is never exactly 34% of the time:

$$f_{peaks} = T^{peaks}/T^{tot} \approx 0.34 \tag{4.4}$$

where T^{peaks} is the cumulative duration of peaks in the time series, and T^{tot} the total duration of the time series.

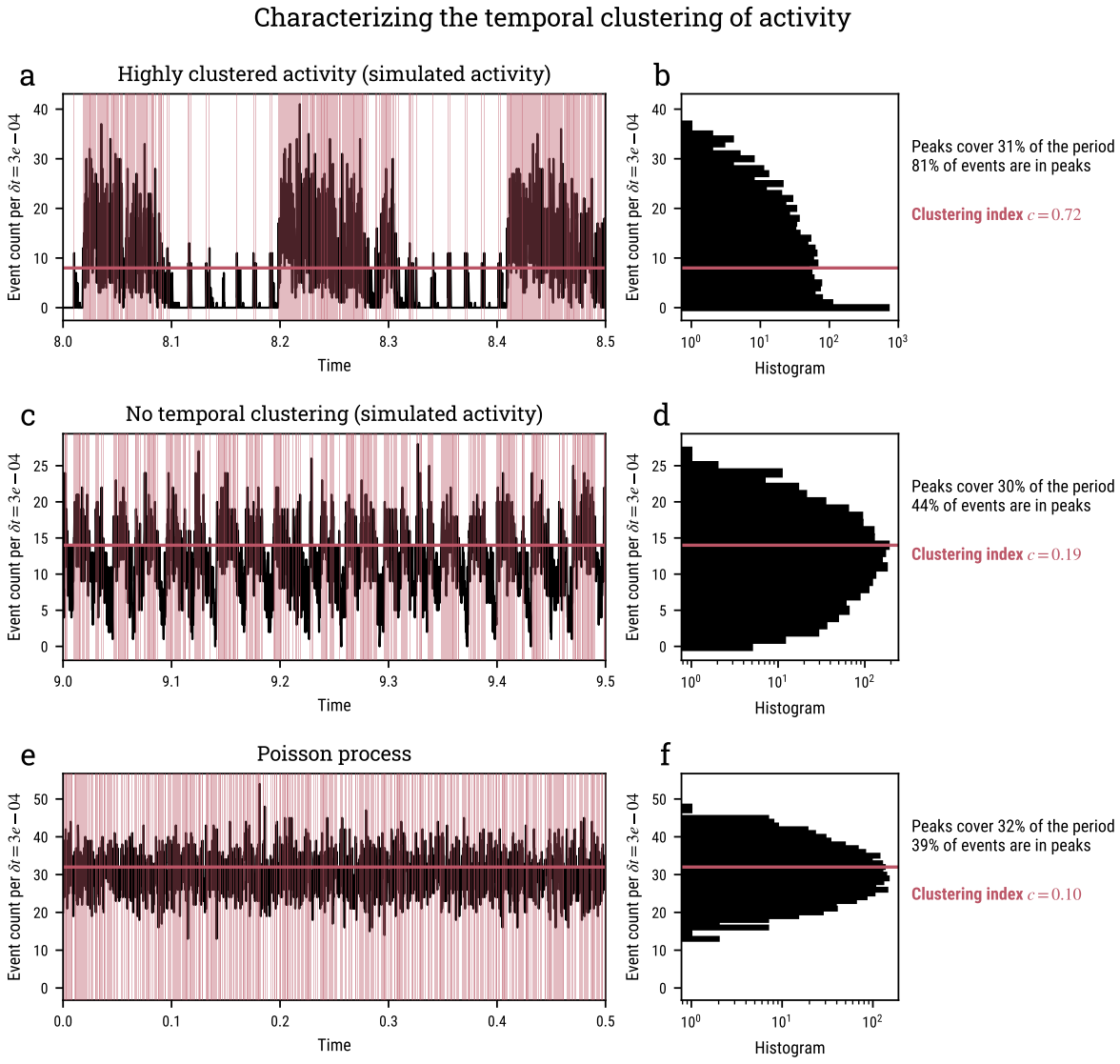

Figure 4.2 — *Clustering analysis of (a), (b) a simulated, highly clustered activity in a clustered valve system with $N_v = 43$ valves ($\overline{d_v} = 1w_v$), $u = 0.3$, under a input flux of $q_{in} = 0.16$, (b), (c) a simulated activity without temporal clustering, in a Poissonian valve system with $N_v = 29$ valves ($\overline{d_v} = 2w_v$), $u = 1.0$, under a input flux of $q_{in} = 0.16$, and (e), (f) a Poisson process, with event rate $r = 30$ events per $\delta t = 3 \times 10^{-4}$ scaled time units. In (a), (c), and (e), the event count time series are represented in black with the threshold defining peaks as the red horizontal line, corresponding to the 66% quantile of the event count distribution, represented in (b), (d) and (f). The fraction of time that peaks represent f_{peaks}, the proportion of events within peaks p_{ev}^{peaks} and clustering index c for each case are listed on the right.*

Although peaks always cover about a third of the studied period, in a clustered time series, most events — more than a third — will occur during peaks, that is 34 % of the time. To discriminate between a clustered and not clustered activity, we will therefore work with the proportion of events that occur within peaks, p_{ev}^{peaks}. When the activity can be described as a Poisson point process, or if the event count is normally distributed around an average value, the events are as much in "peaks" that in the "background", as defined by the 34%-threshold (Fig 4.2c, d, e and f). The number of events in peaks N_{ev}^{peaks} should therefore sum to about a third of events, as peaks are defined the upper tritile of event counts. On the other hand, if the events cluster in time, events should concentrate in peaks. Peaks still cover about 34% of the time series, but most event (at least more than 34% of them) occur in peaks (*e.g* Fig 4.2a and b). A simple measure of clustering can therefore be constructed by mapping linearly the proportion of events in peaks p_{ev}^{peaks} to 0 – 1. We thus define the *clustering index* c: if 100% of events are in peaks, events occur only in clusters and $c = 1$, if only 34% of events occur in peaks, events are more or less as likely to occur in peaks as outside of peaks, the activity is not clustered and $c = 0$.

$$c = \frac{p_{ev}^{peaks} - f_{peaks}}{1 - f_{peaks}} \tag{4.5}$$

where f_{peaks} is the fraction of the studied period that is covered with peaks, that is always approximately $f_{peaks} \approx 0.34$. In Figure 4.2, three cases show values of the clustering index c for two simulations (highly and not temporally clustered) and a Poisson process. We will use the clustering index c as a measure of clustering intensity in observed LFE catalogs (Figure 4.1) and in simulated event catalogs (Section 4.5 and 4.6, Figures 4.7 and 4.9).

4.2.3 Measuring recurrence timescales

In both real cases (Figure 4.1) and simulations (Figure 4.7), clusters of seismic events can exhibit identifiable, characteristic timescales of recurrence. Our aim is to quantify these recurrence timescales, and estimate how variable they are throughout the studied period. To do so, we design an automated analysis that explicitly identifies clusters of events based only on the proximity of their occurence time t_i, classifies clusters based on the number of events they are made of, and finally measures the recurrence of clusters of a same class of size. We will perform this analysis only in cases when the activity is clustered: when more than 50% of events occur in peaks ($c > 0.25$) — peaks are defined as the 34% most active periods of the studied period, see above Subsection 4.2.2. Figure 4.2c to f show two examples of simulations that exhibit no clustering of activity, on which no timescale analysis is therefore per-

formed.

The first step of the recurrence analysis is to identify clusters of events, based on their proximity in time. In order to de-noise the event time time-series, we start by removing all events outside of peaks. We then regroup the remaining events into clusters, by performing a density-based clustering algorithm (DBSCAN, (Ester et al., 1996), *scikit-learn* implementation (Pedregosa et al., 2011)) on their occurence times t_i. The clustering algorithm labels events as isolated or belonging to a cluster based on two parameters: the neighborhood radius (a delay in time, in our case) ϵ and the minimum number of events N_{min} that have to be at a delay of ϵ from one another so that they are considered in the same cluster. Those two parameters therefore provide an estimation of the minimum density of events needed around an event for it to be in a cluster. By iterating from event to event in a dense neighborhood, the algorithm identifies which events are within clusters, and which are isolated. We choose $\epsilon = \max_i(\Delta t_i)/4$, a fourth of the maximum inter-event delay measured in the de-noised event times, and $N_{min} = 10$ for simulated seismicity ($N_{min} = 300$ for the Shikoku case, in Figure 4.1), based on the total number of events in each case. At the end of this step, all events are affiliated to a cluster (labelled) k, or identified as isolated (noise). In order to avoid windowing artifacts, we discard the events of the first and last identified clusters as noise. In the following paragraphs. Figure 4.3a and b depict this first step of the recurrence analysis.

In some cases, the detected clusters can be grouped into identifiable classes of size, and in each class, the clusters recur with a specific delay. In this second step, our objective is therefore to group event clusters based on their sizes S_k, defined as the number of events that belong to it. As cluster sizes sometimes span orders of magnitudes, we perform the DBSCAN clustering algorithm on the logarithm base 10 of cluster sizes. For the DBSCAN parameters, we choose the neighborhood distance $\epsilon = 0.15 * \log_{10}(S_{max}/S_{min})$ where S_{max} and S_{min} are the maximum and minimum cluster sizes in the analyzed case, and $N_{min} = 2$. Those parameters successfully group clusters into classes of different characteristic sizes, while allowing for variability in size within a given class of clusters. At the end of this step, all clusters are labelled as belonging to one or several classes, based on their size. It is more common that one size of cluster only is identified, but in some cases, two (Fig 4.3) or more rarely three classes can be identified with certainty. In the example simulation shown in Figure 4.3b and c, the algorithm detected a class of large clusters (in hot colors) and a class of small clusters (in cold colors).

The final step is to measure the recurrence delay between clusters. Within a class of clusters, we measure the delays ΔT_k between the centroids T_k of contiguous clusters (defined as the average event occurence time within that

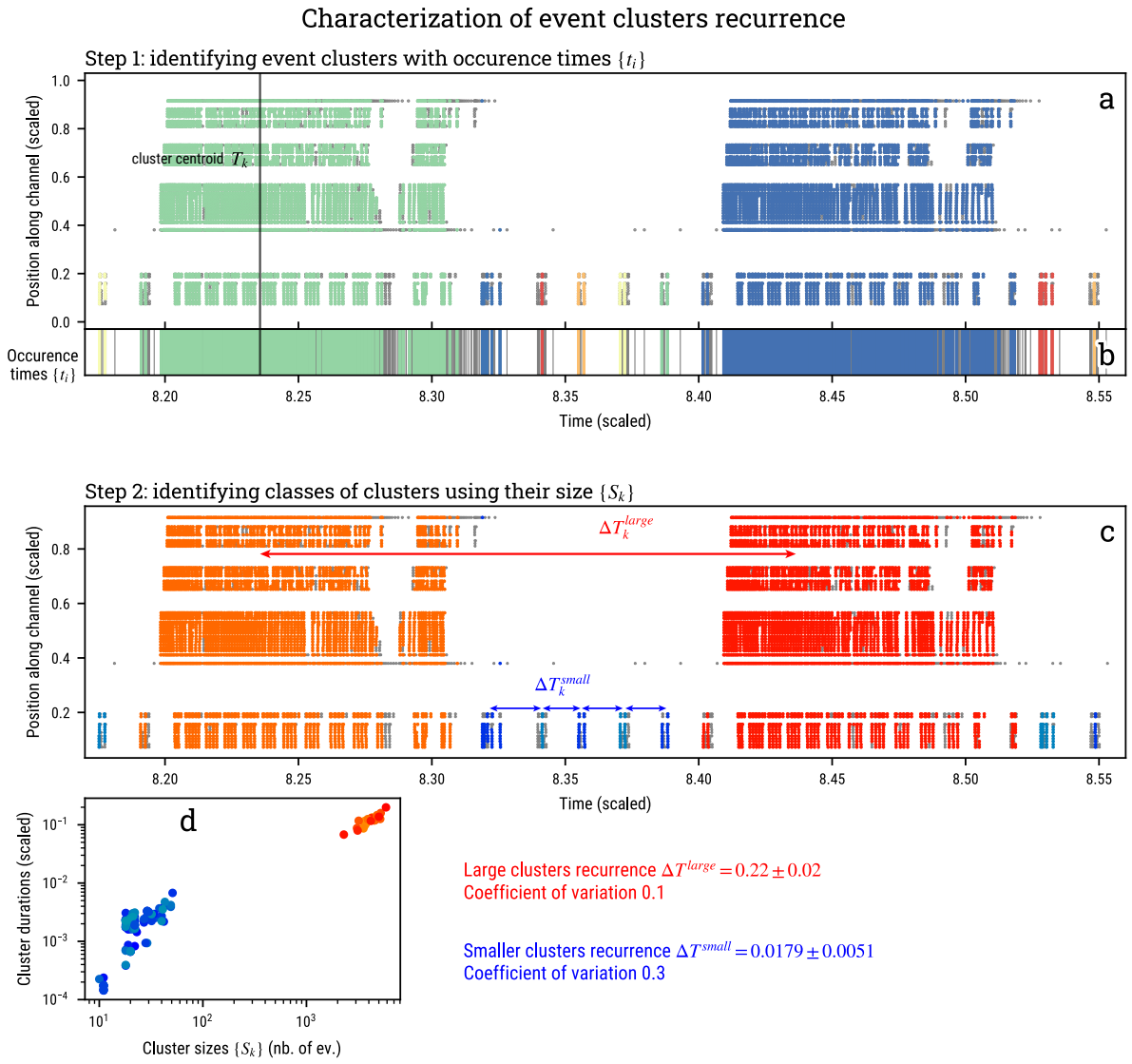

Figure 4.3 — *Recurrence analysis of a simulated, highly clustered activity in a clustered valve system with $N_v = 43$ valves ($\overline{d_v} = 1 w_v$), $u = 0.3$, under a input flux of $q_{in} = 0.16$ (activity count in Figure 4.2a). In a first step, the algorithm detects clusters of events using the occurence times. (a) Time-dip representation of activity, each point corresponds to an events. Events are colored according to which cluster they are labelled into. The grey dots are labelled as noise, either in the de-noising step, or by the clustering algorithm. The clustering algorithm is performed only on occurence times, represented as horizontal lines in (b), with the same color-coding as in (a). The centroid of each cluster T_k is computed as the average occurence time of events that belong to each one of them. In a second step, clusters of events are grouped into classes, based on their sizes. Two sizes of clusters are detected for this simulation, small clusters in blue shades, and large clusters in orange to red shades. (c) Time-dip representation of events, with events colored according to the cluster and class they belong to. The delays ΔT_k between cluster centroids of each class are indicated with arrows. (d) The size-duration distribution of clusters of events. The classifying step only considers the size of clusters.*

cluster). As it appears that both in simulations and real cases the smaller clusters occur more frequently than, and therefore in between, larger clusters, contiguous clusters are considered to be clusters of the same size with no larger clusters occuring in between. In practice, the delays between two clusters is measured only when there are no larger cluster in between (see Figure 4.3c). The average delay $\mathrm{mean}_k(\Delta T_k)$ between clusters of a class gives an estimation of the recurrence timescale for this class, and the standard deviation $\mathrm{std}_k(\Delta T_k)$ allows to estimate how variable it is. The ratio of the standard deviation to the average recurrence timescale $\mathrm{std}_k(\Delta T_k)/\mathrm{mean}_k(\Delta T_k)$, called the coefficient of variation, gives an estimation of how regular the recurrence is, or how periodic it is.

Figures 4.B.1 and 4.B.2 provide additional examples of the clustering and recurrence analysis for the highly clustered, loosely periodic activity of segment 6 of the Shikoku tremor zone (Poiata et al., 2021) and finally an intermediate case, where the simulated seismicity is weakly clustered, and the recurrence is measured with a strong variability.

4.3 A valve model to describe fault zone permeability

As detailed in Chapter 3, Section 3.3, we describe fluid circulation along the permeable fault interface as being focused in channels of higher permeability than the surrounding medium. The channels are one-dimensional, and their permeability is both heterogeneous and dynamic. In this description, the fluid pressure $p(x,t)$ evolves according to a diffusion equation (Equation 3.5), with a diffusivity

$$D(x,t) = \frac{k(x,t)}{\eta\beta\phi}$$

where η is the fluid viscosity, β a fluid-matrix compressibility, ϕ the fault zone permeability, and $k(x,t)$ the permeability of the fault zone. Because we adimensionalize the system, the main control parameter on diffusivity is $k(x,t)$.

Permeability $k(x,t)$ is described in a discrete, binary manner: short segments of the channel have a lower permeability k_{lo} than the surrounding k_{hi}, and can switch between a closed, low-permeability k_{lo} state, to an open, high-permeability $k_{hi} = 20k_{lo}$ state, in response to the pressure differential δp that builds up across the segment. Those dynamic permeability segments are called *valves* and mimic the dynamics of clogging and unclogging of pore throats by colloids or cataclastic fines. In our model, the rapid changes of fluid pressure that follow unclogging of a segment can act as a seismic source or trigger one, and each opening of a valve can be considered an elementary

seismic event. For a detailed description of the clogging/unclogging mechanisms observed in faults, their link to seismicity, and how we model them, the reader can refer to Chapter 3, Section 3.3. In this section, we will succinctly describe the valve mechanism as it is built into our model, in order to explain which valve parameters control its opening/closing cycle, and how.

In our description, the switch between the closed and open state (and *vice versa*) occurs instantaneously, when δp reaches a given threshold. If the valve is closed, it impedes fluid flow around it and δp can increase above the threshold δp_c^{break}. In this case, the permeability unclogs and the valve breaks open, its permeability increases from k_{lo} to k_{hi}. On the other hand, if the valve is open and pressure diffusion across the valve lowers δp to δp_c^{clog}, the permeability clogs, and the valve closes: valve permeability drops from k_{hi} to k_{lo}.

The fluid input rate q_{in} into the system is an essential control parameter that governs if the valve can break open when closed, and close when open. In Chapter 3, we show that two threshold flux values can be derived from the threshold δp using the Darcy law for the flux through a valve in a permanent regime, and that the value of q_{in} relative to those threshold controls if the valve stays closed, open, or opens and closes in cycles when submitted to a constant flux q_{in}. The flux above which a closed valve will eventually close is:

$$q_c^{break} = \frac{\rho}{\eta} k_{lo} \frac{\delta p_c^{break}}{w_v}, \tag{4.6}$$

where ρ and η are the density and viscosity of the fluid. The flux below which an open valve will eventually open is:

$$q_c^{clog} = \frac{\rho}{\eta} k_{hi} \frac{\delta p_c^{clog}}{w_v}. \tag{4.7}$$

In Chapter 3, we demonstrate that in geological media $q_c^{break} < q_c^{clog}$. When $q_c^{break} < q_{in} < q_c^{clog}$, a closed valve will open because q_{in} is higher than the breaking threshold q_c^{break}, and as q_{in} is lower than the clogging threshold q_c^{clog}, the now open valve will eventually close. In this case, the valve will be permanently unsteady, opening when it is loaded enough by the input flux, and closing when the fluid pressure differential across it has diffused to a low enough value to allow it to close, and repeating this sequence in cycles.

The closer the input flux q_{in} is to either threshold values within the unsteady regime range, the closer the valve will be to a permanently closed or open state. For instance, if the flux is just above q_c^{break}, δp will very slowly reach the breaking threshold δp_c^{break}, as the loading speed is comparable with the diffusion speed, allowing fluid to sip through the valve closed permeability at the same time as it slowly loads. When the valve opens, the background flux is so low that the closing threshold is quickly reached. Overall, the valve

Table 4.1 — *Valve parameters for all simulations presented in this chapter*

	Parameter	Value (scaled)
w	Valve width	0.01
k_{hi}	Open valve permeability	1
k_{lo}	Closed valve permeability	0.05
δp_c^{break}	Threshold p difference for opening	0.02
δp_c^{clog}	Threshold p difference for closing	0.0105
q_c^{break}	Flux above which a closed valve can open	0.1
q_c^{clog}	Flux below which an open valve can close	1.05

spends a longer time in the closed state than in the open state when q_{in} is just above q_c^{break}. Conversely, if q_{in} is high, just below q_c^{clog}, the valve takes a much longer time to close when open, and opens very quickly when closed: it spends more time open overall.

Values for valve parameters used throughout this Chapter are listed in Table 4.1. In order to test denser valve distributions than in Chapter 3, we take a valve width w_v twice smaller. Valve width is a critical parameter, as it governs how quickly fluid can sip through the valve, and how strong the fluid flux near a valve has to be to impose a given δp across it. We will show that as two valves of width w_v are close enough, they start behaving as a macro-valve of larger width. Therefore, the width w_v should be considered the elementary width at which the heterogeneity of permeability is defined, but other scales of heterogeneity will emerge in systems of many valves where spatial cluster of valves behave as macro-valves.

Another dimensionless parameter governing the dynamics of a valve is the ratio of closed to open permeability k_{lo}/k_{hi}. As permeability is the only transport property that is variable in space, the value of k_{lo}/k_{hi} describes how quickly fluid pressure diffuses inside a valve relative to outside of it in the high permeability channel. When this ratio is very low, a closed valve behaves like a barrier to fluid diffusion: the effects of the pressure variations outside the valve will dominate the dynamics, and not the diffusion through the valve. In the case where a valve is isolated and the input fluid rate is low and very close to the opening threshold value q_c^{break}, the pressure profile through around and through the closed valve will have time to slowly evolve towards a stable, low flow of fluid through the valve, before eventually opening if $q_{in} > q_c^{break}$. In this case, the diffusion through the valve can be considered an important factor, and the exact value of the ratio matters. However, when several valves are in close proximity, the variations of pressure due to the opening of a neighboring valve will dominate the dynamics. For this reason, we can consider that with $k_{lo}/k_{hi} = 1/20$, closed valves virtu-

ally behave as barriers to the fluid diffusion, and the exact value of this ratio essentially does not influence valve dynamics.

4.3.1 The subduction's hydraulics as a valve system

In the following paragraphs, we describe how to interpret the main parameters controlling seismicity in our model in geological terms, as properties of the hydraulic system in the subduction interface: the criticality of valves, that is the value of the input flux q_{in} relative to the critical opening and closing fluxes q_c^{break} and q_c^{clog}, and the number valves N_v and their distribution.

Valves should be thought of as segments of permeable channels within the fault interface. Their relatively low permeability could emerge from a local reduction in the aperture of fractures or constriction of the cross section of the permeable channel, reducing the the options for the fluid to circulate. Because of this, those segments are prone to clog with the cataclastic fines or colloids that fluid movements carry. The number and proximity of those segments therefore characterizes the heterogeneity or coarseness of the transport properties along the channel in the subduction interface, on a short scale of around 100 m length. As the system is adimensionalized and valves are kept a fixed width in our study, the number of valves N_v represents the proportion of the system that is dynamic, and is thus directly linked with the proportion and scale of the dynamic segments of the permeable system. In reality, the hydraulic structure of the permeable system in the fault interface is at the origin of the heterogeneity of permeability and dynamic properties. The size distribution of impermeable block in the interface, the quality and grain size of the matrix between larger blocks both govern the permeable section and number of available pathways. Those properties are a product of the amount of subducted sediments on top of the oceanic crust, and the fracturation of the upper oceanic crust and overriding plate. More fracturation could for instance result in a larger availability of pathways for the fluid to percolate in or out of the fault interface (Ide, 2010). It would be modelled with a lower number of low-permeability valve segments in the channels along the interface N_v. Valve segments are a short scale heterogeneity, due to fracturing or composition of the interface, which are shaped by larger scale (10–100 km) structural properties of the slab and overriding plate.

Such hydraulic properties like the fracture aperture and size distribution of the finer material in the fault zone is also a fundamental control on how prone to clogging and unclogging the permeability is. Theoretical and experimental studies of clogging in model porous media can help understand how the relative values of the input flux q_{in} and thresholds of opening q_c^{break} and closing q_c^{clog} relate to the structure of the permeable system, and the strength

of the fluid source in the fault zone. For a single constriction of diameter D, the ratio D/d of permeable aperture to particle size d to permeable aperture governs how permanently clogged, intermittently clogged or fully open the permeable constriction is (Souzy et al., 2020). When the constrictions are smaller than 2.5 times the size of particles ($D/d < 2.5$), the constriction is fully and permanently clogged. When the constriction is more than 5 times larger than the particle size ($D/d > 5$), the constriction is fully open, and particles flow through it without clogging it. Finally when $2.5 < D/d < 5$, the constriction clogs and unclogs intermittently, continuously transitionning from a mostly clogged state for relatively large particles compared to the constriction ($D/d \approx 2.5$), to a mostly open state when particles are small compared to the constriction ($D/d \approx 5$). The lower and upper values of the D/d ratio are very similar to the threshold values of flux that allow valve to open or close, as they delimit a range of conditions in which the permeability can be dynamically opened or closed. In reality, the particles carried by the flow in the subduction can be micronic to submillimetric cataclastic fines (Han & Hirose, 2012), or colloid aggregates (Amagai et al., 2019), of micronic scales. In Chapter 3 Section 3.6.2, we found a base permeability for the channel of k_{open} 10^{-14}–10^{-12}m^2, which corresponds to a fracture aperture of about 10 microns (see Appendix 3.B for details on the calculation). Only the finer particles can act in the valving mechanism, but the scales are arguably right to allow for the permeability to be dynamic.

The length of the clogged segment is also directly linked with the pressure it is necessary to apply to unclog the segment: the longer the clog, the higher the pressure needs to be to unclog it (Jäger et al., 2018). Finally, it has been experimentally shown that the input flux of a particle-laden fluid into a porous medium controls the intermittence of its clogging, displaying clear regimes for which at low flux values, the medium remains clogged, and progressively and intermittently unclogs as the fluid input rate increases, until it is fully open (Bianchi, Thielmann, et al., 2018). This behavior is once again very similar to the regime diagram drawn in Chapter 3, Figure 3.5. In subduction zones, the fluid flux into the dynamic permeable channels is controlled by the dehydration rate (source) and amount of fluid that escapes to the overriding plate (sink). The value of q_{in} relative to the critical fluxes that allow opening and closing of valves in our model is thus a very direct description of those phenomena described in porous media, in which clogging and unclogging are controlled by a competition between the hydraulic stressing rate of the input fluid source, and the weakness and healing capabilities of the low aperture segments, resulting from the relative size and shape of the pathways and fines that can clog them.

4.4 Characterizing source interaction in a two-valve system

4.4.1 Valves interact through pressure transients

In order to understand how valves interact through pressure transients and which parameters control how strong and fast this interaction is, we first design systems with two valves, and observe how they evolve. Valves are at equal distance from the center of the channel $x = 0.5$ in normalized length units. The valve width is $w_v = 0.01$, and the distance between them is d_v, expressed as a function of w_v (Fig 4.4a).

In Figure 4.4, we describe a simulation in which a system with two valves at a distance of $d_v = 0.8w_v$ is submitted to a low flux $q_{in} = 0.13$ — close to q_c^{break}, the threshold flux above which closed valves will eventually open. Independently of the initial conditions, we observe that the cycles of pressurization and release of both valves — as seen through δp the pressure difference across each of them — eventually synchronize (Fig 4.4b). When the permanent regime is reached, the two valves open and close synchronously, with a short delay between the first valve's opening (downdip valve) and the second valve's opening (updip valve). The events associated with each opening therefore occur in a two-event burst, recurring every valve cycle.

As we zoom in on the last opening sequence of the simulation (Fig 4.4c), we observe that the updip valve is affected with a short delay by the downdip valve opening and the fluid flux pulse that it triggers. δp across the closed updip valve suddenly rises due to the fluid influx behind it, and as it is already close to failure, it is sufficient to bring it to open. It should be noted that in Chapter 3 Section 3.4.2, we have shown that this triggering interaction does not necessarily occur from the downdip valve towards the updip valve, but that in a two-valve system, the effect of a valve opening updip creates a transiently low pressure in front of the downdip valve, that can trigger its opening.

The triggering interaction between valves is therefore carried by the fluid pressure field in the permeable system. Because it is a diffusive system, the further the triggering pressure transient has to travel to the neighboring valve, the slower and weaker the interaction between the valves. In other words, the distance between valves d_v should be an essential control on the interaction strength and synchronization in this two-valve system.

The sensitivity of valves to small variations of pressure around them is also directly related to their criticality: their being close or far to the threshold of δp that will make them change state — open or close. The amount of time

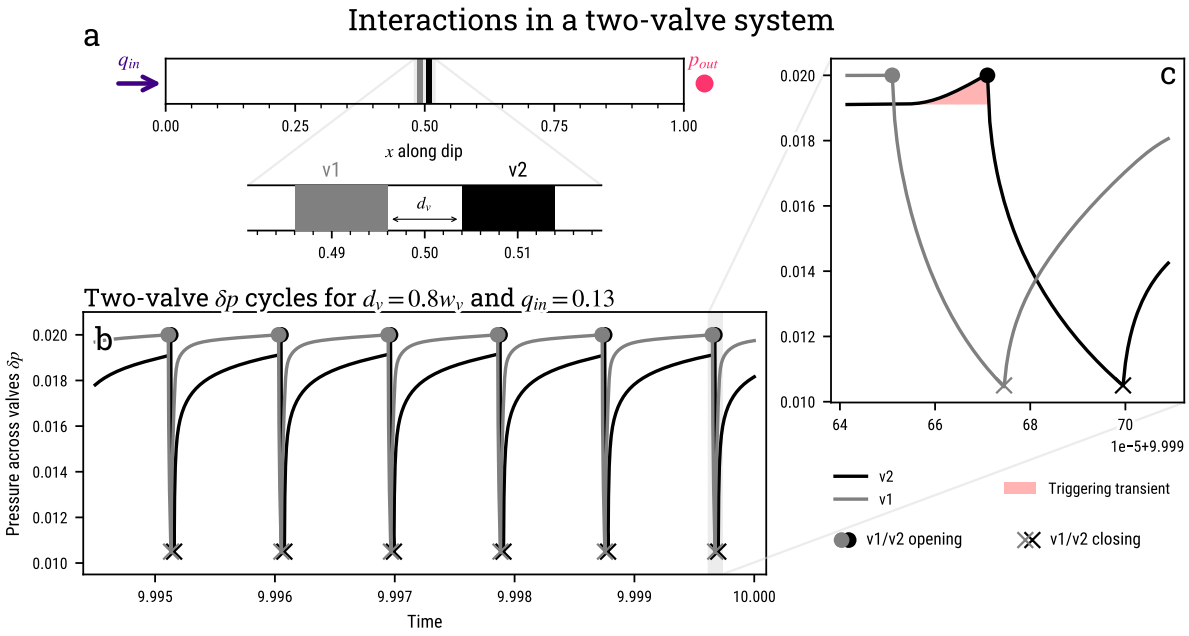

Figure 4.4 — *Interactions in a two-valve system. (a) A system with two valves (v1 and v2) spaced by $d_v = 0.008 = 0.8w_v$, submitted to a constant flux $q_{in} = 0.13$, and a constant pressure output $p_{out} = 0$. (b) Cycles of fluid pressure accumulation and release pressure are shown with the time-series of the pressure difference δp across v1 and v2. Closing and opening events are indicated, and occur when δp reaches a pre-defined threshold. (c) As v1 opens first and when v2 is critically stressed, the pressure transient its opening produces (in red) triggers the opening of v2, with a short delay.*

δp at the valve spends close to threshold is controlled by the value of the input flux q_{in}. The closer q_{in} is to critical values q_c^{break} or q_c^{clog}, the closer to thresholds the valves are. In Figure 4.4b and c, the input flux is $q_{in} = 0.13 \approx q_c^{break} = 0.1$ and it is visible that both v1 and v2 tangentially approach the threshold δp for breaking. Thus, the closer q_{in} is to critical values, the stronger the interactions between two valves should be, as the smallest change of pressure is likely to trigger opening of the valve when it is closed, and closing of the valve when it is open.

4.4.2 Valve spacing controls activity synchronization

In order to characterize the influence of the intervalve distance d_v on the synchronization of valve activity, we design two-valve systems with various d_v, spanning $d_v = 0$ to $20w_v$. All systems are submitted to a constant flux, and we characterize the event recurrence timescales when the permanent regime is reached. Various values of flux are tested for all systems, and in Figure 4.5, we display the results of this experiment for three domains of q_{in} which share similar behavior, and for the full range of intervalve distances.

As the system is noise-free and the valves are identical, during the permanent regime of all simulations, the events occur in identical, repeated se-

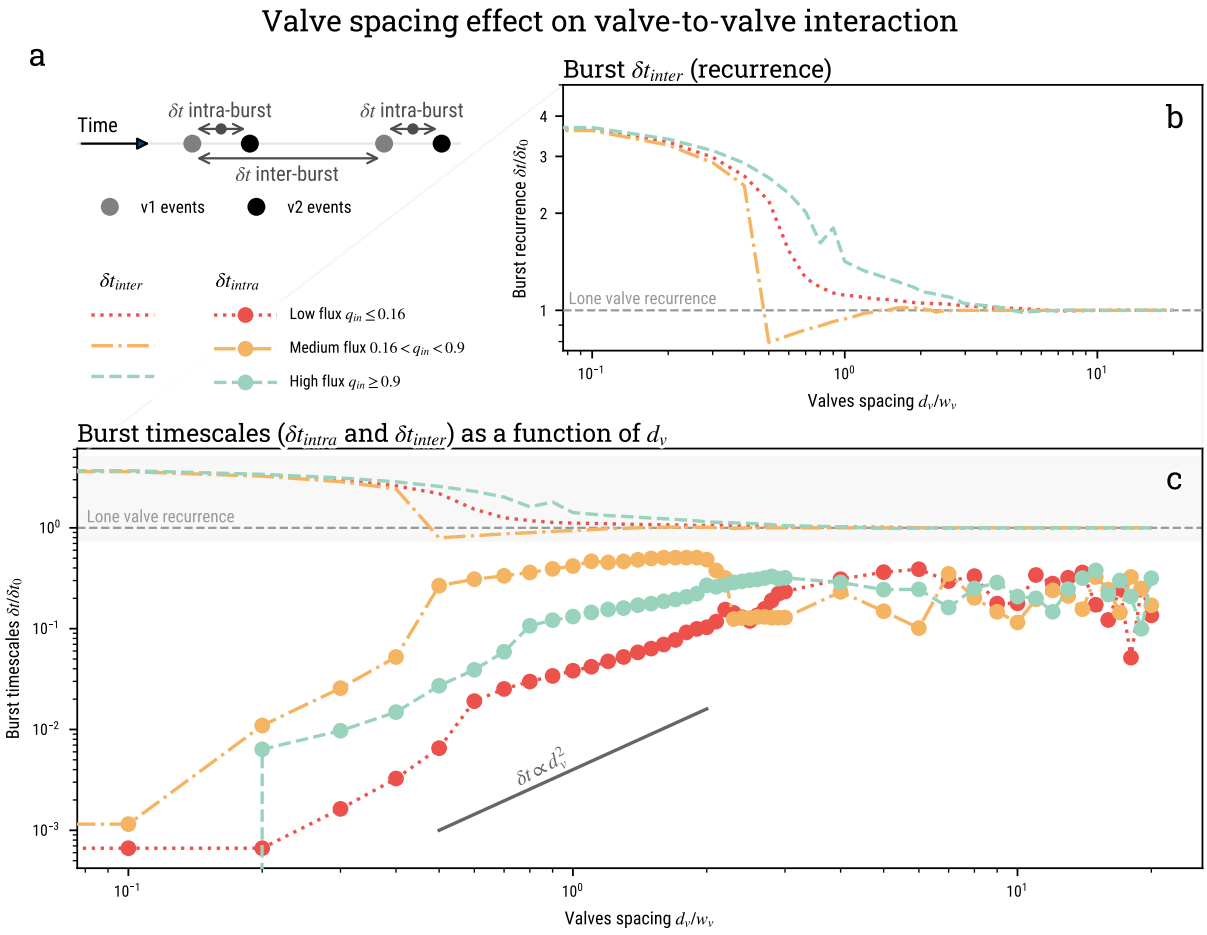

Figure 4.5 — *Effect of valve spacing on valve-to-valve interaction. (a) Two timescales describe a two-event burst: δt_{intra} is the delay between events in the burst, and δt_{inter} is the recurrence delay of the burst. In (b) and (c), we observe how δt_{inter} (no markers on the line) and δt_{intra} (circle markers) evolve as a function of valve spacing for low (red, dotted line), intermediate (yellow, dash-dot line) and high (green, dashed line) flux values. Both timescales are normalized by δt_0, the period of activation of a valve submitted to the same flux. For sufficiently large valve spacing, valves do not interact and act as isolated valves. As valves get closer, events get closer, and the bursts are less frequent.*

quences (Fig 4.5). Two timescales therefore characterize the activity: δt_{intra} the time interval between the first and second opening of the two-event burst, δt_{inter} the time interval in between the beginnings of two neighboring bursts — which can be thought of as the burst recurrence time. In Figure 4.5b and c, we show the evolution of these two timescales. The first observation is that at large distances ($d_v > 5w_v$, Fig 4.5b), bursts — therefore events for each valves — occur with a recurrence corresponding to an isolated valve: the cycle of either valve is not affected by the other valve. In Figure 4.4b and c, both δt_{intra} and δt_{inter} are normalized by δt_0 the period of the cycle of an isolated, identical valve submitted to the same flux.

When the distance between the valves gets shorter, the interaction between valves becomes stronger, producing two effects on the valves' cycle. First, in Figure 4.5c, we observe that the closer the valves are (the lower d_v), the shorter δt_{intra} is. As valves get closer, the triggering transient travels faster from one valve to the other, and therefore, the events are closer in time. Second, in Figure 4.5b, we observe that as valves get very close ($d_v < 0.5w_v$ for $q_{in} = 0.11$), δt_{inter} increases for lower and lower d_v. This means that bursts recur with a longer and longer delay, and that overall, valves produce less events per unit of time. As the inter-event time is so short for such close proximity between valves, the two valves together can be considered as a *macro-valve*. Interestingly, in Figure4.5, we see that for all fluxes, the *macro-valve* consistently activates with about 4 times the delay of an isolated, elementary valve. We reported the emergence of similar macro-valving behavior in systems of many strongly-interacting valves in the previous chapter (Chapter 3, section 3.5.3).

To summarize, a valve interact with its neighbor through pressure transients, and the effect gets stronger as the valves are closer together. This interaction has two effects: *1)* valves synchronize, their activation (opening) is closer in time the closer the valves are together, *2)* the closer the valves, the longer the period of their cycle, and therefore the longer the recurrence period of the two-event bursts. In the extreme case where the valves are almost touching, the synchronization is so strong that they can be considered as a twice wider macro-valve, with a longer period of activation than any of the single valve that it is made of.

Although this experiment was mainly meant to test the interaction strength based on inter-valve distance, a comparison of the curves corresponding to each input flux range in Figure 4.5b and c allows to assess the effect of the q_{in} on the interaction strength. In Fig 4.5b, we see that for low and high q_{in} ranges (red and green curves), which are closer to critical opening and closing thresholds, the deviation of δt_{inter} from the reference cycle period (grey line) happens for valve spacings that are wider than for the medium flux range

(yellow curve). Indeed, when submitted to a medium flux range, valves are further away from criticality most of the time, and they have to be closer neighbors to interact with a similar intensity as when they are closer to criticality. The same observation can be made for the delay between events in bursts δt_{intra}: shorter valve spacings are necessary in the medium flux range to reach a similarly short delay between events in bursts, compared to the high and low, closer to criticality, flux ranges.

In reality, a permeable channel in the fault zone should have many of those valves, distributed according to complex spatial distributions. The elementary interaction we describe here will be key to explain how a given distribution of valve, and therefore structure of the permeable channel, is conducive to the emergence of intermittence, clustered seismicity, or even quasi- or perfect periodicity of bursts.

4.5 Effects of valve proximity in complex valve systems

4.5.1 Statistical description of valve distributions

In order to represent the heterogeneity and dynamic of permeability of a fault channel, we design valve systems with a number of identical valves of width w_v, distributed in more or less regular fashion. Valves are distributed using a Weibull distribution for the inter-valve distance d_v. The probability density function of the distribution is

$$p(d_v) = u \left(\frac{d_v}{d_0}\right)^{u-1} \times \exp\left((-d_v/d_0)^u\right), \tag{4.8}$$

and its mean

$$\overline{d_v} = d_0 \Gamma\left(1 + \frac{1}{u}\right). \tag{4.9}$$

where d_0 is the scale parameter, u the shape parameter of the distribution, and Γ is the gamma function.

We use the Weibull probability distribution because it allows for a range of different distributions within a single and continuous framework. Depending on the value of the shape parameter u in equation 4.8, it can generate valve distributions that go continuously from perfectly regular to highly clustered spatially. Indeed, when $u \to +\infty$, the distribution tends toward a Dirac in d_0, for which all valves are separated by $d_v = d_0$: it is a regular distribution. When $u \to 0$, the Weibull distribution tends to a power law distribution $p(d_v) \propto d_v^{-1}$. In this case, valves form clusters, most of the time, they are spaced with very small d_v, and rarely, a large spacing is drawn, separating

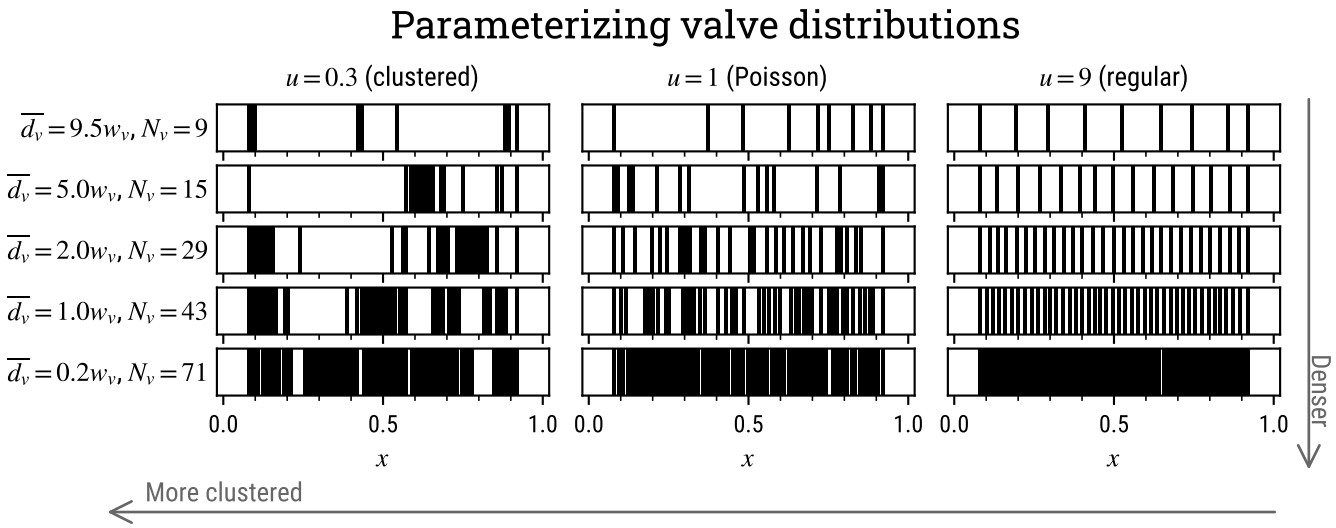

Figure 4.6 — *Parameterizing valve distributions. Valve distributions are created by drawing valve distances d_v using a Weibull distribution. Using the theoretical mean, we can control the valve density, or average valve distance in the domain $\overline{d_v}$. The shape parameter u allows to control how clustered or regularly-spaced valves are in space.*

valve clusters. Finally, for $u = 1$, the Weibull distribution reduces to an exponential distribution $p(d_v) = \exp(-d_v/d_0)/d_0$, of mean $\overline{d_v} = d_0$. In this case, the number of valves in a segment of given length follows a Poisson distribution, valves are more or less homogeneously distributed over the system, even if at random. As a rule of thumb, this distribution produces clustered point distributions for $u < 1$, and more homogeneous and regular valve distributions for $u \geq 1$.

We construct a valve distribution by specifying a buffer zone on each sides of the system, common for all distributions, then by drawing inter-valve distances using the chosen distribution (u and chosen $\overline{d_v}$), and then distributing them on the regular space grid, by simply rounding down the intervalve distance to the closest discrete distance possible. We also ensure that the spacing of the last valve to the one before that is not too far from the target intervalve distance, so that all valves do not end up near the input for the most clustered valve distributions. Figure 4.6 describes the density-clustering (N_v–u) space of distributions available to us using this technique.

4.5.2 Valve distribution control on activity

In Section 4.4.2, we showed using a simplified system that the interaction between two valves gets stronger and faster as they are closer together. As

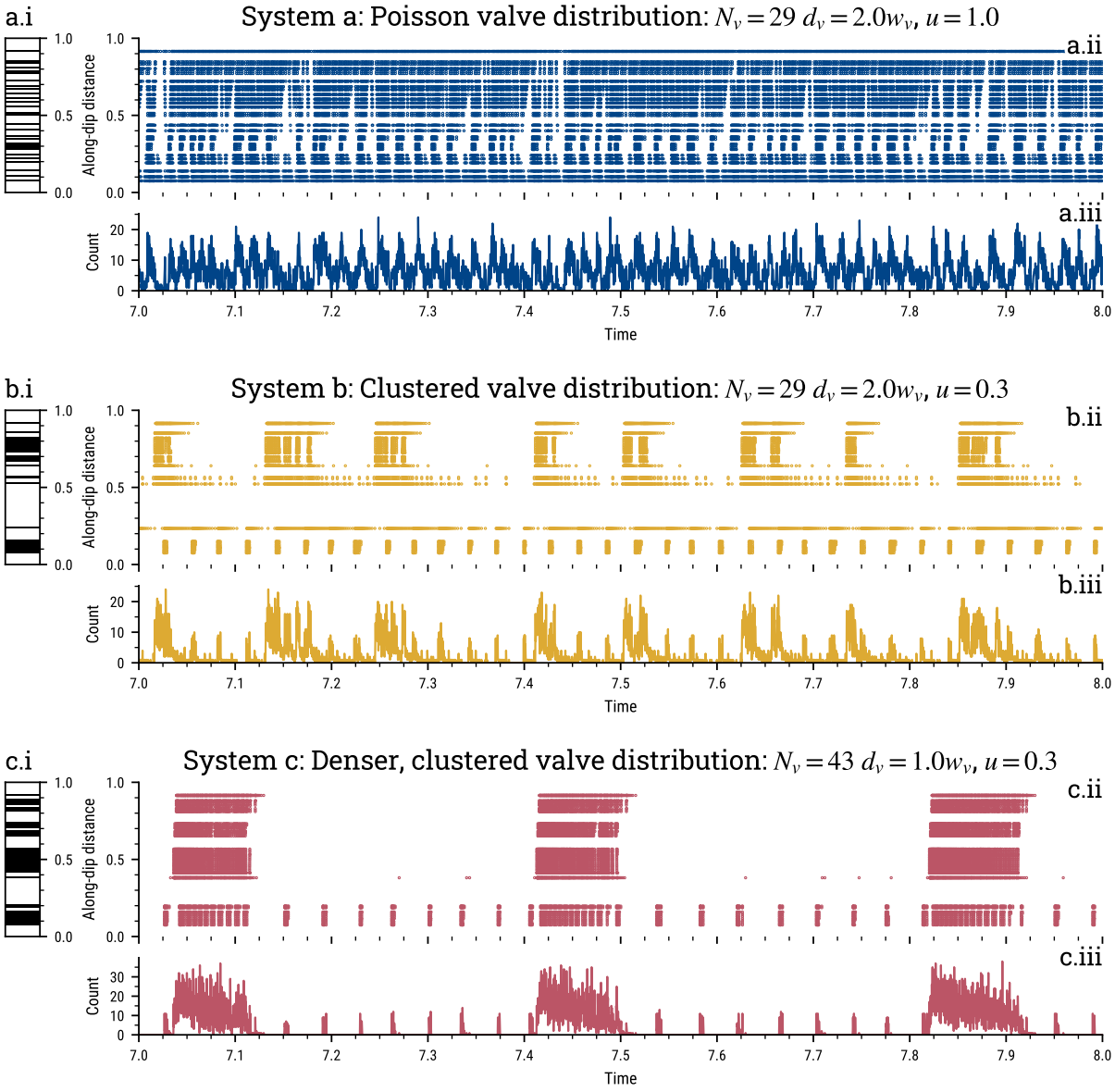

Figure 4.7 — *Synthetic tremor activity for three different valve systems: (a) a "Poisson" system (Weibull $u = 1$, $N_v = 29$ valves), (b) a clustered distribution ($u = 0.3$, $N_v = 29$), (c) a denser, clustered distribution ($u = 0.3$, $N_v = 43$). Panels (a.i), (b.i) and (c.i) represent the valve distributions along the channel. Panels (a.ii), (b.ii) and (c.ii) display the activity along the channel in time, in a time-space diagram where each dot represents the location and time of an opening event. Panels (a.iii), (b.iii) and (c.iii) show event count (per bin of $\delta t = 2.5e-4$) time series. The denser and more clustered the valve system, the more clustered and periodic the activity, and the longer the timescales of recurrence. In other words, the closer the valves get in the system, the more synchronized and long-period the resulting activity seems to become.*

valves get closer, events occur with a shorter and shorter delay after one another, and these two-event bursts recur with a longer and longer period. At this point, we could make the hypothesis that this effect should persist in a more complex system: the denser the valves in the system, the stronger and faster the interactions between them, and therefore, the more clustered in time and long-period the activity should be.

In order to investigate this, we run a basic test using three different valve systems, submitted to the same input flux $q_{in} = 0.13$ (near the critical flux allowing valves to open, $q_c^{break} = 0.1$). The results are presented in Figure 4.7. System a (Fig 4.7a.i, a.ii, a.iii) has $N_v = 29$ valves, an average inter-valve distance of $\overline{d_v} = 2w_v$, and a disorder parameter of $u = 1$, corresponding to an exponential distribution of valve distances, it can be considered rather homogeneous. The activity it produces is clustered in time, occuring in bursts, with however less variability than the other two systems. Indeed, System b (Fig 4.7b.i, b.ii, b.iii) shares the same number of valves and average valve spacing as System a ($N_v = 29$, $\overline{d_v} = 2w_v$), however the higher spatial clustering of valves ($u = 0.3$) creates dense patches of valves in the system, where valves are locally much closer together than the average d_v. The resulting activity is more intermittent, it proceeds in clearly separated bursts — of two sizes, in two different regions of the domain. The burst recurrence is quite variable, but is obviously longer than for bursts produced in System a. Finally, System c (Fig 4.7c.i, c.ii, c.iii) is as spatially clustered as System b ($u = 0.3$), but with more valves ($N_v = 43$, $\overline{d_v} = 1w_v$). It is the system where on average valves are the closest, and also with the most places where locally valves are very close. The activity it produces is the most clustered of the three: it proceeds in bursts of two sizes, almost without any activity otherwise. They occur almost periodically, with a more constant, longer period than System b.

This test is therefore consistent with our hypothesis. The closer the valves get, either due to spatial clustering (lower u) or more numerous valves (higher N_v, lower $\overline{d_v}$), the more synchronized their activity is: they all activate at the same time during bursts, and are inactive outside of those episodes. In addition to it, the activity seems to also display longer and longer recurrence timescales as the valves are closer and closer locally in the system.

4.5.3 Parameterizing valve proximity

In order to systematically confirm that the closer the valves get locally, the more they are interacting, and therefore the more clustered and periodic the activity gets, we design a series of simulations aimed at understanding how activity is shaped by the valve distribution, representing the heterogeneity of

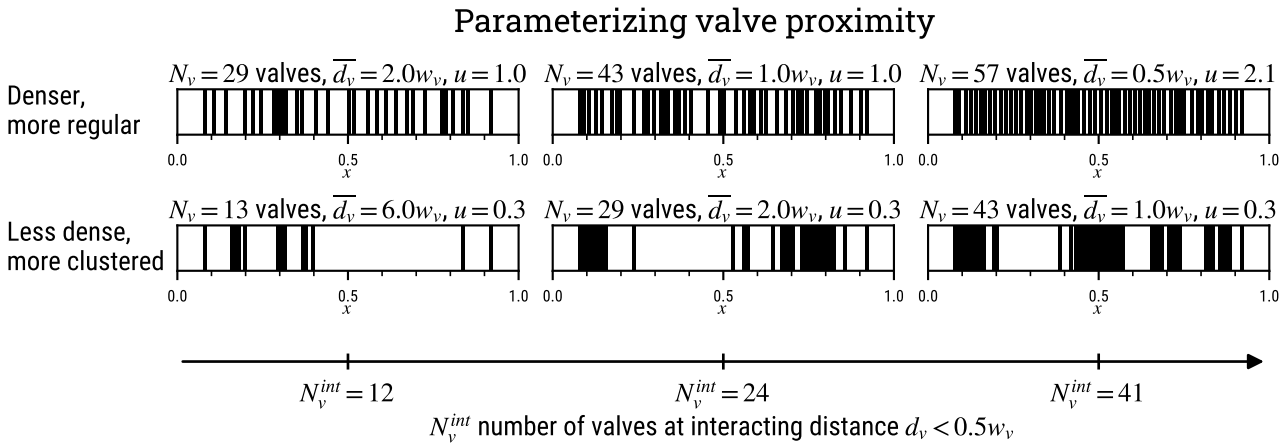

Figure 4.8 — *The number of interacting valves N_v^{int} is a measure of how much valves are close from each other in a valve system, either owing to the density of the system (N_v, $\overline{d_v}$), or to the spatial clustering (u). As valves get closer, they interact more, and N_v^{int} should allow to capture the consequences in the most straightforward way.*

transport properties in the fault channel. We investigate the effects of two parameters describing the valve distribution: the disorder parameter u of the Weibull probability distribution, describing how clustered valves are in space, and the number of valves N_v (bijectively linked to the average inter-valve spacing $\overline{d_v}$), describing how dense the valve distribution is.

We run more than 42,000 simulations, for distributions described by $N_v = 9$–71 ($\overline{d_v} = 9.5w_v$–$0.2w_v$, 16 values), $u = 0.2$–9 (8 values). For each (N_v, u) (128 theoretical distributions), we draw 30 valve systems to average out the effects of specific valve arrangements on the overall behavior. In all systems, valves have identical width, closed permeability and opening/closing δp thresholds (Table 4.1). Each system thus defined (3840 total) is submitted to different values of input flux $q_{in} = 0.11$–1.04 (11 values), with a focus on values of the flux close to the thresholds allowing valve opening ($q_c^{break} = 0.1$) and closing ($q_c^{clog} = 1.05$).

As we showed that valves interact more strongly when they are closer, both a higher level of spatial clustering in the system and a higher valve density put more valves at interacting distance. Systems with higher N_v (lower $\overline{d_v}$) and lower u (more clustered systems) should therefore produce a more clustered activity, allowing the emergence of characteristic recurrence scales. In order to highlight this effect, we will represent the results along a single parameter describing the number of interacting valves in a system: N_v^{int}, which is the number of valves that have a neighbor closer than $0.5w_v$, on either side.

The value of $d_v < 0.5w_v$ as an interacting distance is chosen on the basis of the the two-valve experiments described in Section 4.4: in Figure 4.5c, it is visible that valves interact very strongly at distances lower than $d_v = 1w_v$ and that this effect is even clearer for $d_v > 0.5w_v$. We choose the lower bound, $d_v < 0.5w_v$ for the interacting distance. When the activity characteristics are plotted along N_v^{int}, we capture the effects of the local proximity of valves in the system, either due to spatial clustering or overall density (see next Section). Figure 4.8 shows systems with different N_v^{int}, showing that a similar number of valves can be at interaction distance when the system is dense and not very clustered, and when it is less dense but with stronger spatially clustered valves.

In the next section, we describe the results of those simulations: how a higher number of interacting valves N_v^{int} and specific values of the input flux q_{in} in the system allow for the emergence of temporally clustered and periodic activity.

4.6 Emergence and variability of synchronization in complex valve systems

For all simulations, we measure:

- the activity rate, measured by the average event count per valve in the time period,
- the extent to which activity occurs in clusters with the clustering index c ($c = 0$ events are not clustered at all, $c = 1$ all events occur within clusters),
- and the recurrence timescales of clusters in cases when the activity is clustered in time.

The details of how the latter two measures are computed can be found in Section 4.2. In Figure 4.9, the results are displayed as a function of the number of valves at interacting distance, N_v^{int}. The results displayed in Figure 4.9a, b and c are for all valve distributions, but limited to a low value of flux $q_{in} = 0.13$, close to the critical value $q_c^{break} = 0.1$. Three examples of activity are shown to illustrate the trends visible in the Figure (Fig 4.9d, e and f).

4.6.1 Patterns of activity clustering with high valve proximity

We first observe that as N_v^{int} increases, more valves interact in the system, and they produce less events per valve (Fig 4.9a). This is consistent with the observation made in Figure 4.5, where the period of valve cycles in a two-valve system is longer and longer as they are closer together, and interactions make them act synchronously, as larger, macro-valves.

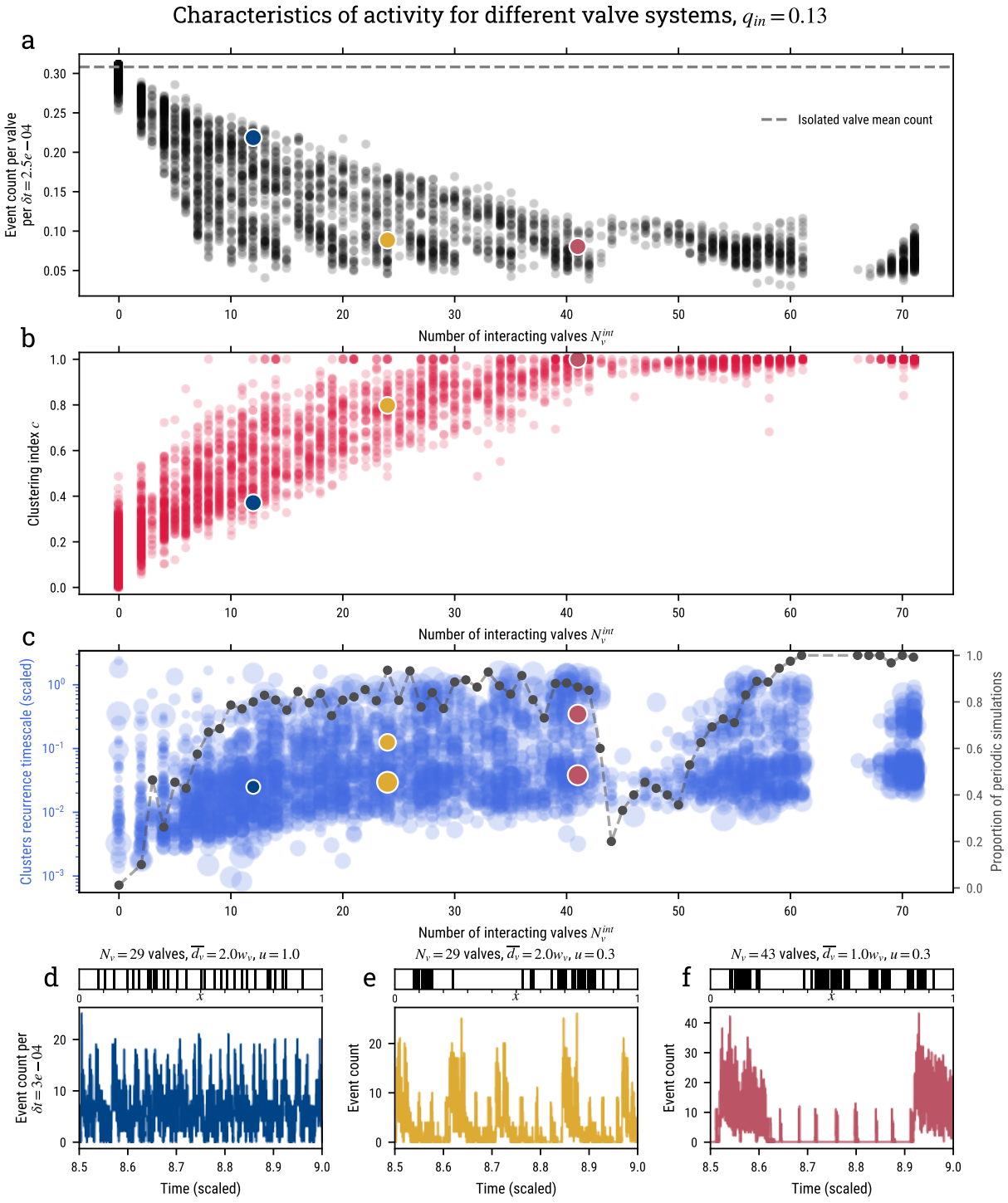

Figure 4.9: Caption on next page

Figure 4.9 — *Intensity, clustering and recurrence timescales of activity for varying levels of interaction in complex valve systems. Results for $q_{in} = 0.13$. (a) Average event count per valve, measuring the activity rate, for varying levels of interactions between valves, parametrized by the number of interacting valves N_v^{int}. (b) Level of activity clustering measured with the clustering index c, as a function of N_v^{int} (c) The detected timescales of cluster recurrence are represented as dots, as a function of the number of interacting valves. The size of the dot scales with the variability of the measured recurrence, estimated as the ratio of the average to the standard deviation of the inter-cluster delays, in the given simulation. The dotted line represents the proportion of periodic simulations (see Section 4.6.2 for details) for each value of N_v^{int}. In panels (a), (b) and (c), the circled, colored dots show the values of clustering and recurrence for three valve systems with displaying increasingly strong valve interactions, as shown in (d), (e) and (f). The three bottom panels show the valve distributions for three systems (top) and a short period of activity represented as the event count in time for three systems (bottom), submitted to $q_{in} = 0.13$.*

As expected, as the number of interacting valves N_v^{int} increases, the activity is more and more clustered in time (Fig 4.9b). When the system is mostly made of interacting valves (high values of N_v^{int}), the activity happens quasi-exclusively in bursts ($c = 1$).

4.6.2 Valve proximity controls reccurence timescales and periodicity of activity

The results for the measurements of recurrence timescales are shown in Figure 4.9c. For each simulation that displays a high level of clustering ($c > 0.25$), recurrence scales are measured as the average of delays ΔT_k between clusters of similar size. The ratio of this average to the standard deviation of the measured delays $\mathrm{mean}_k(\Delta T_k)/\mathrm{std}_k(\Delta T_k)$ gives an estimate of how stable in time the recurrence is, how periodic the activity is. We consider that when $\mathrm{mean}_k(\Delta T_k)/\mathrm{std}_k(\Delta T_k) > 2$, activity is nearly periodic. The recurrence timescale and its variability are shown with the blue dots, which size scales with the stability ratio. The proportion of periodic simulations (as previously defined) for systems sharing a given N_v^{int} is shown with the dotted gray lines.

As more valves interact, valve systems tend to produce a more periodic activity, with longer and longer periods. When most of the system is made up of interacting valves (N_v^{int} above 20–30), several size of clusters and recurrence timescales are detected in the simulated activity, both short- ($T \approx 3 \times 10^{-2}$) and long-period ($T \approx 3 \times 10^{-1}$).

The last three panels (Fig 4.9d, e and f) show examples of activity in three systems of increasing N_v^{int} (same simulations as in Fig 4.7).

It is noteworthy that the periods of activity bursts (5×10^{-3} to 1 scaled time

units for most detected periods) that emerge are orders of magnitude longer than the period of an isolated valve cycle (8.1×10^{-4} scaled time units for an isolated valve with $q_{in} = 0.13$). Figure 4.9 shows that the collective behavior of valves built upon their proximity is key to the emergence of those long periods.

This behavior is governed by the number of interacting valves in the system, but also by the connections between strongly interacting patches of valves in the system. Indeed, it might seem counterintuitive to see that the $x = 0.5$–1 cluster in Figure 4.7b is larger than any clusters in system c in Figure 4.7c, and that it nevertheless produces a shorter period. This is because as system c is denser overall, the smaller valve clusters behave like a large cluster of macrovalves, and generates a longer periodicity as the whole system activates.

The simulations presented in Figure 4.9 span the whole possible space of valve distributions, but are limited to a single value of the input flux, $q_{in} = 0.13$. However, we obtain identical trends along N_v^{int} for different values of the input flux, especially around the critical values q_c^{break} and q_c^{clog}, where valves spend most of the time close to breaking or clogging, and are therefore very sensitive to small variations of pressure, favoring interactions between them. When the flux values are further from those thresholds, valve systems produce an overall less clustered, with much shorter and less stable recurrence of event clusters. In the next paragraphs, we describe the influence of the input flux q_{in} on the characteristic activity that systems produce.

4.6.3 Input flux control on criticality and emergence of synchronization

The experiment described in Section 4.5.3 was designed to test the effects of the heterogeneity of the system in terms of permeability and dynamic structure. Activity style, however, also depends on the fluid input rate q_{in}. For all systems, we test 11 values of the fluid input rate that allow for permanent valve activity ($q_{in} = 0.11$–1.04), to have a vision of how flux affects the synchronization of activity in complex valve systems. Flux values sample densely the flux regions that should show the strongest variation, closer to thresholds of opening $q_c^{break} = 0.1$ and closing $q_c^{clog} = 1.05$. In Figure 4.10, we show measures of activity rate, clustering intensity and recurrence timescales of bursts for systems in which the valve distribution allows a high level of interaction ($N_v^{int} > 20$). We reproduce and generalize the results that we found for a Poissonian distribution of $N_v = 29$ valves (30 different sampling with the same parameters), in Chapter 3, Section 3.5.1, Figure 3.10. The closer q_{in} is to critical values of the flux, the closer valve systems are to staying closed

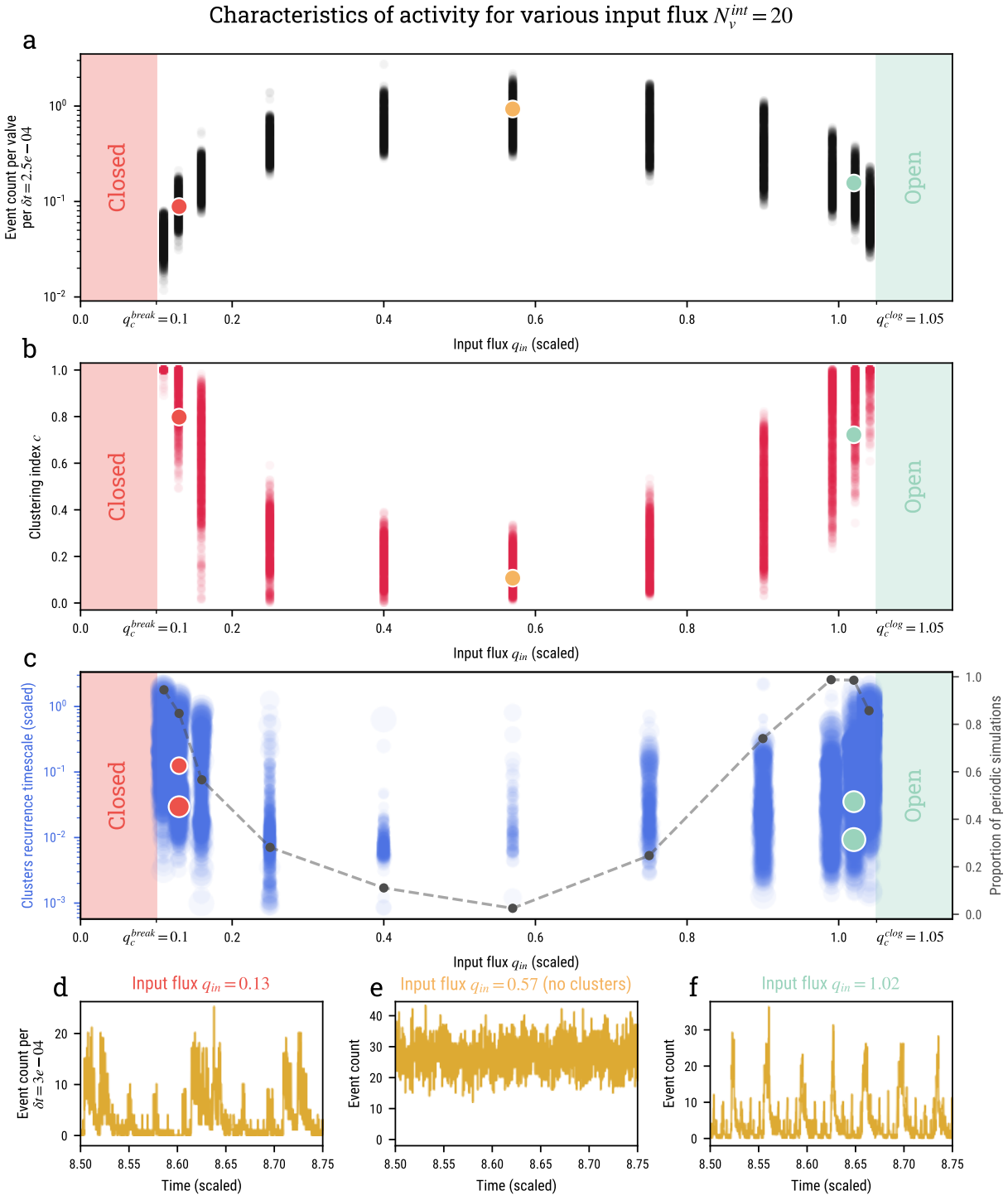

Figure 4.10 Caption on next page.

Figure 4.10 — *Clustering and recurrence timescales for different values of the input flux q_{in}, restricted to highly interacting valve distributions $N_v^{int} > 20$. (b) Level of activity clustering measured with the clustering index c, for different values of q_{in}. (c) The detected timescales of cluster recurrence are represented as dots, as a function of q_{in}. The size of the dot scales with the variability of the measured recurrence, estimated as the ratio of the average to the standard deviation of the inter-cluster delays, in the given simulation. The dotted line represents the proportion of periodic simulations (see text for explanation) for each value of q_{in}. In panels (b) and (c), the domains where the flux value prohibits valve activity are shown with red (all valves closed) and green (all valves closed) patches. The circled, colored dots show the values of clustering and recurrence for three values of increasing values of the input flux, as shown in the three bottom panels. (d) shows the activity for a low, near-critical flux $q_{in} = 0.13$, (e) shows the activity for an intermediate, far from critical input flux $q_{in} = 0.57$, (f) shows the activity for a high flux, near critical $q_{in} = 1.02$. The three simulations are performed with a clustered system ($u = 0.3$) with $N_v = 29$ valves ($\overline{d_v} = 2w_v$), the same system displayed in Figures 4.7b and 4.9e.*

($q_{in} \approx q_c^{break}$) or open ($q_{in} \approx q_c^{clog}$): the average event count per valve is therefore lower (Fig 4.10a), the activity more clustered (Fig 4.10b) and more periodic, with longer periods (Fig 4.10c). When valves in the system witness a flux that is further from critical conditions, they open and close rapidly, without time to interact and build synchronicity: activity is high, less clustered, less periodic, or with shorter periods.

4.7 Discussion

4.7.1 From observed to simulated tremor activity patterns

The spatio-temporal patterns of intermittence of tremor in subduction zones gives the most direct access to minute deformation and hydraulic processes occuring within or around the subduction interface (*e.g.* Bernaudin & Gueydan, 2018; Cruz-Atienza et al., 2018; Luo & Liu, 2019). In this work, we propose a simple representation of the hydraulic processes in the fault based on elementary fault-valve mechanisms, in order to investigate the role that hydraulic properties play in shaping the intermittence of tremor. The main characteristics of tremor we seek to reproduce and understand are the emergence of the strong temporal clustering of events (Frank et al., 2016; Idehara et al., 2014; Poiata et al., 2021), the long, quasi-periodic recurrence of tremor bursts (Brudzinski & Allen, 2007; Frank et al., 2014; A. Husker et al., 2019; Poiata et al., 2021), and the spatial disparities of those two phenomena along the strike of tremor source regions in subduction zones, at scales of tens to hundreds of kilometers (Brudzinski & Allen, 2007; Poiata et al., 2021). Those

patterns have been interpreted by some authors as resulting from the dynamics of slip in conditions of near-lithostatic fluid pressure and heterogeneity of frictional properties of the fault interface (*e.g.* Luo & Liu, 2019; Wech & Creager, 2011). Our work aims to understand how strong transients of permeability and fluid pressure could be a key element in the origin of intermittent seismicity patterns, as hinted by the geological record (Angiboust et al., 2015; Muñoz-Montecinos et al., 2021; Taetz et al., 2018; Tarling et al., 2021).

The model of we developped reproduces such patterns of seismicity thanks to the interaction between elementary seismic sources, through fluid pressure transients in the permeable fault interface. As a nearby valve activates, a given valve will be more likely to activate itself, depending on the strength of the pressure transient that reaches it, and how close it is to activating: how high and close to the opening threshold the fluid pressure gradient is across it at the moment when it feels the activation of its neighbor. In a subduction zone, we assume that many segments of the channels that transport fluid along the interface behave as valves, and that they should interact. When those segments are close enough together, they will activate in unison, by triggering neighbors when activating.

In experiments with complex valve systems, we showed that temporal clustering of activity and long-timescale periodicities emerge when enough valves are in close proximity. The temporal clustering and periodicity of activity in the model can therefore be understood as resulting from the interaction between many neighboring valves that synchronize their activity, behaving as a whole macro-valve which activity is composed of the collective and repeated activation of all the valves that constitute it. As more valves are in close proximity in the system, they form larger and larger spatial clusters (Fig 4.7b, for $x > 0.5$), and clusters of clusters (Fig 4.7c). This can either be due to a high proportion of the system being made of valves (high number of valves N_v, low inter-valve distance $\overline{d_v}$), or the valve system being spatially clustered (parametrized with u, shape parameter of the Weibull distribution). We defined a proximity index that describes how close valve gets in the system: the number of valves at interacting distance N_v^{int}. Under the right flux conditions, valve clusters behave as macro-valves, and we showed that as the number of interacting valves N_v^{int} increases, the valve activity is more and more temporally clustered, and the observed recurrence delay of activity bursts gets longer and longer (Figure 4.9). As the system is adimensionalized and valves are kept a fixed width, N_v^{int} represents the proportion of the system that is in interaction, and is thus directly linked with the scale of the heterogeneity of permeability, with the proportion and scale of the dynamic segments of the permeable system. The spatial scale of the dynamic segment built out of interacting valves seems to therefore directly control the period-

icity: the larger the macro-valve, the longer its loading and unloading cycle will be, and therefore the longer the recurrence of its activation. We see that it is the scale of the heterogeneity of permeability and dynamic properties of the system that seems to govern the seismic behavior of the system. In our simulations, we also showed that the fluid input rate is an essential control on how temporally clustered and periodic the activity gets in a system. More than the absolute value of the input fluid rate q_{in}, it is its value relative to the threshold values of flux that defines the regime the valve is in: permanently closed when the flux is so low that valves cannot unclog $q_{in} < q_c^{break}$, permanently open when the flux is so strong that valves cannot close $q_{in} > q_c^{clog}$, and sustained cycles loading, opening, unloading and closing when the flux allows valves to close and open $q_c^{break} < q_{in} < q_c^{clog}$. When q_{in} is within the regime that allows valve activity, and it is near the threshold values, we showed that valves spend a long time near the critical δp that will trigger opening or closing (Figure 4.4), maximizing the chance that a minute change of pressure from a nearby valve activation will activate the given valve. Therefore, the role of the value of the input flux q_{in} in the fault zone relative to valve properties can be seen as a competition between the loading rate and the strength of valves. The closer to threshold valves are, the weaker they are, and therefore the more susceptible they are to be triggered. In summary, values of q_{in} near the threshold values put valves in a sweet spot for them to synchronize, build temporal clustering and periodicities based on interactions. The closer they are to critical conditions, the more sensitive they are to smaller changes of the pressure field around them. In those conditions, the effective size of the macro-valve increases, as the effective interaction distance increases. A more critical hydraulic system in those terms will therefore produce a more clustered and periodic seismicity, with longer recurrence of activity bursts (Figure 4.10).

Tremor activity observed in subduction zones displays high levels of clustering. In the Shikoku tremor zone for instance (Fig 4.1), we measure a clustering index mostly superior to $c = 0.5$, with wide ($\approx$ 50 km) regions where $c > 0.8$. Although there is no question that the dynamic of slip on the interface should play a role in shaping the long-wavelength spatial patterns activity, our work provides a simple, alternative and complementary framework to interpret those patterns as resulting from the dynamic and structure of the hydrological system: how strong the fluid pressure sources are relative to the strength of permeability valves, how heterogeneous and dynamic the permeability is in the fault interface. The high levels of clustering $c > 0.5$ in Shikoku can be interpreted in two ways, through the lens of our model:

- The valve system that could model the reactive permeability of the fault zone should allow a high level of interactions $N_v^{int} > 20$, either owing

to its density or spatial clustering of valves, segments of low, dynamic permeability that can interact together. For the valve widths we showed in this chapter $w_v = 0.01$, this corresponds to at least 20 % of the system behaving in a valve-like manner, with significant spatial clustering of those elementary segments.

- Only near-threshold valves can produce clustering indices on the level measured in Shikoku ($c > 0.5$). The input flux q_{in} should therefore be quite close to the opening threshold q_c^{break} or to closing the threshold q_c^{clog} of valves in the system. For the former, flux is relatively low, the permeability of valves in tremor zone should therefore be nearly shut on average, and opening with slight variations of fluid pressure. In the latter case, the flux is high, the permeability of the system is nearly fully open, and closes at the slightest local drop of fluid flux. It seems less realistic to have a fully connected, high-flow plumbing system at such depths in the fault-zone, where the permeability seems to close instantly after opening (Tarling et al., 2021). We will therefore assume that q_{in} should be low, close to q_c^{break}, and valves must be mostly closed, and open only in rare bursts.

In the next sections, we first discuss how those parameters can be linked with the hydraulic properties of the subduction interface and how the hydraulic properties of the subduction interface described by N_v^{int} and q_{in} can be inherited from the structure of the oceanic plate that is subducting, and then, how long-wavelength variations of topography of the subducting plate in Shikoku can result in the segmented seismicity we observe there, by shaping the hydraulic dynamics of the fault on such a scale.

In the rest of this discussion, we will use the link developped previously in section 4.3.1 to interpret how the hydraulics of the fault zone are shaped by large-scale heterogeneities of the subducting plate structure.

4.7.2 The hydraulic segmentation of subduction faults

Long-wavelength geophysical observations in subduction zones, of magnetic or gravimetric anomalies for instance, reveal that subduction zones are structuraly segmented on a scale of tens to a hundred of kilometers. This segmentation seems to emerge mostly from the topographic and internal structure of the subducting oceanic plate (Bassett & Watts, 2015; Blakely et al., 2005; Shillington et al., 2015; K. Wang & Bilek, 2014; Wannamaker et al., 2014), which displays heterogeneous structures — ridges, seamounts, fracture zones — on such a scale. As rough terrain enters the subduction, it modifies stress, damages both the subducting and overriding plate, carries more sediments into the subduction interface, and modifies the fluid pressure conditions.

Those factors can directly affect how seismicity manifests in the rough segment by modifying the mechanical properties of the fault zone. And indeed, the structural heterogeneity of the subducting plate often correlates with the spatial variations of seismicity along strike in subduction zones, on a very similar scale as the observed topographic features of the incoming seafloor (Bassett & Watts, 2015; Blakely et al., 2005; Shillington et al., 2015; K. Wang & Bilek, 2014). K. Wang and Bilek (2014) and Bassett and Watts (2015) show that the subduction of a topographically rough feature (seamount or ridge) of an oceanic plate causes zones of aseismic slip, or a larger amount of small earthquakes compared to large earthquakes (larger b-values). As the topographic high plows into the overriding plate, it locally scars the fault zone, which becomes more damaged, and weaker frictionaly, it also generates high fluid pressure conditions, by eroding and carrying into subduction fluid-filled sediments in the accretionary prism, or simply because of its thicker section of hydrated oceanic crust.

Similarly, the topographic features of the subducting seafloor have a strong impact on the hydraulics of the subduction interface. In a study of the spatial and temporal behavior of tremor in the Shikoku subduction, Ide (2010) interprets the striations formed by areas of high, and frequently recurring tremor activity are due to the scars of subducting seamounts, enhancing fault zone permeability and therefore fluid availability in this zone by channeling more fluid along the interface. Different parameters can impact the flux of fluid channeled through the interface, q_{in}. The amount of fluid that is freed and channeled in the interface depends on the importance of the dehydration source, which depends on the volume of crust and sediments that are dehydrating through metamorphic reactions. The thicker the crust, because of a seamount or ridge, the more volume of hydrated crust will dehydrate at depth, increasing q_{in}. The local geometry of the plate also changes how important the dehydration rate is deeper along the slab, and can modify q_{in} (Maury et al., 2018). The fluid input rate into channels also depends on the importance of sinks, where the fluid escapes to the overriding plate. It depends on the permeability contrast between the along-dip/along-strike directions in the fault plane and the direction across the fault plane towards the overriding plate. This contrast would be lowered if rough terrain has strongly damaged the overriding plate: more fluid can escape the interface through fractures in the sole of the overriding lower crust or mantle wedge, decreasing in turn the amount of fluid circulating in the channel, and thus the value of q_{in}.

Additionally, subducting topographic highs also have a strong impact on the structure of the permeable system, and therefore on the number of valving segments N_v, their proximity N_v^{int}, and how close to clogging/unclogging

threshold they are, that is how close q_{in} is to the critical fluxes for opening and closing of valves. A subducting seamount might for instance strongly damage the neighboring of the fault, increasing the number of fluid pathways around the faults, therefore lowering the overall number of valves. The damaging and milling process in the fault could also generate more fines, and favor clogging, thus increasing the value of q_c^{break} higher and closer to the local fluid flux q_{in}. Finally, the criticality of valves can depend on how much silica colloids can precipitate in the fault zone and clog the permeability, which critically depends on the temperature, and therefore on the local geometry of the subduction (Audet & Bürgmann, 2014). Contrary to the input fluid rate, it is harder to map the actual effects of fracturing, block size distribution and sediment content in the fault zone onto the criticality of valves or their spatial distribution. More in situ and geologic studies of the architecture and dynamics of the fault zone are needed to understand how dynamic the permeability in the interface is, and how it relates to the local structure of the subducting plate. We can however use the patterns of seismicity that we observe in Shikoku to link them with structural features of the subducting plate, in order to bring some insight on how the hydraulic system is structured, and how it shapes seismicity in turns.

4.7.3 Hydrological processes shaping tremor intermittence in Shikoku

From Figure 4.1, the Shikoku tremor zone can schematically be divided into three segments based on its activity. Two segments (segment 1 and 3) at each along-strike extremity ($d < 130$ km, and $d > 200$ km, Fig 4.1, Fig 4.11), characterized by a high level of clustering and relatively short timescales of recurrence, and a buffer segment in between, segment 2, characterized by low, almost exclusively clustered activity, with a longer period. In Figure 4.11, we see that the along-strike extent of those segments and spots of high tremor activity within them is quite similar to the size of seamounts on the seafloor of the Philipine plate, or the ones observed in the accretionary prism (Yamazaki & Okamura, 1989), of a about a few tens of kilometers. The alignment of the Kinan seamount chain with the segmented tremor zone along the convergence direction could indicate that such structures on the subducting slab, or their lasting effects on the medium as they plow at depth, are the main factor shaping the segmentation of activity in the Shikoku tremor zone.

In the next paragraphs, we will interpret the characteristic intermittence observed in those segments of tremor zone first as being mainly governed by criticality of the permeability valves in each segment, and then as a symptom of the valve structure of the interface primordially.

4.7.3.1 Criticality conditions

We can interpret the segmentation of intermittence in Shikoku as a symptom of how close valves are to threshold. For simplicity, we consider that flow conditions are such that the metamorphic flux is relatively low, just above to the threshold for which valves can simply bear the pressure gradient it imposes on them, and not break: $q_{in} \approx q_c^{break}$, and that transport properties and valve distribution do not vary significantly along-strike.

If the valves are relatively similar across the whole zone, the lower activity, higher temporal clustering and clearer-defined, longer periodicities in the buffer segment (segment 2, 130 km $< d <$ 200 km along-strike) can be due to a relatively lower metamorphic flux in the region compared to the neighboring regions 1 and 3. The locally lower q_{in} would impose a slower build up of pressure behind the permeability valves, which would spend more time in a closed state, close to their opening threshold. Segment 2 would therefore produce a lower seismicity, and a more clustered, long-period activity than the end segments 1 and 3, as valves would be closer to threshold. In the latter segments ($d <$ 130 km and $d >$ 200 km along-strike), the permeability valves would be further from threshold because of a higher fluid flow, open and close more frequently, with less possibility of interaction, thus reproducing the higher, less clustered seismicity we observe.

The same criticality contrast between segments can also arise from a difference in valve strength, assuming the input fluid flow — and transport properties of the channels — does not vary significantly along-strike. The valves in the buffer, segment 2, could indeed be stronger, with a higher fluid pressure gradients $\delta p_c^{break}/w_v$, but undergoing the same fluid input rate. For a constant input flux along-strike, this results in the same variation of criticality along strike: valves in the buffer region are closer to threshold producing a more clustered and long-period activity, and valves in the segments 1 and 3 framing it are further from threshold, producing a less clustered, more intense and shorter-period activity.

Both these effects can stem from the presence of, or lasting effects of one ore several subducting seamounts (Ide, 2010), that strongly fracture the medium in the end segments of the tremor zone. The amount of fluid that comes through the interface around the tremor source region would be enhanced by a channeling effect, and simply by a higher volume of dehydrating crust at depth. In Figure 4.11, the alignment of the Kinan seamount chain with the subducting seamount detected by Yamazaki and Okamura (1989) and the tremor zone could indicate that the chain extends into the subduction, and could result in the tremor activity patterns observed there. Segment 2 that produces lower, longer-reccurence activity can be a smoother, less damaged

region, in which less fluid is channeled because of a lower channeling effect, and a lower overall permeability. In this case, the low flux create a longer recurrence time of periods of opening and activity.

Although it might explain the observed activity patterns, this interpretation might be at odds with observations of tidal and dynamic triggering on tremor in patches of highest activity in the end segments of the zone, and not in the buffer zone (Chao & Obara, 2016; Chao et al., 2013; Kurihara et al., 2018; Miyazawa et al., 2008). Indeed, if seisimicity in the segments is triggered by minute strains on the interface, it suggests that those segments might actually be closer to criticality: valves would be more sensitive to the very small δp changes across them generated by the dynamic strains of tides and teleseismic waves.

4.7.3.2 Permeability structure

If we make the simplification that the input flux in fault channels, the background transport properties and the permeability valve characteristics all do not significantly change across the strike of the tremor zone, a variation of valve density and clustering in each segment can still explain the segmentation of intermittence. As we showed in Section 4.5.3, the closer the valves locally get in the system — either due to high spatial clustering, or high overall density —, the stronger the interactions between them. With strong interactions come a highly clustered activity in time, with well-defined, long recurrence timescales of clusters of activity. Also, when the interaction between valves is stronger, the activity rate of each valve is lower than when it is further away from its neighbors. We can therefore interpret the characteristic activity in the buffer zone, segment 2, as being due to a higher level of interaction between valves, for instance coming from a higher valve density in this region compared to the neighboring ones. In geological terms, this would mean a lower overall permeability in segment 2, but a larger share of the system being dynamic. This could be due to a more homogeneous permeable system, perhaps because of a relatively smooth segment of oceanic plate being subducted in this region.

In this interpretation, the buffer zone high valve density would behave as an hydrological barrier for the pressure circulation along strike. Although the boundary conditions and geometry we explored for the model are tailored to describe along-dip propagations of seismicity, we can draw from the behavior of the system to imagine how fluid would circulate along-strike, in a network of channels that would extend in both the dip and strike directions, in the whole the tremor zone. Circulations of seismicity along-strike would therefore occur as pressure is transmitted to neighboring segments through along-strike channels. As it meets segments with a higher valve density, the

pressure would preferentially escape along-dip, arresting the seismicity migration. In Figure 4.7a, a dense patch of valves around $x = 0.3$ seems to act such — a barrier between the neighboring parts of the system — and activates in a more clustered, less frequent manner, letting the fluid to circulate more intermittently than in the neighboring regions. This could explain why the buffer zone seems to act as a barrier to large migrations of seismicity in the neighboring segments: it opens and lets pressure transients circulate through more rarely, only when a large enough pressure difference along-strike has built up, depending on the past activity in the neighboring segments.

4.8 Conclusion

In this study, we have shown how the fluid flow and the structure and dynamics of permeability in the subduction fault interface can shape the intermittence of tremor activity, and explain the segmentation of temporal clustering and periodicity of activity observed in Shikoku, Cascadia, or Mexico. We propose that the interaction between elementary tremor sources is mediated by pressure transients, and that their interactions allow temporal clustering and well-defined timescales to emerge. We built a model of transient fluid transport processes in the fault that encapsulates this idea. In our model, events are generated as fluid flow breaks barriers of permeability open in a porous channel within the fault zone. The transient of fluid pressure that result from the sudden opening of permeability can trigger neighboring sources, if they are close enough in space, and close enough to their rupture conditions. Those two factors are the main controls on how valves interact in our system, and we show that they crucially shape the intermittence of the simulated activity: the closer valves are together locally in the system, the closer they are to their opening or closing thresholds, the stronger their interaction, and the more temporally clustered, periodic and longer period the simulated activity is. This framework can bring essential insight into how hydrological processes in the fault zone shape the observed spatial variation of tremor activity. Our model provides a simple but physically-based mechanism to describe the influence of hydrological processes on shaping tremor patterns. While more work is needed to refine the physical description of fluid processes in this framework, and understand how they are connected to deformation and slip in the subduction shear zone, we argue that including dynamic hydrological processes in our interpretations of tremor, and microseismicity patterns in general, is essential to understand fault zone phenomena.

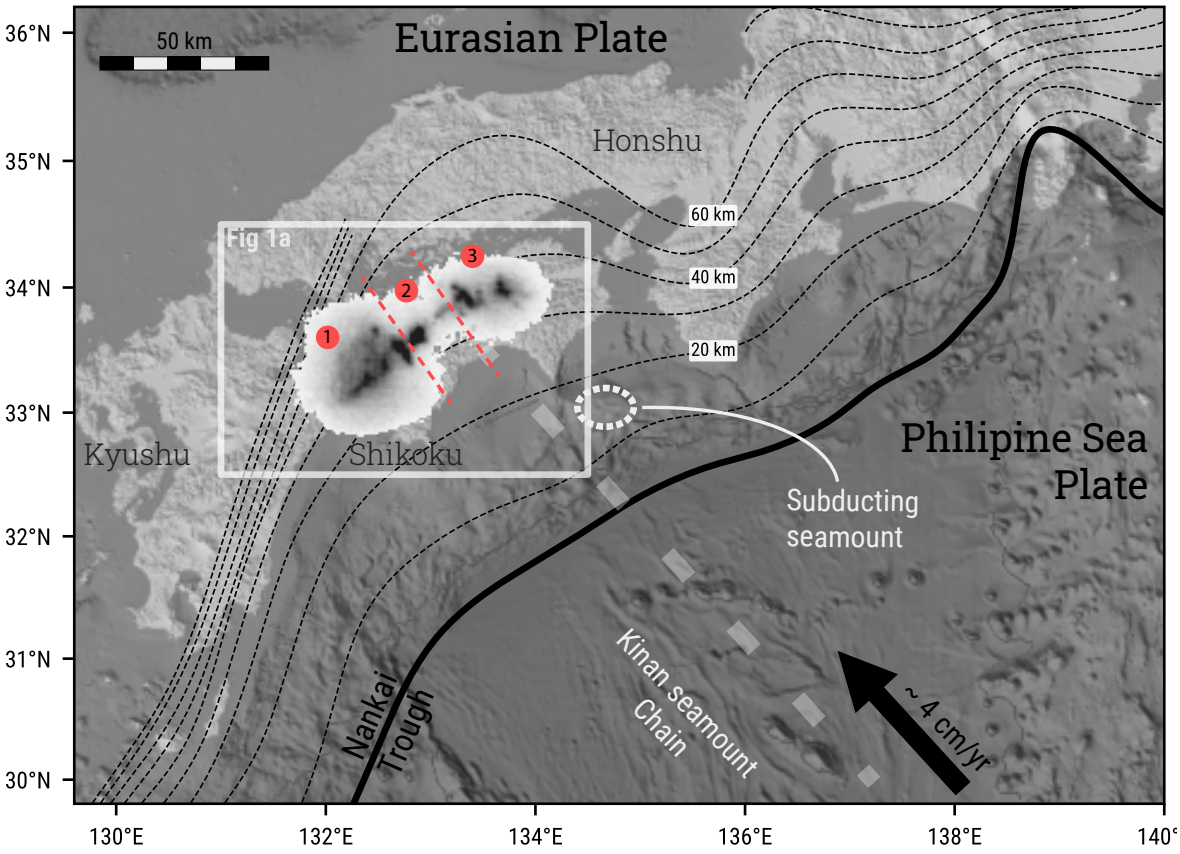

Figure 4.11 *— Regional context of the Shikoku subduction and tremor zone. The trench is outlined in thick black line, and the depth contours of the slab are shown in thin dotted black line (model from Iwasaki et al. (2015)). The black arrow and wide dotted line show the direction of relative convergence of the Philipine plate, towards the Eurasian plate (fixed). The extent of the map in Figure 4.1a is shown with the white box. We single out rough topographic features on the subducting Philipine plate: the Kinan seamount chain, and a subducting seamount (Yamazaki & Okamura, 1989). A 2D histogram overlaid on Shikoku island shows the distribution of activity in the tremor zone, which can be separated in three zones characterized by differents patterns of activity (cf Figure 4.1 for details).*

Appendices to Chapter 4

Contents

4.A Tremor patterns in two other subduction zones

In subductions where the extent of observations along strike is wide enough, the observed tremor activity is segmented along strike, varying both in temporal clustering and recurrence timescale of bursts.

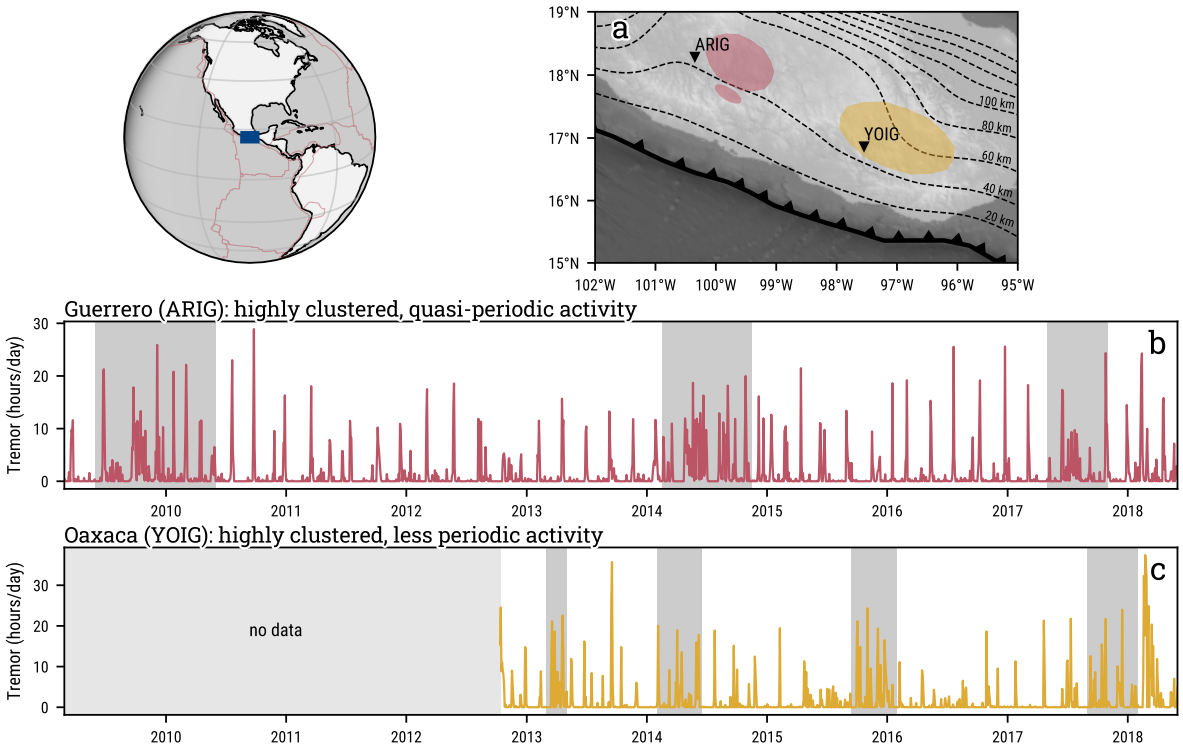

Figure 4.A.1 — *Segmentation of tremor intermittence in Mexico (Central American subduction zone, 2009–2018). (a) Map of tremor activity in the subduction zone. Colored patches outline the extent of the source regions (Brudzinski et al., 2010; Frank et al., 2014). The stations used to detect daily tremor activity are shown with black triangles. Depth contours of the slab from Slab2 (Hayes, 2018). The thick black line outlines the trench. Hours of tremor per day in (b) Guerrero, measured on station ARIG, and (c) Oaxaca, measured on station YOIG. Tremor data from A. Husker et al. (2019). On both (b) and (c) the periods shaded in dark grey represent geodetically detected slow slip events (A. Husker et al., 2019). The two zones show different intermittence patterns. In Guerrero, large bursts of tremor occur quasi-periodically every 2–3 months, in between the intense tremor episodes occurring with SSEs every 3.5 years. In Oaxaca, inter-SSE bursts are less periodic, recurring every 1–3 months, in between longer tremor episodes associated with large SSEs, roughly every 2.5 years.*

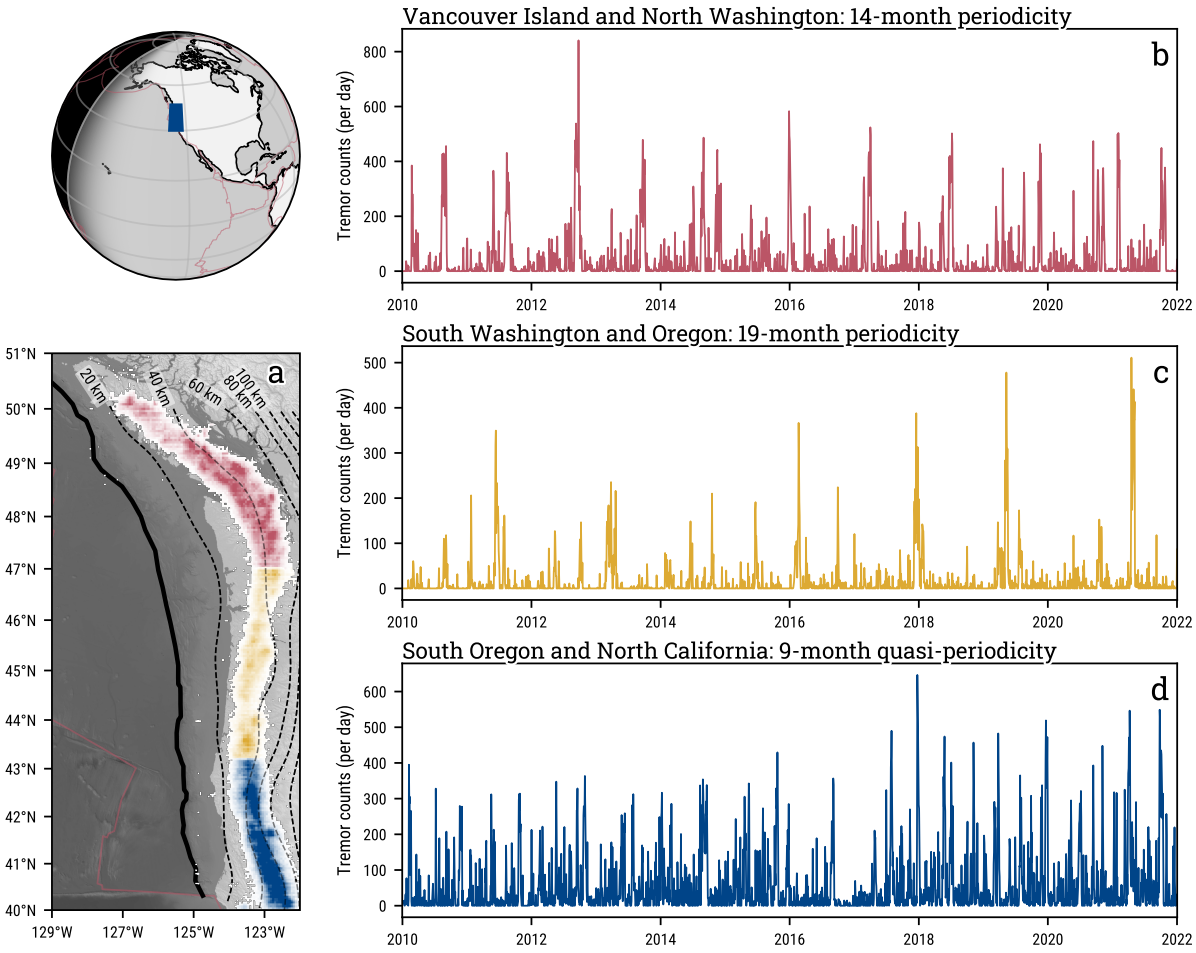

Figure 4.A.2 — *Segmentation of tremor intermittence in Cascadia (2010–2022). (a) Map of tremor activity in the subduction zone, colored according to source density and segmentation (as defined by Brudzinski and Allen (2007)), catalog from Wech (2010); Wech and Creager (2008). Depth contours of the slab from Slab2 (Hayes, 2018). The thick black line outlines the trench. Tremor counts per day under (b) Vancouver Island and Northern Washington, (c) South Washington and Oregon, (d) South Oregon and Northern California. The periodicity estimates are from Brudzinski and Allen (2007). The activity is segmented along strike: the northernmost segment is most periodic, the center segment is less periodic, with a longer timescale of recurrence and higher level of clustering, and the southernmost segment is least clustered, with a shorter recurrence scale of tremor bursts.*

4.B Additional examples of the clustering analysis

In this section, we depict how the clustering analysis characterizes the activity in two additional cases: on observed LFE activity in Shikoku (Fig 4.B.1), and on a synthetic case, exhibiting weakly clustered activity (Fig 4.B.2), which demonstrates the limit of our analysis for weakly clustered activity.

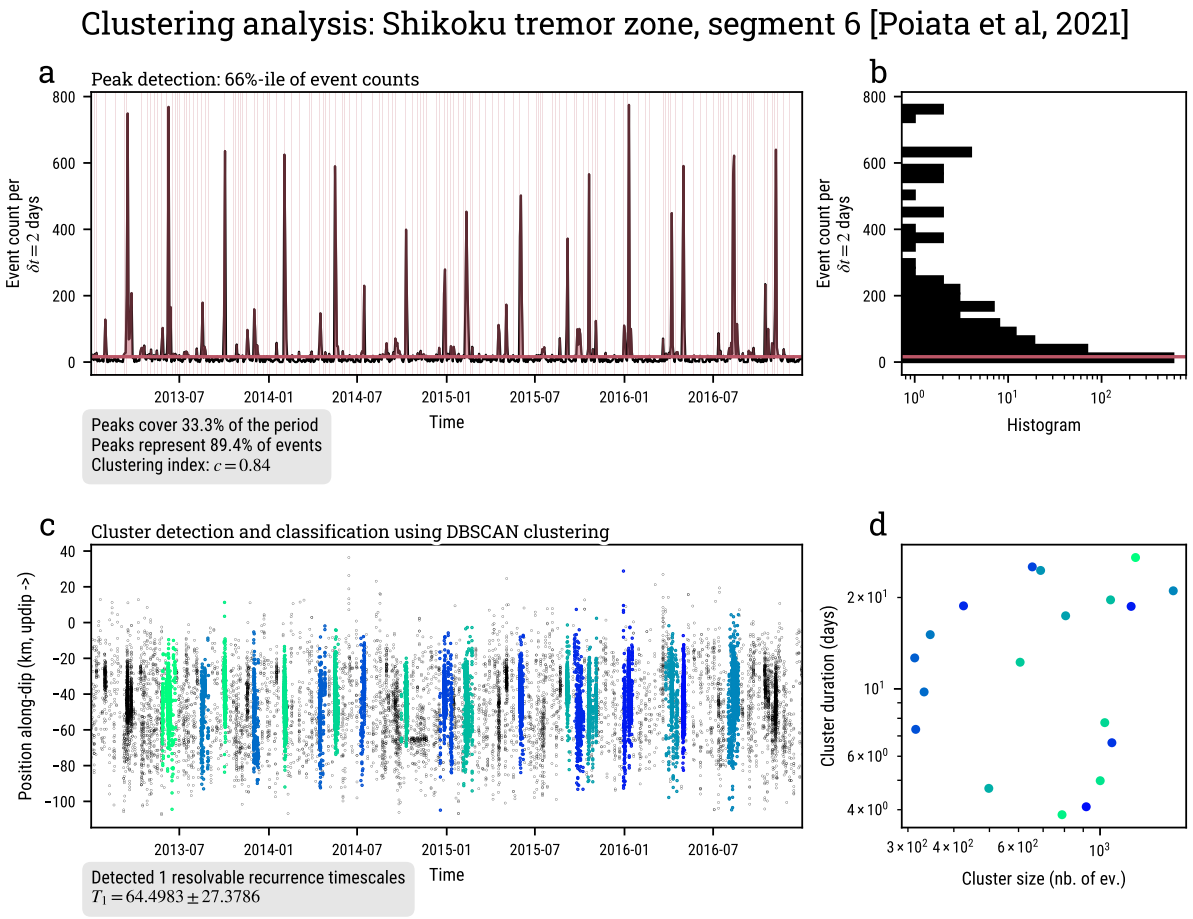

Figure 4.B.1 — *Clustering analysis of LFEs in the segment 6 (Poiata et al., 2021) of the Shikoku tremor zone. (a) Event count time series. The threshold defining peaks is represented as the red line, and corresponds to the 66% quantile of the event count distribution, represented in (b). (c) shows the activity in time and space, projected along the dip of the fault. Colors show how events are labelled into clusters. (d) shows the duration and size distribution of clusters identified for the full simulation. Only one type of cluster is identified by the algorithm in this case.*

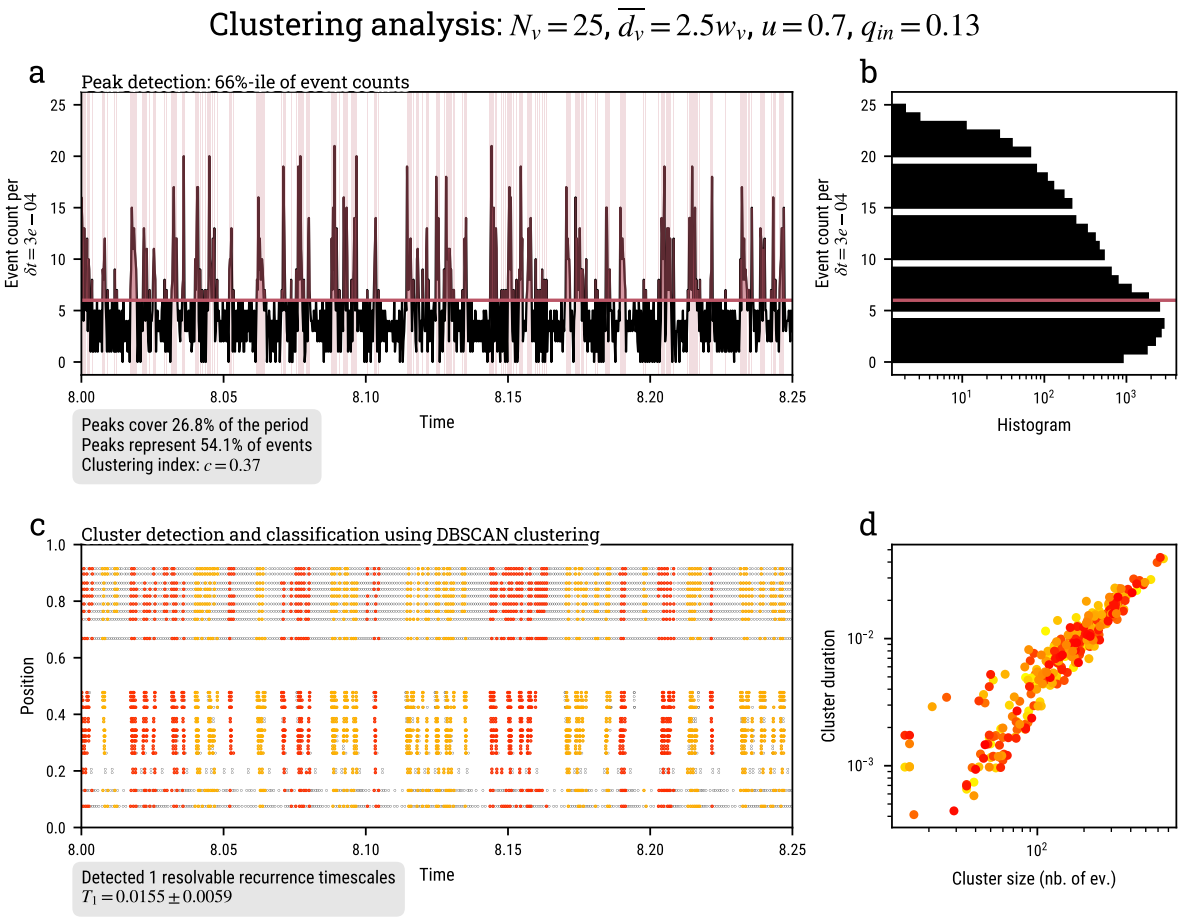

Figure 4.B.2 — *Clustering analysis of a simulated, weakly clustered activity in a clustered valve system with $N_v = 25$ valves ($\overline{d_v} = 2.5w_v$), $u = 0.7$, under a input flux of $q_{in} = 0.13$. (a) Event count time series. The threshold defining peaks is represented as the red line, and corresponds to the 66% quantile of the event count distribution, represented in (b). (c) shows the activity in time and along the channel, colors show how events are labelled into clusters. (d) shows the duration and size distribution of clusters identified for the full simulation. In this case, only one class of clusters is identified by the algorithm, with a high variability of sizes and durations.*

4.C Full distribution space

The next two Figures (Fig 4.C.1 and 4.C.2) show examples of a valve distribution drawn from a Weibull distribution for all $(u, \overline{d_v})$ explored.

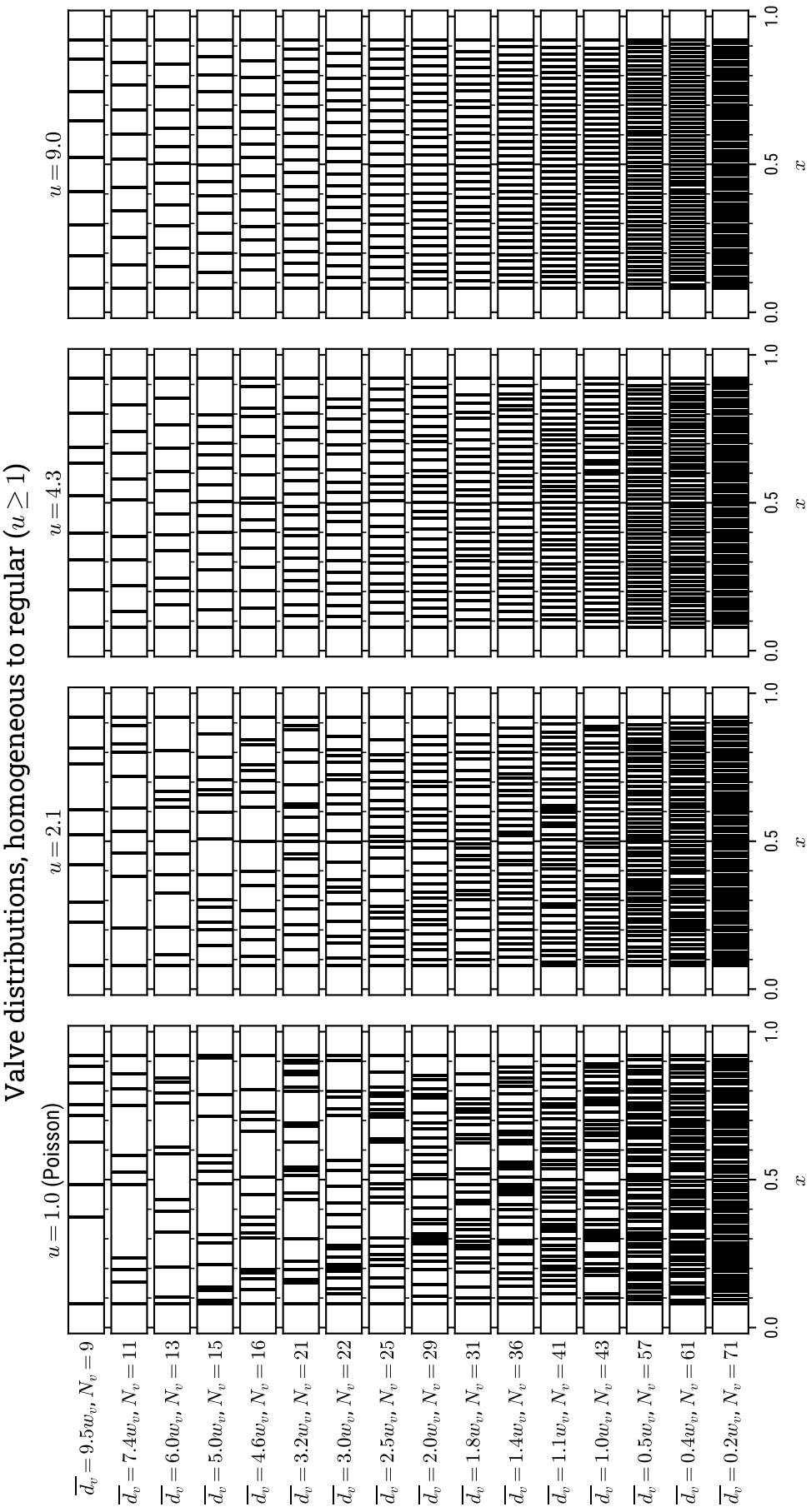

Figure 4.C.1 — *An example of valve distribution drawn from every $(u, \overline{d_v})$ explored in the simulations, here for Poissonian to regular valve distributions.*

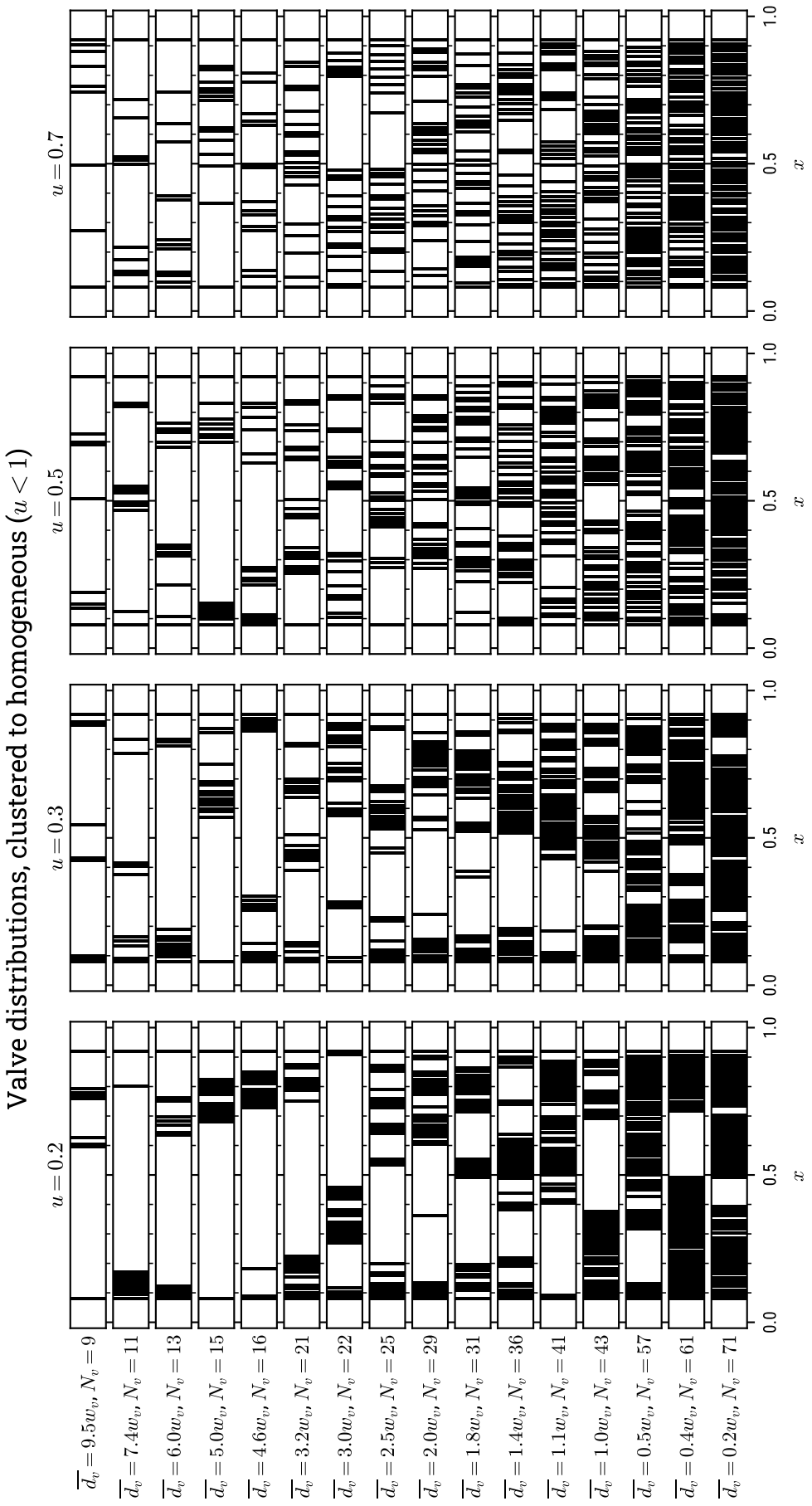

Figure 4.C.2 — *An example of valve distribution drawn from every $(u, \overline{d_v})$ explored in the simulations, here for clustered to Poissonian valve distributions.*

Part IV

Conclusion

Chapter 5

Scope, limitations and perspectives of this work

Contents

To conclude this manuscript, we will first summarize key takeaways from our work. We will then discuss how realistically the physics we base our model of unsteady fluid circulation represents evidence of permeability changes in the fault zone, and how to think about the relationship of the described processes here with slip and deformation in the plate interface. Finally, we will describe how our model could be applied to understand spatio-temporal patterns of volcanic tremor as symptom of unsteady magmatic circulation in volcanoes, before concluding on the more general scope of this model, and what it could contribute to our understanding of geological plumbing systems.

5.1 Summary and scope of this work

[1] In Chapter 2, we show that LFEs in Guerrero, Mexico, seem to have a corner frequency, and therefore duration, independent from their seismic mo-

ment, with a characteristic value just between 2–3 Hz. This behavior is consistent with a source process controlled by the timescale of fluid diffusion in the fault interface. The sudden opening of a permeability barrier in the fault could trigger a fast fluid pressure transient responsible for generating a seismic signal consistent with of LFEs' amplitudes and radiation patterns in subduction zones.

[2] In Chapter 3, we focus on understanding how intermittent, migrating patterns of LFE activity could emerge from fluid pressure transients in the subduction interface. We build a model of circulation of fluid, channelized in a permeable conduit along the dip of the fault zone, fed by a constant metamorphic source. Based on observations that fluid pressure and permeability are heterogeneous, vary strongly and cyclically in the fault, we model the permeability of the fault channel in a binary fashion: high-permeability segments and elementary low-permeability segments. The low permeability segments behave as valves, opening and closing in response to the local fluid pressure gradient. This behavior is based on the physics of clogging and unclogging of a permeable medium conducting a pressurized, particle-laden fluid.

[3] Each sudden opening of a valve segment of the permeable channel generates a strong fluid pressure transient as fluid rushes through the open valve, suddenly decreasing the force applied to the matrix by the impeded flow. This strongly, rapidly varying force can act as a source of seismic waves, and its radiation pattern is both consistent with the radiation pattern of LFEs, and nearly indistinguishable from a shear mechanism on the plate interface, with the geometry of observation of LFEs in subduction zones. Through this explicit association in our description, the fluid circulation model is fully coupled with processes generating seismicity. The actual process generating the seismic event is unknown and still debated, and a small shear rupture triggered by the changing effective normal stress on the fault could also be consistent with our description. However, our focus is to model the interactions between sources, and we leave this subject open for discussion.

[4] We find that in geological conditions, when submitted to a constant flux, permeability valves can open and close in cycles if the flux is high enough that valves can be broken, but low enough that they can heal closed after being broken. Two critical values of flux delimit this operating range for valving and seismic activity: the flux value above which a closed valve will eventually open, and the flux value below which an open valve will necessarily close. When any valve system is submitted to a fluid flux in this range, it generates intermittent pressure, flow and permeability conditions in the fault zone. As seismicity is coupled with the opening of permeability valves, the intermittent loading and unloading of fluid pressure in the hydraulic system produces intermittent seismic behavior. Under a constant source of fluid,

a complex, intermittent behavior of fluid circulation emerges, shaping sustained, permanently intermittent patterns of seismic activity.

[5] As closed valves open when the pressure gradient exceeds a certain threshold across their spatial extent, the flow transient associated with the opening of a neighboring valve can trigger their opening. This triggering interaction can act in both up and downdip directions, by sucking the fluid in front of them if the opening neighbor is in front of the valve, or by pushing more fluid against it, if the opening neighbor is behind it. Valves, and thus seismic sources, therefore interact through the fluid pressure field, and can trigger each other in cascades. This produces fast migrations of activity in the channel, both in the up and downdip directions.

[6] In a system with randomly distributed valves, complex patterns of activity can emerge, reproducing characteristic behavior observed in tremor and LFE activity in subduction zones. As valves interact, their activity synchronizes, and intermittent and quasi-periodic activity can occur. Fast migrations of activity occur as valves cascade open, reproducing fast tremor bursts. From the synchronization of their cycles of fluid pressure loading and unloading, a large-scale valving behavior emerges at the scale of the system. The permeability in the system episodically opens and closes, associated with episodes of high activity, thereby reproducing the fault-valve behavior observed on long timescales at the scale of subduction zones. Building on elementary cascades of activity and synchronous cycles of fluid accumulation at the scale of the system, large scale migrations of activity are produced, and slowly propagate across the whole channel.

[7] In Chapter 4, we explore how the input fluid flux and distribution of the valves in the system control the temporal clustering and timescales of recurrence of activity bursts in our model subduction channel. We start by demonstrating that the strength of interactions in a two valve system depends on the distance between the valves and the flux they are submitted to. The former controls the delay and strength of the triggering pressure transient that travels from the opening valve to its neighbor. The latter controls how close to breaking or critical the neighbor is in average, when it receives the triggering transient from the opening valve. The closer and more critical the valves are, the stronger the interactions are, and therefore the stronger their synchronization.

[8] In a systematic study of how valve distributions affect the simulated seismic activity, we show that the number of valves at interacting distance in the system is a key factor shaping the intermittence of activity. The more valves are interacting in the system, the more clustered and periodic the activity gets, and the longer the observed timescales of recurrence of the bursts. The quantity of interacting valves describes how dynamic and heterogeneous the fault

is, in terms of its permeability. It is a fundamental characteristic of the subduction channel, and should be considered a major factor shaping the activity of LFE and tremor seismicity.

[9] The same result is obtained when flux is set to values near the critical values bounding the operating range for seismic activity. Under such flux conditions, valves spend most of their time closed, and very close to breaking open when the flux is low, or open, near closing conditions when the flux is high. In those cases, valve can change state when they feel minute changes of pressure, and are therefore strongly interacting with their neighbors. Their high criticality produces highly clustered, periodic activity, recurring on long timescales. The input fluid rate into the fault zone is controlled by the kinetic of the dehydration in the subducting oceanic plate. Other controls include channeling effects that concentrate fluid flow as a result of impermeable sealing of the plate interface, or on the contrary, pervasive damaging of the overiding crust allowing fluid to escape the fault zone. We argue that the relationship between sources and sinks of fluid in the fault zone is a second key factor to take into account when understanding how fluid flow processes could shape tremor activity.

[10] A central result of this study is the emergence of long periodicities of activity in a system where isolated sources recur orders of magnitude more frequently. The emerging collective behavior of valves is due to their collective effect on the pressure field. As they interact, they synchronize, and the cumulated effect of their closing shapes cyclic accumulation and releases of pressure on a large scale within the channel. The buildup and release of pressure on such spatial scales is long, as large portions of the fault alternatively fill up and empty, generating the long-term intermittence that we observe when valves interact strongly.

[11] The spatial variations of source and sinks of fluids, the channeling efficiency, dynamics and heterogeneity of the permeable channel can help interpret the segmentation of seismicity in subduction zones as a result of the characteristic of fluid circulation in each segment. Segments where the activity is most clustered could for instance be the theatre of clearly intermittent fluid circulation, due to a low fluid input rate into the fault zone, or high number of valves, that collectively block the fluid flux in the fault, sealing the interface and generating high fluid pressure downdip of the tremor zone, and then collectively breaking, allowing the fluid to episodically escape and producing episodes of high low-frequency seismicity.

[12] The characteristic lengthscale of the segmentation seems to match the size of geological features of the subducting plate, that could influence the hydraulics of the system when such structures reach the depth of the tremorgenic zone. A subducting seamount could cause strong damaging of the fault

and overiding plate, resulting in a lower channeling of fluid in the interface, or in weaker, less critical valves. A locally thickened subducted crust could for instance increase the amount of dehydration, and therefore increase the fluid flow in the fault, generating less critical conditions, thus resulting in a less intermittent seismicity.

The model we have built provides a simple framework to understand how from small scale processes of fluid pressure cycling generated by dynamic permeability, fluid pressure transients can emerge in a subduction channel on a much longer and larger scale, and shape the activity of tremor. In our description, the smaller scale hydraulic processes are directly linked with the activity of elementary sources of tremor, and the interactions between these sources through the pressure field allow them to synchronize. It links in one framework the source of LFEs and their intermittent, migrating activity patterns. We believe this work can help understand better how the complexity of fluid flow processes in the subduction — especially small-scale valving behavior — can shape the activity of tremor, from source to swarm. Although our model only depicts simplified fluid flow mechanisms, it can be used to complexify our understanding of fluid flow in subduction zones by including more dynamic and heterogeneous phenomena, and diagnose their activity using the characteristics of intermittence of tremor or LFE activity in a subduction zone.

5.2 Confronting modeled and observed processes

5.2.1 Changes of permeability in the geological record

The valve mechanism we design for opening and clogging permeability in the fault is based on a simplified model of how pores clog and unclog in a permeable medium channeling a particle-laden fluid. The conditionally intermittent flow through the valve we obtain in our model (Chapter 3, Section 3.4.1, Figures 3.5 and 3.9) is very similar to the one observed in simulations and experiments of filtration of a fluid carrying particles (Bianchi, Thielmann, et al., 2018; Jäger et al., 2017b; Souzy et al., 2020). However, this mechanism has only been observed in the lab (Candela et al., 2014), in shallow crustal faults (Manga et al., 2012) and oil reservoirs (Sahimi et al., 1999), and there exists no direct evidence of its existence deep in the subduction fault zone where tremor occurs. One of the only ways to find evidence for this process would be to find its signature in the geological record, but such short-lived, transient processes would most surely leave no trace in exhumed subduction channel, either because they are so short and transient that their signature would be quickly overprinted by more important processes, or sim-

ply because they do not occur. In this section, we discuss how relevant this mechanism and its physical description is to describe the dynamics of permeability in the fault zone, by comparing it to the geological record of processes associated with fluid flow and tremor in exhumed subduction channels.

Our model of fluid circulation in the fault assumes that fluid is channeled along a permeable conduit in the fault, which is segmented between pockets of highly connected fluids and low permeability barriers in between these pockets. The high permeability segments that form the pockets of fluid can connect when barriers to the flow break, letting the fluid circulate, channeled through the fault zone. The geological evidence seems quite unambiguous that fluid should be channeled from deep and distributed metamorphic sources along the plate interface (Angiboust et al., 2014; Piccoli et al., 2021; Saffer, 2015). In fossilized fault zones, there even is evidence of episodic fluid flow when veins suddenly interconnect domains of overpressurized fluid, forming highly connected networks that channel fluid from external sources (Taetz et al., 2018). In this system, veins would eventually be cemented and permeability would shut down, remodeling the hydraulic network. It is not obvious that as in our model, permeability would close down and reopen in cycles in the same spot, and that valves should remain stable in time.

Evidence of metastomatism around the larger veins indicates that they should remain open for periods of months. In a network of such veins, cataclastic fines or silica colloids could be transported by the flow and clog the permeability, reproducing a valving behavior similar to the one we model. Even if this mechanism really occured, it would occur in micrometer to millimeter wide fractures, and the length of the clogs should also be on the same order of magnitude. In order to generate pressure transients strong and rapid enough to be responsible for hydrofracturation (Muñoz-Montecinos et al., 2021) or the generation of an LFE-like seismic signal (N. M. Shapiro et al., 2018), many strong unclogging events should occur rapidly in cascade in a wide area. Even with large clogs in wide fractures, it seems hard for a synchronous opening at many valves to bridge the gap between the millimetric scale (at most) of the process, and the width ($\sim$ 300 m), surface area ($\sim$ 1000 m^2), and pressure drop (5 MPa) across the valve assumed by N. M. Shapiro et al. (2018) to account for the seismic characteristics of LFEs. In lab experiments, Bianchi, Thielmann, et al. (2018) have shown that the pressure jumps detected as the medium clogs and unclogs follow a power-law size-frequency distribution. Assuming it would be the case in the fault zone, and that this law is valid for pressure jumps that could generate LFEs, small uncloggings should occur orders of magnitudes more frequently than large collective uncloggings that could generate LFEs. Following this line of reasoning, this

phenomena would have to be a pervasive feature of the hydraulic system of subduction zone to explain the observed cyclic behavior of fluid flow, pressure and seismicity in the subduction zone. Although such processes are perhaps unlikely to be responsible for generating LFEs only through fluid pressure transients, their presence in the fault zone would still generate transient, cyclic and migrating fluid pressure as our results show. This might be sufficient to shape complex tremor activity by triggering seismic sources, by transiently lowering the effective stress on near-rupture asperities in the fault.

Exhumed subduction channels tend to show large changes of permeability in the fault zone, which seem to mainly come from mechanisms of hydrofracturation (Muñoz-Montecinos et al., 2021) or vein opening (Platt et al., 2018; Taetz et al., 2018; Tarling et al., 2021). After opening rapidly, the permeability heals due to processes of crystallization in the created fractures (Tarling et al., 2021), or ductile deformation sealing and isolating the fluid-filled, overpressurized cracks (Gratier & Favreau, 2003). The physical description of our model arguably approximates such behavior. Hydrofracturation occurs because of a strong, localized overpressure that overcomes the cohesion of the material in the fault, creating fractures for the fluid to circulate. The opening of valves in our model is quite close to this behavior, as it is controlled by the pressure gradient across low-permeability barriers. However, the mechanical and chemical sealing processes should be mainly pressure and time dependent, and depend only weakly on the pressure gradient. A model that described opening and sealing of elementary fault valves in such a way would have much in common with the physical description we make of the interaction between fluid pressure and permeability. It should reproduce strong and cyclic fluid pressure transients as hydrofracturation and sealing alternate, cascades of permeability openings as pressure diffuses in the overpressurized fault zone allowing near-breaking areas to interact, and be potentially more suited to generate single-force LFEs, because of the larger space and pressure scales involved. A central concept worth exploring would be the role of cohesion and damage in the fault, as it might provide a way to link the mechanics of failure and healing of the rock and the evolution of its permeability. Such a description might even be suitable for a more continuous, less binary description of the system's dynamics, with continuously evolving, continuously defined permeability in the fault, allowing to explore how the hydraulic structure of the system could evolve in time and space.

5.2.2 Interactions between fluid circulation and fault slip

The simple permeability valve model we have developed in this work was aimed at exploring how transient fluid pressure and permeability in the fault

zone could interact, and how they could affect and shape tremor activity. Because our goal is to understand the role of the hydraulic system in a simple system, fault slip is not at all present in the model, not even implicitly, although it seems clear that it should at least be partly implicated in generating tremor. Fault slip and LFE activity are intimately linked, since they occur in the same places at the same time (*e.g.* Rogers, 2003), and LFE activity can even be used to detect the geodetic signature of small slow slip transients otherwise buried in the noise (Frank, Radiguet, et al., 2015). In this interpretation, tremor is generated as brittle asperities rupture when a slip transient occurs on the subduction fault (Ando et al., 2010). The seismic characteristics of LFEs — their radiation pattern mostly — are also consistent with shear slip on the subduction interface (Ide, Shelly, & Beroza, 2007), although observations interpreted that way are sometimes ambiguous, and could better fit a single-force mechanism (Wech & Creager, 2007), as noted by Ohmi and Obara (2002).

The processes of unclogging — or hydrofracturation of low permeability barriers — and transient fluid pressure that we describe should interact closely with slip on the fault. As slip occurs on the fault, be it seismically or aseismically, it generates an extensional regime in the fault zone, allowing extension veins to open and pump fluid into the fault (Kotowski & Behr, 2019), thus strongly modifying the local permeability and fluid pressure in the slipping region. Damaging and dilantancy in and around a slipping portion of the also create permeability (Im et al., 2019b; Mitchell & Faulkner, 2008; Tenthorey & Cox, 2006), and can therefore also affect the fluid pressure field.

On the other hand, it is known that high fluid pressure can trigger slip on a fault by lowering the fault strength. The most plausible cause of an increase of fluid pressure is an input of fluid in a partly sealed region. In a homogeneous channel, such fluid flow is necessarilty associated with a smooth pressure gradient, implying that the high fluid pressures that are required for sliding motion are limited to the proximity of the source. Our study shows how heterogeneous and transient permeability behavior in the fault could generate high fluid pressures locally and transiently, in wide parts of the subduction zone. The collective behavior of valves creates a cumulated effect on fluid pressure that translate into multi-scale fluid pressure increases and drops, that could shape the behavior of fault slip from the source to the subduction scale. Coupling a description of the dynamic hydraulic processes we describe with slip would however require to include a rock mechanics framework, to depict how slip and unclogging/hydrofracturation affect the cohesion, friction and permeability in the fault, and how fluid pressure affects slip in the fault in return. Although it is still a open research question to understand exactly how fluid transport processes and slip on a fault interact, a coupled

model could for instance help assess the time and space scale at which each process could play the predominant role in shaping the activity of tremor.

5.3 Application to volcanic long-period seismicity

The first detections of low-frequency earthquakes and tremor in tectonic settings were quite surprising for researchers who first found them, as such seismic signals had only been detected in volcanoes before (Obara, 2002). Active magmatic systems produce a very diversified seismic activity, which can be divided into many different classes of events based on characteristic of their signal and the processes they are thought to be linked with (B. A. Chouet & Matoza, 2013). One of the main classes — quite similar to earthquakes detected in faults — is composed of events called volcano-tectonic (VT) earthquakes. VT events occur from small ruptures as magma propagation changes stress in the rock around the magmatic system (Roman & Cashman, 2006). Another main class of signals is the long-period (LP) seismicity, composed of LP earthquakes and tremor, which are similar to non-volcanic low-frequency earthquakes and tremor. LP earthquakes and tremor in magmatic systems have a relatively low characteristic frequency compared to VT events, between 1–5 Hz usually (B. A. Chouet, 1996). They seem to relate closely with magma or gass movements in the plumbing system of volcanoes, indicating transient flow events and rapid pressure systems as fluid is transported in the system (B. A. Chouet, 1996). Their activity seems to be a consistent indicator of an impeding eruption, or at least of transient fluid movements in the magmatic systems. Indeed, their activity often migrates back and forth from potential reservoirs in the crust towards the surface, before an eruption (N. M. Shapiro, Droznin, Droznina, Senyukov, et al., 2017). Models of their source all necessitate strong changes of pressure in the magmatic fluid. To list a few, LP signals can be generated by fast flow of magmatic fluid through constricted pathways of the magmatic systems (Benson et al., 2008; Honda & Yomogida, 1993; Julian, 1994; Ukawa & Ohtake, 1987), by the resonance of fluid filled cracks after a strong in- or outflux of fluid (B. Chouet, 1986), or by the sudden nucleation, inflation and resonance of bubbles of gas as pressure drops because of accelerating flow in the magmatic system (Melnik et al., 2020b).

Spatio-temporal patterns of long-period tremor in magmatic systems

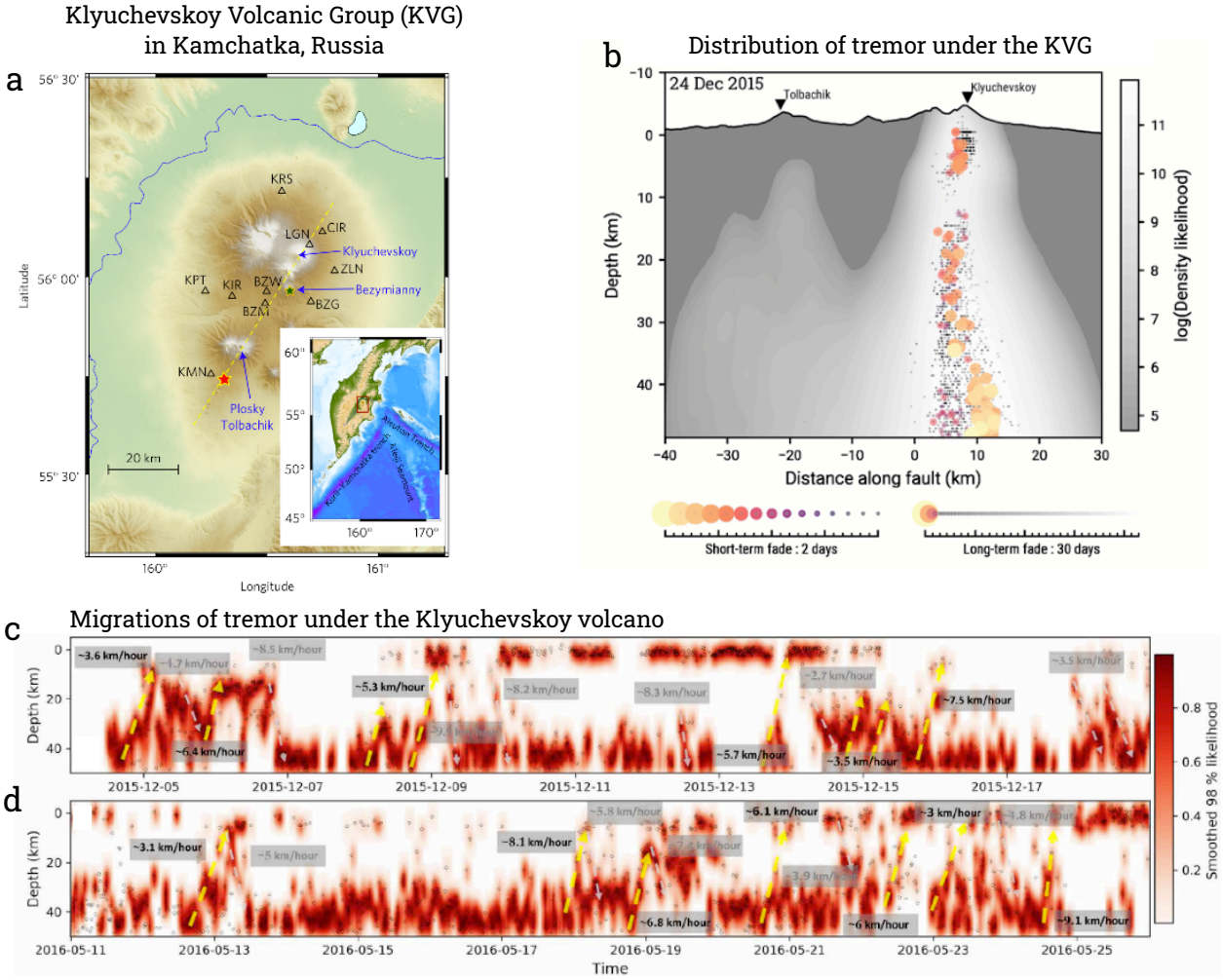

Figure 5.1 — *Migrations of volcanic long-period tremor in the Klyuchevskoy volcanic group (KVG), in Kachatka, Russia.(a) Map view of the KVG, black triangles showing the position of seismic stations. The yellow dotted line represents the location of the profile in panel (b). Map taken from N. M. Shapiro, Droznin, Droznina, Senyukov, et al. (2017). Red and green stars show locations of past eruptive sites. In panel (b), we show the location of detected tremor under the KVG. The grey scale shades indicate spatial density of tremor sources projected on the fault plane indicate as the yellow dashed line in (a). The panel is a still from an animated catalog in Journeau et al. (2022), where each dot corresponds to location emitting tremor. Dots fade in time: yellow are most recent, while orange, red and then black indicate events further and further in the past. A downdip migration is therefore visible: starting about half a day before the 24th Dec. 2015 at 20 km depth, and migrating downdip, where it locates around 45–50 km depth on the 24th Dec 2015. Panels (c) and (d) show the spatio-temporal patterns of activity in a time-depth representation. Each black dot represents a tremor detected at depth. The red hues represent the spatial likelihood function plotted in time, which account for the diffuse nature of tremor sources and the uncertainty in location of the source at a given time. The arrows and velocity labels highlight migrating behavior of tremor, in both the upward and downward direction. Both panels are taken from Journeau et al. (2022).*

The migrations of LP activity sometimes span the whole extent of the magmatic system from deep sources to the surface, traveling in both upward and downward pulses of relatively constant velocities around a few to a few tens of kilometers per hour (Journeau et al., 2022; N. M. Shapiro, Droznin, Droznina, Senyukov, et al., 2017). In Figure 5.1, we display examples of such migrations under the Klyuchevskoy volcanic group. The speeds, directions and extent of those migrations seem to be inconsistent with the flow of fluid in the system, which would for one mainly travel upwards. They are therefore linked with acceleration or deceleration of the flow in the magmatic system, which cause propagating transients of pressure triggering seismic vibrations along the way (B. A. Chouet, 1996; Journeau et al., 2022; N. M. Shapiro, Droznin, Droznina, Senyukov, et al., 2017). The mechanism of transmission of pressure is not well established, as many questions remain regarding the composition and structure of an active magmatic system, and how magmatic fluids flows within it.

A common representation of the magmatic system beneath volcanoes is that magma storage occurs in open, long-lived chambers shallow in the crust, fed by deeper, similar reservoirs through dike-like fractures. Geological evidence, geophysical measurements and modeling thereof seem to point towards a much more distributed system of storage and circulation of magma and gasses, from deep mantellic sources to volcanic vents at the surface. Magmatic systems seem to be organized in wide trans-crustal structures, built from the remnants of repeated injections of magma forming sheet-like structures (sills), that slowly cool down and are heated back up at each reinjection (Annen et al., 2006). The combined effects of magmatic fluid advection and heat transfer forms a complex magmatic "mush" system, in which the melt, crystalline and gas fraction are heterogeneous across the depth of the reservoir, forming an intermittently connected permeable system for magmatic fluids to flow in (Cashman et al., 2017; Sparks et al., 2019). This system is also dynamically remodeled, through processes of injection pressurizing melt-rich portion of the systems, which can then break low-melt-fraction mush seals, triggering sudden flow transient that ascends through the system (Sparks et al., 2019).

The heterogeneity and dynamics of this system could be modeled very directly in the framework we developed in this thesis, to describe how intermittent magmatic transport emerges in this system, generating punctual eruptions, whereas it is fed by an *a priori* constant source of magma deep in the mantle. LP seismicity in volcanoes is clearly linked with rapid flow acceleration in the magmatic system, which seems to be linked with sudden opening of permeability barriers in the description of Sparks et al. (2019). Our malve model of the permeability changes, how they relate to changes of

pressure, and their association with the activation of a seismic source, might therefore be a simple and powerful way to represent elementary flow processes and their relationship to seismicity in the volcanic plumbing system. It could provide a direct interpretation of seismicity migrations as acceleration and decelerations in the flow of magmatic fluid throughout the system. The seismicity can thus be used to try and delineate the active parts of the system, ito understand better the structure and dynamics of the magmatic plumbing system and how it conducts fluid towards the surface.

More precisely, even, our model provides an interpretation for how clustered in time the seismicity gets depending on the strength of the fluid input into the permeable system. Because it changes the average criticality of valves in time, a change of input flux in the system changes the strength of interaction between valves, and therefore their clustering and recurrence behavior.For a progressive reactivation of an initially inactive system, modeled by a vertical channel with valves distributed within it, the progressive increase of flux from low to high values would trigger first a low, extremely clustered seismicity as the system opens intermittently, remaining mainly closed. If the system was submitted to an increasing flux, it would further open, due to the increase of pressure gradient in the fluid, and an increasingly constant, less clustered activity would occur. Such patterns are observed before eruptions in one of the largest volcanic group on the planet, the Klyuchevskoy Volcanic Group (KVG) (Frank et al., 2018). In such cases, our model could provide a straightforward interpretation in terms of fluid flux variations in each part of the system, and — provided it is correctly scaled — provide estimates of the mass of fluid transported throughout the system, or transport properties of the latter, opening promising alleys for volcano monitoring.

Even though these prospects are encouraging, many questions have to be addressed before directly applying our model to volcanoes, in particular regarding the rheology of the fluid and permeability dynamics. The nature and rheology of the fluid (gas or melt?), the strong thermal effects on fluid viscosity, melt-fraction and therefore permeability, the dependence of fluid flow processes on depth or the stage of maturation of the plumbing system are examples of specificities of the magmatic case that need thorough consideration, in order to estimate how applicable and precise the valve system description can be to interpret patterns of seismicity as symptoms of fluid transport processes in volcanoes.

5.4 Beyond the subduction zone

Even though the model we presented is a simplified and non-exhaustive description of the dynamics of permeability and its connection with the source

processes of LFEs and tremor in the subduction zone, it encapsulates key and realistic aspects of how fluid flow seems to occur in the subduction fault and shape seismicity, as shown by geological and geophysical observations:

- Fluid pressure and its gradient should have a strong effect on permeability.
- The opening of permeability should be associated with — caused by, or causing — the generation of seismic waves.
- Neighboring sources should therefore interact through rapid pressure transients in the permeable subduction channel.

It provides a useful conceptual framework to understand how heterogeneous, intermittent fluid pressure conditions can emerge in a fault. Our model of how the seismic source is triggered by the fluid pressure field and affects it in return allows to conceptualize how elementary sources can interact in an hydraulic system, and build up patterns of seismicity.

Beyond the subduction zone, this framework has a broader reach to interpret how fluid unsteadily flows in geologic plumbing systems, magmatic (Journeau et al., 2022) and hydrothermal systems (Wech et al., 2020), permeable reservoirs (Sahimi et al., 1999), faults (Ross et al., 2020), using the seismicity they generate and the hydraulic parameters that can be observed. The permeability valve mechanism is a powerful yet simple description that lets one think of fluid transport as a series of fluid pressure accumulation and release, that shape intermittent transport from a generally constant fluid source towards sinks at the surface, or less active, more diffuse reservoirs of fluid. Transient patterns of fluid flow in geologic systems can help understand seismicity patterns as symptoms of intermittent transport properties and fluid flow in the fault that connect seismic sources, controlling their activation and interaction in time and space. Regardless of the exact processes that trigger the activation of sources or exactly how permeability barriers break, it is a promising framework to explain the role of unsteady fluid circulation processes in shaping the dynamics of a wide range of systems (Gosselin et al., 2020; Materna et al., 2019; Ross et al., 2020; Wech et al., 2020).

References

Abercrombie, R. E. (1995, December). Earthquake source scaling relationships from -1 to 5 M_L using seismograms recorded at 2.5-km depth. *Journal of Geophysical Research: Solid Earth*, *100*(B12), 24015–24036. https://doi.org/10.1029/95JB02397
53, 56, 58

Agbangla, G. C., Bacchin, P., & Climent, E. (2014). Collective dynamics of flowing colloids during pore clogging. *Soft Matter*, *10*(33), 6303–6315. https://doi.org/10.1039/C4SM00869C
74

Ague, J. J. (2014, January). 4.6 - Fluid Flow in the Deep Crust. In H. D. Holland & K. K. Turekian (Eds.), *Treatise on Geochemistry (Second Edition)* (pp. 203–247). Oxford: Elsevier. https://doi.org/10.1016/B978-0-08-095975-7.00306-5
95

Aki, K., & Richards. (2002). *Quantitative Seismology* (Second Edition ed., Vol. 1). University Science Books.
32

Allmann, B. P., & Shearer, P. M. (2009, January). Global variations of stress drop for moderate to large earthquakes: GLOBAL STRESS DROP VARIATIONS. *Journal of Geophysical Research: Solid Earth*, *114*(B1). https://doi.org/10.1029/2008JB005821
26, 35, 36, 42, 43, 57

Amagai, T., Okamoto, A., Niibe, T., Hirano, N., Motomiya, K., & Tsuchiya, N. (2019, December). Silica nanoparticles produced by explosive flash vaporization during earthquakes. *Scientific Reports*, *9*(1), 9738. https://doi.org/10.1038/s41598-019-46320-7
18, 74, 123

Anderson, J. G., Das, S., Boatwright, J., & Scholz, C. H. (1986). Implication of attenuation for studies of the earthquake source. *Earthquake Source Mechanics*, *37*, 311–318.
56

Anderson, J. G., & Hough, S. E. (1984). A model for the shape of the Fourier amplitude spectrum of acceleration at high frequencies. *Bulletin of the Seismological Society of America*, *74*(5), 1969–1993.
53, 57

Anderson, R. N., Uyeda, S., & Miyashiro, A. (1976, February). Geophysical and Geochemical Constraints at Converging Plate Boundaries–Part I: Dehydration in the Downgoing Slab. *Geophysical Journal International*, *44*(2), 333–357. https://doi.org/10.1111/j.1365-246X.1976.tb03660.x
108

Ando, R., Nakata, R., & Hori, T. (2010). A slip pulse model with fault heterogeneity for low-frequency earthquakes and tremor along plate interfaces. *Geophysical Research Letters*, *37*(10). https://doi.org/10.1029/2010GL043056
4, 8, 14, 170

Angiboust, S., Kirsch, J., Oncken, O., Glodny, J., Monié, P., & Rybacki, E. (2015, June). Probing the transition between seismically coupled and decoupled segments along an ancient subduction interface. *Geochemistry, Geophysics, Geosystems*, *16*(6), 1905–1922. https://doi.org/10.1002/2015GC005776
16, 65, 66, 95, 108, 112, 139

Angiboust, S., Pettke, T., De Hoog, J. C. M., Caron, B., & Oncken, O. (2014, May). Channelized Fluid Flow and Eclogite-facies Metasomatism along the Subduction Shear Zone. *Journal of Petrology*, *55*(5), 883–916. https://doi.org/10.1093/petrology/egu010
66, 168

Angiboust, S., Wolf, S., Burov, E., Agard, P., & Yamato, P. (2012). Effect of fluid circulation on subduction interface tectonic processes: Insights from thermo-mechanical numerical modelling. *Earth and Planetary Science Letters*, *357–358*, 238–248. https://doi.org/10.1016/j.epsl.2012.09.012
45

Annen, C., Blundy, J. D., & Sparks, R. S. J. (2006, March). The Genesis of Intermediate and Silicic Magmas in Deep Crustal Hot Zones. *Journal of Petrology*, *47*(3), 505–539. https://doi.org/10.1093/petrology/egi084
173

Aochi, H., Poisson, B., Toussaint, R., Rachez, X., & Schmittbuhl, J. (2013, December). Self-induced seismicity due to fluid circulation along faults. *Geophysical Journal International*, *196*(3), 1544–1563. https://doi.org/10.1093/gji/ggt356
67

Archuleta, R. J., Cranswick, E., Mueller, C., & Spudich, P. (1982, June). Source parameters of the 1980 Mammoth Lakes, California, earthquake sequence. *Journal of Geophysical Research: Solid Earth*, *87*(B6), 4595–4607. https://doi.org/10.1029/JB087iB06p04595
56

Aristide, A. (2020, June). *Modeling Fluid Migration in Subduction Zones.* http://eos.org/science-updates/modeling-fluid-migration-in-subduction-zones.
16

Atkinson, G. M. (1995, October). Attenuation and source parameters of earthquakes in the Cascadia region. *Bulletin of the Seismological Society of America*, *85*(5), 1327–1342. https://doi.org/10.1785/BSSA0850051327
54

Audet, P., & Bürgmann, R. (2014, June). Possible control of subduction zone slow-earthquake periodicity by silica enrichment. *Nature*, *510*(7505), 389–392. https://doi.org/10.1038/nature13391
112, 143

Audet, P., & Kim, Y. (2016, February). Teleseismic constraints on the geological environment of deep episodic slow earthquakes in subduction zone forearcs: A review. *Tectonophysics*, *670*, 1–15. https://doi.org/10.1016/j.tecto.2016.01.005
7, 64, 65

Auradou, H., Drazer, G., Hulin, J. P., & Koplik, J. (2005, September). Permeability anisotropy induced by the shear displacement of rough fracture walls: PERMEABILITY ANISOTROPY. *Water Resources Research*, *41*(9). https://doi.org/10.1029/2005WR003938
67

Baltay, A. S., & Beroza, G. C. (2013, December). Ground-motion prediction from tremor. *Geophysical Research Letters*, *40*(24), 6340–6345.

https://doi.org/10.1002/2013GL058506
56
Barbot, S. (2019). Slow-slip, slow earthquakes, period-two cycles, full and partial ruptures, and deterministic chaos in a single asperity fault. *Tectonophysics*, *768*, 228171. https://doi.org/10.1016/j.tecto.2019.228171
65
Bassett, D., & Watts, A. B. (2015, May). Gravity anomalies, crustal structure, and seismicity at subduction zones: 1. Seafloor roughness and subducting relief: CRUSTAL STRUCTURE AND SEISMICITY: 1. SUBDUCTING RELIEF. *Geochemistry, Geophysics, Geosystems*, *16*(5), 1508–1540. https://doi.org/10.1002/2014GC005684
141, 142
Beaucé, E., Frank, W. B., Paul, A., Campillo, M., & Hilst, R. D. (2019, November). Systematic Detection of Clustered Seismicity Beneath the Southwestern Alps. *Journal of Geophysical Research: Solid Earth*, *124*(11), 11531–11548. https://doi.org/10.1029/2019JB018110
71, 109, 113
Beaucé, E., van der Hilst, R. D., & Campillo, M. (2022, March). *Microseismic Constraints on the State of the North Anatolian Fault Thirteen Years after the 1999 M7.4 Izmit Earthquake* [Preprint]. http://www.essoar.org/doi/10.1002/essoar.10510912.1. Earth and Space Science Open Archive. https://doi.org/10.1002/essoar.10510912.1
109, 113
Beckingham, L. E. (2017). Evaluation of macroscopic porosity-permeability relationships in heterogeneous mineral dissolution and precipitation scenarios. *Water Resources Research*, *53*(12), 10217–10230. https://doi.org/10.1002/2017WR021306
74, 77, 81, 97
Bedford, J. R., Moreno, M., Deng, Z., Oncken, O., Schurr, B., John, T., … Bevis, M. (2020, April). Months-long thousand-kilometre-scale wobbling before great subduction earthquakes. *Nature*, *580*(7805), 628–635. https://doi.org/10.1038/s41586-020-2212-1
4
Beeler, N. M., Thomas, A., Bürgmann, R., & Shelly, D. (2013, November). Inferring fault rheology from low-frequency earthquakes on the San Andreas. *Journal of Geophysical Research: Solid Earth*, *118*(11), 5976–5990. https://doi.org/10.1002/2013JB010118
26, 45, 65
Behr, W. M., & Bürgmann, R. (2021, March). What's down there? The structures, materials and environment of deep-seated slow slip and tremor. *Philosophical Transactions of the Royal Society A: Mathematical, Physical and Engineering Sciences*, *379*(2193), 20200218. https://doi.org/10.1098/rsta.2020.0218
16, 66, 108
Ben-Zion, Y. (2012, May). Episodic tremor and slip on a frictional interface with critical zero weakening in elastic solid. *Geophysical Journal International*, *189*(2), 1159–1168. https://doi.org/10.1111/j.1365-246X.2012.05422.x
65
Benson, P. M., Austria, D. C., Gehne, S., Butcher, E., Harnett, C. E., Fazio, M., … Tomas, R. (2020, December). Laboratory simulations of fluid-induced seismicity, hydraulic fracture, and fluid flow. *Geomechanics for Energy and the Environment*, *24*, 100169. https://doi.org/10.1016/j.gete.2019.100169
9
Benson, P. M., Vinciguerra, S., Meredith, P. G., & Young, R. P. (2008, October). Laboratory Simulation of Volcano Seismicity. *Science*, *322*(5899), 249–252.

https://doi.org/10.1126/science.1161927
2, 9, 66, 77, 171

Bernaudin, M., & Gueydan, F. (2018, April). Episodic Tremor and Slip Explained by Fluid-Enhanced Microfracturing and Sealing. *Geophysical Research Letters*, *45*(8), 3471–3480. https://doi.org/10.1029/2018GL077586
66, 138

Beroza, G. C., & Ide, S. (2011, May). Slow Earthquakes and Nonvolcanic Tremor. *Annual Review of Earth and Planetary Sciences*, *39*(1), 271–296. https://doi.org/10.1146/annurev-earth-040809-152531
25, 64

Bhattacharya, P., & Viesca, R. C. (2019, May). Fluid-induced aseismic fault slip outpaces pore-fluid migration. *Science*, *364*(6439), 464–468. https://doi.org/10.1126/science.aaw7354
3

Bianchi, F., Thielmann, M., de Arcangelis, L., & Herrmann, H. J. (2018, January). Critical Bursts in Filtration. *Physical Review Letters*, *120*(3), 034503. https://doi.org/10.1103/PhysRevLett.120.034503
17, 18, 67, 74, 123, 167, 168

Bianchi, F., Wittel, F. K., Thielmann, M., Trtik, P., & Herrmann, H. J. (2018, March). Tomographic Study of Internal Erosion of Particle Flows in Porous Media. *Transport in Porous Media*, *122*(1), 169–184. https://doi.org/10.1007/s11242-017-0996-8
74

Blakely, R. J., Brocher, T. M., & Wells, R. E. (2005). Subduction-zone magnetic anomalies and implications for hydrated forearc mantle. *Geology*, *33*(6), 445. https://doi.org/10.1130/G21447.1
141, 142

Bocchini, G. M., Martínez-Garzón, P., Harrington, R. M., & Bohnhoff, M. (2021). Does Deep Tectonic Tremor Occur in the Central-Eastern Mediterranean Basin? *Journal of Geophysical Research: Solid Earth*, *126*(1), 2020JB020448. https://doi.org/10.1029/2020JB020448
96

Bostock, M. G., Royer, A. A., Hearn, E. H., & Peacock, S. M. (2012, November). Low frequency earthquakes below southern Vancouver Island. *Geochemistry, Geophysics, Geosystems*, *13*(11), n/a-n/a. https://doi.org/10.1029/2012GC004391
5, 45, 64

Bostock, M. G., Thomas, A. M., Rubin, A. M., & Christensen, N. I. (2017, January). On corner frequencies, attenuation, and low-frequency earthquakes. *Journal of Geophysical Research: Solid Earth*, *122*(1), 543–557. https://doi.org/10.1002/2016JB013405
7, 45, 58

Bostock, M. G., Thomas, A. M., Savard, G., Chuang, L., & Rubin, A. M. (2015). Magnitudes and moment-duration scaling of low-frequency earthquakes beneath southern Vancouver Island. *Journal of Geophysical Research: Solid Earth*, *120*(9), 6329–6350. https://doi.org/10.1002/2015JB012195
5, 8, 10, 12, 26, 27, 35, 36, 37, 38, 42, 43, 66, 68

Bouchon, M. (2003). A review of the discrete wavenumber method. In *Seismic motion, lithospheric structures, earthquake and volcanic sources: The keiiti aki volume* (pp. 445–465). Springer.
33

Brodsky, E. E. (2019, May). The importance of studying small earthquakes. *Science*,

364(6442), 736–737. https://doi.org/10.1126/science.aax2490
2

Brodsky, E. E., & van der Elst, N. J. (2014, May). The Uses of Dynamic Earthquake Triggering. *Annual Review of Earth and Planetary Sciences*, *42*(1), 317–339. https://doi.org/10.1146/annurev-earth-060313-054648
2

Brudzinski, M. R., & Allen, R. M. (2007). Segmentation in episodic tremor and slip all along Cascadia. *Geology*, *35*(10), 907. https://doi.org/10.1130/G23740A.1
14, 69, 109, 111, 112, 138, 151

Brudzinski, M. R., Hinojosa-Prieto, H. R., Schlanser, K. M., Cabral-Cano, E., Arciniega-Ceballos, A., Diaz-Molina, O., & DeMets, C. (2010, August). Nonvolcanic tremor along the Oaxaca segment of the Middle America subduction zone. *Journal of Geophysical Research*, *115*, B00A23. https://doi.org/10.1029/2008JB006061
108, 150

Brune, J. N. (1970). Tectonic stress and the spectra of seismic shear waves from earthquakes. *Journal of geophysical research*, *75*(26), 4997–5009. https://doi.org/10.1029/JB075i026p04997
32, 52, 57

Calvert, A. J., Preston, L. A., & Farahbod, A. M. (2011, August). Sedimentary underplating at the Cascadia mantle-wedge corner revealed by seismic imaging. *Nature Geoscience*, *4*(8), 545–548. https://doi.org/10.1038/ngeo1195
108

Candela, T., Brodsky, E. E., Marone, C., & Elsworth, D. (2014, April). Laboratory evidence for particle mobilization as a mechanism for permeability enhancement via dynamic stressing. *Earth and Planetary Science Letters*, *392*, 279–291. https://doi.org/10.1016/j.epsl.2014.02.025
17, 18, 67, 74, 167

Cappa, F., Guglielmi, Y., & De Barros, L. (2022, December). Transient evolution of permeability and friction in a slowly slipping fault activated by fluid pressurization. *Nature Communications*, *13*(1), 3039. https://doi.org/10.1038/s41467-022-30798-3
3, 17

Cashman, K. V., Sparks, R. S. J., & Blundy, J. D. (2017, March). Vertically extensive and unstable magmatic systems: A unified view of igneous processes. *Science*, *355*(6331), eaag3055. https://doi.org/10.1126/science.aag3055
173

Castro, R. R., Anderson, J. G., & Singh, S. K. (1990, December). Site response, attenuation and source spectra of S waves along the Guerrero, Mexico, subduction zone. *Bulletin of the Seismological Society of America*, *80*(6A), 1481–1503. https://doi.org/10.1785/BSSA08006A1481
53

Cattania, C., & Segall, P. (2019, January). Crack Models of Repeating Earthquakes Predict Observed Moment-Recurrence Scaling. *Journal of Geophysical Research: Solid Earth*, *124*(1), 476–503. https://doi.org/10.1029/2018JB016056
8

Cattania, C., & Segall, P. (2021, April). Precursory Slow Slip and Foreshocks on Rough Faults. *Journal of Geophysical Research: Solid Earth*, *126*(4). https://doi.org/10.1029/2020JB020430
112

Chamberlain, C. J., Shelly, D. R., Townend, J., & Stern, T. A. (2014). Low-frequency

earthquakes reveal punctuated slow slip on the deep extent of the Alpine Fault, New Zealand. *Geochemistry, Geophysics, Geosystems*, *15*(7), 2984–2999.
27, 42

Chao, K., & Obara, K. (2016, January). Triggered tectonic tremor in various types of fault systems of Japan following the 2012 M_w 8.6 Sumatra earthquake: TRIGGERED TREMOR IN JAPAN. *Journal of Geophysical Research: Solid Earth*, *121*(1), 170–187. https://doi.org/10.1002/2015JB012566
145

Chao, K., Peng, Z., Gonzalez-Huizar, H., Aiken, C., Enescu, B., Kao, H., … Matsuzawa, T. (2013, May). A Global Search for Triggered Tremor Following the 2011 Mw 9.0 Tohoku Earthquake. *Bulletin of the Seismological Society of America*, *103*(2B), 1551–1571. https://doi.org/10.1785/0120120171
145

Chestler, S. R., & Creager, K. C. (2017a). Evidence for a scale-limited low-frequency earthquake source process. *Journal of Geophysical Research: Solid Earth*, *122*(4), 3099–3114. https://doi.org/10.1002/2016JB013717
7, 26, 42, 44, 65, 69

Chestler, S. R., & Creager, K. C. (2017b, December). A Model for Low-Frequency Earthquake Slip. *Geochemistry, Geophysics, Geosystems*, *18*(12), 4690–4708. https://doi.org/10.1002/2017GC007253
5

Chouet, B. (1986). Dynamics of a fluid-driven crack in three dimensions by the finite difference method. *Journal of Geophysical Research*, *91*(B14), 13967. https://doi.org/10.1029/JB091iB14p13967
171

Chouet, B., Aki, K., & Tsujiura, M. (1978). Regional variation of the scaling law of earthquake source spectra. *Bulletin of the Seismological Society of America*, *68*(1), 49–79.
56

Chouet, B. A. (1996, March). Long-period volcano seismicity: Its source and use in eruption forecasting. *Nature*, *380*(6572), 309. https://doi.org/10.1038/380309a0
4, 66, 171, 173

Chouet, B. A., & Matoza, R. S. (2013, February). A multi-decadal view of seismic methods for detecting precursors of magma movement and eruption. *Journal of Volcanology and Geothermal Research*, *252*, 108–175. https://doi.org/10.1016/j.jvolgeores.2012.11.013
171

Civan, F. (2016). Modified formulations of particle deposition and removal kinetics in saturated porous media. *Transp Porous Med*, *111*, 381–410. https://doi.org/10.1007/s11242-015-0600-z
74, 76

Cornet, F. H., Helm, J., Poitrenaud, H., & Etchecopar, A. (1997). Seismic and Aseismic Slips Induced by Large-scale Fluid Injections. *Pure appl. geophys.*, *150*, 21.
2

Coutant, O. (2008). *Axitra software.*
33

Cruz-Atienza, V. M., Villafuerte, C., & Bhat, H. S. (2018, December). Rapid tremor migration and pore-pressure waves in subduction zones. *Nature Communications*, *9*(1). https://doi.org/10.1038/s41467-018-05150-3
11, 12, 13, 17, 44, 66, 67, 70, 93, 94, 112, 138

De Barros, L., Cappa, F., Deschamps, A., & Dublanchet, P. (2020, May). Imbricated Aseismic

Slip and Fluid Diffusion Drive a Seismic Swarm in the Corinth Gulf, Greece. *Geophysical Research Letters*, *47*(9). https://doi.org/10.1029/2020GL087142
3

Delbridge, B. G., Carmichael, J. D., Nadeau, R. M., Shelly, D. R., & Bürgmann, R. (2020, May). Geodetic Measurements of Slow-Slip Events Southeast of Parkfield, CA. *Journal of Geophysical Research: Solid Earth*, *125*(5). https://doi.org/10.1029/2019JB019059
64

Delouche, N., Schofield, A. B., & Tabuteau, H. (2020). Dynamics of progressive pore clogging by colloidal aggregates. *Soft Matter*, *16*(43), 9899–9907. https://doi.org/10.1039/D0SM01403F
74

Dieterich, J. H. (1992). Earthquake nucleation on faults with rate-and state-dependent strength. *Tectonophysics*, *211*(1), 115–134. https://doi.org/10.1016/0040-1951(92)90055-B
65

Doan, M. L., Brodsky, E. E., Kano, Y., & Ma, K. F. (2006). In situ measurement of the hydraulic diffusivity of the active Chelungpu Fault, Taiwan. *Geophysical Research Letters*, *33*(16), L16317. https://doi.org/10.1029/2006GL026889
94

Dublanchet, P., & De Barros, L. (2021, January). Dual Seismic Migration Velocities in Seismic Swarms. *Geophysical Research Letters*, *48*(1). https://doi.org/10.1029/2020GL090025
12

Ellsworth, W. L. (2013, July). Injection-Induced Earthquakes. *Science*, *341*(6142), 1225942. https://doi.org/10.1126/science.1225942
2

Eshelby, J. D. (1957). The determination of the elastic field of an ellipsoidal inclusion, and related problems. *Proceedings of the Royal Society of London. Series A. Mathematical and Physical Sciences*, *241*(1226), 376–396.
36

Ester, M., Kriegel, H.-P., Sander, J., & Xu, X. (1996). A Density-Based Algorithm for Discovering Clusters in Large Spatial Databases with Noise. *Proceedings of the 2nd International Conference on Knowledge Discovery and Data mining*, 226–231.
117

Etheridge, M. A., Wall, V. J., Cox, S. F., & Vernon, R. H. (1984, June). High fluid pressures during regional metamorphism and deformation: Implications for mass transport and deformation mechanisms. *Journal of Geophysical Research: Solid Earth*, *89*(B6), 4344–4358. https://doi.org/10.1029/JB089iB06p04344
104

Fagereng, Å., & Sibson, R. H. (2010, August). Mélange rheology and seismic style. *Geology*, *38*(8), 751–754. https://doi.org/10.1130/G30868.1
68

Farge, G., Shapiro, N. M., & Frank, W. B. (2020, August). Moment-Duration Scaling of Low-Frequency Earthquakes in Guerrero, Mexico. *Journal of Geophysical Research: Solid Earth*, *125*(8). https://doi.org/10.1029/2019JB019099
5, 8, 10

Frank, W. B., & Abercrombie, R. E. (2018, February). Adapting the Matched-Filter Search to a Wide-Aperture Network: An Aftershock Sequence and an Earthquake Swarm in Connecticut. *Bulletin of the Seismological Society of America*, *108*(1), 524–532.

https://doi.org/10.1785/0120170190
51

Frank, W. B., & Brodsky, E. E. (2019, October). Daily measurement of slow slip from low-frequency earthquakes is consistent with ordinary earthquake scaling. *Science Advances*, *5*(10), eaaw9386. https://doi.org/10.1126/sciadv.aaw9386
14, 26, 43, 94

Frank, W. B., Radiguet, M., Rousset, B., Shapiro, N. M., Husker, A. L., Kostoglodov, V., … Campillo, M. (2015, April). Uncovering the geodetic signature of silent slip through repeating earthquakes: UNCOVERING SILENT SLIP. *Geophysical Research Letters*, *42*(8), 2774–2779. https://doi.org/10.1002/2015GL063685
2, 8, 64, 71, 108, 170

Frank, W. B., & Shapiro, N. M. (2014, May). Automatic detection of low-frequency earthquakes (LFEs) based on a beamformed network response. *Geophysical Journal International*, *197*(2), 1215–1223. https://doi.org/10.1093/gji/ggu058
7, 27

Frank, W. B., Shapiro, N. M., & Gusev, A. A. (2018, July). Progressive reactivation of the volcanic plumbing system beneath Tolbachik volcano (Kamchatka, Russia) revealed by long-period seismicity. *Earth and Planetary Science Letters*, *493*, 47–56. https://doi.org/10.1016/j.epsl.2018.04.018
174

Frank, W. B., Shapiro, N. M., Husker, A. L., Kostoglodov, V., Bhat, H. S., & Campillo, M. (2015, March). Along-fault pore-pressure evolution during a slow-slip event in Guerrero, Mexico. *Earth and Planetary Science Letters*, *413*, 135–143. https://doi.org/10.1016/j.epsl.2014.12.051
15, 26, 44, 66, 70, 93, 94, 108

Frank, W. B., Shapiro, N. M., Husker, A. L., Kostoglodov, V., Gusev, A. A., & Campillo, M. (2016, April). The evolving interaction of low-frequency earthquakes during transient slip. *Science Advances*, *2*(4), e1501616. https://doi.org/10.1126/sciadv.1501616
14, 15, 71, 87, 93, 109, 113, 138

Frank, W. B., Shapiro, N. M., Husker, A. L., Kostoglodov, V., Romanenko, A., & Campillo, M. (2014, October). Using systematically characterized low-frequency earthquakes as a fault probe in Guerrero, Mexico. *Journal of Geophysical Research: Solid Earth*, *119*(10), 7686–7700. https://doi.org/10.1002/2014JB011457
4, 5, 7, 8, 11, 12, 14, 26, 27, 28, 29, 30, 31, 33, 37, 45, 51, 64, 68, 69, 70, 71, 93, 94, 96, 108, 138, 150

Frank, W. B., Shapiro, N. M., Kostoglodov, V., Husker, A. L., Campillo, M., Payero, J. S., & Prieto, G. A. (2013, June). Low-frequency earthquakes in the Mexican Sweet Spot: LFES IN THE MEXICAN SWEET SPOT. *Geophysical Research Letters*, *40*(11), 2661–2666. https://doi.org/10.1002/grl.50561
27, 28, 33, 64

Frezzotti, M. L., & Ferrando, S. (2015). The chemical behavior of fluids released during deep subduction based on fluid inclusions. *American Mineralogist*, *100*, 352–377. https://doi.org/10.2138/am-2015-4933
65, 73

Ghanbarian, B., Hunt, A. G., Ewing, R. P., & Sahimi, M. (2013). Tortuosity in porous media: A critical review. *Soil Science Society of America Journal*, *77*(5), 1461–1477. https://doi.org/10.2136/sssaj2012.0435
77

Ghosh, A., Vidale, J. E., Sweet, J. R., Creager, K. C., Wech, A. G., Houston, H., & Brodsky,

E. E. (2010, December). Rapid, continuous streaking of tremor in Cascadia. *Geochemistry, Geophysics, Geosystems*, *11*(12), n/a-n/a. https://doi.org/10.1029/2010GC003305
11, 12, 17, 69, 70

Gibbons, S. J., & Ringdal, F. (2006). The detection of low magnitude seismic events using array-based waveform correlation. *Geophysical Journal International*, *165*(1), 149–166. https://doi.org/10.1111/j.1365-246X.2006.02865.x
27

Giger, S. B., Tenthorey, E., Cox, S. F., & Fitz Gerald, J. D. (2007, July). Permeability evolution in quartz fault gouges under hydrothermal conditions. *Journal of Geophysical Research*, *112*(B7). https://doi.org/10.1029/2006JB004828
66

Gold, T., & Soter, S. (1985). Fluid ascent through the solid lithosphere and its relation to earthquakes. *Pure and Applied Geophysics PAGEOPH*, *122*(2-4), 492–530. https://doi.org/10.1007/BF00874614
9

Gomberg, J., Wech, A., Creager, K., Obara, K., & Agnew, D. (2016, June). Reconsidering earthquake scaling. *Geophysical Research Letters*, *43*(12), 6243–6251. https://doi.org/10.1002/2016GL069967
26, 43, 70

Gosselin, J. M., Audet, P., Estève, C., McLellan, M., Mosher, S. G., & Schaeffer, A. J. (2020, January). Seismic evidence for megathrust fault-valve behavior during episodic tremor and slip. *Science Advances*, *6*(4), eaay5174. https://doi.org/10.1126/sciadv.aay5174
15, 66, 108, 112, 175

Gratier, J.-P., & Favreau, P. (2003). Modeling fluid transfer along California faults when integrating pressure solution crack sealing and compaction processes. , 25.
169

Guglielmi, Y., Cappa, F., Avouac, J.-P., Henry, P., & Elsworth, D. (2015, June). Seismicity triggered by fluid injection-induced aseismic slip. *Science*, *348*(6240), 1224–1226. https://doi.org/10.1126/science.aab0476
3

Gutemberg, B., & Richter, C. F. (1944). Frequency of earthquakes in California. *Bulletin of the Seismological society of America*, *34*(4), 185–188.
2, 7

Halpaap, F., Rondenay, S., Perrin, A., Goes, S., Ottemöller, L., Austrheim, H., … Eeken, T. (2019, April). Earthquakes track subduction fluids from slab source to mantle wedge sink. *Science Advances*, *5*(4), eaav7369. https://doi.org/10.1126/sciadv.aav7369
112

Han, R., & Hirose, T. (2012, October). Clay–clast aggregates in fault gouge: An unequivocal indicator of seismic faulting at shallow depths? *Journal of Structural Geology*, *43*, 92–99. https://doi.org/10.1016/j.jsg.2012.07.008
18, 74, 123

Hayes, G. (2018). *Slab2 - A Comprehensive Subduction Zone Geometry Model.* U.S. Geological Survey. https://doi.org/10.5066/F7PV6JNV
69, 111, 150, 151

Hendriyana, A. (2021). Influence of structure and pore pressure of plate interface on tectonic tremor in the Nankai subduction zone, Japan. *Earth and Planetary Science Letters*, 12.
94

Hirose, H., Asano, Y., Obara, K., Kimura, T., Matsuzawa, T., Tanaka, S., & Maeda, T. (2010, December). Slow Earthquakes Linked Along Dip in the Nankai Subduction Zone: Fig. 1. *Science*, *330*(6010), 1502–1502. https://doi.org/10.1126/science.1197102
66

Honda, S., & Yomogida, K. (1993, February). Periodic magma movement in the conduit with a barrier: A model for the volcanic tremor. *Geophysical Research Letters*, *20*(3), 229–232. https://doi.org/10.1029/92GL02959
8, 95, 171

Horálek, J., & Fischer, T. (2008, October). Role of crustal fluids in triggering the West Bohemia/Vogtland earthquake swarms: Just what we know (a review). *Studia Geophysica et Geodaetica*, *52*(4), 455–478. https://doi.org/10.1007/s11200-008-0032-0
3

Hotovec-Ellis, A. J., Shelly, D. R., Hill, D. P., Pitt, A. M., Dawson, P. B., & Chouet, B. A. (2018, August). Deep fluid pathways beneath Mammoth Mountain, California, illuminated by migrating earthquake swarms. *Science Advances*, *4*(8), eaat5258. https://doi.org/10.1126/sciadv.aat5258
2, 3

Houston, H. (2001). Influence of depth, focal mechanism, and tectonic setting on the shape and duration of earthquake source time functions. *Journal of Geophysical Research: Solid Earth*, *106*(B6), 11137–11150. https://doi.org/10.1029/2000JB900468
26, 42

Houston, H., Delbridge, B. G., Wech, A. G., & Creager, K. C. (2011, June). Rapid tremor reversals in Cascadia generated by a weakened plate interface. *Nature Geoscience*, *4*(6), 404–409. https://doi.org/10.1038/ngeo1157
12, 26, 70

Humphrey, J. R., Jr., & Anderson, J. G. (1992, August). Shear-wave attenuation and site response in Guerrero, Mexico. *Bulletin of the Seismological Society of America*, *82*(4), 1622–1645. https://doi.org/10.1785/BSSA0820041622
53

Husker, A., Frank, W. B., Gonzalez, G., Avila, L., Kostoglodov, V., & Kazachkina, E. (2019, January). Characteristic Tectonic Tremor Activity Observed Over Multiple Slow Slip Cycles in the Mexican Subduction Zone. *Journal of Geophysical Research: Solid Earth*, *124*(1), 599–608. https://doi.org/10.1029/2018JB016517
14, 109, 111, 138, 150

Husker, A., Stubailo, I., Lukac, M., Naik, V., Guy, R., Davis, P., & Estrin, D. (2008). WiLSoN: The wirelessly linked seismological network and its application in the middle american subduction experiment. *Seismological Research Letters*, *79*, 438–443.
27

Husker, A. L., Kostoglodov, V., Cruz-Atienza, V. M., Legrand, D., Shapiro, N. M., Payero, J. S., … Huesca-Pérez, E. (2012). Temporal variations of non-volcanic tremor (NVT) locations in the Mexican subduction zone: Finding the NVT sweet spot. *Geochemistry, Geophysics, Geosystems*, *13*(3), n/a–n/a. https://doi.org/10.1029/2011GC003916
64, 69

Hyndman, R. D., McCrory, P. A., Wech, A., Kao, H., & Ague, J. (2015, June). Cascadia subducting plate fluids channelled to fore-arc mantle corner: ETS and silica deposition. *Journal of Geophysical Research: Solid Earth*, *120*(6), 4344–4358. https://doi.org/10.1002/2015JB011920
65, 77, 79

Ide, S. (2008). A Brownian walk model for slow earthquakes. *Geophysical Research Letters*,

35(17). https://doi.org/10.1029/2008GL034821
42, 43

Ide, S. (2010, July). Striations, duration, migration and tidal response in deep tremor. *Nature*, *466*(7304), 356–359. https://doi.org/10.1038/nature09251
69, 112, 122, 142, 144

Ide, S. (2012, March). Variety and spatial heterogeneity of tectonic tremor worldwide. *Journal of Geophysical Research: Solid Earth*, *117*(B3). https://doi.org/10.1029/2011JB008840
11, 12, 70

Ide, S. (2014). Modeling fast and slow earthquakes at various scales. *Proceedings of the Japan Academy. Series B, Physical and biological sciences*, *90(8)*, 259–277. https://doi.org/10.2183/pjab.90.259
65

Ide, S., Beroza, G. C., Prejean, S. G., & Ellsworth, W. L. (2003, May). Apparent break in earthquake scaling due to path and site effects on deep borehole recordings: SMALL EARTHQUAKE SCALING IN LONG VALLEY. *Journal of Geophysical Research: Solid Earth*, *108*(B5). https://doi.org/10.1029/2001JB001617
7

Ide, S., Beroza, G. C., Shelly, D. R., & Uchide, T. (2007, May). A scaling law for slow earthquakes. *Nature*, *447*(7140), 76–79. https://doi.org/10.1038/nature05780
4, 26, 35, 36, 37, 43

Ide, S., & Maury, J. (2018). Seismic Moment, Seismic Energy, and Source Duration of Slow Earthquakes: Application of Brownian slow earthquake model to three major subduction zones. *Geophysical Research Letters*, *45*(7), 3059–3067. https://doi.org/10.1002/2018GL077461
42

Ide, S., Shelly, D. R., & Beroza, G. C. (2007, February). Mechanism of deep low frequency earthquakes: Further evidence that deep non-volcanic tremor is generated by shear slip on the plate interface. *Geophysical Research Letters*, *34*(3). https://doi.org/10.1029/2006GL028890
8, 9, 170

Idehara, K., Yabe, S., & Ide, S. (2014, December). Regional and global variations in the temporal clustering of tectonic tremor activity. *Earth, Planets and Space*, *66*(1), 66. https://doi.org/10.1186/1880-5981-66-66
70, 71, 108, 109, 113, 138

Iglesias, A., Clayton, R. W., Pérez-Campos, X., Singh, S., Pacheco, J. F., García, D., & Valdés-González, C. (2010). S wave velocity structure below central Mexico using high-resolution surface wave tomography. *Journal of Geophysical Research: Solid Earth*, *115*(B6).
33

Im, K., Elsworth, D., & Wang, C. (2019a). Cyclic permeability evolution during repose then reactivation of fractures and faults. *Journal of Geophysical Research: Solid Earth*, *124*(5), 4492–4506. https://doi.org/10.1029/2019JB017309
67

Im, K., Elsworth, D., & Wang, C. (2019b, May). Cyclic Permeability Evolution During Repose Then Reactivation of Fractures and Faults. *Journal of Geophysical Research: Solid Earth*, *124*(5), 4492–4506. https://doi.org/10.1029/2019JB017309
17, 170

Ito, Y., & Obara, K. (2006). Very low frequency earthquakes within accretionary prisms are

very low stress-drop earthquakes. *Geophysical Research Letters*, *33*(9).
44

Iwasaki, T., Sato, H., Ishiyama, T., Shinohara, M., & Hashima, A. (2015). Fundamental structure model of island arcs and subducted plates in and around Japan. In *AGU Fall Meeting Abstracts* (Vol. 2015, p. T31B-2878).
147

Jäger, R., Mendoza, M., & Herrmann, H. J. (2017a, January). Channelization in porous media driven by erosion and deposition. *Physical Review E*, *95*(1), 013110. https://doi.org/10.1103/PhysRevE.95.013110
66

Jäger, R., Mendoza, M., & Herrmann, H. J. (2017b, September). The Mechanism behind Erosive Bursts in Porous Media. *Physical Review Letters*, *119*(12), 124501. https://doi.org/10.1103/PhysRevLett.119.124501
18, 67, 74, 167

Jäger, R., Mendoza, M., & Herrmann, H. J. (2018, July). Clogging at pore scale and pressure-induced erosion. *Physical Review Fluids*, *3*(7), 074302. https://doi.org/10.1103/PhysRevFluids.3.074302
18, 76, 123

Journeau, C., Shapiro, N. M., Seydoux, L., Soubestre, J., Koulakov, I. Y., Jakovlev, A. V., … Jaupart, C. (2022, February). Seismic tremor reveals active trans-crustal magmatic system beneath Kamchatka volcanoes. *Science Advances*, *8*(5), eabj1571. https://doi.org/10.1126/sciadv.abj1571
2, 172, 173, 175

Julian, B. R. (1994, June). Volcanic tremor: Nonlinear excitation by fluid flow. *Journal of Geophysical Research: Solid Earth*, *99*(B6), 11859–11877. https://doi.org/10.1029/93JB03129
8, 66, 171

Kanamori, H., & Anderson, D. L. (1975). Theoretical basis of some empirical relations in seismology. *Bulletin of the Seismological Society of America*, *65*(5), 1073–1095.
7, 26, 43

Kano, M., Kato, A., Ando, R., & Obara, K. (2018, February). Strength of tremor patches along deep transition zone of a megathrust. *Scientific Reports*, *8*(1), 3655. https://doi.org/10.1038/s41598-018-22048-8
112

Kao, H., Shan, S.-J., Dragert, H., & Rogers, G. (2009, November). Northern Cascadia episodic tremor and slip: A decade of tremor observations from 1997 to 2007: NORTHERN CASCADIA ETS. *Journal of Geophysical Research: Solid Earth*, *114*(B11). https://doi.org/10.1029/2008JB006046
11, 70

Kao, H., Shan, S.-J., Dragert, H., Rogers, G., Cassidy, J. F., & Ramachandran, K. (2005). A wide depth distribution of seismic tremors along the northern Cascadia margin. *Nature*, *436*, 841–844. https://doi.org/10.1038/nature03903
44, 64

Kato, A., & Nakagawa, S. (2020, September). Detection of deep low-frequency earthquakes in the Nankai subduction zone over 11 years using a matched filter technique. *Earth, Planets and Space*, *72*(1), 128. https://doi.org/10.1186/s40623-020-01257-4
11

Katsumata, A., & Kamaya, N. (2003). Low-frequency continuous tremor around the Moho discontinuity away from volcanoes in the southwest Japan. *Geophysical Research*

Letters, *30*(1).
4, 44

Kim, Y., Clayton, R. W., & Jackson, J. M. (2010, June). Geometry and seismic properties of the subducting Cocos plate in central Mexico. *Journal of Geophysical Research*, *115*(B6). https://doi.org/10.1029/2009JB006942
28, 70

Kostoglodov, V., Husker, A., Shapiro, N. M., Payero, J. S., Campillo, M., Cotte, N., & Clayton, R. (2010). The 2006 slow slip event and nonvolcanic tremor in the Mexican subduction zone. *Geophysical Research Letters*, *37*(24). https://doi.org/10.1029/2010GL045424
27, 64, 66, 69

Kostoglodov, V., & Pacheco, J. F. (1999). *Cien años de sismicidad en méxico, instituto de geofísica, universidad nacional autónoma de méxico.*
27

Kotowski, A. J., & Behr, W. M. (2019, August). Length scales and types of heterogeneities along the deep subduction interface: Insights from exhumed rocks on Syros Island, Greece. *Geosphere*, *15*(4), 1038–1065. https://doi.org/10.1130/GES02037.1
68, 112, 170

Koyanagi, R. Y., Chouet, B., & Aki, K. (1987). Origin of volcanic tremor in Hawaii. *US Geological Survey Professional Paper*, *1350*(2), 1221–1257.
4

Kudrolli, A., & Clotet, X. (2016, July). Evolution of Porosity and Channelization of an Erosive Medium Driven by Fluid Flow. *Physical Review Letters*, *117*(2), 028001. https://doi.org/10.1103/PhysRevLett.117.028001
74, 81

Kurihara, R., Obara, K., Takeo, A., & Maeda, T. (2018, April). Migration of Deep Low-Frequency Tremor Triggered by Teleseismic Earthquakes in the Southwest Japan Subduction Zone. *Geophysical Research Letters*, *45*(8), 3413–3419. https://doi.org/10.1002/2017GL076779
145

Lay, T., Kanamori, H., Ammon, C. J., Koper, K. D., Hutko, A. R., Ye, L., … Rushing, T. M. (2012, April). Depth-varying rupture properties of subduction zone megathrust faults: MEGATHRUST RUPTURE DOMAINS. *Journal of Geophysical Research: Solid Earth*, *117*(B4), n/a-n/a. https://doi.org/10.1029/2011JB009133
5, 8

Lengliné, O., Lamourette, L., Vivin, L., Cuenot, N., & Schmittbuhl, J. (2014). Fluid-induced earthquakes with variable stress drop. *Journal of Geophysical Research: Solid Earth*, *119*(12), 8900–8913. https://doi.org/10.1002/2014JB011282
3, 43, 44

Lin, Y.-Y., Ma, K.-F., Kanamori, H., Song, T.-R. A., Lapusta, N., & Tsai, V. C. (2016, August). Evidence for non-self-similarity of microearthquakes recorded at a Taiwan borehole seismometer array. *Geophysical Journal International*, *206*(2), 757–773. https://doi.org/10.1093/gji/ggw172
3, 43, 44

Liu, Y., & Rice, J. R. (2007). Spontaneous and triggered aseismic deformation transients in a subduction fault model. *Journal of Geophysical Research: Solid Earth*, *112*(B9). https://doi.org/10.1029/2007JB004930
65

Lowen, S. B., & Teich, M. C. (2005). *Fractal-Based Point Processes* (Vol. 366). Hoboken, New

Jersey: John Wiley and Sons, Inc.
87, 114

Luo, Y., & Liu, Z. (2019). Rate-and-State Model Casts New Insight into Episodic Tremor and Slow-slip Variability in Cascadia. *Geophysical Research Letters*, 11.
8, 14, 15, 65, 97, 112, 138, 139

Luo, Y., & Liu, Z. (2021, December). Fault zone heterogeneities explain depth-dependent pattern and evolution of slow earthquakes in Cascadia. *Nature Communications*, *12*(1), 1959. https://doi.org/10.1038/s41467-021-22232-x
15

Madariaga, R. (1976). Dynamics of an expanding circular fault. *Bulletin of the Seismological Society of America*, *66*(3), 639–666.
36, 40

Mahdyiar, M. (1984). Attenuation properties of the Petatlan region, Mexico, and a local magnitude scale for microearthquakes in this area. *Ph. D. Thesis*.
53

Majer, E. L., Baria, R., Stark, M., Oates, S., Bommer, J., Smith, B., & Asanuma, H. (2007, June). Induced seismicity associated with Enhanced Geothermal Systems. *Geothermics*, *36*(3), 185–222. https://doi.org/10.1016/j.geothermics.2007.03.003
2

Manga, M., Beresnev, I., Brodsky, E. E., Elkhoury, J. E., Elsworth, D., Ingebritsen, S. E., … Wang, C.-Y. (2012). Changes in permeability caused by transient stresses: Field observations, experiments, and mechanisms. *Reviews of Geophysics*, *50*(2). https://doi.org/10.1029/2011RG000382
18, 67, 74, 75, 167

Manning, C. E. (1997). Coupled reaction and flow in subduction zones: Silica metasomatism in the mantle wedge. In *Fluid flow and transport in rocks* (pp. 139–148). Springer.
65, 73

Materna, K., Bartlow, N., Wech, A., Williams, C., & Bürgmann, R. (2019, November). Dynamically Triggered Changes of Plate Interface Coupling in Southern Cascadia. *Geophysical Research Letters*, *46*(22), 12890–12899. https://doi.org/10.1029/2019GL084395
175

Maury, J., Ide, S., Cruz-Atienza, V. M., & Kostoglodov, V. (2018, February). Spatiotemporal Variations in Slow Earthquakes Along the Mexican Subduction Zone. *Journal of Geophysical Research: Solid Earth*, *123*(2), 1559–1575. https://doi.org/10.1002/2017JB014690
112, 142

McDowell-Boyer, L. M., Hunt, J. R., & Sitar, N. (1986). Particle transport through porous media. *Water Resources Research*, *22*(13), 1901–1921. https://doi.org/10.1029/WR022i013p01901
74, 77, 81, 97

Melnik, O., Lyakhovsky, V., Shapiro, N. M., Galina, N., & Bergal-Kuvikas, O. (2020a). Deep long period volcanic earthquakes generated by degassing of volatile-rich basaltic magmas. *Nature Communications*, *11*(1), 3918. https://doi.org/10.1038/s41467-020-17759-4
66

Melnik, O., Lyakhovsky, V., Shapiro, N. M., Galina, N., & Bergal-Kuvikas, O. (2020b, December). Deep long period volcanic earthquakes generated by degassing of volatile-rich basaltic magmas. *Nature Communications*, *11*(1), 3918.

https://doi.org/10.1038/s41467-020-17759-4
171
Miller, S. A., & Nur, A. (2000). Permeability as a toggle switch in fluid-controlled crustal processes. *Earth and Planetary Science Letters*, 14.
76, 81
Mitchell, T. M., & Faulkner, D. R. (2008, November). Experimental measurements of permeability evolution during triaxial compression of initially intact crystalline rocks and implications for fluid flow in fault zones. *Journal of Geophysical Research*, *113*(B11), B11412. https://doi.org/10.1029/2008JB005588
17, 170
Miyazawa, M., Brodsky, E. E., & Mori, J. (2008, October). Learning from dynamic triggering of low-frequency tremor in subduction zones. *Earth, Planets and Space*, *60*(10), e17-e20. https://doi.org/10.1186/BF03352858
145
Muñoz-Montecinos, J., Angiboust, S., Garcia-Casco, A., Glodny, J., & Bebout, G. (2021, March). Episodic hydrofracturing and large-scale flushing along deep subduction interfaces: Implications for fluid transfer and carbon recycling (Zagros Orogen, southeastern Iran). *Chemical Geology*, 120173. https://doi.org/10.1016/j.chemgeo.2021.120173
16, 104, 112, 139, 168, 169
Muñoz-Montecinos, J., Angiboust, S., Garcia-Casco, A., & Raimondo, T. (2022). Shattered veins elucidate brittle creep processes in the deep slow slip and tremor region. *submitted to Tectonics*.
112
Müller, T. M., Gurevich, B., & Lebedev, M. (2010, September). Seismic wave attenuation and dispersion resulting from wave-induced flow in porous rocks — A review. *GEOPHYSICS*, *75*(5), 75A147-75A164. https://doi.org/10.1190/1.3463417
58
Nakajima, J., & Hasegawa, A. (2016, December). Tremor activity inhibited by well-drained conditions above a megathrust. *Nature Communications*, *7*(1), 13863. https://doi.org/10.1038/ncomms13863
112
Nakajima, J., & Uchida, N. (2018, May). Repeated drainage from megathrusts during episodic slow slip. *Nature Geoscience*, *11*(5), 351–356. https://doi.org/10.1038/s41561-018-0090-z
108
Nicholson, C., & Wesson, R. L. (1992). Triggered earthquakes and deep well activities. *Pure and Applied Geophysics*, *139*, 18.
2
Norton, D., & Knapp, R. (1977). Transport phenomena in hydrothermal systems: The nature of porosity. *Am. J. Sci.;(United States)*, *277*.
104
Obara, K. (2002, May). Nonvolcanic Deep Tremor Associated with Subduction in Southwest Japan. *Science*, *296*(5573), 1679–1681. https://doi.org/10.1126/science.1070378
4, 44, 64, 108, 171
Obara, K., Hirose, H., Yamamizu, F., & Kasahara, K. (2004, December). Episodic slow slip events accompanied by non-volcanic tremors in southwest Japan subduction zone: EPISODIC SLOW SLIP AND TREMOR IN JAPAN. *Geophysical Research Letters*, *31*(23). https://doi.org/10.1029/2004GL020848

4, 8, 14, 108

Ohmi, S., & Obara, K. (2002, August). Deep low-frequency earthquakes beneath the focal region of the Mw 6.7 2000 Western Tottori earthquake: DLF BENEATH THE FOCAL REGION OF THE 2000 WESTERN TOTTORI EQ. *Geophysical Research Letters*, *29*(16), 54-1-54-4. https://doi.org/10.1029/2001GL014469
9, 170

Okamoto, A. (2019, April). Formation of silica particles from supercritical fluids and its impacts on the hydrological properties in the crust. In *EGU General Assembly Conference Abstracts* (Vol. 21, p. 4614). Vienna.
74

Omori, F. (1895). *On the after-shocks of earthquakes* (Unpublished doctoral dissertation). The University of Tokyo.
2

Ordaz, M., & Singh, S. K. (1992, February). Source spectra and spectral attenuation of seismic waves from Mexican earthquakes, and evidence of amplification in the hill zone of Mexico City. *Bulletin of the Seismological Society of America*, *82*(1), 24–43.
33, 53, 57

Ottemöller, L., Shapiro, N. M., Krishna Singh, S., & Pacheco, J. F. (2002, January). Lateral variation of *Lg* wave propagation in southern Mexico: *LG* WAVE PROPAGATION IN SOUTHERN MEXICO. *Journal of Geophysical Research: Solid Earth*, *107*(B1), ESE 3-1-ESE 3-13. https://doi.org/10.1029/2001JB000206
53, 54

Pardo, M., & Suárez, G. (1995, July). Shape of the subducted Rivera and Cocos plates in southern Mexico: Seismic and tectonic implications. *Journal of Geophysical Research: Solid Earth*, *100*(B7), 12357–12373. https://doi.org/10.1029/95JB00919
70

Payero, J. S., Kostoglodov, V., Shapiro, N., Mikumo, T., Iglesias, A., Pérez-Campos, X., & Clayton, R. W. (2008). Nonvolcanic tremor observed in the Mexican subduction zone. *Geophysical Research Letters*, *35*(7).
27, 30, 64, 69

Peacock, S. M., Christensen, N. I., Bostock, M. G., & Audet, P. (2011, May). High pore pressures and porosity at 35 km depth in the Cascadia subduction zone. *Geology*, *39*(5), 471–474. https://doi.org/10.1130/G31649.1
64, 65, 93

Pedregosa, F., Varoquaux, G., Gramfort, A., Michel, V., Thirion, B., Grisel, O., … Duchesnay, É. (2011). Scikit-learn: Machine Learning in Python. *Journal of Machine Learning Research*, *12*(85), 2825–2830.
117

Perez-Campos, X., Kim, Y., Husker, A., Davis, P., Clayton, R., Iglesias, A., … Gurnis, M. (2008). Horizontal subduction and truncation of the Cocos plate beneath Central Mexico. *Geophysical Research Letters*, *35*, L18303. https://doi.org/10.1029/2008GL035127
27

Piccoli, F., Ague, J. J., Chu, X., Tian, M., & Brovarone, A. V. (2021, February). Field-based evidence for intra-slab high-permeability channel formation at eclogite-facies conditions during subduction. *Geochemistry, Geophysics, Geosystems*. https://doi.org/10.1029/2020GC009520
95, 168

Platt, J. P., Xia, H., & Schmidt, W. L. (2018, December). Rheology and stress in subduction

zones around the aseismic/seismic transition. *Progress in Earth and Planetary Science*, *5*(1), 24. https://doi.org/10.1186/s40645-018-0183-8
5, 65, 66, 112, 169

Poiata, N., Vilotte, J.-P., Shapiro, N. M., Supino, M., & Obara, K. (2021, November). Complexity of Deep Low-Frequency Earthquake Activity in Shikoku (Japan) Imaged From the Analysis of Continuous Seismic Data. *Journal of Geophysical Research: Solid Earth*, *126*(11). https://doi.org/10.1029/2021JB022138
4, 11, 14, 69, 109, 111, 112, 113, 119, 138, 153

Prasianakis, N. I., Curti, E., Kosakowski, G., Poonoosamy, J., & Churakov, S. V. (2017, December). Deciphering pore-level precipitation mechanisms. *Scientific Reports*, *7*(1), 13765. https://doi.org/10.1038/s41598-017-14142-0
19

Press, W. H., Teukolsky, S. A., Vetterling, W. T., & Flannery, B. P. (2007). *Numerical Recipes - The Art of Numerical Computing* (Third Edition ed.). Cambridge University Press.
80

Prieto, G. A., Shearer, P. M., Vernon, F. L., & Kilb, D. (2004). Earthquake source scaling and self-similarity estimation from stacking P and S spectra. *Journal of Geophysical Research: Solid Earth*, *109*(B8).
26, 42, 43

Radiguet, M., Cotton, F., Vergnolle, M., Campillo, M., Walpersdorf, A., Cotte, N., & Kostoglodov, V. (2012a). Slow slip events and strain accumulation in the Guerrero gap, Mexico. *Journal of Geophysical Research: Solid Earth*, *117*(B4).
27

Radiguet, M., Cotton, F., Vergnolle, M., Campillo, M., Walpersdorf, A., Cotte, N., & Kostoglodov, V. (2012b). Slow slip events and strain accumulation in the Guerrero gap, Mexico. *Journal of Geophysical Research: Solid Earth*, *117*(B4). https://doi.org/10.1029/2011JB008801
71

Raleigh, C. B., Healy, J. H., & Bredehoeft, J. D. (1972). Faulting and crustal stress at Rangely, Colorado. *Washington DC American Geophysical Union Geophysical Monograph Series*, *16*, 275–284.
2

Ramsay, J. G. (1980, March). The crack–seal mechanism of rock deformation. *Nature*, *284*(5752), 135–139. https://doi.org/10.1038/284135a0
104

Rice, J. R. (1992, January). Chapter 20 Fault Stress States, Pore Pressure Distributions, and the Weakness of the San Andreas Fault. In B. Evans & T.-f. Wong (Eds.), *International Geophysics* (Vol. 51, pp. 475–503). Academic Press. https://doi.org/10.1016/S0074-6142(08)62835-1
13, 17

Rogers, G. (2003, June). Episodic Tremor and Slip on the Cascadia Subduction Zone: The Chatter of Silent Slip. *Science*, *300*(5627), 1942–1943. https://doi.org/10.1126/science.1084783
4, 8, 14, 64, 108, 170

Roman, D. C., & Cashman, K. V. (2006). The origin of volcano-tectonic earthquake swarms. *Geology*, *34*(6), 457. https://doi.org/10.1130/G22269.1
171

Ross, Z. E., Cochran, E. S., Trugman, D. T., & Smith, J. D. (2020, June). 3D fault architecture controls the dynamism of earthquake swarms. *Science*, *368*(6497), 1357–1361.

https://doi.org/10.1126/science.abb0779
2, 3, 13, 175

Ross, Z. E., Rollins, C., Cochran, E. S., Hauksson, E., Avouac, J.-P., & Ben-Zion, Y. (2017, August). Aftershocks driven by afterslip and fluid pressure sweeping through a fault-fracture mesh: Aftershocks From Afterslip and Fluids. *Geophysical Research Letters*, *44*(16), 8260–8267. https://doi.org/10.1002/2017GL074634
3

Ross, Z. E., Trugman, D. T., Hauksson, E., & Shearer, P. M. (2019, May). Searching for hidden earthquakes in Southern California. *Science*, *364*(6442), 767–771. https://doi.org/10.1126/science.aaw6888
2

Rousset, B., Bürgmann, R., & Campillo, M. (2019, February). Slow slip events in the roots of the San Andreas fault. *Science Advances*, *5*(2), eaav3274. https://doi.org/10.1126/sciadv.aav3274
2, 8, 64

Royer, A. A., Thomas, A. M., & Bostock, M. G. (2015, January). Tidal modulation and triggering of low-frequency earthquakes in northern Cascadia. *Journal of Geophysical Research: Solid Earth*, *120*(1), 384–405. https://doi.org/10.1002/2014JB011430
45, 65

Rubin, A. M., & Armbruster, J. G. (2013, December). Imaging slow slip fronts in Cascadia with high precision cross-station tremor locations: IMAGING SLOW SLIP FRONTS IN CASCADIA. *Geochemistry, Geophysics, Geosystems*, *14*(12), 5371–5392. https://doi.org/10.1002/2013GC005031
2, 5

Rubinstein, J. L., Gomberg, J., Vidale, J. E., Wech, A. G., Kao, H., Creager, K. C., & Rogers, G. (2009, February). Seismic wave triggering of nonvolcanic tremor, episodic tremor and slip, and earthquakes on Vancouver Island. *Journal of Geophysical Research*, *114*, B00A01. https://doi.org/10.1029/2008JB005875
45, 65

Rubinstein, J. L., La Rocca, M., Vidale, J. E., Creager, K. C., & Wech, A. G. (2008, January). Tidal Modulation of Nonvolcanic Tremor. *Science*, *319*(5860), 186–189. https://doi.org/10.1126/science.1150558
45, 65

Saffer, D. M. (2015, February). The permeability of active subduction plate boundary faults. *Geofluids*, *15*(1-2), 193–215. https://doi.org/10.1111/gfl.12103
66, 94, 168

Saffer, D. M., & Tobin, H. J. (2011, May). Hydrogeology and Mechanics of Subduction Zone Forearcs: Fluid Flow and Pore Pressure. *Annual Review of Earth and Planetary Sciences*, *39*(1), 157–186. https://doi.org/10.1146/annurev-earth-040610-133408
65

Sahimi, M., Mehrabi, A. R., Mirzaee, N., & Rassamdana, H. (1999). The Effect of Asphalt Precipitation on Flow Behavior and Production of a Fractured Carbonate Oil Reservoir During Gas Injection. *Transport in porous media*, *41*(3), 325–347.
18, 67, 75, 167, 175

Sammis, C. G., & Bostock, M. G. (2021). A Granular Jamming Model for Low-Frequency Earthquakes. *Journal of Geophysical Research: Solid Earth*, *126*(7), e2021JB021963. https://doi.org/10.1029/2021JB021963
65, 66

Scholz, C. H. (1998, January). Earthquakes and friction laws. *Nature*, *391*(6662), 37–42.

https://doi.org/10.1038/34097
5

Segall, P., & Rice, J. R. (1995, November). Dilatancy, compaction, and slip instability of a fluid-infiltrated fault. *Journal of Geophysical Research: Solid Earth*, *100*(B11), 22155–22171. https://doi.org/10.1029/95JB02403
67

Segall, P., Rubin, A. M., Bradley, A. M., & Rice, J. R. (2010, December). Dilatant strengthening as a mechanism for slow slip events. *Journal of Geophysical Research*, *115*(B12), B12305. https://doi.org/10.1029/2010JB007449
17, 108

Shapiro, N. M., Campillo, M., Kaminski, E., Vilotte, J.-P., & Jaupart, C. (2018, October). Low-Frequency Earthquakes and Pore Pressure Transients in Subduction Zones. *Geophysical Research Letters*, *45*(20), 11,083–11,094. https://doi.org/10.1029/2018GL079893
8, 9, 10, 13, 15, 19, 44, 45, 66, 68, 77, 95, 112, 168

Shapiro, N. M., Droznin, D., Droznina, S., Senuykov, S., Gusev, A., & Gordeev, E. (2017). Deep and shallow long-period volcanic seismicity linked by fluid-pressure transfer. *Nature Geosci.*, *10*, 442–445. https://doi.org/10.1038/ngeo2952
67

Shapiro, N. M., Droznin, D. V., Droznina, S. Y., Senyukov, S. L., Gusev, A. A., & Gordeev, E. I. (2017, June). Deep and shallow long-period volcanic seismicity linked by fluid-pressure transfer. *Nature Geoscience*, *10*(6), 442–445. https://doi.org/10.1038/ngeo2952
171, 172, 173

Shapiro, S. A. (2015). *Fluid-Induced Seismicity*. Cambridge: Cambridge University Press. https://doi.org/10.1017/CBO9781139051132
11

Shapiro, S. A., Rothert, E., Rath, V., & Rindschwentner, J. (2002, January). Characterization of fluid transport properties of reservoirs using induced microseismicity. *GEOPHYSICS*, *67*(1), 212–220. https://doi.org/10.1190/1.1451597
3, 11

Shelly, D. R. (2015, February). Complexity of the deep San Andreas Fault zone defined by cascading tremor. *Nature Geoscience*, *8*(2), 145–151. https://doi.org/10.1038/ngeo2335
70

Shelly, D. R., Beroza, G. C., & Ide, S. (2007a, October). Complex evolution of transient slip derived from precise tremor locations in western Shikoku, Japan: EVOLUTION OF TRANSIENT SLIP. *Geochemistry, Geophysics, Geosystems*, *8*(10), n/a-n/a. https://doi.org/10.1029/2007GC001640
4, 11, 12

Shelly, D. R., Beroza, G. C., & Ide, S. (2007b, March). Non-volcanic tremor and low-frequency earthquake swarms. *Nature*, *446*(7133), 305–307. https://doi.org/10.1038/nature05666
5, 7, 37, 65, 108

Shelly, D. R., Beroza, G. C., Ide, S., & Nakamula, S. (2006, July). Low-frequency earthquakes in Shikoku, Japan, and their relationship to episodic tremor and slip. *Nature*, *442*(7099), 188–191. https://doi.org/10.1038/nature04931
5, 45, 64, 108, 109

Shelly, D. R., Hill, D. P., Massin, F., Farrell, J., Smith, R. B., & Taira, T. (2013, September). A

fluid-driven earthquake swarm on the margin of the Yellowstone caldera: FLUID-DRIVEN YELLOWSTONE SWARM. *Journal of Geophysical Research: Solid Earth*, *118*(9), 4872–4886. https://doi.org/10.1002/jgrb.50362
3

Shibazaki, B., & Iio, Y. (2003). On the physical mechanism of silent slip events along the deeper part of the seismogenic zone. *Geophysical Research Letters*, *30*(9).
65

Shillington, D. J., Bécel, A., Nedimović, M. R., Kuehn, H., Webb, S. C., Abers, G. A., … Mattei-Salicrup, G. A. (2015, December). Link between plate fabric, hydration and subduction zone seismicity in Alaska. *Nature Geoscience*, *8*(12), 961–964. https://doi.org/10.1038/ngeo2586
141, 142

Shvab, I., & Sadus, R. J. (2015, July). Thermophysical properties of supercritical water and bond flexibility. *Physical Review E*, *92*(1), 012124. https://doi.org/10.1103/PhysRevE.92.012124
93

Sibson, R. (1992, September). Implications of fault-valve behaviour for rupture nucleation and recurrence. *Tectonophysics*, *211*(1-4), 283–293. https://doi.org/10.1016/0040-1951(92)90065-E
15, 67, 108

Sibson, R. H. (2013, July). Stress switching in subduction forearcs: Implications for overpressure containment and strength cycling on megathrusts. *Tectonophysics*, *600*, 142–152. https://doi.org/10.1016/j.tecto.2013.02.035
108

Singh, S. K., Mena, E., Anderson, J. G., Quaas, R., & Lermo, J. (1990). Source spectra and RMS acceleration of Mexican subduction zone earthquakes. *pure and applied geophysics*, *133*(3), 447–474.
53

Skarbek, R. M., & Rempel, A. W. (2016, February). Dehydration-induced porosity waves and episodic tremor and slip: POROSITY WAVES AND ETS. *Geochemistry, Geophysics, Geosystems*, *17*(2), 442–469. https://doi.org/10.1002/2015GC006155
13, 17

Song, T.-R. A., Helmberger, D. V., Brudzinski, M. R., Clayton, R. W., Davis, P., Perez-Campos, X., & Singh, S. K. (2009, April). Subducting Slab Ultra-Slow Velocity Layer Coincident with Silent Earthquakes in Southern Mexico. *Science*, *324*(5926), 502–506. https://doi.org/10.1126/science.1167595
64

Souzy, M., Zuriguel, I., & Marin, A. (2020, June). Transition from clogging to continuous flow in constricted particle suspensions. *Physical Review E*, *101*(6), 060901. https://doi.org/10.1103/PhysRevE.101.060901
18, 123, 167

Sparks, R. S. J., Annen, C., Blundy, J. D., Cashman, K. V., Rust, A. C., & Jackson, M. D. (2019, February). Formation and dynamics of magma reservoirs. *Philosophical Transactions of the Royal Society A: Mathematical, Physical and Engineering Sciences*, *377*(2139), 20180019. https://doi.org/10.1098/rsta.2018.0019
173

Supino, M., Poiata, N., Festa, G., Vilotte, J. P., Satriano, C., & Obara, K. (2020, April). Self-similarity of low-frequency earthquakes. *Scientific Reports*, *10*(1), 1–9. https://doi.org/10.1038/s41598-020-63584-6

7, 8, 26, 36, 42, 52, 65

Taetz, S., John, T., Bröcker, M., Spandler, C., & Stracke, A. (2018, January). Fast intraslab fluid-flow events linked to pulses of high pore fluid pressure at the subducted plate interface. *Earth and Planetary Science Letters*, *482*, 33–43. https://doi.org/10.1016/j.epsl.2017.10.044
16, 66, 77, 112, 139, 168, 169

Takahashi, T., Obana, K., Yamamoto, Y., Nakanishi, A., Kodaira, S., & Kaneda, Y. (2014, October). *S* wave attenuation structure on the western side of the Nankai subduction zone: Implications for fluid distribution and dynamics: S-wave Q-1 in Nankai subduction zone. *Journal of Geophysical Research: Solid Earth*, *119*(10), 7805–7822. https://doi.org/10.1002/2014JB011103
54, 58

Tanaka, Y., Suzuki, T., Imanishi, Y., Okubo, S., Zhang, X., Ando, M., … Hiraoka, Y. (2018, December). Temporal gravity anomalies observed in the Tokai area and a possible relationship with slow slips. *Earth, Planets and Space*, *70*(1), 25. https://doi.org/10.1186/s40623-018-0797-5
16, 66, 108

Tarling, M. S., Smith, S. A., Rooney, J. S., Viti, C., & Gordon, K. C. (2021, June). A common type of mineralogical banding in serpentine crack-seal veins. *Earth and Planetary Science Letters*, *564*, 116930. https://doi.org/10.1016/j.epsl.2021.116930
16, 112, 139, 141, 169

Tarling, M. S., Smith, S. A. F., & Scott, J. M. (2019, December). Fluid overpressure from chemical reactions in serpentinite within the source region of deep episodic tremor. *Nature Geoscience*, *12*(12), 1034–1042. https://doi.org/10.1038/s41561-019-0470-z
95

Tenthorey, E., & Cox, S. F. (2006). Cohesive strengthening of fault zones during the interseismic period: An experimental study. *Journal of Geophysical Research*, *111*(B9), B09202. https://doi.org/10.1029/2005JB004122
17, 170

Thomas, A. M., Beroza, G. C., & Shelly, D. R. (2016). Constraints on the source parameters of low-frequency earthquakes on the San Andreas Fault. *Geophysical Research Letters*, *43*(4), 1464–1471. https://doi.org/10.1002/2015GL067173
8, 36, 37

Thomas, A. M., Nadeau, R. M., & Bürgmann, R. (2009, December). Tremor-tide correlations and near-lithostatic pore pressure on the deep San Andreas fault. *Nature*, *462*(7276), 1048–1051. https://doi.org/10.1038/nature08654
65

Thomson, D. J. (1982). Spectrum estimation and harmonic analysis. *Proceedings of the IEEE*, *70*(9), 1055–1096.
33

Tompkins, M. J., & Christensen, N. I. (2001, April). Ultrasonic *P* - and *S* -wave attenuation in oceanic basalt. *Geophysical Journal International*, *145*(1), 172–186. https://doi.org/10.1046/j.0956-540x.2001.01354.x
45

Ukawa, M., & Ohtake, M. (1987). A monochromatic earthquake suggesting deep-seated magmatic activity beneath the Izu-Ooshima Volcano, Japan. *Journal of Geophysical Research*, *92*(B12), 12649. https://doi.org/10.1029/JB092iB12p12649
8, 171

van den Ende, M., Chen, J., Ampuero, J.-P., & Niemeijer, A. (2018, May). A comparison

between rate-and-state friction and microphysical models, based on numerical simulations of fault slip. *Tectonophysics*, *733*, 273–295. https://doi.org/10.1016/j.tecto.2017.11.040
65

van Keken, P. E., Hacker, B. R., Syracuse, E. M., & Abers, G. A. (2011, January). Subduction factory: 4. Depth-dependent flux of H_2O from subducting slabs worldwide. *Journal of Geophysical Research*, *116*(B1). https://doi.org/10.1029/2010JB007922
45, 65, 77, 95

Wang, K., & Bilek, S. L. (2014, January). Invited review paper: Fault creep caused by subduction of rough seafloor relief. *Tectonophysics*, *610*, 1–24. https://doi.org/10.1016/j.tecto.2013.11.024
141, 142

Wang, Z., & Zhao, D. (2019, December). Updated attenuation tomography of Japan subduction zone. *Geophysical Journal International*, *219*(3), 1679–1697. https://doi.org/10.1093/gji/ggz339
56

Wannamaker, P. E., Evans, R. L., Bedrosian, P. A., Unsworth, M. J., Maris, V., & McGary, R. S. (2014, November). Segmentation of plate coupling, fate of subduction fluids, and modes of arc magmatism in Cascadia, inferred from magnetotelluric resistivity. *Geochemistry, Geophysics, Geosystems*, *15*(11), 4230–4253. https://doi.org/10.1002/2014GC005509
65, 108, 141

Warren-Smith, E., Fry, B., Wallace, L., Chon, E., Henrys, S., Sheehan, A., … Lebedev, S. (2019, May). Episodic stress and fluid pressure cycling in subducting oceanic crust during slow slip. *Nature Geoscience*, 1. https://doi.org/10.1038/s41561-019-0367-x
16, 66, 108

Warren-Smith, E., Chamberlain, C. J., Lamb, S., & Townend, J. (2017, July). High-Precision Analysis of an Aftershock Sequence Using Matched-Filter Detection: The 4 May 2015 M_L 6 Wanaka Earthquake, Southern Alps, New Zealand. *Seismological Research Letters*, *88*(4), 1065–1077. https://doi.org/10.1785/0220170016
51

Wech, A. G. (2010, July). Interactive Tremor Monitoring. *Seismological Research Letters*, *81*(4), 664–669. https://doi.org/10.1785/gssrl.81.4.664
151

Wech, A. G., & Creager, K. C. (2007, November). Cascadia tremor polarization evidence for plate interface slip. *Geophysical Research Letters*, *34*(22), L22306. https://doi.org/10.1029/2007GL031167
9, 170

Wech, A. G., & Creager, K. C. (2008, October). Automated detection and location of Cascadia tremor. *Geophysical Research Letters*, *35*(20), L20302. https://doi.org/10.1029/2008GL035458
109, 111, 151

Wech, A. G., & Creager, K. C. (2011, September). A continuum of stress, strength and slip in the Cascadia subduction zone. *Nature Geoscience*, *4*(9), 624–628. https://doi.org/10.1038/ngeo1215
70, 71, 96, 112, 139

Wech, A. G., Thelen, W. A., & Thomas, A. M. (2020, May). Deep long-period earthquakes generated by second boiling beneath Mauna Kea volcano. *Science*, *368*(6492), 775–779. https://doi.org/10.1126/science.aba4798

67, 175

Wei, S., Avouac, J.-P., Hudnut, K. W., Donnellan, A., Parker, J. W., Graves, R. W., … Eneva, M. (2015, July). The 2012 Brawley swarm triggered by injection-induced aseismic slip. *Earth and Planetary Science Letters*, *422*, 115–125. https://doi.org/10.1016/j.epsl.2015.03.054
3

Wei, X., Xu, J., Liu, Y., & Chen, X. (2021, December). The slow self-arresting nature of low-frequency earthquakes. *Nature Communications*, *12*(1), 5464. https://doi.org/10.1038/s41467-021-25823-w
8

Wibberley, C. A. J. (2002, November). Hydraulic diffusivity of fault gouge zones and implications for thermal pressurization during seismic slip. *Earth, Planets and Space*, *54*(11), 1153–1171. https://doi.org/10.1186/BF03353317
93

Williams, R. T., Mozley, P. S., Sharp, W. D., & Goodwin, L. B. (2019, November). U-Th Dating of Syntectonic Calcite Veins Reveals the Dynamic Nature of Fracture Cementation and Healing in Faults. *Geophysical Research Letters*, *46*(22), 12900–12908. https://doi.org/10.1029/2019GL085403
66

Yabe, S., Baltay, A. S., Ide, S., & Beroza, G. C. (2014, August). Seismic-Wave Attenuation Determined from Tectonic Tremor in Multiple Subduction Zones. *Bulletin of the Seismological Society of America*, *104*(4), 2043–2059. https://doi.org/10.1785/0120140032
56, 57

Yamazaki, T., & Okamura, Y. (1989, March). Subducting seamounts and deformation of overriding forearc wedges around Japan. *Tectonophysics*, *160*(1), 207–229. https://doi.org/10.1016/0040-1951(89)90392-2
143, 144, 147

Zhu, W., Allison, K. L., Dunham, E. M., & Yang, Y. (2020, December). Fault valving and pore pressure evolution in simulations of earthquake sequences and aseismic slip. *Nature Communications*, *11*(1), 4833. https://doi.org/10.1038/s41467-020-18598-z
15, 66, 67

List of Figures

List of Tables